

**MODELING RESIDUAL STRESS EVOLUTION IN
THERMAL SPRAY COATINGS USING HYBRID
COMPUTATIONAL APPROACH**

BY
ABBA ABDULHAMID ABUBAKAR

A Dissertation Presented to the
DEANSHIP OF GRADUATE STUDIES
KING FAHD UNIVERSITY OF PETROLEUM & MINERALS
DHAHRAN, SAUDI ARABIA

In Partial Fulfillment of the
Requirements for the Degree of

DOCTOR OF PHILOSOPHY
In

MECHANICAL ENGINEERING

DECEMBER, 2018


KING FAHD UNIVERSITY OF PETROLEUM & MINERALS

DHAHRAN- 31261, SAUDI ARABIA

DEANSHIP OF GRADUATE STUDIES

This thesis, written by ABBA ABDULHAMID ABUBAKAR under the direction of his thesis advisor and approved by his thesis committee, has been presented and accepted by the Dean of Graduate Studies, in partial fulfillment of the requirements for the degree of **DOCTOR OF PHILOSOPHY IN MECHANICAL ENGINEERING.**



Dr. Zuhair M. Gasem
Department Chairman



Dr. Salam A. Zummo
Dean of Graduate Studies

22/4/19
DATE





Dr. Abul Fazal M. Arif
(Advisor)


Dr. S. Sohail Akhtar
(Co-Advisor)


Dr. Nekar Merah
(Member)


Dr. Nasser M. Al Aqeeli
(Member)


Dr. Anwar Ul-Hamid
(Member)

[Dedicated to my family |

ACKNOWLEDGMENTS

Completing this PhD study has been a truly transformative experience for me and it would not have been possible without the support and guidance of many people.

Foremost, I would like to express my special appreciation and thanks to my advisor, Dr. Abul Fazal M. Arif. He has been a tremendous mentor throughout my PhD studies. During course work, he ensured that I built very strong background of my research area. Similarly, his advice on research and career has been invaluable. Without his guidance and constant feedback, this PhD would not have been achievable. I could not have imagined having a better advisor and mentor for my PhD study.

Also, my sincere gratitude goes to my co-advisor, Dr. S. Sohail Akhtar, who happened to be my master's thesis advisor. Through him, I developed strong analytical skills and learnt how to deal with complex problems in a systematic way. That greatly helped me during my PhD studies. Also, he has been always supportive during my PhD studies. His guidance helped me in all the time of research and writing of this thesis.

I would also like to thank the rest of my thesis committee members: Prof. Necar Merah, Prof. Nasir Al-Agili, and Dr. Anwar-ul-Hamid, for their encouragement, insightful comments, and hard questions. I would also like to extend my sincere gratitude to the graduate coordinator, Dr. Esmail M. A. Mokheimer, and the chairman of mechanical engineering department, Dr. Zuhair M. Gasem, for giving me all the required support at KFUPM. I also appreciate the support of Dr. Jaafar Albinmousa and Dr. Khaled S. Al-thel during my PhD studies at KFUPM.

I thank my fellow lab mates in Stress Analysis Laboratory.: Hafiz Kabeer Chisti, Usama Siddiqui, Ibrahim Balarabe Mansir, and Dr. Akeem Yusuf Adesina, for the stimulating discussions, and for the sleepless nights we spent together. Also, I thank all my friends and the Nigerian community in KFUPM.

My appreciation also goes to Dr. Abubakar B. Aliyu, Dr. Isah A. Yola, Dr. Ibrahim Abdullahi, Dr. Abdullahi A. Adamu and all other lecturers at the department of mechanical engineering, Bayero University Kano. They spent a lot of effort in training me during my five years of bachelor's degree study. I also appreciate all supports given to me by B.U.K. during my graduate study at KFUPM.

Last but not the least; I would like to thank my entire family, parents, wife, daughter, brothers, sisters and other relatives, for supporting me spiritually throughout my study at KFUPM.

TABLE OF CONTENTS

ACKNOWLEDGMENTS.....	V
TABLE OF CONTENTS.....	VII
LIST OF TABLES.....	XI
LIST OF FIGURES.....	XIII
LIST OF ABBREVIATIONS.....	XXI
ABSTRACT.....	XXII
ملخص الرسالة.....	XXIV
CHAPTER 1 INTRODUCTION.....	1
1.1 Background	1
1.2 Statement of the problem	4
1.3 Motivation for research.....	5
1.3.1 Challenges in residual stress measurement	5
1.3.2 Dependence of residual stresses on the process parameters.....	6
1.3.3 Lack of effective residual stress prediction models.....	7
1.3.4 Influence of residual stress on coating failure	8
1.4 Research goals and approach	9
1.5 Dissertation outline	10
CHAPTER 2 LITERATURE REVIEW	13
2.1 Sources of residual stress	13
2.1.1 Thermal mismatch stress.....	13

2.1.2	Peening stress	17
2.1.3	Stress induced by substrate surface pre-treatment.....	18
2.1.4	Other sources: multiphase systems, discontinuities, etc..	19
2.2	Difficulty in measuring residual stresses: Why modeling?	19
2.3	Analytical models for prediction of residual stress	25
2.3.1	Theoretical quenching stress models	25
2.3.2	Semi-empirical quenching stress models.....	29
2.3.3	Post-deposition mismatch stress models	31
2.3.4	Overall residual stress model	37
2.3.5	Comparison of various analytical models	39
2.4	Numerical models for the prediction of the residual stresses.....	46
2.4.1	Modeling of post-deposition mismatch stresses using conventional thermal stress analysis ...	47
2.4.2	Modeling of residual stress evolution using element birth-kill approach	48
2.4.3	Issues with element birth-kill approach	58
2.4.4	Modeling of localized stresses using image-based FEM.....	60
2.5	Summary of literature survey.....	64
2.5.1	Analytical model for residual stress in coatings.....	64
2.5.2	Finite element modeling of residual stress in coatings	65
CHAPTER 3 RESEARCH OBJECTIVES AND METHODOLOGY		71
3.1	Objectives	72
3.2	Scope and limitations.....	72
3.3	Research methodology	73
CHAPTER 4 HYBRID COMPUTATIONAL MODEL		78
4.1	General modeling assumptions adopted.....	79

4.2	Governing equations	79
4.2.1	Spray process modeling	79
4.2.2	Geometric modeling of splats	81
4.2.3	Thermo-mechanical modeling	85
4.2.4	Initial and Boundary conditions	91
4.3	Numerical Model	93
4.3.1	SPH formulation	93
4.3.2	Finite element formulation	95
4.4	Numerical implementation	99
4.5	Material properties and simulation parameters	103
 CHAPTER 5 CHARACTERIZATION, MECHANICAL TESTS AND RESIDUAL STRESS MEASUREMENTS.....		107
5.1	Samples preparation and process parameters.....	108
5.2	Material characterization and mechanical tests	109
5.3	Residual stress measurements using hole drilling method	112
5.3.1	Procedure for the experiment	112
5.3.2	Calibration of influence coefficients	115
5.3.3	Estimation of stress profile by Tsui and Clyne model	119
 CHAPTER 6 MICROSCOPY, EFFECTIVE PROPERTIES AND RESIDUAL STRESS PROFILE		122
6.1	Coating characterization.....	122
6.2	Mechanical properties obtained from microindentation	133
6.3	Residual stress profiling with hole drilling method	135
6.4	Cohesive strength of the coatings.....	148
6.5	Concluding remarks.....	149

CHAPTER 7 SINGLE SPLAT ANALYSIS.....	151
7.1 Splat formation on point cloud	151
7.1.1 Validation of point cloud deposition model	152
7.1.2 Single droplet deposition	154
7.1.3 Effect of process parameters on splat formation.....	158
7.2 Geometric modeling of splats	160
7.3 Thermo-mechanical analysis using FEM	164
7.3.1 Validation of numerical model	164
7.3.2 Numerical prediction of temperature distribution and residual stress field developed in single YSZ splat without consideration of microcracks	169
7.3.3 Numerical prediction of temperature distribution, residual stress field and cracks formation in single YSZ splat.....	176
7.3.4 Numerical prediction of temperature distribution and residual stress field developed in single Ni-20%Al splat.....	186
7.4 Concluding remarks	191
CHAPTER 8 MULTIPLE SPLATS FORMATION, INTERACTION AND RESIDUAL STRESS EVOLUTION.....	193
8.1 Splat formation on point cloud	193
8.2 Simulation of coating microstructure in form of FE mesh.....	201
8.3 Numerical prediction of temperature distribution, residual stress and microcracks in multiple YSZ splats	204
8.4 Numerical prediction of temperature distribution and residual stress developed in multilayered YSZ coating.....	212
8.4.1 Temperature distribution.....	215
8.4.2 Residual stress evolution	222
8.5 Numerical difficulties commonly encountered with the splat-by-splat model	237
8.6 Concluding remarks	238

CHAPTER 9 EFFECTIVE PREDICTION OF RESIDUAL STRESS IN MULTILAYERED COATINGS.....	239
9.1 From point cloud to merged-mesh model	240
9.2 Numerical prediction of temperature distribution and residual stress developed in conventional YSZ coating deposited on SS310	248
9.2.1 Temperature distribution	248
9.2.2 Residual stress evolution	256
9.3 Numerical prediction of temperature distribution and residual stress in conventional Ni-20%Al coating deposited on SS310.....	263
9.3.1 Temperature distribution	264
9.3.2 Residual stress evolution	268
9.4 Concluding remarks.....	274
CHAPTER 10 CONCLUSIONS AND RECOMMENDATIONS.....	276
10.1 Major findings from experimental work.....	277
10.2 Major findings from numerical work	278
10.3 Recommendation for future directions	280
10.3.1 Point cloud deposition model.....	280
10.3.2 Point cloud processing algorithms	281
10.3.3 Thermo-mechanical finite element modeling	282
10.3.4 Experimental measurements.....	283
REFERENCES.....	284
APPENDIX	301
VITAE.....	312

LIST OF TABLES

Table 1-1: Dependence of process parameters on residual stresses	6
Table 2-1: Material properties of selected coatings for analysis	40
Table 4-1: Material inputs data to simulation	104
Table 5-1: Coating powder characteristics and process parameters	109
Table 5-2: Parameters required for estimation of stress profile with Tsui and Clyne model	120
Table 6-1: Surface roughness parameter values	132
Table 6-2: Mechanical properties of coating specimens obtained from microindentation tests	134
Table 7-1: Mesh convergence test and analysis of computational time for single droplet analysis.....	167
Table 8-1: Information on tetrahedral element size and quality	202
Table 8-2: Analysis of computational times for multi-layer analysis.....	214
Table 9-1: Comparison of degree of freedoms (dof) of layer-by-layer mesh with that of merged mesh	241
Table-A1: Comparison of numerical results obtained with birth-death technique with experiments	301

LIST OF FIGURES

Figure 1-1: A typical description of Air Plasma Spraying of TBC showing (a) feedstock powder (b) a single splat (cracked due to thermal shock) (c) assemblage of splats forming the coating [12]	3
Figure 2-1: Quenching stress formation (at microscale) during single splat solidification	15
Figure 2-2: Bending of substrate material (during deposition) due to quenching stresses developed after deposition of coating sub-layer.....	15
Figure 2-3: Bending of substrate/coating after (a) coating deposition, (b) post-deposition cooling.....	17
Figure 2-4: Peening stress developed during coating deposition.....	18
Figure 2-5: Comparison of theoretical and measured quenching stress developed in (a) alumina (ceramic), (b) nickel (metallic) coatings as a function of substrate temperature.	28
Figure 2-6: Variation of Z values along the thickness direction (for multilayer coatings)32	32
Figure 2-7: Comparing various prediction of thermal misfit (or mismatch) stresses for (a) TBC system deposited at 1000°C, (b) Alumina coating deposited at 840°C, (c) NiCoCrAlY coating deposited at 620°C, (d) variation of misfit stresses with temperature change as predicted by Zhang et al.	44
Figure 2-8: Effect of coating thickness on thermal mismatch (or misfit) stresses (using Zhang’s model and same properties as that Table-1) (a) for Alumina coating, (b) for NiCoCrAlY coating.....	45
Figure 2-9: (a) Effect of gradient exponent on variation of misfit stress along coating thickness for TBC (interface is at $z=0$ according to Eq.(12)), (b) Effect of quenching stress on alumina and NiCoCrAlY coatings (using Tsui and Clyne’s model).....	45
Figure 2-10: Residual stress variation along the thickness of alumina coating; (a) Effect of substrate preheating to 393 K on residual stress state of alumina coatings [65], (b) Effect of deposition/process cooling rate on residual stresses induced in alumina coatings [102].....	51
Figure 2-11: (a) Effect of coating thickness and substrate pre-heating to 80 °C on residual stress state of HVOF Ti coating [126], [127], (b) Variation of simulated thermal, peening and final residual stresses along thickness of SS 316-coating - effect of particle velocity demonstrated ([128], [129])	57
Figure 3-1: A typical schematic for thermal spray process deposition on flat substrate ..	73
Figure 3-2: Proposed methodology for the multiscale computational model.....	73
Figure 4-1: Release/impact of sprayed droplets on substrate in layer-wise fashion (axis directions are shown)	91

Figure 4-2: Proposed hybrid computational approach: (a) droplets impact, spread and interaction using SPH, (b) Splats solidification and residual stress evolution using FEM.....	93
Figure 4-3: Flowchart for the numerical implementation of the proposed approach	102
Figure 4-4: Flowchart for implementation of PC-to-FE conversion algorithms	103
Figure 5-1: (a) Hole drilling set-up by Vishay micro-measurements (drilling YSZ sample), (b) strain gauge indicator, (c) drilling of NiCrAl coating sample, (d) bonded strain gauge having soldered wires.	115
Figure 5-2: Mapped mesh used for hole drilling simulation: (a) top view, (b) side view	118
Figure 5-3: Computational simulation of hole drilling experiment: (a) at start of drilling, (b) after drilling, (c) mapped mesh used for analysis	119
Figure 6-1: Optical micrograph showing cross-sectional view of Ni-20% Al coating: (a) & (b) shown at two different locations	125
Figure 6-2: Real microstructure image of Ni-20% Al coating: (a) x500 magnification, (b) Zoomed region 1, (c) Zoomed region 2	126
Figure 6-3: Optical micrograph showing cross-sectional view of TBC: (a) 160 μm YSZ top coat, 40 μm NiCrAl bond coat & (b) 280 μm YSZ top coat , 80 μm NiCrAl bond coat and (c) Zoomed region 1 from (a), (d) Zoomed region 2 from (b)	127
Figure 6-4: SEM micrograph showing cross-sectional view of Ni-20% coating layers showing: (a) total coating thickness and inhomogeneities at smaller magnification, (b)-(d) pores and interlamellar cracks at higher magnification	128
Figure 6-5: SEM micrograph showing cross-sectional view of coating layers showing: (a)-(b) thickness and inhomogeneities of the coating layers at smaller magnification, (c)-(d) cracks and pores at higher magnification	129
Figure 6-6: SEM micrograph showing surface morphology of the coating layer at low and high magnifications: (a)-(b) Ni-20% Al, (c)-(d) YSZ	131
Figure 6-7: Surface roughness profile obtained for 3D optical micrograph: (a) Ni-20% Al specimen, (b) TBC specimen	132
Figure 6-8: Loading-unloading curves obtained from micro-indentation: (a) test conducted on along cross section and (b) test conducted on surface (each curve is average of 10 experiments)	133
Figure 6-9: Optical micrographs showing indented coating at: (a) 1000 magnification and (b) 200 magnification.....	134
Figure 6-10: Effective coating properties obtained from nanoindentation: (a) Elastic modulus and (b) Hardness	135
Figure 6-11: Variation elastic strain in x-direction during hole drilling process at depth of: (a) 0 μm , (b) 360 μm and (c) 800 μm	137

Figure 6-12: 3D plots of in-plane stress field developed during drilling: (a) normal stress in x-direction, (b) normal stress in y-direction and (c) shear stress in xy plane.....	138
Figure 6-13: Variation elastic strain in x-direction during hole drilling process at depth of: (a) 0 μm , (b) 360 μm and (c) 800 μm	139
Figure 6-14: 3D plots of in-plane stress field developed during drilling: (a) normal stress in x-direction, (b) normal stress in y-direction and (c) shear stress in xy plane.....	140
Figure 6-15: calibrated nominal strain and stresses developed in x and y directions: (a) & (c) for Ni-20%Al and (b) & (d) for TBC	141
Figure 6-16: Influence coefficients used for calculation of stress profile: (a) Ni-20%Al and (b) TBC	142
Figure 6-17: Effects of anisotropy on influence coefficients for: (a) Ni-20%Al coating and (b) TBC	142
Figure 6-18: Micro-strain readings measured at each drilling increment: (a) Ni-20%Al and (b) TBC	143
Figure 6-19: Residual stress profile developed along depth: (a) Ni-20%Al and (b) TBC (thick sample).....	146
Figure 6-20: Results obtained from thin TBC sample: (a) Incremental strain reading and (b) Residual stress profile	147
Figure 6-21: Stress profiles developed along depth showing: (a) repeatability for Ni-20%Al coating, (b) repeatability for TBC, (c) influence of orthotropy for Ni-20%Al coating, (d) influence of orthotropy for TBC.	148
Figure 6-22: (a) critical load required for cohesive failure of coatings, (b) optical micrograph showing scratch track	149
Figure 7-1: Comparison of spread factor variation with initial impact velocity for YSZ droplet as predicted by SPH (current results) and CEL/experiment (by Zhu et al. [164]).....	153
Figure 7-2: Ni-20%Al droplet deposited with initial impact velocity of 100 m/s obtained with: (a) volume of fluid (VOF) method [189] (b) current deposition model, (c) experiments (only final splat geometry shown) [189].....	154
Figure 7-3: Qualitative comparison of results for YSZ droplet deposited with high initial impact velocity of 190 m/s; (a) experiments [188], (b) CEL model [164], (c) current SPH model.....	155
Figure 7-4: 3D displacement of YSZ droplet (mm) deposited with an initial impact velocity of 60 m/s.....	156
Figure 7-5: Velocity magnitude (mm/s) during deformation of YSZ droplet (in 2D) with initial impact velocity of 60 m/s	156
Figure 7-6: Splat formation process at various spreading time for Ni-20%Al droplet: (a)- (b) Side view, (c) top view.....	157

Figure 7-7: Temporal variation of maximum spread factor for the Ni-20%Al and YSZ droplets considered in Fig. 24 and Fig. 25.....	158
Figure 7-8: Influence of droplet impact velocity and temperature on spread factor for (a) 60 μm size YSZ droplet, (b) 54 μm size Ni droplet	160
Figure 7-9: PC-to-FE mesh conversion for splats ((a)-(d)) of intricate shapes	162
Figure 7-10: Conversion from PC-to-FE mesh for several splat geometries having various geometrical complexities	163
Figure 7-11: (a) Coarse mesh and (b) Fine mesh of single splat (sectional view).....	168
Figure 7-12: Convergence of numerical results: (a)-(b) temperature & (c)-(d) deposition stress.....	169
Figure 7-13: (a) variation of system energy with time & (b) comparison of stress profile to that of the analytical model.....	169
Figure 7-14: (a) Temperature evolution ($^{\circ}\text{C}$) and (b) quenching stress (MPa) evolution during splat solidification	173
Figure 7-15: (a) temperature profile along depth at centroid, (b) temperature profile along radial direction at 3 μm above the surface of the coating, (c) radial deposition stress variation depth at the centroid, (d) radial deposition stress variation along the radial direction at 3 μm above the surface of the coating	174
Figure 7-16: Temporal variation of (a) temperature, (b) stress at three points, A, B and C	175
Figure 7-17: (a) Residual stress profile along the axial direction, (b) Residual stress along the radial direction	175
Figure 7-18: Residual stress developed in (a) x-direction and (b) y-direction for single splat analysis	176
Figure 7-19: Cross section view of YSZ splat showing evolution of (a) temperature ($^{\circ}\text{C}$), (b) von Mises quenching stress (MPa) and (c) damage parameter at 0, 300 and 2000 μs	179
Figure 7-20: Top view of splat showing final state of splat at room temperature: (a) cracked YSZ splat, (b) equivalent tensile cracking strain, and (c) von Mises residual stress	180
Figure 7-21: SEM images of cracked YSZ splat deposited on SS310 showing: (a) & (b) spalled splat deposited at low substrate temperature, (c)&(d) well adhered splat deposited at higher substrate temperature [183].....	181
Figure 7-22: (a) Temperature profile along radius of splat, (b) temporal variation of temperature, (c) radial stress profile developed along radius of splat, and (d) temporal variation of radial stress ((a) and (c) were taken at 3 μm above coating interface, while (b) and (d) were taken at integration points of three elements)	184

Figure 7-23: Temporal variation of (a) first principal stress, (b) in-plane shear stress and (c) equivalent cracking strain at integration points of three elements, (d) radial residual stress profile developed along radius and thickness of coating.....	185
Figure 7-24: Cross section view of Ni splat showing evolution of (a) temperature ($^{\circ}\text{C}$), (b) equivalent plastic strain and (c) von Mises quenching stress before and after solidification (i.e. at 0 and 100 μs)	188
Figure 7-25: (a) Temperature profile along radius of splat, (b) temporal variation of temperature, (c) radial stress profile developed along radius of splat, and (d) temporal variation of radial stress ((a) and (c) were taken at 3 μm above coating interface, while (b) and (d) were taken at integration points of three elements).....	189
Figure 7-26: Cross section view of Ni splats final distribution of: (a) equivalent plastic strain & (b) residual stresses after cooling to room temperature	192
Figure 8-1: Possible scenarios for the interaction of two Ni droplets initially having offset of: (a) 1 mm, (b) 2 mm, (c) 3 mm, and (d) 4 mm	195
Figure 8-2: Demonstration of multiple droplets interaction: (a) two far YSZ droplets, (b) two near-by YSZ droplets, (c) nine near-by YSZ droplets (first layer), (d) nine near-by YSZ droplets (third layer).....	196
Figure 8-3: Droplet impact on pre-deposited splats: (a) new splat formed directly on top of old splat, (b) new splat formed half-way on top of old splat.....	197
Figure 8-4: Droplet impact on rough surface: (a) splats geometry formed after deposition on bond coat, (b) zoomed view of splats interface formed.....	198
Figure 8-5: Velocity magnitude after multi-droplet deposition for (a) second layer and (b) fourth layer	200
Figure 8-6: FE mesh for interacting splats deposited on rough target surface	203
Figure 8-7: 3D tetrahedral FE mesh of splats deposited in five layers.....	203
Figure 8-8: Top view of two far away splats: (a) before solidification starts, (b) after solidification (at 500 μs), (c) quenching stress, (d) formation of microcracks	207
Figure 8-9: Top view of directly touching splats: (a) before solidification, (b) after solidification (at 400 μs), (c) quenching stress, (d) formation of microcracks	208
Figure 8-10: Temperature distribution after solidification of two interacting splats after 4000 μs : (a) one directly on top of the other and (b) two droplets having offset of 0.05 mm.....	209
Figure 8-11: Quenching stress after solidification of two interacting splats after 4000 μs : (a) one directly on top of the other and (b) two droplets having offset of 0.05 mm.	209

Figure 8-12: Temperature distribution during solidification of interacting splats that impact on rough target surface after: (a) 0 μ s, (b) 400 μ s, and (c) 2000 μ s	210
Figure 8-13: Quenching stress field during solidification of interacting splats that impact on rough target surface after: (a) 0 μ s, (b) 400 μ s, and (c) 2000 μ s	211
Figure 8-14: Microcracks formed during solidification of interacting splats that impact on rough target surface: (a) isometric view and (b) cross section view.....	212
Figure 8-15: Evolution of temperature after deposition of (a) second layer and (b) fourth layer.....	216
Figure 8-16: (a) Top view, (b) side view, and (c) cross-sectional view of temperature distribution developed after deposition of 5th layer	217
Figure 8-17: Five points selected for the analysis of results.....	219
Figure 8-18: Temperature profile developed along depth after deposition of 5th layer, (b) Temperature profile developed along depth after deposition of 1st-5th layer, (c) Evolution of temperature during deposition of 5th layer and (d) Evolution of temperature during deposition of 5th layer.....	220
Figure 8-19: (a) Variation of temperature along width and length of coating, (b) Thermal history of three different points from start of deposition to end of cool-down	220
Figure 8-20: Quenching (von Mises) stress field developed after deposition of (a) second and (b) fourth layer	223
Figure 8-21: Cross-sectional view of von Mises stress field for (a) deposition stress and (b) residual stress in five-layer coating in: (a) x-direction, (b) y-direction	224
Figure 8-22: Bi-axial in-plane stress profiles at A: (a) stress in x-direction, and (b) stress in y-direction	228
Figure 8-23: Comparison of residual stress profile (at A) with experimental results: (a) Stress in x-direction and (b) Stress in y-direction.....	229
Figure 8-24: Comparison of stress profiles developed along point A: (a) in-plane normal deposition and residual stresses (acting in the z-direction), (b) von Mises deposition and residual stresses, (c) shear deposition and residual stress profile (acting in the xy-direction), and (d) maximum principal deposition and residual stress profile.....	231
Figure 8-25: Comparison of bi-axial in-plane stress profiles (acting in the x-direction) developed along various points: (a) B, (b) C, (c) D, (d) E.....	232
Figure 8-26: Comparison of residual stress profiles at point B: (a) in y-direction, (b) in z-direction, (c) shear in xy-direction, (d) von Mises.....	233
Figure 8-27: Comparison of residual stress profiles at point C: (a) in y-direction, (b) in z-direction, (c) shear in xy-direction, (d) von Mises.....	234
Figure 8-28: Comparison of residual stress profiles at point D: (a) in y-direction, (b) in z-direction, (c) shear in xy-direction, (d) von Mises.....	234

Figure 8-29: Bi-axial in-plane residual stress profile (acting in the x-direction) from C-to-B at 10 μm above interface, (b) Downward displacement of coating-substrate layers (in positive z-direction) during deposition and post-deposition stage.....	236
Figure 9-1: Conversion to merged mesh for Pass-1: (a) top view and (b) bottom view (LEFT-layer-by-layer mesh, RIGHT-merged mesh).....	242
Figure 9-2: Conversion to merged mesh for Pass-1: (a) side view and (b) isometric view (TOP-layer-by-layer mesh, BOTTOM-merged mesh)	243
Figure 9-3: Conversion to merged mesh for Pass-2: (a) top view and (b) bottom view (LEFT-layer-by-layer mesh, RIGHT-merged mesh).....	244
Figure 9-4: Conversion to merged mesh for Pass-2: (a) side view and (b) isometric view (TOP-layer-by-layer mesh, BOTTOM-merged mesh)	245
Figure 9-5: (a) 3D view of simulated coating microstructure, (b) 3D cross sectional view of simulated coating microstructure.....	246
Figure 9-6: Cross sectional views of simulated coating microstructure at the cut planes along: (a) $x=125\text{ mm}$, (b) $x=100\text{ mm}$, (c) $x =74$, (d) $x=-75$, (e) $x=-100$, and (f) $x=-125$	247
Figure 9-7: Temperature distribution ($^{\circ}\text{C}$) developed during solidification of first pass of YSZ coating: (a) at 0 μs , (b) at 100 μs , (c) at 200 μs , (d) at 400 μs , and (d) at 500 μs , and (e) at 1000 μs	250
Figure 9-8: Temperature distribution ($^{\circ}\text{C}$) developed during solidification of third pass of YSZ coating: (a) at 4000 μs , (b) at 5000 μs , (c) at 5500 μs , (d) at 6000 μs , and (d) at 7000 μs , and (e) at 9000 μs	251
Figure 9-9: (a) to (f)- Temperature distribution ($^{\circ}\text{C}$) at the selected cross sections after complete solidification of fourth pass of YSZ coating	254
Figure 9-10: (a) Temperature profile along depth at points A, B, C, D and E, (b) Temperature profile along width of coating middle section, (c) Temporal variation of temperature points within specific passes during deposition, (d) Temporal variation of temperature at points A, C and E on coating surface	255
Figure 9-11: Quenching (von Mises) stress field developed during solidification of first pass of YSZ coating: (a) at 0 μs , (b) at 100 μs , (c) at 200 μs , (d) at 400 μs , and (d) at 500 μs , and (e) at 1000 μs	257
Figure 9 12: Quenching (von Mises) stress field developed during solidification of third pass of YSZ coating: (a) at 4000 μs , (b) at 6000 μs , (c) at 9000 μs	258
Figure 9-13: Temperature distribution at the selected cross sections after complete solidification of fourth pass of YSZ coating.....	259
Figure 9-14: Quenching and residual stress profile along depth of coating: (a) Stress in X-direction at A, (b) Stress in X-direction at B, (c) Stress in Y-direction at A, and (d) Stress in Y-direction at B.....	262

Figure 9-15: Quenching and residual stress profile along depth of coating: (a) Stress in Z-direction at A, (b) Stress in XY-direction at A, (c) von Mises stress at A, and (d) Equivalent tensile strain at A	263
Figure 9-16: Temperature distribution ($^{\circ}\text{C}$) developed during solidification of Ni-20%Al coating: (a) first pass at 0 μs , (b) at first pass at 100 μs , (c) first pass at 500 μs , (d) second pass at 1300 μs , and (e) third pass at 2100 μs	266
Figure 9-17: (a) to (f)- Temperature distribution ($^{\circ}\text{C}$) at the selected cross sections after complete solidification of fourth pass of YSZ coating	267
Figure 9-18: (a) Temperature profile along depth at points A, B, C, D and E, (b) Temperature profile along width of coating surface, (c) Temporal variation of temperature points within specific passes during deposition, (d) Temporal variation of temperature at points A, C and E on coating surface	268
Figure 9-19: Temperature distribution ($^{\circ}\text{C}$) developed during solidification of Ni-20%Al coating: (a) first pass at 0 μs , (b) at first pass at 100 μs , (c) first pass at 500 μs , (d) second pass at 1300 μs , and (e) third pass at 2100 μs	271
Figure 9-20: (a) to (f)- Temperature distribution ($^{\circ}\text{C}$) at several cross sections after complete solidification of fourth pass of YSZ coating	272
Figure 9-21: Quenching and residual stress profile along depth of coating: (a) Stress in X-direction at A, (b) Stress in X-direction at B, (c) Stress in Y-direction at A, and (d) Stress in Y-direction at B	273
Figure 9-22: Quenching and residual stress profile along depth of coating: (a) Stress in Z-direction at A, (b) Stress in XY-direction at A, (c) von Mises stress at A, and (d) Equivalent tensile strain at A	274
Figure A1: Conversion to merged mesh for Pass-3: (a) top view and (b) bottom view (LEFT-layer-by-layer mesh, RIGHT-merged mesh)	303
Figure A2: Conversion to merged mesh for Pass-3: (a) side view and (b) isometric view (LEFT-layer-by-layer mesh, RIGHT-merged mesh)	304
Figure A3: Conversion to merged mesh for Pass-4: (a) top view and (b) bottom view (LEFT-layer-by-layer mesh, RIGHT-merged mesh)	305
Figure A4: Conversion to merged mesh for Pass-3: (a) side view and (b) isometric view (LEFT-layer-by-layer mesh, RIGHT-merged mesh)	306
Figure A5: Five points selected for analysis: A (0,0), B(-125, 125), C(125,125), D(125,-125), and E (-125,-125). All dimensions in mm.	307
Figure A6: Quenching stress developed after solidification of fourth pass of YSZ coating: (a) von Mises stress, (b) normal stress in x-direction, (c) normal stress in y-direction, (d) shear stress in xy-plane, and (e) maximum principal stress....	308
Figure A7: Displacement field (mm) developed after solidification of fourth pass of YSZ coating: (a) displacement magnitude and (b) displacement in x-direction ...	309
Figure A8: Displacement field (mm) developed after solidification of fourth pass of YSZ coating: (a) displacement magnitude and (b) displacement in x-direction ...	310

Figure A9: Quenching stress developed after solidification of fourth pass of Ni-20%Al coating: (a) normal stress in x-direction, (b) normal stress in y-direction, and (c) shear stress in xy-plane..... 311

LIST OF ABBREVIATIONS

PC	:	Point Cloud
FE	:	Finite Element
SPH	:	Smooth Particle Hydrodynamics
FEM	:	Finite Element Model
FEA	:	Finite Element Analysis
TSC	:	Thermal Spray Coating
APS	:	Air Plasma Spray Process
HVOF	:	High-Velocity-Oxy-Fuel
D-gun	:	Detonation gun
1D	:	one dimension(al)
2D	:	two dimension(al)
3D	:	three dimension(al)
STL	:	Stereolithography
RVE	:	Representative Volume Element

ABSTRACT

Full Name : [ABBA ABDULHAMID ABUBAKAR]
Thesis Title : [Modeling Residual Stress Evolution in Thermal Spray Coatings using Hybrid Computational Approach]
Major Field : [MECHANICAL ENGINEERING]
Date of Degree : [December 2018]

Thermal spray coatings are usually deposited by first heating the feedstock (powder) material into a series of molten or semi-molten droplets before being applied to the substrate surface. As a result of large deformation, complex interaction and material mismatch occurring during the thermal spray process, residual stresses are induced. Residual stress is one of the main contributing factors that determine the constitutive behavior and lifetime of coatings.

In the present study, an innovative numerical modeling approach for thermal spray coating deposition process is proposed, implemented and evaluated. The proposed approach is hybrid in nature and able to predict evolution of residual stress very effectively. Being hybrid, the approach combines the use of point cloud and finite elements to model droplets impact/deformation and thermo-mechanical analyses of deposited coating respectively. The theoretical framework developed in the present work is the first contribution where vigorous process modeling (taking process parameters as inputs) is used to numerically predict the evolution of residual stress in thermal spray coatings. Even though the approach was implemented with help of standard packages (i.e. ABAQUS and MeshLab), it is implementable in any platform and regardless of the numerical methods used for discretization or types of coating-substrate materials used.

The hybrid computational approach is used to predict residual stresses and associated defects developed in plasma-sprayed ceramic (YSZ) and metallic (Ni-20%Al) coatings deposited on stainless steel substrate. The numerical predictions are validated against experimental results obtained from microscopic studies, mechanical tests and hole drilling experiments. The experimental results show that, the metallic Ni-20%Al coating developed tensile residual stresses, while the YSZ top coat of TBC developed compressive residual stresses. In both cases, the residual stress profiles developed along depth of coating layers are highly non-linear, position-dependent as well as equi-biaxial due to highly inhomogeneous nature of the coating layers. Furthermore, very low shear stresses were measured for the Ni-20%Al and YSZ coating layers.

The numerical results obtained with the hybrid computational model show that, the use of realistic process parameters yields more reliable estimation of residual stresses in thermal spray coatings. The model predicts a residual stress profile that is position-dependent and highly non-linear along the length and thickness of the Ni-20%Al and YSZ coating layer. Also, the numerical results show that the residual stress profiles developed in the Ni-20%Al and YSZ coating layers are equi-biaxial and exhibits very low shear stress. It is found that, the Ni-20%Al coating developed a tensile residual stress profile along depth. While, the YSZ top coat developed compressive stress profile along depth. Both stress profiles compare well to the results obtained experimentally. Furthermore, it is found that splat solidification and presence of internal defects in coating layer strongly affect the evolution of temperature and residual stress in thermal spray coatings. In future works, the new approach can serve as a versatile tool for effective prediction of the relationship between coating process parameters, residual stress and failure mechanisms.

ملخص الرسالة

الاسم الكامل: أبا عبد الحميد أبو بكر

عنوان الرسالة: نمذجة تطور الإجهاد المتبقي في الطلاء بالرش الحراري باستخدام منهج حسابي هجين
التخصص: هندسة ميكانيكا

تاريخ الدرجة العلمية: ديسمبر 2018

عادةً ما يتم ترسيب الطلاء بالرش الحراري عن طريق تسخين المواد الأولية (المسحوق) أولاً في سلسلة من القطرات المنصهرة أو شبه المنصهرة قبل تطبيقها على سطح الجسم. نتيجة للتغير الشكلي الكبير والتفاعل المعقد وعدم تطابق المواد التي تحدث أثناء عملية الرش الحراري ، يتولد إجهاد متبقي بعد العملية. الإجهاد المتبقي هو أحد العوامل المساهمة الرئيسية التي تحدد السلوك التأسيسي وعمر الطلاء.

في هذه الدراسة ، يتم اقتراح وتنفيذ طريقة مبتكرة للنمذجة العددية لعملية ترسيب طلاء الرش الحراري. المنهج المقترح هجين بطبيعته وقادر على التنبؤ بتطور الإجهاد المتبقي بشكل فعال للغاية. كونه هجين، فإن النهج يجمع بين استخدام طريقتي الغمامة النقطية والعناصر المحدودة، لنمذجة تأثير القطرات وتغيرها شكلياً، ولنمذجة التحليلات الحرارية الميكانيكية للطلاء المترسبة، على التوالي.

يمثل الإطار النظري الذي تم تطويره في العمل الحالي أول مساهمة يتم فيها استخدام نمذجة عملية قوية (مع أخذ عوامل العملية كمدخلات) للتنبؤ العددي بتطور الإجهاد المتبقي. على الرغم من أن هذا النهج تم تنفيذه بمساعدة بعض الحزم القياسية، فإنه قابل للتنفيذ في أي منصة وبغض النظر عن الطرق العددية المستخدمة للتقدير، أو أنواع مواد طلاء الجسم المستخدمة.

يستخدم المنهج الحسابي الهجين للتنبؤ بالجهود المتبقية والعيوب المرتبطة بها والتي تم تطويرها في السيراميك المطلي بالبلازما والطلاء المعدني (نيكل – 20% ألومنيوم) المرشوش على الركيزة المصنوعة من الفولاذ المقاوم للصدأ. تتم مقارنة التنبؤات العددية بالنتائج التجريبية من الدراسات الميكروسكوبية، التجارب الميكانيكية وتجارب ثقب الحفر. النتائج التجريبية تظهر أن الطلاء المعدني (نيكل – 20% ألومنيوم) ينتج إجهاد شد متبقي، بينما الطلاء

العلوي (YSZ) من (TBC) ينتج إجهاد ضغط متبقي. في الحالتين فإن الشكل الناتج للإجهاد المتبقي في عمق طبقات الطلاء غير خطي بدرجة كبيرة ويعتمد على الموقع. بالإضافة إلى ذلك، كمية منخفضة جدا من إجهاد القص وجدت في طبقات الطلاءين (نيكل – 20% ألومنيوم) و (YSZ).

أظهرت النتائج العددية التي تم الحصول عليها باستخدام النموذج الحسابي الهجين ، أن استخدام معلمات العملية الواقعية ينتج عنه تقدير أكثر موثوقية للضغوط المتبقية في الطلاء بالرش الحراري. يتنبأ النموذج بمظهر جانبي من الإجهاد المتبقي يعتمد على الموضع وغير خطي بدرجة كبيرة بطول وسمك طبقة الطلاءين (نيكل – 20% ألومنيوم) و (YSZ). أيضا ، أظهرت النتائج العددية أن ملامح الإجهاد المتبقية التي تم تطويرها في طبقات الطلاءين (نيكل – 20% ألومنيوم) و (YSZ) هي ثنائية المحور وتتميز بإجهاد قص منخفض للغاية. لقد وجد أن طلاء (نيكل – 20% ألومنيوم) قد طور شكل إجهاد متبقي شدي على طول العمق. في حين طورت الطبقة العلوية YSZ شكل إجهاد ضغطي على طول العمق. كل من ملامح الإجهاد مقارنة بشكل جيد مع النتائج التي تم الحصول عليها تجريبيا. علاوة على ذلك ، فقد وجد أن تصلب بعض الأجزاء ووجود عيوب داخلية في طبقة الطلاء تؤثر بشدة على تطور درجة الحرارة والإجهاد المتبقي في الطلاء بالرش الحراري. في الأعمال المستقبلية ، يمكن أن يكون النهج الجديد بمثابة أداة متعددة الاستخدامات للتنبؤ الفعال بالعلاقة بين عوامل عملية الطلاء والضغط المتبقي وآليات الفشل.

CHAPTER 1

INTRODUCTION

1.1 Background

Thermal spray coatings (TSCs) are advanced coatings that are deposited on a substrate surface through heating of a feedstock material (usually in the form of powder or wire) to molten state (as demonstrated in Figure 1-1) [1]. The thermal energy supplied during thermal spray process softens the feedstock material and enables effective deformation of the molten droplets to form a highly-dense coating layer [2]. Thermal spray processes are used extensively in highly advanced industries, such as aerospace, automotive, electronics, telecommunications, energy, consumer products, nuclear, medical, and oil and gas industries. In most of the applications, TSCs are used to improve the thermal, wear, cohesive, corrosion or chemical resistance of substrate surfaces. However, new types of coating applications such as anti-bacterial coatings, osmotic filtering, biocompatible coatings, superconductive coatings, functionally graded coatings, etc. are recently developed [3].

TSCs are classified according to the way the heating of the feedstock material is carried out, i.e. either through combustion or direct (joule) heating [2], [4]. Among the combustion-driven processes, high-velocity oxy-fuel (HVOF) process is the most suitable spray process nowadays due to its numerous advantages over the common flame spray

process [5], [6]. It utilizes combustion for the heating of feedstock material into molten or semi-molten droplets, which are propelled at high velocities before their impact on the substrate surface. HVOF is considered more powerful than other thermal spray processes (such as plasma and flame spray) because it results in highly dense coating layer with higher adhesion strength, consumes less energy, and exhibits lower oxide content [7]–[9]. The main drawbacks of HVOF includes its high cost, pollution to the environment and reaction of combustion gasses with coating material. On the other hand, plasma spray process is more common among the processes that use direct electric (joule) heating for droplet deposition. With high energy thermal plasma, the feedstock (powder) particles are first molten into multiple droplets before being propelled (or deposited) to the substrate surface. Plasma spray is widely used due to cost, lower overall environmental impact, and flexibility with regards to coating materials [2], [10]. However, due to the lower deposition rate (with droplets impact velocity ranging from 150-400 m/s) [11], it often results in coating layer having high level of porosity. This is not the case with HVOF because droplets impact velocities can be as high as 1000 m/s [11]. A common drawback to all thermal spray processes is that the interaction between the various process (input) parameters makes it difficult to control the coating quality [3]. Consequently, high residual stresses are developed, and the coating microstructure is filled with various forms of defects (e.g. pores, cracks, splat interfaces, second-phase particles, etc.) which significantly affect the properties and lifetime of the coating layer.

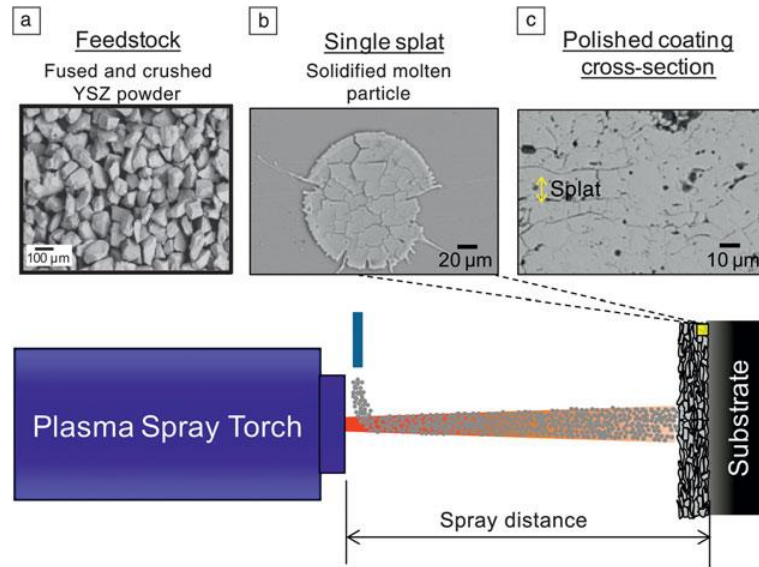


Figure 1-1: A typical description of Air Plasma Spraying of TBC showing (a) feedstock powder (b) a single splat (cracked due to thermal shock) (c) assemblage of splats forming the coating [12]

Residual stresses are stresses that remain in a structure after manufacturing, processing or removal of external loads. Mostly, residual stresses occur due to change in shape, size or properties of solid materials. They can be useful or harmful depending on the type of materials or products involved. Tensile residual stresses are known to be more harmful than compressive residual stresses due to the tendency for premature failure through crack propagation. Residual stresses developed in TSCs affect their adhesion strength, cohesive strength, thermal resistance, corrosion resistance, and service lifetime [13]–[20]. Residual stresses are known to evolve during and after coating deposition; thus, their prediction is highly complicated due to overdependence on process history. The deposition stresses (occurring at microscale and mesoscale) can be due to the sudden cooling or solidification of splats, peening action of droplets on a pre-deposited layer or high thermal gradient developed during deposition [21]. Post-deposition stresses (occurring at macroscale) are developed after cooling the coating to room temperature due to differential contraction or mismatch in coefficient of thermal expansion (CTE)

between the coating and substrate. Similarly, substrate geometry and prior surface treatment (e.g. grit blasting or roller burnishing) significantly influence the residual stress state of the sprayed coatings [22]–[24]. During service, residual stresses may be affected severely by large loads, chemical reactions, phase transformations, through-thickness thermal gradient, creep, etc. [25]–[28]. Thus, the overall residual stress state is the aggregate of stresses developed because of various phenomena occurring at different length and time scales. In fact, the residual stress state often reverses (i.e. from tension to compression or vice versa) after the coating is cooled to room temperature. This leads to complexity and uncertainty in determining the nature and magnitude of the residual stress state of TSCs [10]. Therefore, full tracking of the residual stress state will help in effective optimization of thermal spray process for enhanced coating performance and durability.

1.2 Statement of the problem

Previously, major experiments (such as X-ray diffraction, curvature measurements, neutron diffraction, and hole-drilling methods) have been used to estimate residual stresses developed in coatings. In a literature survey [29], it is found that many challenges encountered during the experiments have limited their feasibility for detailed analysis. On the other hand, realistic numerical modeling of the residual stresses developed in coatings has been very challenging due to common numerical difficulties encountered during computations. Using the existing numerical schemes, problems such as excessive mesh distortion, computational intensity, convergence difficulties, and interaction of multiple domains make effective residual stress modeling not feasible. Lagrangian schemes (such as finite element, and finite volume), mainly pose problems of excessive mesh distortion

which leads to high computational intensity and numerical convergent difficulties. On the other hand, Eulerian schemes (such as phase field, level-set, volume of fluid, etc) has inherent problems of domain (interface) coalescence and high computational costs. Therefore, the current dissertation mainly deals with the development of an alternative numerical scheme that can effectively predict the evolution of residual stress and internal defects in TSCs. The scheme should not only be robust but also computationally inexpensive and able to link coating process parameters with residual stress evolution in coatings.

1.3 Motivation for research

1.3.1 Challenges in residual stress measurement

Over the years, various experimental set-ups for measurement of residual stresses in TSCs have been developed [13]. X-ray diffraction, curvature measurements, neutron diffraction, indentation, and incremental hole-drilling methods are frequently used. However, each of the experimental methods has its own limitations related to specimen and material types, cost, and resolution of measurements. With curvature method, it is often difficult to transform the data into a stress state and careful monitoring of beam deflection using sensors is required [13]. X-ray diffraction method is restricted to crystalline coatings and gives inaccurate (surface) stress values due to limited X-rays penetration depth and uncertainties in determining the elastic parameters [30], [31] . Neutron diffraction is very expensive and difficult to obtain sufficiently accurate data due to low scattering intensities [32]. Incremental hole-drilling method [33], [34] is time-consuming, highly restrictive, semi-destructive and does not give sufficiently accurate results for very thin and low yield coating layer. In indentation method, it is difficult to

translate the results into a stress state due to the narrow region of indentation depth. A common problem with all methods discussed is that, the resolution of measurement is very low. Consequently, they result in rough stress estimates which do not account for the presence of imperfections (such as pores, cracks, inclusions, etc) that fill the microstructure of coatings. Furthermore, extensive residual stress analysis cannot be done experimentally due to the various limitations discussed previously. Therefore, the development of an innovative numerical approach for the prediction of residual stresses developed in these coatings is essential.

1.3.2 Dependence of residual stresses on the process parameters

Residual stresses are highly dependent on the spray process conditions (or parameters) as demonstrated in Table 1-1. Table 1-1 was developed after an intensive literature survey on the effect of process parameters/conditions on residual stresses developed in TSCs. The effect of the process parameters on residual stresses was assigned relative weight values which indicates the influence of various parameters on residual stresses developed in coatings. From Table 1-1, the parameters having the strongest influence on residual stresses are initial particle (impact) temperature, velocity, substrate temperature, properties mismatch between coating and substrate and the final cooling rate. Therefore, a robust computational tool is required for effective investigation of the spray process parameters on residual stress state of coatings.

Table 1-1: Dependence of process parameters on residual stresses

Process parameter	Effect on residual stress
Increase in particle size	+2
Increase in particle velocity	-3

Increase particle temperature	+4
Increase in final cooling rate	+/-5
Increase in plasma spray rate	-3
Increase in surface roughness or preparation	+/-2
Increase in structural and thermal properties	+/-5
Increase in thickness of coating	+/-2
Increase in substrate curvature	+/-1
Increase in substrate temperature	+/-4

1.3.3 Lack of effective residual stress prediction models

Due to the limitations of experimental measurement of residual stresses in TSCs, several residual stress models have been developed. Analytical models were mostly derived using the theory of elasticity and several assumptions were adopted to simplify their closed-form solutions. With the recent advancement in computation, numerical modeling is more popular for the analysis of engineering systems. As finite element method (FEM) is more common than other numerical methods, it has been used by many researchers to predict residual stresses in TSCs [26]. Most of the researchers use the element birth-kill (FEM) approach to track the evolution of residual stress in TSCs. Its advantage is that, the approach considers both deposition and post-deposition stresses during the computation. Image-based finite element schemes have been recently used to predict localized stresses developed due to the imperfections (e.g. cracks, pores, inclusions, etc.) that fill coating microstructure [35], [36]. An attempt to predict residual stresses by coupling computational fluid dynamics (CFD) with finite element method [37] was also made. All these models have various issues as discussed extensively in Chapter 2. The

results given by those models were sometimes not accurate both in qualitative and quantitative sense.

Therefore, there is a need for the development of enhanced and computationally efficient numerical methodology for numerical prediction of residual stresses in TSCs. The methodology should be developed such that it is applicable to all types of thermal spray processes (such as plasma spray, flame spray, HVOF, D-Gun, cold spray, painting, etc) which have widespread industrial application.

1.3.4 Influence of residual stress on coating failure

Correlations exist between residual stress and coating failure as found in many previous research works. For instance, Khan and Liao [19] investigated the effect of substrate surface roughness and coating deposition temperature on the adhesion strength of coatings. They found that the adhesion strength (or fracture toughness) of coatings is significantly affected by the nature and magnitude of the induced residual stresses. Similarly, McGrann et al. [38] investigated the effect of residual stresses on the fatigue life of TSCs. They found that the fatigue life of coatings is directly dependent on the sign and magnitudes of residual stresses. Araujo et al. [14] also found that the reduction of the bond strength of coatings with an increase in thickness is directly related to the influence of residual stresses. Ranjbar-Far et al. [38] also made the same observation when they numerically determined the effect of residual stresses on the lifetime of TSCs using finite element method. Only post-deposition residual stresses were included in the stress calculation. A detailed review of the effect of residual stresses on the fracture toughness or bond strength of coatings is given by Clyne and Gill [13].

It can be seen that, in most of the works, residual stress is considered as an integral part of the factors that lead to coatings failure. The residual stress has a direct correlation with coating adhesion strength, damage behavior and lifetime of coatings. Therefore, in order to effectively study damage behavior of coatings, there is need for the development of an innovative approach for numerical prediction of residual stress in coatings.

1.4 Research goals and approach

In the present study, an innovative numerical modeling approach for thermal spray coating deposition process is proposed, implemented and evaluated. The proposed approach is hybrid in nature and able to predict evolution of residual stress very effectively. Being hybrid, the approach combines the use of point cloud and finite elements to model droplets impact/deformation and thermo-mechanical analyses of deposited coating respectively. The approach is used to predict residual stresses and associated defects developed in plasma-sprayed ceramic (YSZ) and metallic (Ni-20%Al) coatings deposited on stainless steel substrate. The numerical predictions are validated against experimental results obtained from microscopic studies, mechanical tests and hole drilling experiments.

Smooth particle hydrodynamics (SPH) is used to model the spray/deposition process where droplets impact, spread and interaction (or coating layer build-up) is simulated on point clouds. The point cloud is converted to finite element domain using recent tools for point cloud processing. Then, the converted domains (in form of meshed layers) are used for thermo-mechanical analysis using the finite element method (FEM). Non-linear constitutive behavior of coatings which have been difficult to accommodate with previous numerical schemes are adequately tackled with the current approach. SPH is

selected for deposition modeling on point cloud as it is meshless, robust in handling large deformation and computationally inexpensive. On the other hand, FEM is selected for thermo-mechanical analysis because of its high computational stability.

Using the current approach, residual stress is determined as an aggregate of stresses developed during two regimes, i.e. deposition (quenching) stresses developed during solidification and post-deposition (mismatch) stresses developed when the coating layer is cooled to room temperature. It is shown that the approach works with single droplet, multiple droplets and multiple coating layers deposited on metallic substrate under different initial conditions. It is also demonstrated that the approach presented here is robust in handling complexities arising during deposition of realistic coatings such as local stress relaxation, presence of inhomogeneities (such as cracks, pores, and interfaces), multiple splats interaction, and high undulation of coated surface. Therefore, the approach is not only realistic but more effective in predicting residual stress profile developed in TSCs.

1.5 Dissertation outline

The structure of the dissertation is as follows:

In chapter 1, introduction to thermal spray process and residual stress development in coatings is given. Then, the background of research problem, motivation and research approach are briefly stated.

In chapter 2, intensive literature survey on the research topic is given. Then, the gaps available in the literature are highlighted.

In chapter 3, main research objectives and scope/limitation are restated. This is followed by brief explanation of the methodology used to achieve the research objectives.

In chapter 4, the hybrid computational model and related formulations are explained in detailed.

In chapter 5, experimental procedures for the various experiments conducted (i.e. hole drilling, material characterization and mechanical properties measurement) are given in detail. This is followed by discussion about relevant formulations required for estimation of residual stresses using strain data obtained from experimental hole-drilling set-up.

In chapter 6, the results obtained from material characterization and mechanical tests conducted such as optical microscopy, SEM, 3D surface roughness measurement, micro-indentation and scratch test are discussed. This is followed by extensive discussion about the results of the hole drilling experiment in terms of residual stress profile developed in the coatings. The residual stress results are interpreted using the information revealed from the various tests conducted. Limitations of the hole drilling method in capturing micro-stresses developed near coating internal defects are highlighted.

In chapter 7, the hybrid model is used to model the deposition of single ceramic and metallic droplets on stainless steel. The results obtained are validated by comparing with that of the literature. The robustness of this approach is demonstrated with the single particle deposition. The accuracy and computational efficiency of the approach is improved based on several studies involving single droplets.

In chapter 8, the hybrid model is used to model the deposition of multiple droplets, their interaction and evolution of residual stress/internal defects. It is shown that, the approach

equally applies to cases involving multiple droplets deposition that may involve several coating layers. The results obtained are analyzed and validated by comparing with that of the hole drilling experiment and/or literature.

In chapter 9, the hybrid approach is extended to be applicable to thick coatings. In this regard, an effective strategy is introduced where various coating sub-layers are merged in order to minimize computational difficulties with little compromise on quality of results. This strategy is applied to the ceramic and metallic coatings considered for the present study. The results obtained are analyzed and validated by comparing with that of the hole drilling experiment and literature.

In chapter 10, the main conclusions from the research work conducted are given and future directions are stated. |

CHAPTER 2

LITERATURE REVIEW

This chapter presents an overview of the various models used for the prediction of residual stresses developed in thermal spray coatings (TSCs). The literature survey presented here has been published in Journal of Thermal Spray Technology [29].

Firstly, brief discussion about the various sources of residual stress in coatings is given. Then, discussion about the main difficulties often encountered when measuring residual stresses in coatings is given. This is followed by extensive discussion about the previous analytical and numerical models used for the prediction of residual stresses in coatings. The results given by those models are critically analyzed with emphasis on accuracy and comparison with the results obtained from experiments. Lastly, the limitations of the existing models and future works that need to be done to make the models more effective are highlighted.

2.1 Sources of residual stress

2.1.1 Thermal mismatch stress

During thermal spray process, thermal mismatch (or misfit) strain occurs due to the differences in temperature and coefficient of thermal expansion (CTE) between the coating and substrate materials. With high CTE mismatch, the misfit strain is appreciably high and results in thermal mismatch stresses due to uneven contraction of coating and substrate layers. Due to the complicated nature of the process, the evolution of thermal

mismatch stress is highly process (parameters) dependent and significantly affected by various processes occurring at different time and length scales. Generally, TSC process is divided into two stages, i.e. deposition stage (involving layer-by-layer coating growth to the required thickness) and post-deposition stage (involving the final cool down of the coating to room temperature). Thus, the thermal mismatch stresses are classified according to the stages, i.e thermal-deposition (or quenching) stress and post-deposition mismatch stresses which are discussed as follows.

- a) **Quenching stress:** The term “quenching stress” is commonly used in literature to describe stresses that are developed because of the sudden solidification of the molten particles (or deposited splats) upon their impact on the substrate (or pre-deposited coating) surface. During coating growth and deposition, quenching stress evolves due to processes occurring at varying time and length scales. At the microscale, the sudden solidification and shrinkage (occurring within 10-100 μs) of individual splats results in the formation of tensile stresses due to thermal mismatch and constraining of the shrinking splats by the interfacial bond [2], [3], [21] (as demonstrated in Figure 2-1). This interfacial bonding is established by various mechanisms including mechanical, diffusional or chemical processes. With the arrival of new sets of droplets, the splat-level quenching stress field is significantly influenced by the high thermal flux and impact energy of the newly deposited droplets. Consequently, at the mesoscale, steep through-thickness thermal gradient is developed (within hundreds of splats) which leads to slight bending or distortion of the substrate layer (depending on the degree of thermal mismatch). The thermal gradient is severe and more harmful for the case of

ceramic coatings due to their low thermal conductivity [2], [13]. The slight distortion/bending of the substrate layer is necessary for the composite system to attain equilibrium (by force and momentum balance) while accommodating the high quenching stresses developed within the coating sub-layers (as demonstrated in Figure 2-2).

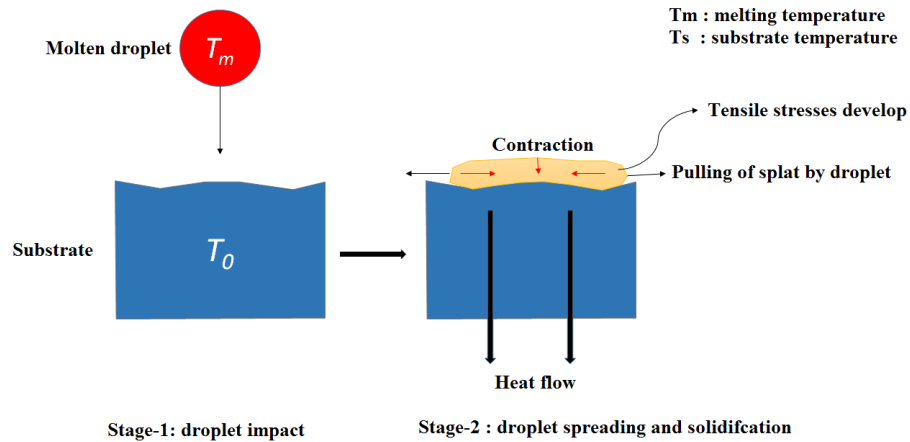


Figure 2-1: Quenching stress formation (at microscale) during single splat solidification

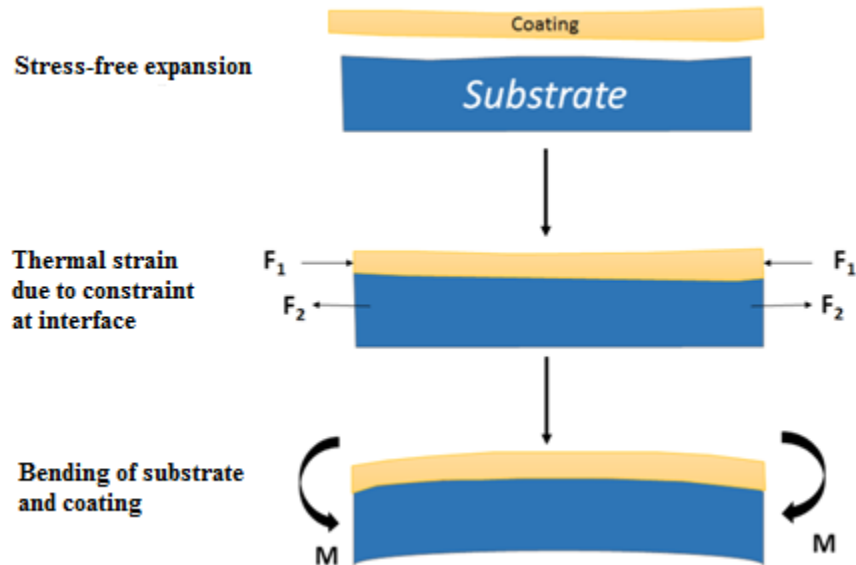


Figure 2-2: Bending of substrate material (during deposition) due to quenching stresses developed after deposition of coating sub-layer

b) **Post-deposition mismatch stress:** Likewise, the evolution of thermal stresses extends to the post-deposition stage when the deposited coating is finally cooled to room temperature. Upon its final cool down, uneven contraction occurs between the coating and substrate materials near the interface region; obviously due to difference/mismatch in properties. Being a macro-level stress, the post-deposition mismatch stress has the highest magnitude and significantly influences the final residual stress state as demonstrated in Figure 2-3. Also, the mass or thickness of the coating has a strong correlation with the post-deposition mismatch stress and bond strength of coatings. For coatings having lower CTE than the substrate (e.g. ceramic coatings), the post-deposition mismatch stress is usually compressive; thus, it helps in reducing the severity of the tensile quenching stresses at the coating/substrate interface. On the other hand, coatings having a CTE that is higher than that of the substrate (e.g. most metallic coatings) result in tensile post deposition mismatch stress state. However, the tensile post-deposition mismatch and quenching stresses (in metallic coatings) are usually balanced by the high peening (compressive) stress associated with most metallic coatings. Therefore, minimization of post-deposition mismatch stresses (through careful selection of coating and substrate materials combination, their thicknesses and operating temperatures) is required for enhanced durability and performance of coatings [39].

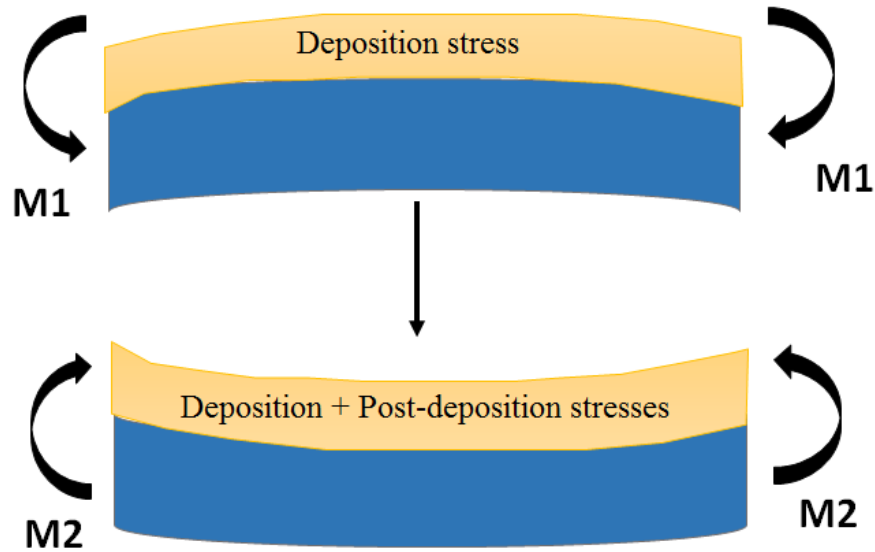


Figure 2-3: Bending of substrate/coating after (a) coating deposition, (b) post-deposition cooling

2.1.2 Peening stress

In thermal spray literature, stresses that are developed due to particle impact on substrate (or previous coating layer) surface are called peening or impact stresses (shown in Figure 2-4) [2]. Due to the type of reaction forces produced by impact, peening residual stresses are usually compressive. Thus, peening stresses reduce the severity of quenching stress and result in a non-linear compressive residual stress state in coatings as demonstrated in previous research works [40]–[42]. Peening immensely contributes to the overall residual stress profile, especially in metallic coatings that are deposited by high-speed thermal spray processes such as HVOF and D-Gun. Since metallic coatings are susceptible to large plastic deformations, very high peening (compressive) stresses occur due to the conversion of droplet kinetic energy into sound, plastic work, and heat energy. While in ceramic coatings, the resulting peening (compressive) stresses often reduce the severity

of the quenching (tensile) stress, initiate microcracks due to stress wave propagation and partially close the numerous voids/cracks that fill the microstructure of ceramic coatings.

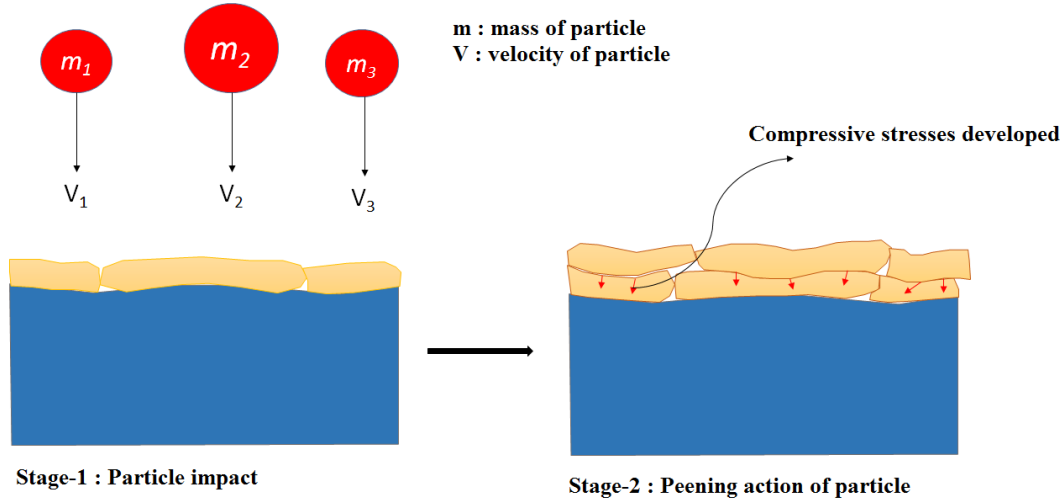


Figure 2-4: Peening stress developed during coating deposition

2.1.3 Stress induced by substrate surface pre-treatment

Before coating deposition, the usual practice is to roughen the substrate surface and induce initial compressive (or peening) stresses in order to improve the adhesion strength of the coating. This is mostly achieved by grit-blasting, process whereby hard particles are blasted on the surface of the substrate material in order to improve its surface properties (mainly surface roughness, grain size, and hardness). Thus, the sharp changes due to substrate surface asperities (generated by grit-blasting) help to improve the bond strength at the coating/substrate interface. Furthermore, grit-blasting induces some initial compressive (peening) stresses on the surface of the substrate and this greatly influences the eventual magnitude and direction of residual stresses developed in the substrate at the end of the coating deposition process, especially near the interface. Moreover, pre-heating the substrate to higher temperatures is commonly carried out to reduce the severity of quenching stresses especially near the coating/substrate interface. Surface

structuring/texturing by laser treatment, machining, grinding/brushing, degreasing and chemical surface treatment are also processes that affect the stress state developed within the coating and substrate layers.

2.1.4 Other sources: multiphase systems, discontinuities, coating post-treatment and in-service loads

In coatings, residual stresses can also be induced by other phenomena which are commonly considered as minor sources and occur only under certain loading or environmental conditions. The emergence of new crystals or phase transformations in coatings leads to the development of residual stresses due to volumetric expansions and inelastic deformations [2], [43], [44]. Compositional variation of second-phase particles along the thickness of coating significantly affects the residual stress formation due to a gradual change in properties (e.g. in functionally graded TBCs [45]). The presence of pores, cracks, and hard inclusions leads to the development of higher residual stresses due to localized phenomena and high stress gradients [46]. Shot peening and roller burnishing also significantly affect the residual stresses developed within the coating as demonstrated by Luzin et al. [47] and Klusemann et al. [48]. Residual stress state of coatings is also affected by in-service loadings which induce inelastic deformations (e.g. creep, sintering, precipitations, chemical reactions, phase transformations, etc.) and reduce the integrity of coatings.

2.2 Difficulty in measuring residual stresses: Why modeling?

Over the years, various experimental set-ups for accurate estimation of residual stresses in coatings have been developed. X-ray diffraction, in-situ curvature measurements,

neutron diffraction, and incremental hole-drilling methods are frequently used. The first three tests are non-destructive, while the last is semi-destructive. Using each technique, residual stresses developed in TSCs have been measured and evaluated to a certain level of accuracy. However, each of the experimental methods has its own limitations which will be discussed in the following paragraphs (starting with the non-destructive tests).

The diffraction methods are non-destructive, and the popular ones used so far are: neutron and x-ray diffraction. Due to its high penetration depth, neutron diffraction provides good estimate of residual stress profile up to deeper locations within the substrate layer. Ahmed et al. [49] compared the results obtained by neutron diffraction and incremental hole drilling method as applied to WC–NiCrBSi coatings deposited on stainless steel. They found that significant deviations exist between results obtained with these two methods, especially near the coating-substrate interface. They found that the near-interface stresses predicted with neutron diffraction are 4-6 times higher than that of the incremental hole drilling method. This is because, neutron diffraction can predict the high micro-stresses developed near imperfections (such as cracks, pores, inclusions, second-phases, etc.), unlike hole drilling method which is only capable of measuring macro-stresses. Neutron diffraction has also been used to estimate the stress profile developed in several other types of coatings as previously done by Ahmad et al. [49] and Faisal et al. [50]. The high cost of measurement is the main limitation of neutron diffraction. Neutrons of sufficient intensity are normally required for reliable estimation of residual strain variation with depth of the coating layer. For this reason, x-ray diffraction is more common for experimental prediction of residual stress in TSCs.

With x-ray diffraction (XRD), the sample is scanned at several tilt (ϕ) angles and the variation of d-spacing with $\sin^2\phi$ is used to estimate the stress level developed in the coating layer. Several material constants are required for reliable estimation of the stresses using this method. Chen et al. [51] used XRD to estimate residual stresses developed near the surface of thermal barrier coating (TBC). They found that the compressive residual stresses developed in the topcoat layer are strongly dependent on evolution of coating effective modulus. Oladijo et al. [30] also used XRD to estimate the residual stress developed near the surface of WC-Co coating deposited on several metallic substrates. They found that the residual stress developed in the coating layer significantly depend on the substrate type due to variation of splat solidification rate. They found that the coating layer deposited on aluminum and brass substrates develop compressive residual stress, while that deposited on the super-invar substrate develop tensile stresses. XRD has also been used for experimental residual stress analysis in many previous works related to coatings. The main problems with XRD is low penetration depth and uncertainties associated with determination of reliable constants required for the stress calculation [30]. Consequently, XRD is only used to determine near surface residual stresses (within 5-10 μm in depth) as previously discussed. For prediction of stresses developed at deeper locations within the coating layer, it is necessary to conduct the experiment with high energy synchrotron XRD as done recently by Weyant et al. [52] and Li et al. [53]. But analysis with synchrotron XRD is very expensive due scarcity of the equipment worldwide. Another method used to stresses developed at deeper locations is combination of XRD with layer removal through EDM or electropolishing as previously done by Kingswell et al. [54] and Minh et al. [55]. However, it widely

reported that the initial stress state of the coating layer may change due to additional stresses developed by the layer removal process. Therefore, to standardize this approach, there is need for further investigation of the influence of layer removal process on residual stress profile which is very tedious task.

The second non-destructive technique is the in-situ curvature method which was first proposed by Stoney [56] and later improved by Brenner and Senderoff [57]. The method involves the continuous monitoring of the substrate curvature during both coating deposition and post-deposition cooling [13], [58]. During coating deposition, the quenching stresses developed within deposited coating are accommodated by the substrate material for the composite system to reach stability/equilibrium. Consequently, a slight change of substrate curvature occurs due to the balancing of the overall forces and moment acting on the system. Moreover, the substrate curvature undergoes further changes after post-deposition cooling due to uneven contraction and thermal mismatch between the coating and substrate. With in-situ curvature method, the change in curvature or displacement of the substrate during the spray process is monitored with the aid of In situ Coating Properties (ICP) sensor (as described in a recent study by Mutter et al.[58]), which uses a laser to accurately estimate the central displacement of the substrate layer. The substrate curvature can be predicted to a high level of accuracy such that even the vibration resulting from the sudden impact of sprayed droplets or plasma plume is detected. The temperature of the top and bottom of the substrate (measured continuously with the help of thermocouple) helps in predicting the associated thermal gradient developed during the process. Using the curvature and temperature readings, the evolving residual stresses and coating properties (e.g. effective elastic modulus and stress-strain

response) are calculated (using models by Stoney [56] and Brenner and Senderoff [57]) as a function of the process history. So far, In situ curvature measurement is the only experimental technique that can be used to track the evolution of residual stresses (both deposition and post-deposition stresses predicted separately) during the thermal spray process. The method is non-destructive, real-time and widely used by many researchers (such as Totemeier et al.[59], Sampath et al.[60] and Zhang et al. [61]) to effectively predict residual stresses and effective properties of coatings. It can be even used to determine the quality of coatings (i.e. whether there is cracking/delamination or not) by comparing the effective properties given by the coating with that of standard/acceptable specimens. Despite its numerous advantages, the in-situ curvature method also has important limitations. Firstly, the method is only applicable to model samples having a specific thickness and shape. Thus, it will be difficult to estimate residual stresses developed in actual (coated) components that are commonly used in the industries. The stress state determined using the model samples will not be the same as that of actual components due to difference in thermal history. Similarly, it usually difficult to transform the curvature data into stress state for thick coatings produced by high energy processes (e.g. HVOF and D-Gun) due to the assumptions adopted by Stoney [56] and Brenner and Senderoff [57]. Furthermore, the estimation of residual stresses is inaccurate for some coating systems due to the negligence of non-linear material behavior (e.g. plastic deformation, cracking, etc.) occurring during post-deposition cooling. Another setback is that, it will be difficult and costly to optimize the coating process due to the need for repetitive coating of several specimens to obtain sufficient data for optimization.

Thus, the development of an effective and calibrated model is necessary for such optimization tasks.

For the semi-destructive tests, the incremental hole-drilling method is among the most commonly used techniques for the measurement of residual stresses [62]. This is partly due to its simplicity, portability, availability, flexibility with regards to sample materials, and its ability to track residual stress variation with depth. The incremental hole drilling method has been used to determine the variation of residual stresses along the thickness of TSCs. Due to the heterogeneous nature of coating systems, a significant amount of errors is detected in the final stress results when standard calibration coefficients are used for the residual stress calculation. Thus, Valente et al. [34] proposed a methodology for the accurate determination of residual stresses in TSCs by using the finite element method to numerically determine the required calibration coefficients. Using the approach, Montay et al. [63] predicted residual stresses developed in zirconia, alumina and tungsten carbide thermal sprayed coatings. Escribano and Gadow [64] also proposed the use of high speed drilling and milling process in order to reduce the errors resulting from temperature rise, plastic deformations and crack propagation (due to the drill cutting forces). As done by Valente et al., the correct calibration coefficients were determined using finite element analysis. Also, Buchmann et al. [65], [66], Santana et al. [33] and Held and Gibmeier [67] successfully measured residual stress profile in coatings using the incremental hole-drilling method. Thus, the hole drilling method has been widely used to estimate the residual stress state of TSC. The method can be used to measure residual stresses up to a depth resolution of 10 μm as shown by Escribano and Gadow [64], Buchmann et al. [65], [66] and Grant et al. [68]. However, the accuracy of the

method is often affected by several factors [33], [34] such as human errors arising from the tedious nature of measurements, high sensitivity and susceptibility to experimental errors, semi-destructive nature, complicated stress calculation procedure (especially for low yield and highly brittle coatings), and difficult interpretation of results. For this reason, improvement of the method has been achieved recently (by Sebastiani et al. [69], Korsunsky et al. [70] and Winiarski and Withers [71], [71]) whereby the hole drilling experiment is conducted in SEM chamber using incremental focused ion beam (FIB) milling and drilling in combination with high resolution digital image correlation (DIC). Due to high resolution of measurement, this new approach has opened a new research trend on the determination of micro-residual stresses developed in thin coatings, micro-components and devices. However, more work needs to be done in order to standardize the approach for experimental residual stress measurement.

Therefore, the various limitations of each experimental techniques have made it difficult to carry out an intensive experimental investigation of residual stresses developed in coatings. Thus, all the available experimental methods are not suitable for optimization of the process for enhanced durability and quality of coatings. For this reason, various models have been developed for the prediction of residual stresses in TSCs as discussed in subsequent sections.

2.3 Analytical models for prediction of residual stress

2.3.1 Theoretical quenching stress models

Theoretically, quenching stresses are more difficult to calculate than the other residual stress components. This is due to the phase change phenomena (or dynamics) associated

with particle impact, spread, and solidification. As explained previously, the quenching stress is mainly tensile because most materials shrink upon solidification. The quenching stress is usually calculated from the following relation [72]–[74]:

$$\sigma_{qc} = E_{sp} \int_{T_s}^{T_{sp}} \alpha_c(T) dT \quad (2.1)$$

Thus, the maximum value of the quenching stress has been analytically derived as [72]–[74]:

$$\sigma_{qc} = E_{sp} \cdot \alpha_{sp} \cdot (T_{sp} - T_s) \quad (2.2)$$

where E_{sp} is the elastic modulus of the splat, α_{sp} is the coefficient of thermal expansion of the splat, T_{sp} is the solidification temperature of the splat, and T_s is the substrate temperature.

The theoretical quenching stress (represented in Eq.(2.2)) gives very high stress values as compared to the actual quenching stress. For instance, the theoretical value of quenching stress for alumina (ceramic) coating (for 1000C cooling) was found to be 100 MPa which is far greater than the actual value of 10 MPa [72]. Similarly, the typical observed quenching stress for nickel (metallic) coatings (deposited by APS) is less than 100 MPa which is far less than the theoretical value, 1 GPa [72]. This discrepancy has been attributed to the assumption that the elastic moduli of deposited splats are the same as that of the bulk materials [72]. Various researchers have used three-point bending, nanoindentation, and acoustic analysis to measure the effective modulus of TSCs. Typically, lower than bulk values are found due to porosity, microcracks and to the

lamellar microstructure [72], [75], [76]. Kuroda et al. [72] observed that the measured elastic modulus of coating deposit was one-third and one-sixth of the bulk for metallic and ceramic coatings, respectively. Thus, they suggested that a good approximation is to use effective values of elastic modulus of coatings (instead of that of the bulk material) as E_{sp} in Eq.(2.1) and Eq.(2.2).

Another reason for the differences between theoretical quenching stress values (given by Eq.(2.1) and Eq.(2.2)) and those experimentally observed is stress relaxation occurring due to various mechanisms, as demonstrated in previous work [72]. In metallic coatings, the stresses relax by splat edge relaxation, plastic yielding, creep, and interfacial sliding. On the other hand, residual stresses in ceramic coatings relax by micro-cracking (due to thermal shock) and interfacial sliding. A detailed discussion of the relaxation mechanisms was made in previous work [72]. Valente et al. [77] suggested that the theoretical quenching stress (in Eq.(2.1) and Eq.(2.2)) should be reduced by multiplying T_{sp} with a reduction factor, $\xi = 0 \rightarrow 1$. They suggested that the value of ξ should be 0.6 to accommodate stress relaxation by yielding and creep. However, it was not clear if the same reduction factor applies to other stress relaxation mechanisms such as microcracking, interfacial sliding, and edge relaxation. We carried out investigations on the validity of the above suggestions for correction of the theoretical quenching stress values of thermally sprayed alumina (ceramic) and nickel (metallic) coatings. For the purpose of comparison, properties of alumina and nickel, as experimentally measured by Kuroda et al., were used with melting temperatures of 2277°C and 1435°C, respectively. As shown in Figure 2-5 (a) and (b), it can be seen that the comparison of theoretical and corrected maximum quenching stress values (as given by Eq.(2.2)) with experiments is

not good. Moreover, there was no good qualitative comparison in the case of alumina. This is because quenching stress strongly depends not only on the substrate temperature but also other factors such as substrate surface preparation, chemical compatibility, thermal spray process, etc.

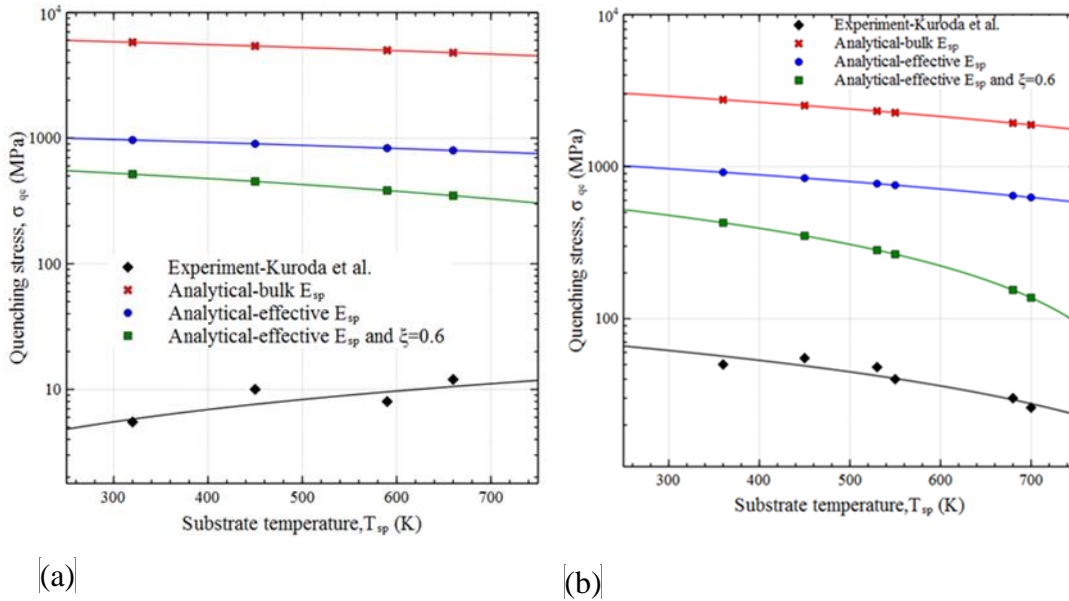


Figure 2-5: Comparison of theoretical and measured quenching stress developed in (a) alumina (ceramic), (b) nickel (metallic) coatings as a function of substrate temperature.

For most ceramic coatings, the interface adhesion strength is more dependent on diffusion or chemical compatibility than mechanical bonding (as discussed in section 13.4.2 of [2]). For this reason, the actual quenching stress is commonly found to increase linearly with substrate temperature due to higher rates of diffusion (or chemical bond energy) at the coating/substrate interface as shown in Figure 7 (a). On the contrary, metallic coatings (e.g. nickel) display a quenching stress which decreases with substrate temperature due to plastic deformation and/or creep. However, other metallic coatings (e.g. molybdenum) showed that quenching stress increases with substrate temperature and then starts decreasing due to the partial melting or softening of the coating material

[72]. Thus, for these coating materials, both diffusion and mechanical bonding play role in determining the adhesion strength. Quenching stresses also depend on the type of thermal spray process. For example, quenching stresses developed by HVOF process was found to be noticeably different from APS process [32], [78] due to the lower deposition temperature of HVOF coatings. Therefore, the quenching stress evolution is intricately dependent on many factors that can hardly be controlled during the process; thus, further theoretical understanding of the quenching stress is required.

2.3.2 Semi-empirical quenching stress models

Due to the various challenges and limitations of using the existing quenching stress model, several semi-empirical models have been used to predict the quenching stresses developed during TSC. These are analytical models that require experimental data of the change in the substrate curvature (as recorded by ICP sensor or other means) during the thermal spray process; hence, they are termed as “semi-empirical”. Stoney [56] first derived the relationship between in-plane stresses developed in deposited thin film/coating and the radius of curvature of the substrate. He arrived at a final relation for the uniform in-plane stress developed in the deposit/coating using laminate theory (based on only linear elastic response) by balancing the forces and moments acting on the entire coating system (as shown in Eq. (2.3)).

$$\sigma_{qc} = \frac{E_s \cdot t_s^2}{6 \cdot \delta r \cdot t_c} \text{ for plane stress} \quad (2.3)$$

where σ_{qc} is the deposition (or quenching) stress developed in the coating, E_s is the elastic modulus of substrate, t_s is the thickness of substrate, δr is the change in radius of

curvature due to deposition, and t_c is the total thickness of the deposit. The change in curvature of the substrate (usually obtained using ICP sensor) is determined by taking the inverse of the radius, i.e. $\delta k = \frac{1}{\delta r}$. For plane strain condition, the substrate elastic modulus is replaced by $\frac{E_s}{(1-\nu_s)}$ with ν_s being the Poisson's ratio of the substrate material.

It has been shown by many researchers that ([59], [79], [80]) Stoney's model gives a good approximation for the quenching stresses developed in thin coatings such as those deposited by thermal spray process (with a deviation of less than 10%). What is interesting is the fact that, Stoney's model does not require the effective elastic modulus of the coating and still gives a good approximation to the deposition stresses. However, for thick coatings whose elastic modulus is comparable to that of the substrate, Soderberg [81] observed that Stoney's model results in significant errors due to the negligence of the coating elastic modulus. Thus, Brenner and Senderoff [57] corrected this error by adding a term to Eq. (2.3) which includes the effect of elastic modulus and thickness of the deposited coating on the developed quenching stress (as shown in Eq.(2.4)).

$$\sigma_{qc} = \frac{E_s \cdot t_s \cdot (t_s + \chi^{5/4} \cdot t_c)}{6 \cdot \delta r \cdot t_c} \quad (2.4)$$

where $\chi = \frac{E_c}{E_s}$ is the coating-substrate elastic modulus ratio. It is important to note that,

both Eq.(2.3) and (2.4) predict a quenching stress that is uniform and does not vary in the thickness direction of the coating.

2.3.3 Post-deposition mismatch stress models

The first analytical model for the prediction of elastic thermal mismatch stresses developed in a two-layer composite structure was developed by Timoshenko [82] based on the classical beam theory. Since then, many researchers have utilized his model to obtain thermal stress distribution in layered (composite) structures. For instance, Hans and Evans [83] predicted the thermal mismatch stresses developed in metal/ceramic composite materials using the model by Timoshenko. Liu and Murarka [84] also used it to predict the thermal mismatch stresses developed in coated semiconductor device. Many applications of Timoshenko's model can be found in the literature [85]–[89]. However, it is difficult to predict mismatch residual stresses in multilayer coatings using Timoshenko's model. This is due to many unknowns, complex interfacial (compatibility) conditions, and thin nature of the coating as compared to the substrate material. Thus, it is necessary to establish an elegant way of deriving an analytical model for thermal mismatch stresses in coatings. The laminate theory, first developed by Stoney [56], has been recently used as an alternative as it is suitable for very thin coatings. The only problem of the laminate theory may result in complex formulations which may be difficult to handle analytically. Thus, this necessitates the use of approximate solutions to predict post deposition (thermal) mismatch stresses developed in TSCs.

Hsueh [90] and Zhang et al. [91] developed an approximate solution to Stoney's model (for multilayered composite systems) by additively decomposing the elastic strain tensor (ϵ) into uniform and bending strain parts as shown in Eq.(2.5). Using Eq.(2.5), continuity (or compatibility) conditions are implicitly satisfied at the interface between the various composite layers.

$$\varepsilon = c + \frac{z - t_b}{r}, \quad \text{for } -t_s \leq z \leq t_n \quad \text{and} \quad t_n = \sum_{i=1}^n t_i \quad (2.5)$$

where z is the coordinate along the thickness of the coating (shown in Figure 2-6), c is the uniform strain, $z = t_b$ is the position of the bending axis, r is the radius of curvature, t_s is the substrate thickness, t_n is the free surface of the topmost coating layer, t_i is the thickness of i^{th} -coating layer.

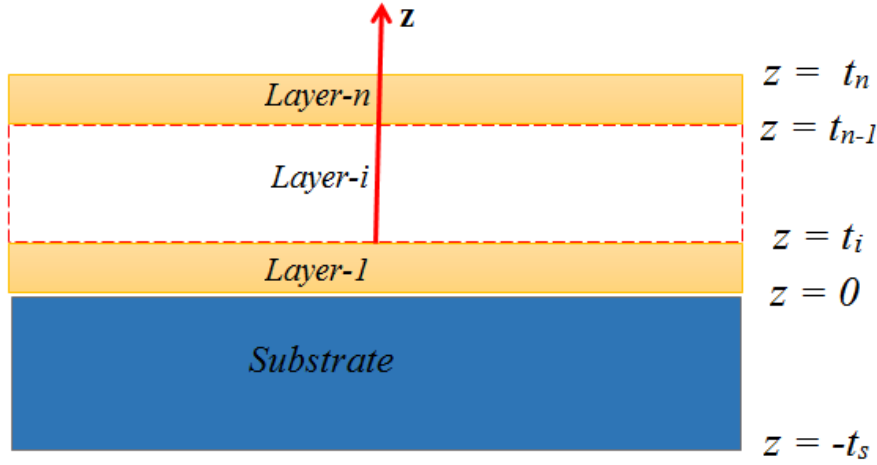


Figure 2-6: Variation of Z values along the thickness direction (for multilayer coatings)

Thus, Hsueh and Zhang et al. used Eq.(2.5) to derive the exact solutions for the uniform strain, position of the bending axis, and curvature of multilayer coating system. Due to the use of slightly different expressions for the approximate position of the bending axis, Hsueh and Zhang et al. obtained different expressions for the post-deposition mismatch stresses. Hsueh derived the following expressions for the in-plane stresses developed in the coating (σ_i) and substrate (σ_s) (based on first-order approximation) as:

$$\sigma_s = \frac{2}{t_s^2} \left(3z + 2t_s - \frac{2}{E_s} \sum_{j=1}^n E_j t_j \right) \cdot \sum_{i=1}^n E_i t_i (\alpha_i - \alpha_s) \cdot \Delta T, \quad \text{for } -t_s \leq z \leq 0 \quad (2.6)$$

$$\sigma_i = \left(E_i \left((\alpha_s - \alpha_i) + 4 \sum_{j=1}^n \frac{E_j t_j (\alpha_j - \alpha_s)}{E_s t_s} \right) \right) \cdot \Delta T, \quad \text{for } i = 1, 2, 3, \dots, n \quad (2.7)$$

where E is the effective elastic modulus (which is elastic modulus divided by $(1-\nu)$ for plane strain case), ν is Poisson's ratio, α is the CTE, and ΔT is the change in temperature due to cooling. Note that i denotes each coating layer and S denotes the substrate layer.

While Zhang et al. obtained the following expressions (based on first-order approximation):

$$\sigma_s = E_s \left[\sum_{i=1}^n \frac{E_i t_i (\alpha_i - \alpha_s) \cdot \Delta T}{E_s t_s} + 6 \sum_{i=1}^n \frac{E_i t_i (\alpha_i - \alpha_s) \cdot \Delta T}{E_s t_s^2} \left(z + \frac{t_s}{2} - \sum_{i=1}^n \frac{E_i t_i \left(2 \sum_{j=0}^{i-1} t_j + t_i \right)}{E_s t_s} \right) \right], \text{ for } -t_s \leq z \leq 0 \quad (2.8)$$

$$\sigma_i = E_i \left[(\alpha_s - \alpha_i) \cdot \Delta T - \sum_{j=1}^n \frac{E_j t_j (\alpha_j - \alpha_s) \cdot \Delta T}{E_s t_s} + 6 \sum_{i=1}^n \frac{E_i t_i (\alpha_i - \alpha_s) \cdot \Delta T}{E_s t_s^2} \left(z + \frac{t_s}{2} - \sum_{i=1}^n \frac{E_i t_i \left(2 \sum_{1}^{i-1} t_i + t_i \right)}{E_s t_s} \right) \right] \\ , \text{ for } i = 1, 2, 3, \dots, n \quad (2.9)$$

Both Hsueh and Zhang et al. showed that the reduction of the above equations further using zero-order approximation results in a previous solution obtained by Townsend et al. [92]. Thus, adopting zero-order approximation will result in the following final expression which can only be applied to coatings of extremely small thickness:

$$\sigma_s = \frac{2(3z + 2t_s)}{t_s^2} \sum_{i=1}^n E_i t_i (\alpha_i - \alpha_s) \cdot \Delta T, \quad \text{for } -t_s \leq z \leq 0 \quad (2.10)$$

$$\sigma_i = E_i (\alpha_s - \alpha_i) \cdot \Delta T, \quad \text{for } i = 1, 2, 3, \dots, n \quad (2.11)$$

However, the expression in Eq. (2.11) shows that the stress induced in each coating layer is independent of the thickness, curvature, and properties of the other coating layers which obviously lead to inaccurate results as demonstrated by Eq.(2.9). Hsueh [90] used Eq.(2.6) and (2.7) to predict post-deposition mismatch stresses developed in five-layered AlGa laser diodes. He observed that zero-order and first-order approximations lead to conflicting predictions due to the use of elastic moduli that are independent of temperature. Also, Zhang et al. [91] used Eq. (2.8) and (2.9) to predict post-deposition mismatch stresses developed in thermal barrier coating (TBC). Unlike Hsueh, Zhang et al. found that the induced stresses are not uniform but decrease linearly along the thickness direction of the coating. They showed that the bending part of the strain tensor may be neglected in the closed-form expression for coatings of very small thickness and low elastic modulus.

In another work, Hsueh and Lee [93] and Zhang et al. [94] applied the model to predict post-deposition mismatch stresses in compositionally (or functionally) graded coatings. In that case, the residual stresses are not only due to CTE misfit between the respective layers but also due to the variation of compositions along the coating thickness. Thus, modified expressions for the effective elastic modulus and CTE are used as properties of the graded layers in Eq. (2.6)-(2.9). For a graded coating layer that is composed of two

distinct materials ‘a’ and ‘b’, the effective elastic modulus (E_g) and CTE (α_g) of the graded layer are given by:

$$E_g = E_a + (E_b - E_a) \cdot \left(\frac{z}{t_g} \right)^n \quad (2.12)$$

$$\alpha_g = \alpha_a + (\alpha_b - \alpha_a) \cdot \left(\frac{z}{t_g} \right)^n \quad (2.13)$$

where: E_a and α_a are the elastic modulus and the CTE of material ‘a’ (i.e. material of major concentration at $z=0$), E_b and α_b are elastic modulus and CTE of material ‘b’ (i.e. material of major concentration at $z=t_g$), n is the gradient exponent which determines how the mixture of the two materials varies along the coating thickness. For instance, in a compositionally graded TBC layer $n=0$ when there is no NiCrAlY composition and $n=\infty$ when there is 100% NiCrAlY composition.

Using Eq. (2.12) and (2.13), Hsueh and Lee [93] analyzed the post-deposition stresses developed in TBC having functionally graded bond coat layer. Hsueh and Lee found that unlike in the top coat layer, stress state of the bond coat layer is significantly affected by the compositional gradient (with minimum stress level developed at $n = 6$). Zhang et al. [94] also used Eq. (2.12) and (2.13) to model TBC system with the graded phase of NiCrAlY alloy within the ceramic top coat. They found that the use of graded top coat layer leads to lower values of post-deposition stresses due to a reduction in CTE mismatch near the interface region. But they observed that stresses induced on the top coat surface were constant and independent of the compositional gradient. The main

limitation of Hsueh's and Zhang's model is that they considered that the materials of the individual coating and substrate layers are isotropic, temperature-independent, and subjected only to pure elastic strain. Up to now, their models have not been extended to accommodate anisotropy or non-linear behavior of coatings due to the resulting mathematical complexities.

In order to investigate the effect of substrate geometry and surface asperity on post-deposition mismatch stresses, Gong and Clarke [95] first developed a two-concentric (two-layer) model that predict the effect of substrate surface roughness on the induced thermal stresses. Then, Hsueh and Fuller [96] and Zhang et al. [97] extended it further to three (three-layer) and four-concentric (four-layer) models and investigated the effect of substrate surface roughness on the induced mismatch stresses. Then, Song et al. [98] finally developed a four-concentric (four-layer) model that predict the effect of both substrate surface roughness and macro-curvature. All the concentric models were derived using the theory of linear elasticity and isotropic material behavior. After long derivations, Song et al. arrived at the final expressions for the radial stresses developed near the undulation of the substrate. They found that increasing the undulation amplitude and decreasing the undulation wavelength result in increased mismatch stresses near the interface. They also found that the macro-curvature of substrate significantly affects the stress distributions, especially near regions of high-stress concentrations, e.g. edges, interface, etc. Therefore, it can be concluded that post-deposition mismatch stresses developed in coatings are greatly affected by not only CTE mismatch, but also substrate macro-curvature and surface roughness.

2.3.4 Overall residual stress model

To the best of our knowledge, analytical models which combine the various contributions of residual stresses are few in the literature. Tsui and Clyne [99] were the first to develop a simple and straightforward analytical expression which combines both quenching and post-deposition mismatch stresses using Stoney's model in combination with thermo-elasticity (heat transfer not included in the analysis). Tsui and Clyne did not derive analytical equations for the quenching stress, but instead quenching stress (obtained from experiments or other models) serves directly as input to the combined model [72]–[74]. However, unlike the models previously presented (in section 3.2), Tsui and Clyne's model represents the coating as an aggregate of sub-individual layers which are deposited in discrete steps, while at each step, the force and momentum are balanced. Thus, the model is more realistic as it takes into consideration the layer-by-layer growth or evolution of the quenching stress and simultaneously integrating it with the post-deposition mismatch stress to give the overall residual stress state. The model can predict residual stress variation with deposition temperature, material properties and dimensions of the coating and substrate. However, its main limitation is that it cannot take temperature-dependent material properties due to difficulties associated with finding a closed-form solution for such a problem. The final expressions (obtained by Tsui and Clyne) for the in-plane residual stresses developed (after deposition of i th sub-layer) at the top and bottom of the substrate are [99]:

$$\sigma_{sb} = \sigma_s \Big|_{y=-H} = \sum_{i=1}^n \left(\frac{-E_s F_i}{b(H E_s + (i-1)w E_d)} + E_s (\kappa_i - \kappa_{i-1})(H + \delta_i) \right) - \frac{F_{(CTE)}}{bH} + E_s (\kappa_c - \kappa_n)(H + \delta_n) \quad (2.14)$$

$$\sigma_{st} = \sigma_s \Big|_{y=0} = \sum_{i=1}^n \left(\frac{-E_s F_i}{b(HE_s + (i-1)wE_d)} + E_s(\kappa_i - \kappa_{i-1})\delta_i \right) - \frac{F_{(CTE)}}{bH} + E_s(\kappa_c - \kappa_n)\delta_n$$

(2.15)

where H is the thickness of substrate, b is the width of substrate/coating, w is the thickness of deposited coating, κ is the curvature, δ is the position of neutral axis (measured from the coating/substrate interface as demonstrated in Figure 8), F is the force developed in coating layer (a function of quenching stress) and $F_{(CTE)}$ is the force that arises due to misfit strain during final cooling. Note that n is the total number of deposited layers, s denotes the substrate and d denotes deposit (or coating layer). More details regarding the derivation can be obtained from [99].

The total stress developed at the midpoint of the i^{th} sub-layer within the coating is [99]:

$$\begin{aligned} \sigma_{di} = \sigma_d \Big|_{y=(i-1/2)w} &= \frac{F_i}{bw} - E_d(\kappa_i - \kappa_{i-1}) \left(\left(i - \frac{1}{2} \right) w - \delta_i \right) \\ &+ \sum_{j=i+1}^n \left(\frac{-E_d F_j}{b(HE_s + (j-1)wE_d)} - E_d(\kappa_j - \kappa_{j-1}) \left(\left(i - \frac{1}{2} \right) w - \delta_j \right) \right) + \frac{F_{(CTE)}}{bh} - E_d(\kappa_c - \kappa_n) \left(\left(i - \frac{1}{2} \right) w - \delta_n \right) \end{aligned}$$

for $1 \leq i \leq n$

(2.16)

Tsui and Clyne tested the model on APS NiCrAlY coating on a PK33 substrate (at 420°C deposition temperature), VPS B4C coating on Ti-6Al-4V (at 500°C deposition temperature) and APS ZrO2 coating on PK33 (at 500°C deposition temperature). They found an acceptable agreement between analytically and numerically predicted results. For APS NiCrAlY coating, they found that the negligence of quenching stress results in a large error due to since metallic coatings have low CTE mismatch and higher quenching

stress. For VPS B4C coating, they found that the residual stress is dependent on both quenching and thermal mismatch stress at equal proportions. For APS ZrO₂ coating, the quenching stress is not very significant due to stress relaxation by micro-cracking; thus the overall residual stress state is mainly dependent on the thermal mismatch stress. Similarly, Bolelli et al. [100] experimentally measured peening stress and integrated it with the quenching stress in Tsui and Clyne's model to successfully make a good estimate of residual stresses developed in functionally graded WC-Co/NiAl coatings deposited by HVOF. In another work, Tsui and Clyne [99] developed a similar analytical model for coatings sprayed on hollow cylindrical geometry (i.e. having some initial curvature). In that case, stresses are developed only due to quenching and expansion rather than bending. They also tested the model using the same set of materials and process conditions presented in [99]. They found that curved substrates having a large radius of curvature result in lower residual stresses than planar substrates.

2.3.5 Comparison of various analytical models

For the purpose of comparison, we have evaluated and compared the post-deposition mismatch stresses (as given by various analytical models) developed in several types of coatings that are cooled from deposition to room temperature, i.e. 25°C. Conventional TBC (deposited on 304 stainless steel), alumina (deposited on 316 stainless steel), and NiCoCrAlY (deposited on aluminum AA1100 alloy) were the coatings selected for the analysis. The properties of TBC, alumina and NiCoCrAlY were selected from the work of Wu et al. [101], Lui et al. [102], and Gan et al. [103] respectively (as shown in Table 2-1). From Figure 2-7 (a), it can be observed that there is a linear variation of the mismatch stresses (developed in the substrate) along the thickness direction. Moreover,

only Zhang’s model predicts linear variation of developed mismatch stresses along the thickness direction of the coating. This is evident from Eq. (7) and (9), it can be seen that the model by Hsueh (shown in Eq.(7)) does not depend on z-coordinate (i.e. along the thickness of coating). Due to the use of zero-order approximation, the model by Townsend et al. has clearly over-estimated the stresses developed in both the substrate and coating. Thus, Zhang’s model seems to be more effective in predicting the residual stresses in TSCs. The same observations were made when the analysis was carried out on alumina and NiCoCrAlY coatings as shown in Figure 2-7 (b) and (c) respectively. All the analytical results give values that are reasonably close due to the adoption of similar assumptions during their derivation. However, their main limitation is that they all lead to unrealistically higher stresses that may not actually represent the true residual stress state in coatings. The residual stresses computed with elasto-plastic models by Wu et al. [101], Liu et al. [102], and Gan et al. [103]) are far lower than the elastically predicted stresses. Thus, it is necessary to consider non-linear material behavior in future derivations. Otherwise, numerical methods should be used to compute the induced residual stresses. A common observation is that tensile stresses are developed in coatings that have higher CTE than the substrate material, and vice versa. Thus, for improved coating life, the selection of coating/substrate material combination should be done carefully such that tensile thermal-mismatch stresses are minimized while maintaining optimum values of other properties required for the smooth performance of the coating.

Table 2-1: Material properties of selected coatings for analysis

S/N	Material	Properties used @ deposition temperature	Source
1	TBC (top coat)	$E=500 \text{ GPa}$, $\nu=0.2$, $\alpha=10.34 \times 10^{-6} / ^\circ\text{C}$ @	[101]

	BC (bond coat) 304 stainless steel (substrate)	1025°C $E=109 \text{ GPa}, \nu=0.3, \alpha=16 \times 10^{-6} / ^\circ\text{C} @$ 1025°C $E=152 \text{ GPa}, \nu=0.27, \alpha=1.96 \times 10^{-6} / ^\circ\text{C} @$ 1025°C	
2	Alumina 316 stainless steel (substrate)	$E=84.7 \text{ GPa}, \nu=0.24, \alpha=9.68 \times 10^{-6} / ^\circ\text{C} @$ 865°C $E=152 \text{ GPa}, \nu=0.27, \alpha=1.96 \times 10^{-6} / ^\circ\text{C} @$ 865°C	[102]
3	NiCoCrAlY Al 1100 (substrate)	$E=225 \text{ GPa}, \nu=0.3, \alpha=14.0 \times 10^{-6} / ^\circ\text{C} @$ 645°C $E=68.9 \text{ GPa}, \nu=0.33, \alpha=23.6 \times 10^{-6} / ^\circ\text{C} @$ 645°C	[103]

E-Elastic modulus, ν -Poisson's ratio, α -coefficient of thermal expansion

As expected, post-deposition mismatch stresses increase with coatings deposition temperature as shown in Figure 2-7 (d); implying that coating deposition should be optimized such that the deposition occurs at the lowest possible temperature while keeping other essential coating properties intact. Figure 2-8 (a) and (b) show that the mismatch stress distribution is largely affected by the deposited coating thickness. It can be seen from Figure 2-8 (a) and (b) that the stress distribution for an alumina coating differs from that of a NiCoCrAlY coating. This is obvious since the elastic properties, substrate material, and CTE mismatch for both alumina and NiCoCrAlY coating systems differ. Thus, the two results cannot be compared. However, in general sense, we can say that tensile stress state becomes more tensile and compressive stress state becomes more

compressive when the coating thickness is increased. Figure 2-9 (a) show that post-deposition mismatch stresses are severely affected by compositional variation of second-phase particles within a TBC deposited on a bond coat (with properties obtained from [101]). Thus, through compositional variation, the life-time of the coating may increase by reducing the magnitude of tensile residual stresses near the top coat/ bond coat interface.

The effect of quenching stress on ceramic (alumina) and metallic (NiCoCrAlY) coatings was investigated using the analytical model developed by Tsui and Clyne [99] (implemented in MATLAB). Based on previous research by Liu et al. [102], and Gan et al. [103], the quenching stress in alumina and NiCoCrAlY were selected as 10 MPa and 300 MPa respectively. As shown in Figure 2-9 (b), the model correctly predicts that the quenching stress is more important in metallic coatings. As reported previously, the quenching stress in ceramic coatings is largely relieved by intense microcracking (which occurs as a result of thermal shock), and this complicates the modeling of quenching stresses in ceramic coatings. Since Liu et al. [102] and Gan et al. [103] used elastoplastic constitutive behavior for the top coat materials, we could not compare their results with the one presented in Figure 2-9 (b). However, the magnitude of the predicted residual stresses (as given in Figure 2-9 (b)) falls within the acceptable range. Thus, the model by Tsui and Clyne can be used as an effective tool in coating design if the correct value of quenching stress and effective elastic modulus are used. It should be improved further to consider temperature-dependent material behavior and nonlinear constitutive behavior.

Based on the results presented, analytical models can predict residual stress profile in coatings within a certain order of accuracy. But the effectiveness of the analytical model

for being used as a tool for the process optimization has been hindered by the various simplifying assumptions adopted. All the models were derived based on the theory of linear elasticity and therefore may predict very high (inaccurate) stress values. Residual stresses in coatings may develop as a result of non-linear constitutive behavior [41], [104], depending on the materials and process condition used. In fact, recent findings have shown that the mechanical behavior of ceramic coatings is non-linear elastic at low temperatures [105] and highly inelastic at high temperatures [106], [107]. Therefore, it can be said that the analytical models developed so far are not very effective in predicting residual stresses in ceramic coatings. Consequently, there is a need for the extension of the available models to handling non-linear constitutive behavior. Also, there has not been any analytical model for the prediction of peening stresses as well. Due to computational advancements, heat and momentum transfer between impacting droplets and substrates can be easily modeled. Thus, simple empirical models for the prediction of peening stress can be developed using the results obtained from single-splat analysis using the numerical model. Additional empirical models that consider the effects of particle process parameters (such as particle size, temperature, velocity, etc.) on the induced residual stresses can also be another interesting study. However, we must keep in mind that analytical modeling is mostly limited by the mathematical complexities associated with obtaining closed-form solutions to engineering problems. That is why it is often necessary to use numerical method for the modeling of residual stress evolution in coatings.

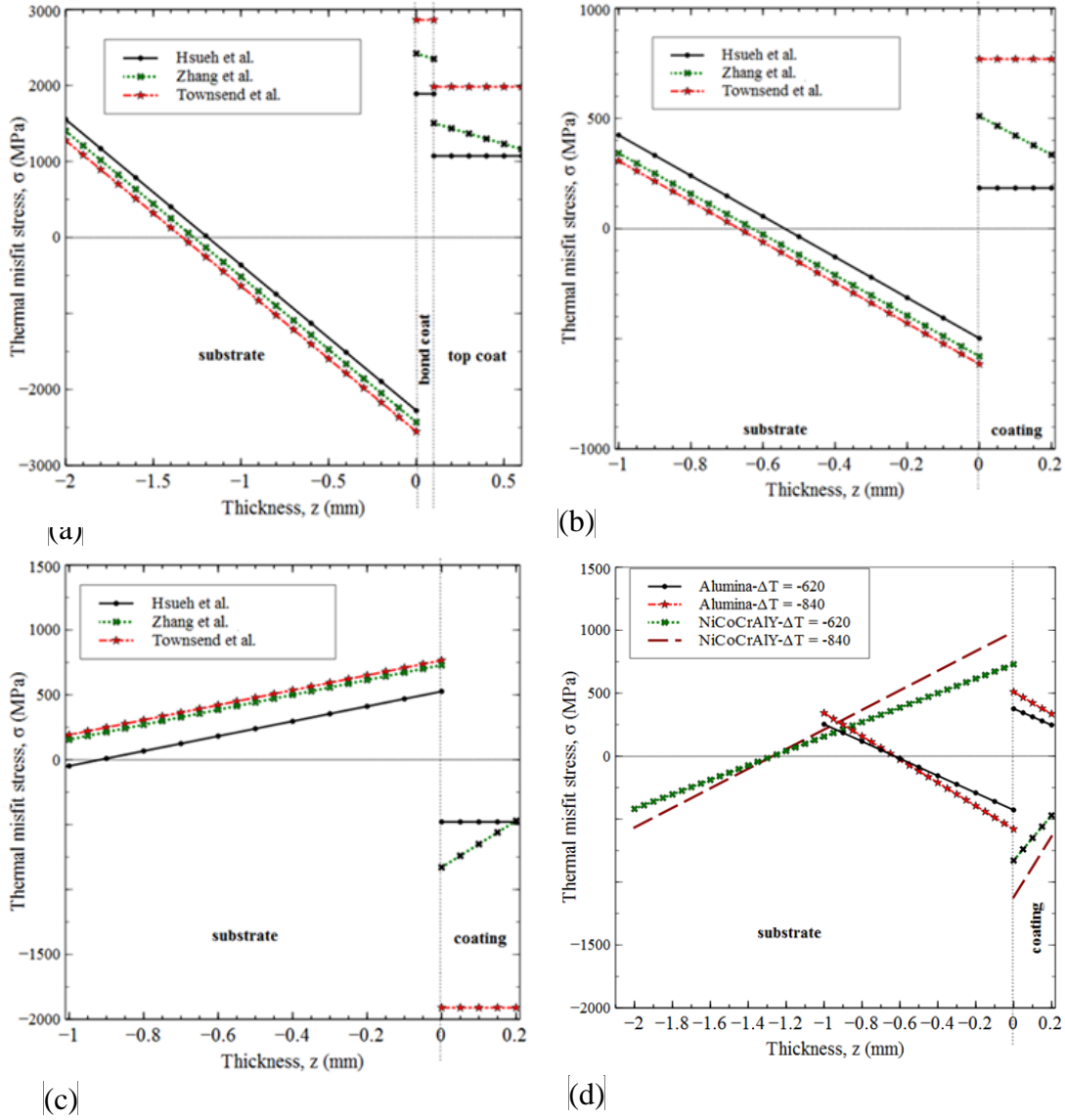


Figure 2-7: Comparing various prediction of thermal misfit (or mismatch) stresses for (a) TBC system deposited at 1000°C, (b) Alumina coating deposited at 840°C, (c) NiCoCrAlY coating deposited at 620°C, (d) variation of misfit stresses with temperature change as predicted by Zhang et al.

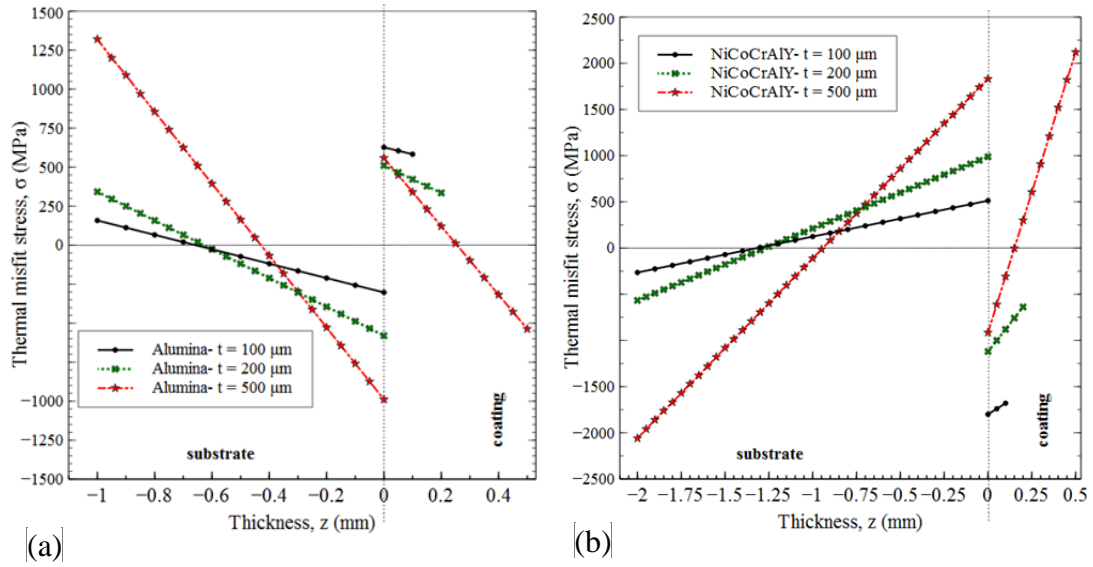


Figure 2-8: Effect of coating thickness on thermal mismatch (or misfit) stresses (using Zhang’s model and same properties as that Table-1) (a) for Alumina coating, (b) for NiCoCrAlY coating

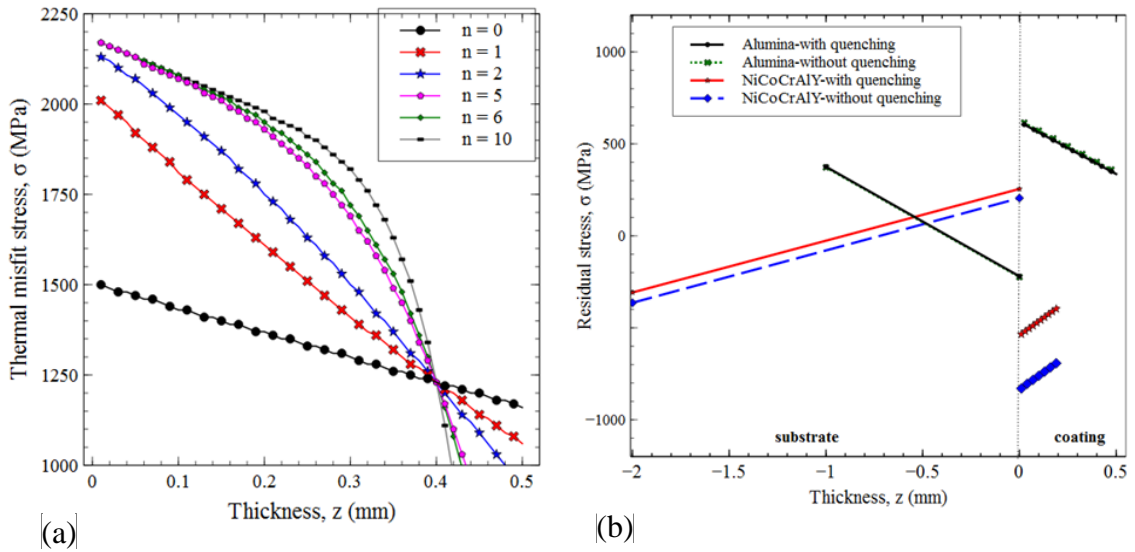


Figure 2-9: (a) Effect of gradient exponent on variation of misfit stress along coating thickness for TBC (interface is at $z=0$ according to Eq.(12)), (b) Effect of quenching stress on alumina and NiCoCrAlY coatings (using Tsui and Clyne’s model)

2.4 Numerical models for the prediction of the residual stresses

Due to recent advancement made in computational methods, the prediction of residual stresses in TSCs has been largely done using numerical methods. Finite difference method (FDM) is obsolete and has many limitations. Thus, the prediction of residual stresses in TSCs using FDM can be found only in few research works [108], [109]. Recently, residual stress development has been largely modeled using the finite element method. This is not surprising as finite element method is more popular than other numerical schemes due its flexibility and suitability of handling complex geometries and transient boundary conditions. Modeling of residual stresses with finite element method is done using conventional finite element formulation for thermal-stress analysis. This formulation couples the energy equation and local-force balance (stress-equilibrium) equation for the evolution of temperature and displacements respectively. Since finite element formulation of thermal-stress analysis is very common, the derivation of such formulation will not be presented in the present study. However, more details can be obtained from previous research work [110], [111]. The constitutive behavior of the material can be elastic or inelastic depending on the coating material and process conditions. Recently, modified finite element schemes such as the birth-death element technique, explicit-implicit finite element scheme, and image-based finite element schemes are used to model residual stress formation in TSCs. During our discussions, we will give more emphasis to recent results only.

2.4.1 Modeling of post-deposition mismatch stresses using conventional thermal stress analysis

For the sake of clarity, the discussion will start with the simplest numerical model which involves the use of conventional thermal-stress formulation to model only post-deposition cooling and predict the resulting mismatch stresses. Using this formulation, deposition stresses are neglected. Consequently, the finite element analysis often over or underestimates the residual stress field due to the negligence of the layer-by-layer evolution of residual stresses. Also, perfect interfacial boundary conditions are usually adopted at the interface. These inadequacies have resulted in mostly poor results. For this reason, this methodology has only been used by few researchers as discussed below.

Jiang et al. [112] predicted the effect of holes on residual stresses developed in TBC system using conventional linear elastic thermal stress analysis. They observed that the specimen dimension, spray process, coating thickness, and hole radius all influence the stress distribution. They found that the radius of the hole had more influence on the induced residual stress field than other factors investigated. Quantitatively, the numerical results obtained by Jiang et al. were not validated possibly due to lack of experimental data for validation. But a point of contention is whether a pure elastic model will give an accurate prediction of the induced residual stresses as coatings are susceptible to non-linear deformations. Unlike Jiang et al., Yilbas and Arif [31] used elastoplastic material model to predict residual stresses developed in Inconel 625-type Ni-based alloy coatings using conventional thermal-stress formulation. They found that the numerically predicted residual stress is closer to the experimental values than the results obtained using previous analytical (elastic) model [113]. Thus, they asserted that numerical models give

a more accurate estimate of the induced residual stresses. Furthermore, Zhang et al. [114] and Khor and Gu [17] carried out a numerical investigation of residual stress state in functionally graded coatings (FGC) using conventional thermal-stress analysis. They found that the bond strength and lifetime of FGC are significantly higher than that of the conventional (duplex) coatings due to the gradual change of properties near the coating/substrate interface. Even though the results presented by Zhang et al. agreed with experiments qualitatively, there was no quantitative validation for the model. Zhang et al. [114] also suggested that the various layers in FGC should be deposited at lower process cooling rates in order to minimize the residual stresses. Recently, these are the only few papers used the conventional thermal stress analysis to predict residual stresses in TSCs. Thus, the utilization of proper schemes for accurate prediction of the residual stresses is required as discussed in the next section.

2.4.2 Modeling of residual stress evolution using element birth-kill approach

As discussed previously, it is not possible to consider deposition stresses using the methodology discussed in the preceding section where only post-deposition cooling is modeled. As discussed, the results obtained from such schemes will hardly be reliable and accurate. In order to take into consideration, the deposition stresses (such as quenching and peening), a popular technique known as the element birth-kill technique is commonly used. This is a numerical procedure where elements are activated or deactivated at a given time step according to a certain criterion which can be set manually. The implementation of such technique in any finite element code is very straightforward. To “kill” (or deactivate) an element, magnitudes of material properties such as stiffness, conductivity, heat capacity, etc. are reduced to quasi-zero states by

multiplying with a reduction factor, commonly taken as 1×10^{-6} . On the other hand, all elements that are required to be “born” (or reactivated) are multiplied by a unity reduction factor. Numerical activation/deactivation of the elements is usually done using a user-defined algorithm that is designed based on the process history.

When applied to the coating process, the element birth-kill approach is commonly used to model the layer-by-layer evolution of the deposition (quenching or peening) stresses based on the process time, gun location, gun speed, spray rate and deposited coating thickness. The thermal deposition (or quenching) stresses are mainly predicted using thermal-stress formulation applied only to the activated elements, while peening deposition stresses are predicted using explicit finite element impact models. The heat influx due to heating of substrate/coating sub-layer by plasma plume and contact with molten droplets is normally considered by the inclusion of additional heat source terms to the energy equation. In order to adequately capture the gun movement, the heat source term is defined to be both space and time dependent (according to process history) using Gaussian distribution as done in [65], [102], [115]. Similarly, heat loss from the pre-deposited coating surface through convection and radiation is represented by another heat source term. After correct prediction of the deposition stresses using element birth-death technique, post-deposition mismatch stresses are computed and added to the pre-existing deposition stresses to give the final residual stress field. Many researchers have used this technique to provide a better estimation of residual stresses in coatings (as demonstrated in Table 2), and detailed discussion and analysis of their findings follow.

Considering thermal stresses only

The discussions will start with alumina/titania coatings as follows. The prediction of residual stresses using element birth-kill approach started with a research group from Germany (i.e. Buchmann et al. [65], [115] and Wenzelburger et al. [116], [117]) who investigated the effect of process parameters on residual stress field developed in alumina and titania coatings deposited inside engine cylinder liner tube. They found that the residual stress field developed in the coating was compressive due to the stress relaxation of the quenching (tensile) stress by microcracking. The results were found to be only qualitatively comparable to experimental ones (obtained by incremental hole-drilling method) due to the modeling of the coating material behavior using a purely elastic material behavior. As expected, their model predicts lower compressive residual stresses or even tensile stresses with higher substrate cooling rates (during deposition) due to higher quenching stresses. On the other hand, they found that substrate preheating resulted in more compressive stresses as shown in Figure 2-10. Thus, it is desirable to preheat the substrate material before coating deposition to minimize the development of tensile residual stresses which might initiate interfacial cracks. However, substrate preheating should not be done to the extent of its mechanical failure or chemical interactions with the environment. Another analysis by Liu et al. [102] and Zhao et al. [118] (using similar approach) revealed that the residual stresses developed in thermally sprayed alumina coatings are mainly compressive. In fact, Liu et al. tracked the evolution of the residual stress and found that it changes from tensile to compressive after cooling to room temperature as shown Figure 2-10. As demonstrated in the Figure, Liu et al. also found that lower substrate cooling rate resulted in higher compressive residual stresses due to lower quenching stresses. As an improvement on the model used by Buchmann et

al. and Wenzelburger et al., Liu et al. used an elastic-perfectly plastic material model to restrict the induced tensile (quenching) stresses to about 10 MPa (as experimentally determined) in order to consider the relaxation of the quenching stress by microcracking. Though the model results look good qualitatively, there was a large discrepancy between the modeled and experimentally measured residual stresses obtained by curvature method which may be due to the restriction of the coating yield strength. Due to the use of the more realistic material model, Zhao et al. found that the overall residual stress values were reasonably comparable with experimental results obtained by XRD technique. In another analysis, Valente et al. [77] found that the contribution of quenching stress is very negligible for alumina coatings (around 10-15 MPa) especially when the post-deposition thermal mismatch stress is as high as 100 MPa. But nevertheless, the addition of the quenching stress resulted in numerical values that were closer to experimental results and show that coating might fail at free edges of the specimen.

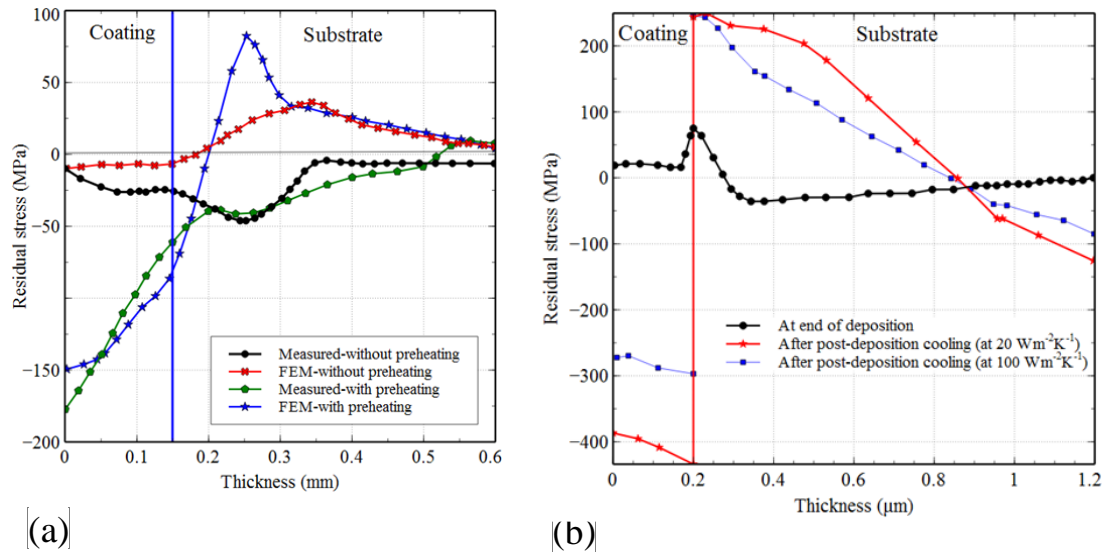


Figure 2-10: Residual stress variation along the thickness of alumina coating; (a) Effect of substrate preheating to 393 K on residual stress state of alumina coatings [65], (b) Effect of deposition/process cooling rate on residual stresses induced in alumina coatings [102].

For thermal barrier coatings (TBCs), yttria-stabilized zirconia and NiCrAl are the most commonly adopted materials for the top and bond coats. Thermally-grown oxide emerges as third layer in between the top coat and bond coat. The residual stresses in TBCs were also frequently modeled using element birth-kill approach. Starting with the research works carried out with a pure elastic material model for the topcoat, Fogarassy et al. [119] and Lugscheider and Nickel [120] modeled the evolution of residual stresses in TBC and observed that very high stresses (with large deviation from experiments) were predicted. Using similar approach, Lee et al. [121] found the TC/BC interface was the most critical region for the failure of coatings due to the formation of high tensile (quenching) stresses near the top coat/bond coat interface. Wang et al. [122] also found that the regions of high stress concentration (mostly existing near the free sample edges, interfaces, and defects) serve as the weak points where the failure of coatings initiates at the micro-level. However, they found that the overall effect of defects on the macroscale is helpful as it relaxes the post-deposition mismatch stresses which have a greater influence on the lifetime of ceramic coatings. Consequently, the presence of defects limits the distortion or bending of coated samples due to lower mismatch stresses. Based on similar residual analysis, Wang et al. suggested the use of double-layer top coat for TBC applications in future due to lower residual stresses and longer lifetime as compared to conventional single-layer top coat system. Most of the results presented in the works deviate largely from experimental ones. This may be due to the use of elastic constitutive behavior for the modeling of the top coat. Thus, we studied and categorized the papers in which elastoplastic models were used.

Using the birth-kill approach and elastic-perfectly plastic material model, Bengtsson and Persson [123] modeled residual stress evolution in TBC. As done by Liu et al. (for alumina coatings), quenching stress relaxation due to microcracking was considered by limiting the tensile yield strength of the material to lower values. Even though the qualitative validation of their results is not sound, they found qualitative agreement between the predicted effective plastic strain and experimentally measured vertical crack density. They also observed that the final residual stress state of the coating is compressive and high crack density was developed near the coating/substrate interface due to the development high quenching stresses near this region. In conventional birth-death element technique, the nodes of the dead elements will not take part in the calculation as long as they are inactive. Consequently, severe distortion of some inactive elements occurs since they share nodes with the active elements. To avoid this severe distortion, Wu et al. [101] developed the “modified element birth-death technique”, a significant contribution on the modeling of residual stress evolution in TBCs. Using the modified approach, a group of “soft/hypothetical elements” with suitable properties were added to appropriate locations within the model. These elements could undergo large deformation at low stress levels with little influence on other active elements. Unlike in previous research works, Wu et al. used Drucker-Prager criterion [124] to predict the stresses developed in the top coat since it is closer to capturing brittle behavior as compared to the elastic-perfectly plastic model. They also modeled the quenching stress relaxation in the top coat (due to microcracking) by restricting the tensile stresses to low values. The analysis was carried out on axisymmetric geometry. They found that while the radial residual stress was compressive and linearly increase with depth, the

axial residual stress was tensile and nonlinear along the depth of coating. They asserted that these stress states may lead to the delamination of the coating. As expected, the radial stresses were found to be considerably higher than the axial stresses. The residual displacements obtained using the modified finite element model was found to accurately agree with experimental results obtained by the hole-drilling method.

As solidification time (or melting temperature) of metallic coatings is considerably lower than that of high temperature ceramics, the modeling of residual stress evolution become more complicated due to the need to include peening stresses. For this reason, most metallic coatings are deposited with HVOF process which results in improved bond strength due to higher peening stresses. Thus, we found only few research works in which the modeling of residual stress evolution in metallic coatings was done by considering thermal stresses only. Gan et al. [103] modeled residual stresses developed during deposition of nickel–cobalt (NiCoCrAlY) alloy on an aluminum disc (AA1100) substrate using birth-death element technique. They assumed that the coating undergoes elastoplastic deformation with bilinear kinematic hardening. The displacements given by the model compared well with the ones obtained by laser displacement sensor except for the fact that random fluctuations of displacement and stress values were observed from the experimental results. This is likely due to the slight vibration caused by the spray gun movement, instantaneous impact of sprayed particles and heterogeneous nature of the coating microstructure. As found in ceramic coatings, they found that preheating the substrate prior to coating deposition result in decreased residual stresses due to lower quenching stresses. In another research work, Gan et al. [125] applied the model to TBC

and found that the displacements obtained by the model compare well with experimental ones.

Considering both peening and thermal stresses

As mentioned previously, the contribution from peening stress is only significant when the particle (or droplet) impact velocity or spray rate is very high. Generally speaking, the particle impact velocity is relatively lower in plasma spray process than HVOF and D-Gun. Thus, for HVOF and D-Gun processes, the peening stress is an essential component of the residual stress state. Metallic coatings are commonly sprayed with HVOF because of the need for higher bond strength and density. Due to the non-linearity associated with modeling impact, explicit finite element schemes are commonly used for the modeling of peening stresses. Explicit schemes are very effective in solving nonlinear dynamic finite element problems such as impact, crash analysis, large plastic deformations, etc. However, the main disadvantage of explicit schemes is their slowness due to the need for using extremely small-time steps. Furthermore, the analysis often becomes tedious due to the need to couple together results from both explicit and implicit finite element schemes. Nevertheless, coupled implicit-explicit schemes have been used recently to predict residual stresses in metallic coatings. The explicit scheme is used to predict the peening stresses, while the implicit scheme is used to model thermal stress evolution using element birth-kill approach.

Zimmerman [126], [127] predicted residual stresses in Ti coating (deposited on Al₂O₃ cylindrical disk sample by D-Gun) using this approach. They carried out the computation in two stages and using 2D axisymmetric model, the first stage modeled stress-state and

temperature distribution induced during the impact of the coating onto the substrate using an explicit finite element scheme. Then, the second stage used the results of the first stage to predict the overall residual stresses using an implicit thermo-mechanical model (developed based on birth-death element technique). They assumed that when sprayed particles are deposited on solidified splats, 80% of the kinetic energy of sprayed particles is converted into heat energy and plastic work. They also assumed perfect and uniform contact condition at splats interface and that the temperature and stress fields developed by three particles are the same for all the layers. Even though a slight discrepancy was found when the numerically predicted in-situ curvature was compared with experimental one (measured with digital dial gauge), the sudden change in stress state within the thickness of coating seems confusing (shown in Figure 2-11 (a)). This may be due to high stresses developed near defects. The results (from Figure 2-11 (a)) also show that the radial compressive residual stresses are higher at regions near the coating/substrate interface. Moreover, larger coating thickness was found to have a negligible effect on the stress state near the interface as depicted in Figure 2-11 (a). It can also be seen (from Figure 2-11 (a)) that substrate pre-heating results in negligible change in residual stresses within both the substrate and coating layers. However, they observed that the residual stresses increased with coating thickness in some regions. Similar analysis was carried out with HVOF coatings with slightly different assumptions by Lyphout et al. [32] and Bansal et al. [128], [129]. Both Lyphout et al. and Bansal et al. assumed that the peening stresses developed due to the impact of one particle is the same for the whole coating layer at a particle time step or layer level. Lyphout et al. [32] found that the coating thickness did not have a significant effect on the developed residual stresses and that the

high compressive residual stresses developed in HVOF coatings are the reasons for their good bond strength. Bansal et al. [128] made a somewhat different assumption, that 90% of the kinetic energy is dissipated as heat. In order to incorporate the effect of strain, strain rate, and temperature on the developed stress fields during impact, they used Johnson-Cook model for predicting the resulting peening stress using an explicit finite element scheme. It can be seen from Figure 2-11 (b) that higher particle impact velocities result in higher compressive stresses. Elhoriny et al. [130] also used a similar approach to predict residual stresses in Al₂O₃ coating. But instead of modeling quenching and peening stresses developed by single droplet, they considered large sets of material blocks consisting of a chunk of particles. They found the peening stresses to be considerably lower in ceramic coatings due to their high yield strength and porous nature. Nevertheless, the inclusion of peening stress helped in predicting residual stresses that were closer to the ones measured by the hole-drilling method.

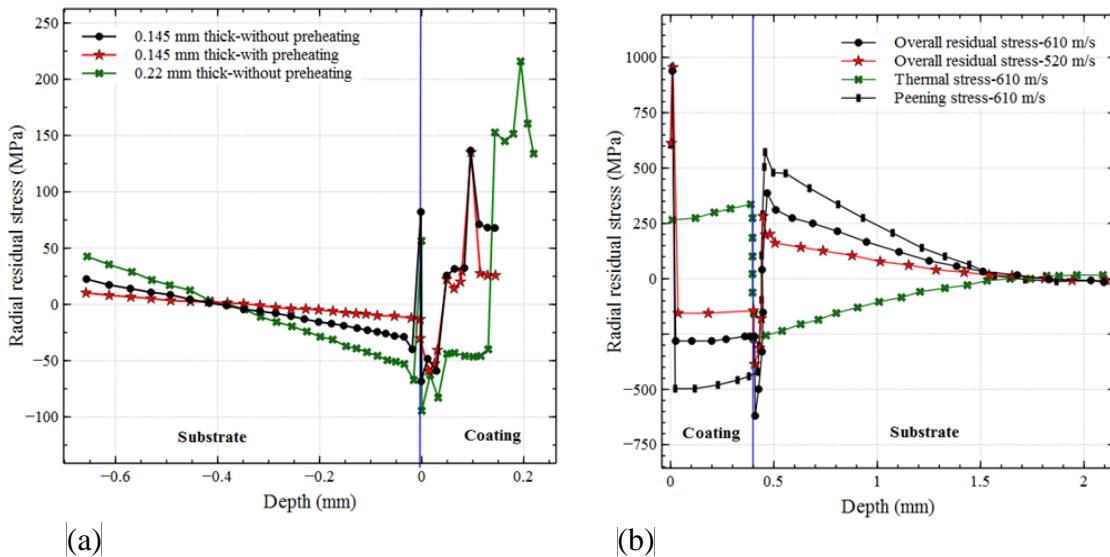


Figure 2-11: (a) Effect of coating thickness and substrate pre-heating to 80 °C on residual stress state of HVOF Ti coating [126], [127], (b) Variation of simulated thermal, peening and final residual stresses along thickness of SS 316-coating - effect of particle velocity demonstrated ([128], [129])

2.4.3 Issues with element birth-kill approach

Based on the reviewed papers, the birth-death technique is currently the most effective approach of modeling residual stresses in TSCs. The method combines both deposition and post-deposition stresses to give the overall residual stress state. The element-wise activation/deactivation of elements can be elegantly done using data from thermal spray deposition history. However, certain problems are often encountered when modeling residual stresses using this approach. First, the prediction of the actual value of quenching stresses is very challenging due to stress relaxation by microcracking, plastic deformation, creep, interfacial sliding and imperfect bonding. The microcracking is very common in ceramic coatings, while other stress relaxation mechanisms are most encountered in metallic coatings. Several researchers have considered stress relaxation by limiting the maximum quenching stress to a low value using certain elastoplastic material models (e.g. ideally plastic model, Drucker-Prager model, etc). However, there is a need for the development of a properly calibrated model based on more experimental findings of the stress relaxation mechanisms. This will not only relax the macro-stresses developed within the entire coating layer but also help to determine the localized residual stresses developed near the defects or imperfections that fill the coating microstructure. Using the localized stresses, the regions where coating failure might initiate can be correctly predicted, thus opening a new trend for the study of residual stress influence on failure mechanism and lifetime of TSCs.

Furthermore, the use of homogeneous, isotropic, and linear elastoplastic material model for the predicting of residual stresses usually affects the quality of the stress results obtained using birth-death technique. The mechanical behavior of TSCs is more likely to

be non-linear and inelastic due to the presence of many types of defects (such as voids, cracks, interfaces, inclusions, etc.). Recent findings have shown that the mechanical behavior of TSCs is usually non-linear elastic and nonlinear inelastic depending on temperature and extent of loading ([105]–[107]). Moreover, the nature of thermal spray process is such that coating properties are expected to vary with directions due to the splat-splat growth of the coating. The properties in the thickness direction are expected to be remarkably different with that of the horizontal direction. Thus, the use of isotropic material model is clearly wrong. The negligence of heterogeneity and anisotropy is the main reason why the numerical models cannot predict the stress fluctuations that were observed experimentally. Similarly, the poor quantitative comparison of the numerical results with experimental ones is due to these and other issues (such negligence of proper convection and radiation heat transfer sources).

With regards to coupling the element birth-kill approach with peening stresses (using explicit schemes), the quantitative and qualitative comparison of the numerical and experimental results looks better with the addition of peening stresses. However, several assumptions adopted in the research work presented lack sound basis. For instance, Zimmerman [126] assumed that 80% of the kinetic energy of sprayed particles is converted into heat energy and plastic work during the impact of the sprayed particles. While Bansal et al. [128] assumed that 90% of the kinetic energy is dissipated as heat. Since the sprayed particles hardly rebound after impact, it is expected that almost 100% of the kinetic energy will be converted to plastic work, heat, elastic wave propagation, and sound (with the energy dissipated as elastic wave and sound being negligible). Thus, this issue needs to be clarified further and a standard need to be set for future research

work. Also, perfect contact is assumed between impacting particles and substrate surface. However, thermal contact resistance should play a unique role in determining the amount of heat energy transferred to the substrate, especially at such a small length scale. Thus, a thorough investigation of the effects of these assumptions should be carried out in future. Despite the promising results obtained, the birth-death technique needs to be improved further. Still, the method predicts residual stress field that considerably deviates from experimental one as demonstrated in Table-A1 in Appendix. Also, it should be modified in such a way that it can capture the complex interactions between deposition process parameters for effective prediction of residual stresses.

2.4.4 Modeling of localized stresses using image-based FEM

As discussed previously, TSCs are full of heterogeneities or irregularly shaped regions which may include cracks, pores, second-phase particles, splat interfaces, etc. But the modeling of residual stresses in TSCs is often carried out using homogeneous material models, thus resulting in the deviations observed between the numerical results and experimental one. Moreover, the available damage models used for failure prediction in TSCs are developed based on the assumption of homogenous material constitutive behavior which may not capture the true damage mechanisms of coatings. Apart from the difficulty associated with the geometric representation of the heterogeneities using CAD programs, numerical computations become very intensive due to high geometric non-linearity, poor mesh quality, and numerical discontinuities. This has led to the development of new numerical schemes or tools for adequate handling of heterogeneous material behavior. Recently, image-based (or object-oriented) finite element scheme is commonly used for constitutive modeling of heterogeneous materials. Image-based finite

element method started with the work of Hollister and Riemer [131] in 1993. Then, Tereda et al. [132] demonstrated the potential of image-based finite element modeling of materials using real (or complex) microstructure and homogenization technique. Later, an objected-oriented finite element method (OOF) for the modeling of materials using real images of microstructure was developed by Langer et al. [133]. Since then OOF has been used in modeling of heterogeneous materials. OOF uses adaptive meshing algorithms to convert the microstructure image to a high quality finite element mesh. Due to the fact that image-based finite element schemes are not very common in commercial packages, only a few researchers used such methodology in modeling residual stresses in coatings.

Hsueh et al. [134] analyzed the effect of substrate surface roughness or asperity on residual stresses developed in TBCs using a linear thermo-elastic analysis in OOF. They considered only thermal mismatch stresses developed as a result of the post-deposition cooling, the presence of localized regions (or defects) and surface undulation of the bond coat. Pores and cracks were the main microstructural defects considered in the model. As expected, they found that very high localized stresses were induced at regions surrounding the defects. Therefore, they found that substrate surface roughness (represented by sinusoidal curve) resulted in high localized residual stresses (in the GPa range) with the convex and concave portions of the top coat and bond coat materials having tensile and compressive stresses respectively. Due to the difficulty of experimental measurement of residual stresses at the micro-level, Hsueh et al. could not provide quantitative validation of the presented stress results. Similarly, Klusemann et al. [48] numerically predicted residual stresses developed in thermal-sprayed WC-Co coating on steel substrate using OOF. They used images obtained from both optical

microscopy and scanning electron microscopy (SEM) to estimate the thermal mismatch stresses developed after the deposited coating was cooled to room temperature. Unlike Hsueh et al., they modeled the resulting mismatch stresses using an elastoplastic material model (for both coating and substrate) and considered initial compressive stresses induced on the substrate during the surface preparation (by roller burnishing) process. They compared the thermal mismatch stress field developed in a homogeneous microstructure with that of a microstructure that is filled with numerous defects, such as the presence of dispersed Co particles within WC matrix, voids, cracks, surface undulation, splat interfaces, etc. They found that the average stress distribution within the coating is the same for both the homogeneous and real-microstructure model. However, they observed several fluctuations of stress values within the coating due to the formation of high localized stresses near regions of the imperfections. Thus, image-based residual stress models could be used to investigate the mechanism of coating failure by fracture initiation and propagation. The residual stresses were found to reduce with coating depth, mainly tensile on the surface and compressive at regions near the coating/substrate interface. It is important to note that the stress state near the coating interface is compressive in both the substrate and coating material. This is favorable to the life of the coating since compressive stresses usually result in increased delamination fracture toughness.

Mostaghimi et al. [35] applied their previously developed stochastic model to simulate the microstructure of Ni coating deposited on a stainless steel substrate by the HVOF. Using an image of the simulated microstructure, they used a linear elastic thermo-mechanical model (implemented in OOF) to predict the mismatch stresses developed

after cooling the deposited coating to room temperature. Voids were the only source of discontinuities considered for the analysis. They demonstrated that the average mismatch stresses were mainly found to be tensile within the coating, with some fluctuating values of both tensile and compressive stresses developed near localized regions. They also found that the presence of pores/voids resulted in a reduced average stress level within the coating due to local stress relaxation. However, there was no quantitative validation of both the average and localized residual stresses, possibly due to lack of experimental data for the validation of both the localized and macro-stresses (average size of voids and cracks being around 2 μm). Another issue is that, small stress values were observed at the image boundaries due to the nature of boundary conditions used for the analysis. Then, this question the validity of results obtained from image-based finite element schemes especially that the accuracy of finite element results significantly depend on the quality of elements that are near to the geometrical discontinuities within the simulated microstructure.

Based on our discussions, it can be seen that very few research works have been carried out using this approach. This is mainly due to the lack of clear methodology to model deposition stresses using microstructural images. The microstructural images are usually obtained after the coating build-up, hence, only post-deposition mismatch stresses can be estimated. Additionally, the occurrence of noise signals in an image poses difficulties during conversion of the image to finite element mesh. Due to the presence of noise and intricate defects shapes, the formation of spurious finite elements (having bad aspect ratio) leads to inaccurate results and prolonged simulation time. Thus, better ways of eliminating the noise signals (without compromising contents) and finite element

meshing should be developed. Mostaghimi et al. [35] were the only research group that predicted the residual stresses developed in TSCs using microstructure images obtained from the stochastic process model. However, the residual stress model is not stochastic and can capture only post-deposition misfit stresses. It will be interesting to develop a stochastic residual stress model in order to effectively capture the randomness associated with residual stress evolution in TSCs. With this, issues like deposition stress relaxation, the inclusion of peening stresses and stress concentration near imperfections will be properly considered. Consequently, numerical prediction of residual stresses will be more realistic and may pave way for the development of coating failure/damage and lifetime prediction models.

2.5 Summary of literature survey

2.5.1 Analytical model for residual stress in coatings

Various analytical models have been developed and used for the prediction of residual stresses in TSCs. Several discussions have been previously made on the flaws of the analytical models. Due to the limitations of analytical modeling, the following gaps are identified in the literature:

- a) With the recent advancement in material science, a thorough investigation for the correct estimation of the elastic modulus of single splat (to be used in Eq.(2.1) and Eq.(2.2)) and that of the entire coating is required. There is not enough justification for the assumption that the elastic modulus of individual splats is the same as that of the entire coating layer (taking defects into consideration).

- b) An analytical model for accurate prediction of the peening stress is required. Closed-form expressions can be derived based on the change of energy state of sprayed particles during impact. Otherwise, effective empirical models should be developed using finite element analysis. The development of effective peening stress model will greatly improve the analytical model by Tsui and Clyne which is currently in use by many researchers.
- c) As heat transfer analysis is not included in the derivation of mismatch stresses, energy equation should be considered in future. Furthermore, temperature-dependence of material properties should be considered when deriving analytical models in future.

2.5.2 Finite element modeling of residual stress in coatings

Various approaches have been used in modeling residual stress state of coatings using finite element method. Numerical predictions based on birth-kill finite element schemes have been shown to be quite reasonably closer to the experimentally measured residual stresses. Image-based finite element schemes have been restricted to the prediction of only post-deposition thermal misfit stresses. But they provide an elegant way of predicting the localized stress regions which may serve as potential failure initiation sites in thermal sprayed coatings. Therefore, the finite element method is a very powerful tool that can be used to predict residual stresses in coatings. We are highlighting various ways in which the prediction of residual stresses can be more effective, realistic and useful in the following sections.

Element birth-kill approach: Points of consideration for future simulations

As seen in many research works, element birth-kill approach is currently the most widely used and acceptable way of numerically estimating residual stresses in TSCs. When applying such approach, it is necessary to adopt certain assumptions to minimize implementation difficulties. Consequently, the results are usually not as accurate as required especially when compared with those of experiments. We have identified several corrections or suggestions for the improvement of the stress results in future.

1. The “Modified” element birth-kill approach based on an algorithm developed by Wu et al. [101] (as discussed in section 5.2.1) should be used in future. It helps to improve the quality of the stress results by minimizing large distortion at the nodes that are common to “born” and “killed” elements.
2. The coating elements should be activated block-by-block (instead of layer-by-layer) in order to correctly track the evolution of the residual stresses as adopted in recent works by Elhoriny et al. [130] and Berthelsen et al. [135].
3. The main simulation parameters required to predict deposition stresses (such as effective modulus, convection, radiation coefficients, thermal contact resistance, stress relaxation, the percentage of kinetic (peening) energy that is converted to plastic work and heat, etc.) should be calibrated using the stress values obtained by ICP sensor. It is currently not easy to determine the values of these simulation parameters. In this way, the calibrated model can easily be used for optimization of the process without the need to perform too many experiments. This is the essence of modeling.
4. It is well known that finite element formulations give average stress results at the interfacial nodes (of two dissimilar materials) when perfect (or glued/tied

constraint) bonding is assumed at the interface. This will ensure the continuity of displacement fields across the interface. The stress values are not continuous along the interface as demonstrated with the analytical models shown in Figure (11) and (12). A common practice is to decompose the stress at interfacial nodes into individual values. However, the results presented in most research works have not done this. This should be corrected in future.

5. The mechanical behavior of the coating material should be simulated with realistic constitutive models such as non-linear elastic and/or inelastic behavior presented in the recent papers [105]–[107].
6. The birth-kill approach can be applied to an image-based mesh in order to add deposition stresses. Even though the image/mesh is obtained after the coating has been cooled to room temperature, the deposition stresses can still be predicted since the mesh nodes can deform. If the sharpness of the defects is too small, there can be challenges with mesh refinement near defects. In such a case, a smaller portion of the image (in the form of representative volume element or RVE) should be modeled and integrated into a multiscale modeling framework.
7. As commonly observed experimentally, cracking of ceramic coatings occurs after post-deposition cooling to room temperature. Thus, it will be interesting to consider adding a damage model during post-deposition stage in future.

Process modeling using meshless Lagrangian solvers

Based on the review presented, we have seen that the main challenge of numerical residual stress modeling is the prediction of deposition (both quenching and peening) stresses due to complications arising from stress relaxation. Therefore, there is a need for

the development of an effective and computationally efficient model for the prediction of deposition stresses during the thermal spray process. With Eulerian schemes (e.g. phase field, level-set, volume of fluid, etc), it is difficult to track splat interfaces due to the problem of coalescence (inherent in the formulation). Furthermore, Eulerian schemes require relatively higher mesh density or computational resources as compared to meshfree Lagrangian schemes.

In future, meshfree parallel Graphics Processing Units (GPU) compatible Lagrangian solvers can be used to effectively model the deposition process as well as stresses. Each particle (or droplet) can be represented as a separate meshless Lagrangian domain consisting of only nodes or point cloud having unique initial and boundary condition. Recent meshless methods such as smooth particle hydrodynamics (as in [136]–[138]) and discrete gradient method (as in [139], [140]) can be used to model large deformation problems on point cloud. The process of splat formation and solidification can be simulated on the point cloud using non-isothermal fluid-structure interaction model. Interestingly, information on the solidification front during the phase change process (as given by the energy equation) can be directly used to compute the associated quenching stresses using stress-equilibrium equation. By the conversion of the discrete points to finite element mesh, residual stress relaxation processes (such as thermal shock, inelastic deformations, and damage) can be easily modeled using new numerical schemes (e.g. extended finite element method [141], discontinuous Galerkin's method [142], cohesive zone models [143], etc.) that are more stable than meshless approaches. However, the stability of the meshless schemes can be improved such that they can be used to model that as well. For high energy processes (such as HVOF), peening stress is implicitly

represented at the fluid-fluid or fluid-structure interface. Thus, there is no need for the ambiguous assumptions usually adopted when solving for the peening stresses. The main limitation of this approach is that it can only be used to model the stresses associated with the deposition of few sprayed particles (less than hundred) due to the need for the implementation of several interfacial boundary conditions during particles interaction. Even with that, it is necessary to distribute the solution across parallel processors.

Using this approach, a thorough investigation on the effect of the process parameters (such as particle temperature, velocity and size, gun speed, gun path, deposition temperature, substrate temperature, spray rate, and cooling condition) and their interactions on residual stresses can be carried out. Several design charts can be developed by conducting the analysis on only 1-6 particles. These design charts will greatly help in material selection and optimization of the process. Particles are sprayed with randomly (statistically) distributed parameters (such as size, velocity and temperature); thus, residual stress evolution is stochastic. Therefore, stochastic residual stress prediction tool can be developed using established rules for stress-parameter correlations as obtained from the design charts. Furthermore, this approach can be used to generate several representative volume elements (RVEs) having localized residual stresses (at the microscale). Within multiscale modeling framework, the correlation between localized stresses (existing near discontinuities) and macro-residual stress field can be easily established using computational homogenization [144], [145]; thus, paving a new way for investigation the effects of localized residual stresses on the constitutive behavior of coatings (e.g. property estimation and damage).

Using the above suggestions, a robust model that may serve as a versatile tool for investigating the relationship between process parameters, coating microstructure, and coating properties may be developed. This may be used in conjunction with fracture-based damage models to investigate all possible failure mechanisms of coatings. It may serve as a tool for optimization of thermal spray process for enhanced coating quality and performance.

CHAPTER 3

RESEARCH OBJECTIVES AND METHODOLOGY

Based on the extensive literature survey presented, it can be seen that various limitations of previous models have made it difficult to obtain a reliable prediction of residual stresses in thermal spray coatings (TSCs). Most of the models are immensely simplified; thus, they do not account for non-linear mechanical behavior of TSCs. Therefore, there is need for the development of innovative and efficient computational approach for reliable estimation of residual stress in TSCs.

In the present study, an innovative hybrid computational approach for numerical modeling of residual stress in TSCs is proposed, implemented and evaluated. The hybrid approach uses point cloud to model the spray deposition process and finite elements to model the heat transfer and deformation occurring during the process. The point cloud model is solved using the popular meshless numerical method, smooth particle hydrodynamics (SPH), due to its fastness and robustness in handling large deformation problems. Using SPH, multiple droplets impact, spread and interaction which leads to the coating layer build-up is simulated on point clouds. Using recent algorithms developed for point cloud processing, the point cloud of simulated coating microstructure is converted into meshed layers that are composed of typical internal defects found in coatings. The conversion of point cloud to meshed domain is necessary as grid-based schemes are more suitable and stable with regards to structural analysis. The thermo-mechanical analysis of deposited coating layer is conducted using finite element method

(FEM) where the redistribution of temperature, displacement and stress fields during the coating process are computed.

The hybrid approach is used to predict residual stresses and associated defects developed in plasma-sprayed ceramic (YSZ) and metallic (Ni-20%Al) coatings deposited on stainless steel substrate. The numerical predictions are validated against experimental results obtained from microscopic studies, mechanical tests and hole drilling experiments. The approach can tackle common material non-linearities (such splats solidification (or quenching), plastic deformation, and microcracking occurring during the spray process. The residual stress is determined from the summation of deposition and post-deposition (mismatch) stresses obtained by cooling coating to room temperature. The new approach is expected to yield more realistic estimation of residual stress profile developed in TSCs.

3.1 Objectives

Thus, the objectives of the present study are as follows:

1. To develop an effective computational methodology for numerical prediction of residual stress in thermal spray coatings.
2. To validate or calibrate the model using experimental studies
3. To demonstrate the effectiveness of the methodology in predicting residual stress profile developed in coatings used for industrial applications.

3.2 Scope and limitations

Several modeling assumptions are adopted based on evidence from the literature as will be highlighted in Chapter 4. Most of these assumptions generally hold for any thermal

spray process. However, the hybrid method presented here is solely developed for air plasma spray (APS) process due to its widespread use.

3.3 Research methodology

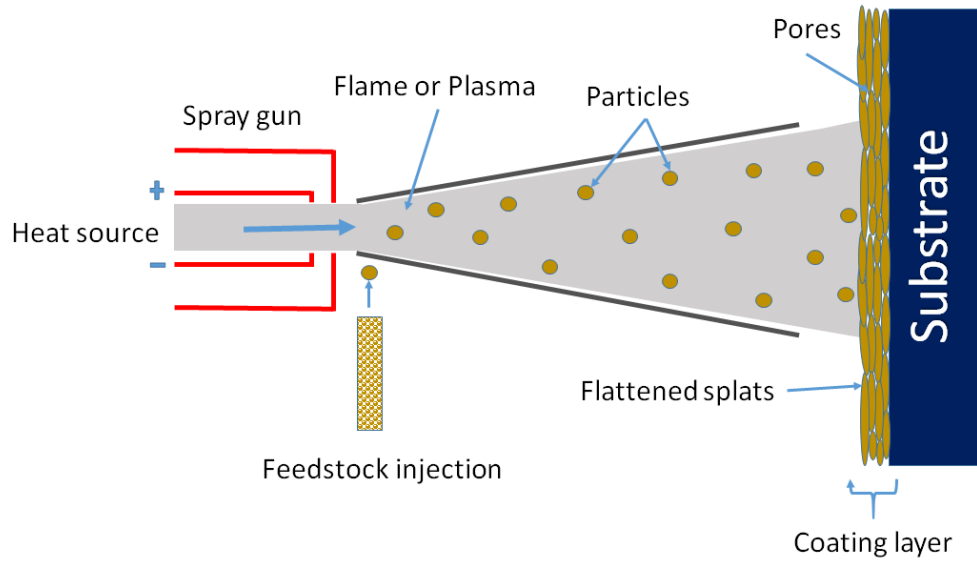


Figure 3-1: A typical schematic for thermal spray process deposition on flat substrate

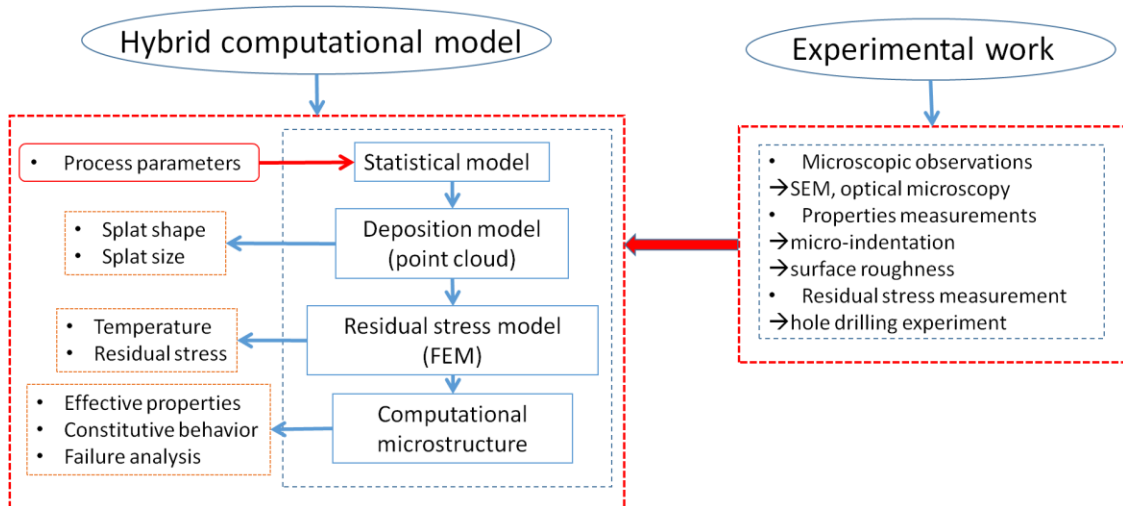


Figure 3-2: Proposed methodology for the multiscale computational model

To capture the dependence of residual stress on the spray process, there is need for the modeling of the coating deposition process. The spray process strongly influences the

dynamics of splat formation, solidification and layer growth as demonstrated in Figure 3-1. The most influential process parameters are initial droplet size, droplet impact velocity, droplet temperature, substrate temperature, substrate surface roughness and spray path. According to previous experimental works, the distribution/variation of these parameters can be statistically represented with some mean and standard deviation. Therefore, for more realistic modeling, statistically distributed process parameters are taken as inputs to the deposition model developed in present work (as demonstrated in Figure 3-2). The deposition model is required for the numerical simulation of multiple droplets impact, spread and deformation on point cloud. Upon impact, the droplets deform into flattened disk-like structures, commonly known as coating “splats”. For realistic spray process model, the geometry (shape and size) and interaction of deposited splats need to be simulated. Due to complexity of spray process, the geometry of interacting (or nearest neighbor) splats is somewhat intricate. Also, apart from complexity of splat shapes, the large deformation associated with multiple splats interaction leads to severe numerical difficulties (such as excessive mesh distortion, high computational intensity, coalescence of splat interfaces) when solved with finite element schemes. Consequently, the coating deposition model is discretized on point cloud and solved using the recent meshless scheme for numerical solution of large deformation problems, smooth particle hydrodynamics (SPH) [1].

Due to its high stability and suitability of solving multi-physics problems, the finite element method (FEM) is used to compute the temperature distribution and associated stresses developed during the process. In that case, the point cloud of simulated splats needs to be converted into meshed computational domains that are composed of high-

quality finite elements. This is the most difficult step during the implementation of the hybrid approach because several recent algorithms for point cloud data processing (such as alpha-shape, poisson disk sampling algorithm, quadratic edge decimation, etc) are required for such task. The FE domain of splat structures are stacked layer-by-layer to form a coating sub-layer (having thickness of around 7 μm) that contains the typical defects found in TSCs. Usually, 2-4 sub-layers makes a single pass (having thickness of around 25 μm) and 6-11 passes are required to reach the total thickness of typical coating layer.

Therefore, thermo-mechanical analysis of the coating process is conducted using FEM. The analysis is done for two temporal regimes, i.e. deposition and post-deposition regimes. In deposition regime, the temperature distribution and stresses developed due splat solidification/quenching is numerically predicted in a pass-by-pass manner until the required coating thickness is attained (as in typical thermal spray process). While, in the post-deposition regime, the final temperature distribution and stress field developed when the deposited coating and substrate layers are cooled to room temperature are predicted. The aggregation of stresses developed during these two regimes gives the residual stress field. Numerically, this is achieved by cooling the coating and substrate layers to room temperature while retaining the strain history developed during deposition. If additional stresses are induced from other sources (such as substrate curvature, surface roughness, surface pretreatment and coating post-treatment), they must be added to the deposition and post-deposition stresses to get the final residual stress field. Thus, using the hybrid approach, simulated coating microstructure having initial residual stress field is computationally generated. The simulated microstructure can be used for further

advanced studies such as determination of effective coating properties, investigation of coating constitutive behavior under external loads and failure analysis.

In the current dissertation work, the hybrid approach will be used to study the evolution of residual stress and internal defects in ceramic (YSZ) and metallic (Ni-20%Al) coatings deposited on metallic substrates. Several experiments were conducted with real coating samples in order to support/validate the numerical results obtained with the hybrid approach. Firstly, optical microscopy is used to confirm the total thickness and surface roughness of the coating and have some idea about the extent and nature of defects (such as pores, cracks, splat interfaces, and inclusions) present in the coating microstructure. Then, the various defects are compared with that of the simulated microstructure. Secondly, scanning electron microscope (SEM) is used to get detailed information about the defects present in the coating microstructure. The high resolution of SEM enables the identification of internal coating defects existing at smaller (micro) scale. Important micro-features like microcracks and interfaces present within the coating layer are critically analyzed. The SEM also reveals more information about the surface morphology of the coatings which can help in interpretation of the results obtained from surface roughness measurement. The coating surface roughness was measured using surface profilometer.

Due to high level of porosity and heterogeneous nature of the coating layer, the effective properties of the coating are not the same as that of bulk material. Important properties required for the present study are hardness, elastic modulus and coating cohesion/adhesion strength. Therefore, microindentation is used to obtain a good estimate of coating hardness and elastic modulus. Also, scratch test is conducted in order to

determine the cohesion or adhesion strength of coatings. Lastly, residual stresses developed in the coating samples are measured using the hole drilling experiment. Rosette strain gauges bonded on the surface of the coating are used to measure strain relaxation occurring when a hole is drilled incrementally through the thickness of coating and substrate layers. With the aid of finite element analysis, incremental strain relaxation data is converted to residual stress. By comparing with the experimental residual stress profile, the results of the hybrid approach are validated.

CHAPTER 4

HYBRID COMPUTATIONAL MODEL

In the present study, an innovative hybrid computational approach for modeling thermal spray deposition is proposed, implemented and evaluated. The approach utilizes both point clouds and finite elements to model the evolution of residual stress in thermal spray coatings (TSCs). Smooth particle hydrodynamics (SPH) is used to model the deposition process whereby droplets impact, spread and interaction (or coating layer build-up) is simulated on point clouds. Point cloud processing tools are used to convert the deformed coating splat structures into high quality 3D finite element mesh that is composed of coating internal defects. Finite element method (FEM) is used to model heat transfer and structural deformation occurring during the process. Important aspects of the coating process such as splats solidification (or quenching), evolution of quenching microcracks and material mismatch are considered during the computation. Thus, the residual stress is determined from the summation of deposition and post-deposition (mismatch stresses). This is achieved by cooling coating and substrate layers to room temperature. The approach presented here is robust in handling complexities encountered during the spray process such as multiple splats interaction, influence of inclusion (or foreign) particles, and undulation of pre-deposited coating/substrate surface.

4.1 General modeling assumptions adopted

Prior to discussions about the governing equations for the present numerical model, the various assumptions adopted for the numerical model will be highlighted. Based on the findings presented in previous research works, these assumptions are considered valid.

1. For APS process, it is widely considered that droplet spreading time is one order of magnitude less than the solidification time (e.g. in Ref. [2], [146]). Thus, solidification starts after droplet deformation completes. This decouples the fluid flow and energy equations.
2. In the literature [2], the mechanism of diffusion at splat interfaces is very fast (i.e. within time scale of droplet spreading). Therefore, for simplicity, perfect mechanical bonding between interfaces is assumed.
3. The impact of plasma particle is considered to occur in a direction that is normal to the substrate surface.
4. Any form of heat transfer by convection and radiation during droplet flight is negligible based on previous findings [147].
5. For APS process, peening stresses developed during deposition are negligible due to low kinetic energy of impacting droplets.

4.2 Governing equations

4.2.1 Spray process modeling

The simulation of multiple droplets impact, deformation and solidification should be an integral part of a typical thermal spray deposition modeling. The shape and size of deposited splats depend mainly on the initial droplets size, impact velocity and

undulation of target surface; temperature has little effect in that regards. Consequently, the fluid (Navier-Stokes') equations for laminar, viscous and semi-incompressible flow is used to model the impact and spread of droplets as expressed in Equations (4.1) and (4.2).

$$\frac{\partial \rho}{\partial t} + (\rho v_i)_{,i} = 0 \quad (4.1)$$

$$\rho \frac{\partial v_i}{\partial t} + \rho v_j v_{i,j} = b_i + (-p \delta_{ij} + \tau_{ij})_{,j} \quad (4.2)$$

Where: ρ is density, v_i is velocity field, b_i is body force per unit volume, p is pressure, τ_{ij} is viscous shear stress and t is time.

Due to its high computational efficiency, the flow equations are solved on point cloud (PC) using an explicit-meshless scheme based on SPH formulation. This requires semi-incompressibility (or small change in density) to allow for the initiation of numerical iterations. Thus, the initial fluid pressure is defined as a function of density according to the linear form of Mie-Gruneisen equation of state as:

$$p = \frac{\rho_0 c_0 \eta}{(1 - s\eta)^2} \left(1 - \frac{\Gamma_0 \eta}{2} \right) + \Gamma_0 \rho_0 E_m \quad (4.3)$$

Where ρ_0 is the reference (or initial) density, E_m is specific internal energy, Γ_0 , c_0 , and η are all material constants obtained by fitting to experimental data.

4.2.2 Geometric modeling of splats

After modeling of the splats shape, size and orientation using the flow equations solved on point clouds, the geometric modeling of splat structures follows. As previously

discussed, it is very difficult to conduct thermo-mechanical analysis of the process with the SPH meshless scheme due to stability problems. Thus, each simulated splat represented as point cloud is converted into high-quality finite element (FE) domain using recent algorithms developed for point cloud data processing. The following algorithms are used for the conversion process:

1. **Poisson-disk sampling:** The initial point cloud of deposited splats (obtained from SPH simulation) usually contains too few points for efficient conversion to finite element mesh. Therefore, Poisson-disk sampling algorithm (developed by Corsini et al. [148]) is used to populate the original point sets to the required density that will be sufficient for mesh generation. As commonly defined [149], Poisson-disk sampling is a finite set of points $Z = \{z_i \in S; i = 1, 2, \dots, n\}$ such that

$$\forall z_i \in Z, \quad \forall Q \subseteq S : P(z_i \in Q) = \iint_Q dx \quad \text{and} \quad \forall z_i, z_j \in Z : \|z_i - z_j\| \geq 2r.$$

The algorithm does not add points outside the domain of interest.

2. **3D alpha-shape:** This is an algorithm that is commonly used to reconstruct the geometric surface of objects using point cloud data. The algorithm which was first developed by Edelsbrunner [150] and recently improved by Kamberov [151] requires the user to provide an optimum α -value. According to the original definition by Edelsbrunner: if S is a finite set of \mathbb{R}^3 and α is a real number that falls within the range $0 < \alpha < \infty$, then the 3D α -shape of S is a polytype that is neither necessarily convex nor necessarily connected. Optimum α -value is required for effective reconstruction of splat topology. If the α -value is too small, cavities (or unwanted holes) will emerge on the splat surface. While, large

α -value results in generation of highly rough splat surface in form of stereolithographic (STL) mesh.

3. **Poisson surface reconstruction:** Despite its ability to accurately capture surface topology of splats, alpha-shape algorithm often results in triangulated (surface) elements of poor aspect ratio due to explicit representation of the surface. To improve the quality and smoothness of the surface, Poisson surface reconstruction algorithm (developed by Kazhdan and Hoppe (2013)) is used to implicitly reconstruct the STL mesh using Poisson's equation. This requires the computation of gradient (or outward normal vectors) at each $z_i \in S$ point to obtain an implicit scalar function (ξ) that fits the original splat surface with minimum error (or deviation) as expressed in equation (4.4)-(4.6).

$$\min_{\xi} \|\nabla \xi - \vec{V}\| = 0 \quad (4.4)$$

Equation (4.4) then simplifies to:

$$\nabla \|\nabla \xi - \vec{V}\| = 0 \quad \Rightarrow \quad \Delta \xi = \nabla \cdot \vec{V} \quad (4.5)$$

and,

$$\vec{V}(i) \approx \sum_{z \in S} |p_z| \tilde{F}_{z,p}(i) z \cdot \vec{N} \quad (4.6)$$

Where p_s is the patch area for the integration, \tilde{F} is smoothing filter and \vec{N} is outward-normal vector; all at the point $s.p$.

Poisson's surface reconstruction algorithm is generally faster than other implicit surface reconstruction methods (such as RBF, least squares, distance function, multi-level partition of unity implicits, etc) as it uses sparse matrix (with only 1-inside domain and 0-outside domain values). The algorithm has also proven to handle noisy data more efficiently than the other methods due to local support of implicit function. The only drawback is that it needs consistent normal orientation. For highly irregular shapes, nearest neighbor outward normal vectors may appear to be staggy with some vectors pointing inwards. In that case, the resulting mesh will not be good; thus, normal vectors should be recomputed with sufficient number of points per normal.

4. **Quadratic edge decimation:** Obviously, the high quality STL mesh generated with Poisson's surface reconstruction algorithm is convertible to 3D FE mesh. However, it will result in too many elements and/or degree of freedom which will consume unrealistically high computational resources. Therefore, the number of elements is reduced to optimum value using quadratic edge decimation algorithm developed by [154]. This algorithm reduces the number of simplicial complexes in a given polytype iteratively with little compromise on shape, size and computational costs. Using the algorithm, two vertices along an edge degenerates into a single vertex which reconnects with other simplified vertices to form a new edge. The new position of the vertices and length of new edges for the polytype are determined by optimizing the following standard quadratic error metric given in Equation (4.7) [154]:

$$Q_{ij} = A_{ij}y_iy_j + 2b_iy_j + C_{ij} \quad (4.7)$$

Where $A_{ij} = n_i n_j$, $b_i = -A_{ij} p_j$, $C_{ij} = A_{ij} p_i p_j$, n_i is outward normal vector at each vertex denoted by vector p_i and y_i is any point away from p_i but located at same tangent plane containing p_i . Thus, Equation (4.7) yields a minimum value of y_i when $\nabla Q_{ij} = 0$ which can be obtained iteratively.

5. **Least square subdivision surface (LS3):** After the size of STL mesh is optimized with quadratic edge decimation, it is necessary to re-smooth the splat surface using LS3 algorithm before exporting to commercial FE packages for thermo-mechanical analysis. LS3 repositioned vertices the vertices of the mesh such that a coherent 3D FE mesh is generated. Details about this algorithm and implementation should be checked elsewhere [155].
6. **STL-FE mesh conversion:** This is the last stage of the geometric reconstruction step where the STL mesh developed using the algorithms is converted into a solid 3D FE mesh. This can be achieved easily using several plugins available in commercial CAD/FE packages such as ABAQUS, COMSOL, ANSYS, HYPERMESH, etc.

4.2.3 Thermo-mechanical modeling

Having passed through the steps of deposition and geometric reconstruction, next is thermo-mechanical finite element analysis for the prediction of temperature distribution, residual stress, plastic strain and microcracks. The basic equations of micro-thermo-mechanics are used to solved for these variables. The large difference in initial temperatures of the splats and substrate (during the deposition) results in steep thermal gradient that increases with depth of the coating layer. Most of the heat loss during the

process is in form of latent heat release (due to splat solidification/quenching) to the substrate (or predeposited layer) via conduction. Splat quenching process is highly complicated as it results in extensive microcracking (in ceramic coatings) and interface sliding during coating process. This result in development of complex stress profile associated with the presence of several critical locations (e.g. cracks, pores, interfaces, inclusions, lamella etc) affected by stress concentration. Negligible heat is lost to the surrounding through convection and radiation during solidification. On the contrary, large heat is lost through convection during post-deposition, i.e. after the coated component is finally cooled to room temperatures.

Therefore, in the present study, the energy equation (in enthalpy form as expressed in Eq. (4.8)) is used to predict the evolution of temperature during the coating process. Various form of heat transfer such as splats solidification/re-melting and convection are considered due to their influence on spray process. Based on results obtained by previous semi-empirical model [156], we found that the temperature has little effect on the shape and size of splats. Thus, to reduce computational cost, the energy equation is not coupled to the flow equations. Instead, the deposition model is calibrated to capture the minor influence of temperature on the flow pattern using the semi-empirical model [156].

$$\rho \frac{\partial h}{\partial t} = -k_i T_{,ii} \quad (4.8)$$

Where: h is enthalpy, k is thermal conductivity, and T is temperature.

The enthalpy change during solidification relates to the temperature and specific heat capacity through the equation:

$$dh(T) = C_p(T)dT \quad (4.9)$$

The specific heat capacity (C_p) of the coating layer is given by:

$$C_p(T) = C_{ps}(T) + \frac{L_f}{T_m} \cdot \varphi + C_{pl}$$

(4.10)

Where C_{ps} is specific heat capacity of the solid, C_{pl} is specific heat capacity of liquid, L_f is latent heat of fusion, and φ is a dirac-delta function with non-zero values outside the mushy zone.

On the other hand, the basic equations of micro-mechanics (i.e. local-force balance equations) are used to solve for the deformation of the coating and substrate layers during solidification and post-deposition cool down stages (as shown in Eq.(4.11)). During thermo-mechanical deformation, it is expected that very little plastic heat is dissipated. Therefore, to reduce computational intensity further, sequential coupled thermal-stress analysis is considered here; thus, the temperature coupling terms are not reflected in Eq. (4.11).

$$\rho \frac{\partial^2 u_i}{\partial t^2} = \sigma_{ij,j} + \rho b_i \quad (4.11)$$

Where: u_i is displacement field, σ_{ij} is stress tensor, ρ is density, b_i is body force per unit mass and $\frac{\partial^2 u_i}{\partial t^2}$ is directional acceleration.

The stresses (σ_{ij}) developed during deformation are related to the elastic strain tensor (ε_{ij}^{el}) according to Hooke's law as given in Equation (4.12). The elastic strain tensor (ε_{ij}^{el}) is defined in terms of total strain (ε_{ij}), thermal strain (ε_{ij}^{th}) and plastic strain (ε_{ij}^{pl}) tensors using additive decomposition theorem (as shown in Equation (4.13)).

$$\sigma_{ij} = C_{ijkl} : \varepsilon_{ij}^{el}$$

(4.12)

$$\varepsilon_{ij}^{el} = \varepsilon_{ij} - \varepsilon_{ij}^{th} - \varepsilon_{ij}^{pl} \quad (4.13)$$

The total strain tensor, based on large deformation theorem, is expressed as:

$$\varepsilon_{ij} = \frac{1}{2} (u_{i,j} + u_{j,i} + u_{k,i} \cdot u_{k,j}) \quad (4.14)$$

The thermal strain is developed due to mismatch in coefficient of thermal expansion of coating and substrate layers as expressed in Eq.(4.15).

$$\varepsilon_{ij}^{th} = \int_{T_{ref}}^T \alpha(T) \cdot dT \quad (4.15)$$

The metallic coating and substrate material undergo plastic deformation during coating deposition. Therefore, their constitutive behavior will be modeled using an elasto-plastic model based on multilinear isotropic hardening rule or Johnson cook model which requires the definition of several yield stresses. If von Mises equivalent stress (σ_{vm}) is used, the yield criterion can be expressed as:

$$Q = \sigma_{eq} - \sigma_{yp} \leq 0 \quad (4.16)$$

Where, σ_{yp} is the hardening function which is defined as the non-linear portion of the stress-strain curve. When only two yield stress points are defined, the hardening function reduces to bilinear isotropic hardening model. When John-son cook model is used, the yield function is defined according to the function:

$$\sigma_{yp} = \left[A + B(\bar{\varepsilon}^{pl})^n \right] \left[1 + C \ln \left(\frac{d\bar{\varepsilon}^{pl}}{d\bar{\varepsilon}_0^{pl}} \right) \right] (1 - \hat{\theta}^m) \quad (4.17)$$

Where: $\bar{\varepsilon}^{pl}$ equivalent plastic strain variable, $\hat{\theta}$ is non-dimensional temperature, A , B , m , n and $\bar{\varepsilon}_0^{pl}$ are all material constants to be obtained by fitting with experimental data.

Then, the flow rule or plastic strain rate is expressed as:

$$d\varepsilon_{ij}^p = d\lambda \frac{\partial Q}{\partial \sigma_{ij}} = \frac{3}{2} d\lambda \frac{S_{ij}}{\sigma_{eq}} \quad (4.18)$$

Where: $d\varepsilon_{ij}^p$ is the increment of the plastic strain tensor, Q is yield function, S_{ij} is deviatoric stress tensor, σ_{eq} is von Mises stress and $d\lambda$ is a plastic multiplier which is a scalar function of plastic strain.

The equivalent stress based on von Mises yield criteria is usually expressed as a function of deviatoric stress tensor as:

$$\sigma_{eq} = \sqrt{\frac{3}{2} S_{ij} : S_{ij}} \quad (4.19)$$

Due to their brittle nature, ceramic coatings undergo negligible plastic deformation and develop very high tensile quenching stresses. These high stresses often relax through extensive micro-cracking due to thermal shock. As modeling of crack evolution during

thermal shock is highly complicated, the tensile quenching (deposition) stress developed during solidification is commonly predicted with elastic-perfectly plastic material model. The model restricts the tensile stresses to extremely low values that correspond to that of cracked domains [101]. In the present study, apart from use of the elastic-perfectly plastic model, an additional study is presented whereby the continuum damage model developed for ceramics (recently developed by Shao et al. [157]) is used to model quenching stresses and crack evolution in the ceramic coating layer. According to the model, a crack is initiated when the norm of principal tensile stresses reaches the tensile strength of the material and its propagation proceeds in the direction of maximum tensile strain. In that case, a scalar damage variable ($d(t)$) is used to ensure continuous degradation of the original stiffness (C_{ij}^0) up to complete as expressed in Eq. (4.20).

$$C_{ij} = (1 - d(t)) \cdot C_{ij}^0 \quad (4.20)$$

Where, C_{ij} is the degraded stiffness of the material which varies with time and location.

The scalar damage variable is expressed as:

$$d(t) = \begin{cases} 0 & 0 \leq \varepsilon_{eqt}(t) \leq \varepsilon_{ck} \\ \frac{\varepsilon_{eqt}(t) - 2\varepsilon_{ck}^2}{2\varepsilon_{ck} - \varepsilon_{ck} \cdot \varepsilon_{eqt}(t)} & \varepsilon_{ck} \leq \varepsilon_{eqt}(t) \leq 2\varepsilon_{ck} \\ 1 & \varepsilon_{eqt}(t) > 2\varepsilon_{ck} \end{cases} \quad (4.21)$$

Where, ε_{eqt} is equivalent tensile strain, ε_{ck} is tensile cracking strain and $2\varepsilon_{ck}$ is ultimate tensile strain of the material. The equivalent tensile strain of the material is defined in terms of the three principal strains ($\varepsilon_1, \varepsilon_2$ and ε_3) as:

$$\varepsilon_{eqt} = \sqrt{\langle \varepsilon_1 \rangle^2 + \langle \varepsilon_2 \rangle^2 + \langle \varepsilon_3 \rangle^2} \quad (4.22)$$

To ensure that only tensile principal strains contribute to cracking, we define the operator

$\langle \rangle$ as $\langle \varepsilon_i \rangle = \frac{|\varepsilon_i| - \varepsilon_i}{2}$. The tensile cracking strain of the material is commonly expressed

as:

$$\varepsilon_{ck} = \frac{\sigma_{ck}}{E^0} \quad (4.23)$$

Where, σ_{ck} is the uniaxial cracking stress, i.e. stress at which cracks initiate and E^0 is the original elastic modulus of material.

Equally, the scalar damage variable is used to prevent conduction of heat through cracked elements according to the equation Eq. (4.24).

$$k_i = (1 - d(t)) \cdot k_i^0 \quad (4.24)$$

4.2.3 Initial and Boundary conditions

Geometry and initial conditions

As in typical spray process, the sprayed powder particles (or droplets) are assumed to be spherical and having certain diameter (as demonstrated in Figure 4-1). When many particles are considered, their diameter can vary randomly based on statistical distribution determined from experiments. The droplets are released layer wise and deform to form splat structures upon impact; thus, the geometry of splat structures is reconstructed using numerical tools. The substrate is flat for most of the analysis and its dimensions ($300 \times 300 \times 600 \text{ mm}^3$) are optimized such that the effect of boundary condition on results

is minimal. However, we have demonstrated that the current approach works equally for rough substrate which is the usual case in most practical coatings.

After selection of the computational domains, other initial values need to be provided. The model requires initial droplets impact velocities and temperature. In case of multiple droplets, these values are often randomly selected based on previous statistical distributions obtained experimentally. As in typical spray process, the substrate is preheated to constant temperature of 700°C. The preheating is necessary for ceramic coatings to minimize cracking (due to thermal shock) and improve coating adhesion.

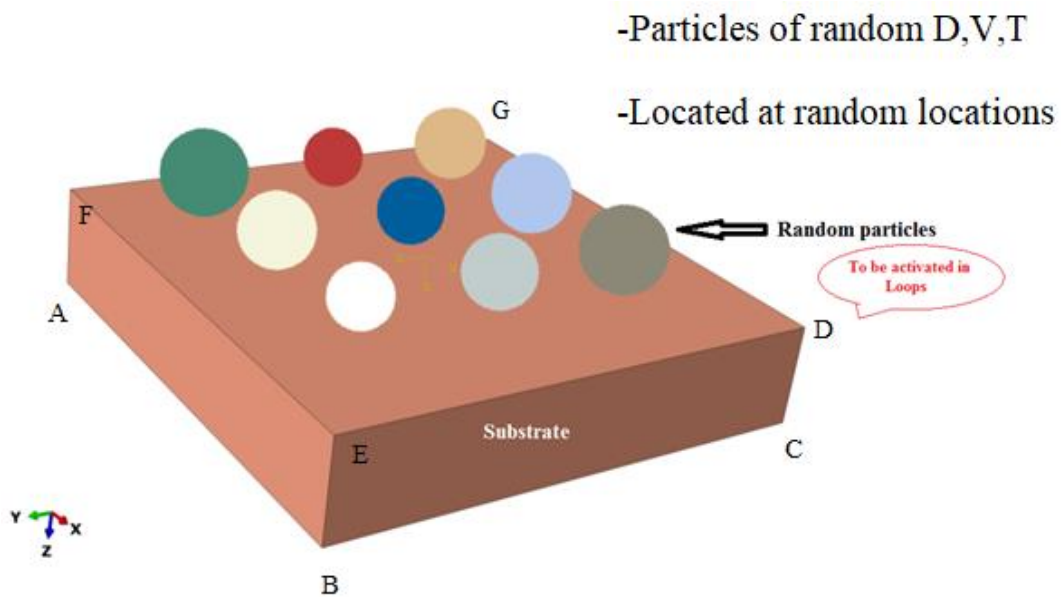


Figure 4-1: Release/impact of sprayed droplets on substrate in layer-wise fashion (axis directions are shown)

Boundary conditions

Fluid-structure interaction (wall) boundary condition is defined at the droplet-substrate and droplet- splats interfaces. For simplicity, splat-substrate and splat-splat interfaces are assumed to have perfect contact as commonly adopted [101], [158]. According to

previous investigation by Ruhl [159], the thermal contact resistance does not affect the splat formation process for the range of Biot number for typical thermal spray deposition. Thus, the thermal contact resistance only delays solidification during droplet deformation, but it has minimal effect on the deformation pattern and temperature distribution. The substrate is fixed in space only during droplet impact by constraining the degree of freedoms of the bottom space. Symmetry (with respect to both temperature and displacements) is defined on two side faces of the substrate geometry. While, the other two side faces are constraint to deform uniformly in the y and x-directions respectively. The degree of freedoms of the boundary nodes at the other two (opposite) side faces are constrained (or coupled) such that they move together, and periodicity is preserved. Convective boundary condition is applied on the two side faces (having coupled boundary condition) and bottom face of the substrate. To avoid rigid body motion during thermo-mechanical modeling, one corner node is constrained to move in all directions.

4.3 Numerical Model

As the hybrid computational approach involves the coupling of SPH-based point cloud model with FEM (demonstrated in Figure 4-2), formulations for the two different numerical methods are described in following sections.

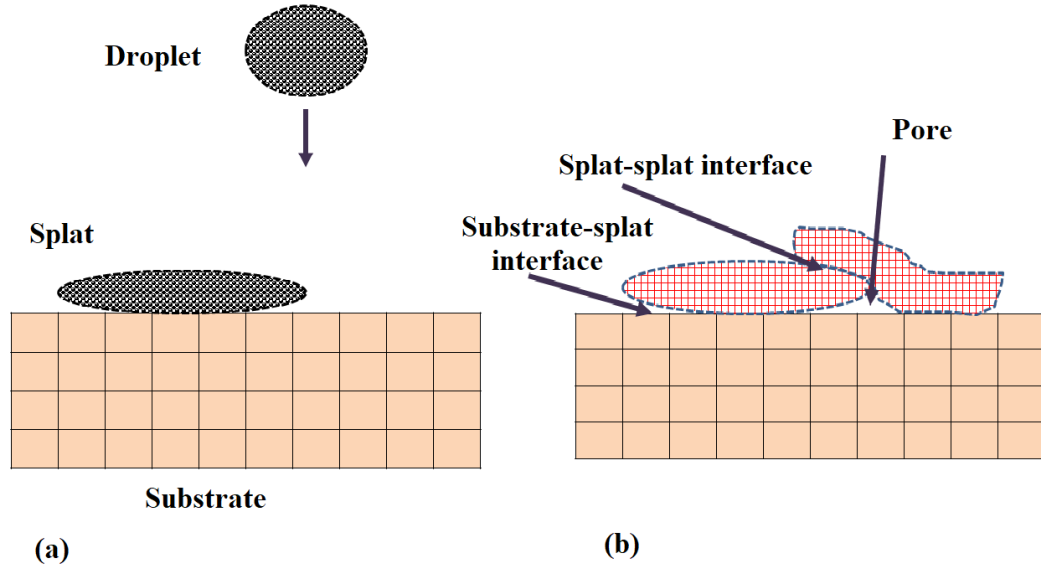


Figure 4-2: Proposed hybrid computational approach: (a) droplets impact, spread and interaction using SPH, (b) Splats solidification and residual stress evolution using FEM

4.3.1 SPH formulation

SPH formulation is Lagrangian and developed based on explicit time stepping scheme. With SPH, the flow of fluid is represented using a set of particles having unique physical properties such as density, viscosity, pressure, etc. The solution across the fluid domain is obtained using the kernel (or smoothing) functions. For simplicity and fastness, we have adopted the cubic spline kernel function, $W(\zeta, h)$, developed by Monaghan [160] which is expressed as:

$$W(\zeta, h) = \alpha \times \begin{cases} \frac{2}{3} - \zeta^2 + \frac{1}{2}\zeta^3, & 0 \leq \zeta < 1 \\ \frac{1}{6}(2 - \zeta^2), & 1 \leq \zeta < 2 \\ 0, & \zeta \geq 2 \end{cases} \quad (4.25)$$

Where the two constants, ζ and α are given as:

$$\zeta = \frac{\bar{r}_i - \bar{r}_j}{h} \quad (4.26)$$

$$\alpha = \begin{cases} 1/h & \text{for 1D} \\ 15/7\pi h^2 & \text{for 2D} \\ 3/2\pi h^3 & \text{for 3D} \end{cases} \quad (4.27)$$

SPH formulation is written in material time-derivative form; thus, semi-incompressibility is required to initiate the iterations for computation of velocity field. The semi-compressibility does not result in significant errors if the kernel contains an appreciable number of particles. The SPH formulation for the conservation of mass (or continuity) equation can be expressed as:

$$\frac{D\rho_i}{Dt} = \sum_{j=1}^n m_j \bar{v}_{ij} \cdot \nabla_i W_{ij} \quad (4.28)$$

Where \bar{v}_{ij} is the velocity of particle-i relative to that of particle-j.

While, the SPH form of the conservation of momentum equation can be expressed as:

$$\frac{D\bar{v}_i}{Dt} = -\sum_{j=1}^n m_j \left(\frac{p_i}{\rho_i^2} + \frac{p_j}{\rho_j^2} \right) \nabla_i W_{ij} + \sum_{j=1}^n m_j \left(\frac{\tau_i}{\rho_i^2} + \frac{\tau_j}{\rho_j^2} \right) \cdot \nabla_i W_{ij} + \bar{b} \quad (4.29)$$

Where p is pressure, τ is viscous stress tensor and \bar{b} is body force.

The interaction between several SPH domains (or point cloud of droplets) is inherent in SPH formulation such that one droplet domain will not penetrate another or the substrate body during deformation. Thus, multiple droplets interaction can be handled easily using SPH. The fluid-structure (or droplet-substrate) interaction is implemented by identifying

the surface of the substrate (or wall) to be consisting of ghost particles having equal velocity magnitude and opposite directions as that of the boundary SPH particles.

4.3.2 Finite element formulation

Using the converted FE mesh of splats, a thermo-mechanical analysis is conducted to predict the evolution of residual stress during the spray process. As mentioned earlier, the energy equation is sequentially-coupled to the local-force balance equation. According to the law of energy conservation, the variation of energy within the system can be represented as:

$$\int_V \rho \frac{\partial h}{\partial t} dV = \int_V -kT_{,ii} dV + \int_S q_i n_i dS \quad (4.30)$$

Using Galerkin's finite element approximation and backward Euler time step (Δt), the variational form of the energy equation (i.e. the thermal problem) is given by:

$$\int_V [N]^T \cdot \rho(T) \cdot \{\dot{H}\} dV + \int_V [B]^T \cdot k(T) \cdot [B] dV - \int_{A_h} [N]^T \cdot h_{cv}(T) \cdot (T - T_{air}) dA = 0 \quad (4.31)$$

Where $\rho(T)$ is density, $\{H\}$ is nodal enthalpy matrix, $k(T)$ is thermal-conductivity, $[N]$ is element interpolation matrix, $[B]$ is derivate of interpolation matrix, h_{cv} is convection heat transfer coefficient on external boundaries, and T_{air} is ambient temperature.

Using Newton's iteration to linearize equation (4.31), we obtain the following discretized form of the equation as:

$$[K_{th}] \{ \Delta T_{i+1}^{t+\Delta t} \} = \{ R_T \} \quad (4.32)$$

Where,

$$[K_{th}] = \int_V [N]^T \rho \left(\frac{dH}{dT} \right)_i^{t+\Delta t} [N] dV + \int_V [B]^T k_i^{t+\Delta t} [B] dV - \int_{A_h} [N]^T h_{cv}^t [N] dA, \quad \text{i.e. thermal}$$

properties matrix.

$$\{ R_T \} = \int_{A_h} [N]^T h_{cv}^t (T_i^{t+\Delta t} - T_{air}^t) dA - \frac{1}{\Delta t} \int_V [N]^T \rho (H_i^{t+\Delta t} - H^t) dV - \int_V [B]^T k^t [B] dV, \quad \text{i.e.}$$

thermal load vector.

Using Equation (4.32), the nodal temperature at each time step is found by solving the resulting algebraic form of equations. The latent heat release during solidification process

is accounted for at each time step in the term, $\left(\frac{dH}{dT} \right)_i^{t+\Delta t}$, representing the effective heat

capacity of the material.

While, according to the law of conservation of momentum, the acceleration of the system can be represented as:

$$\int_V \rho \frac{\partial^2 u_i}{\partial t^2} dV = \int_S \sigma_{ij} n_j dS + \int_V \rho b_i dV$$

(4.33)

Simplifying using divergence theory results into:

$$\int_V \rho \frac{\partial^2 u_i}{\partial t^2} dV = - \int_V \sigma_{ij,j} dV + \int_S \sigma_{ij} n_j dS + \int_V \rho b_i dV \quad (4.34)$$

Applying principle of virtual work, the variational form of the stress-equilibrium equation (given in Equation (4.33)) is given as:

$$\int_V \rho [N]^T \{\ddot{U}\} [N] dV = - \int_V [B]^T [\sigma] dV + \int_S [N]^T \{t\} dS + \int_V \rho [N]^T \{g\} dV \quad (4.35)$$

Where $\{U\}$ is nodal displacement vector, $[\sigma]$ is internal stress tensor, $\{t\}$ is boundary traction vector, and $\{g\}$ is body force vector.

From Equation (4.35), it can be seen that the inertia of the system can be generally expressed as the difference between external forces (P_{ext}) acting on the body and internal forces developed due to stress field (P_{in}) leading to dynamic equilibrium as expressed in Equation(4.36).

$$[M]\{\ddot{U}\} = \{P_{ext}\} - \{P_{in}\} \quad (4.36)$$

Where $[M]$ is the mass matrix.

At each time step, the temperature distribution obtained using Equation (4.32) is used to compute thermal strains and corresponding internal stresses which are used to predict the displacement or deformation of the bodies involved as given in Equation (4.37).

$$\Delta\sigma = C : \Delta\varepsilon^{el}; \quad \text{where } \Delta\varepsilon^{el} = \Delta\varepsilon^T - \alpha\Delta T - \Delta\varepsilon^{pl} \quad (4.37)$$

For explicit-dynamic schemes, the inertia term is retained and the solution to Equation (4.36) is obtained by computing the acceleration of the system and integrating it to obtain the corresponding velocity and displacements using a conditionally stable explicit central

difference scheme. Using the explicit-dynamic scheme, the solution of highly dynamic and nonlinear but short duration problems becomes very efficient and computationally inexpensive as there is no need for the inversion of the resulting complex stiffness matrix; the problem can be solved using only the diagonal mass matrix.

$$\{\ddot{U}\}^t = [M]^{-1} \{ \{P_{ext}\} - \{P_{in}\} \}^t \quad (4.38)$$

Using central difference scheme, the velocity and displacements can be expressed as:

$$\{\dot{U}\}^{t+\frac{\Delta t}{2}} = \{\dot{U}\}^{t-\frac{\Delta t}{2}} + \left(\frac{\Delta t^{t+\Delta t} + \Delta t^t}{2} \right) \cdot \ddot{U}^t \quad (4.39)$$

$$U^{t+\frac{\Delta t}{2}} = U^t + \Delta t^{t+\Delta t} \cdot \dot{U}^{t+\frac{\Delta t}{2}} \quad (4.40)$$

For a stable solution, the minimum (or stable) time step required to solve an explicit-dynamic problem is usually estimated using the minimum element size and dilatational wave speed of the material.

For an implicit-static procedure, the acceleration term defined in Equation (4.36) vanishes such that static equilibrium is ensured. In that case, the stiffness matrix can be inverted directly to obtain the displacement field values using an algebraic system of equations (given in Equation (4.41)). But instead of direct inversion of the stiffness matrix, an iterative scheme based on Newton-Raphson is commonly used to obtain the solution using fictitious time steps as expressed in Equation (4.41).

$$[K]_i^{t+\Delta t} \{ \Delta U \}_i^{t+\Delta t} = \{ P_{ext} \}_{i+1}^{t+\Delta t} - \{ P_{in} \}_i^{t+\Delta t} \quad (4.41)$$

Where $[K] = \int_V [B]^T [J] [B] dV$ is the stiffness matrix and $[J] = \frac{\partial \Delta \sigma}{\partial \Delta \varepsilon}$ is the Jacobian matrix.

4.4 Numerical implementation

Thermal spray process can be divided into sub-regimes, i.e. multiple droplets impact and spreading (occurs within 0-2 μ s), solidification of splat layers (occurs within 20-500 μ s) and post-deposition cooling to room temperature (occurs within 1-50 s). As the time scale of these regimes differs considerably, a sequentially-coupled approach is adopted during the implementation of the hybrid model. Thus, the flow (Navier-Stokes') equations are solved solely for prediction of splat formation process during the first regime. Then, the reconstructed FE mesh of splat structures is used to solve for quenching stresses developed during splat solidification (i.e. second regime). Lastly, the results of the second regime are read as an initial condition for computation of mismatch stresses developed when the coated structure is finally cooled to room temperature. This coupling greatly improves the computational efficiency of the model without much compromise on results quality.

The numerical implementation of the several models adopted here is demonstrated in Figure 4-3. These include the point cloud model for simulation of multiple droplets deposition, point cloud processing for geometric modeling of splats and thermo-mechanical finite element model for the numerical prediction of plastic strain, crack evolution and residual stress. The point cloud model is solved using the popular meshless method, smooth particle hydrodynamics (SPH). As SPH is both lagrangian and explicit in time, the point cloud model is implemented in the environment of commercial package,

ABAQUS/Explicit. PC3D elements (discretized with the cubic kernel) are used to compute spread factor, velocity field and splats geometry developed upon impact of multiple droplets. Using previous semi-empirical model developed by Aziz and Chandra [156], the model is calibrated to correct for minor deviation resulting from negligence of temperature, surface tension and contact angle. Interestingly, it is found that, the point cloud model is able to capture the complex interaction multiple droplets as commonly encountered during the spray process.

In the second step, point cloud processing tools (implemented in Meshlab and python codes) are used to reconstruct the geometry of deposited splats in form of FE mesh. As demonstrated in Figure 4-4, the point cloud data of deformed splat structures is first extracted using python codes. Then, Poisson-disk sampling algorithm is used to increase the density of point cloud to the level required for effective reconstruction of splat geometry. This is followed by 3D alpha-shape algorithm which is used to reconstruct surface topology of splats in form of STL mesh. Poisson surface reconstruction algorithm is also used to implicitly regenerate a coherent STL mesh which has elements of higher quality elements. If required, quadratic-edge decimation and least square subdivision surface algorithms are jointly used to optimize mesh STL density and quality respectively. The final step involves conversion of STL mesh into high quality 3D FE mesh which is achieved using tri-to-tetra element conversion algorithm in ABAQUS/CAE.

With the reconstructed 3D FE mesh, thermo-mechanical finite element analysis is conducted to predict temperature distribution, plastic deformation, crack formation and residual stress during thermal spray process. The thermo-mechanical model is

implemented in ABAQUS/Standard based on implicit-integration scheme using 4-node tetrahedral linear coupled temperature-displacement element (C3DT4). As large deformation occurs mainly during droplet impact and spread, we do not expect any plastic heat dissipation during the process. Consequently, a segregated solution technique involving simultaneous computation of temperature and displacement fields (but without the structural coupling terms) is used. The segregated technique is more computational efficient and accurate than sequentially-coupled thermal stress analysis as there is no need for reading or re-writing of solution data at each time step. A prototype finite element model showed that explicit-dynamic finite element scheme is more computationally efficient in solving for the deposition stresses due to the highly dynamic, nonlinear and fast nature of thermal spray deposition process. However, it is not suitable for analysis involving extensive plastic deformation (in metals) and cracks formation (in ceramics) due to stability problems. Therefore, the implicit scheme is more appropriate for the computation of deposition stresses. As in real process, the computation is carried out in two main regimes, i.e. deposition (quenching) and post-deposition stages. In the first stage, temperature and deposition stresses developed during splats solidification/quenching are numerically predicted. In the second stage, temperature distribution and mismatch stresses developed when coating and substrate layers are cooled to room temperature are numerically predicted.

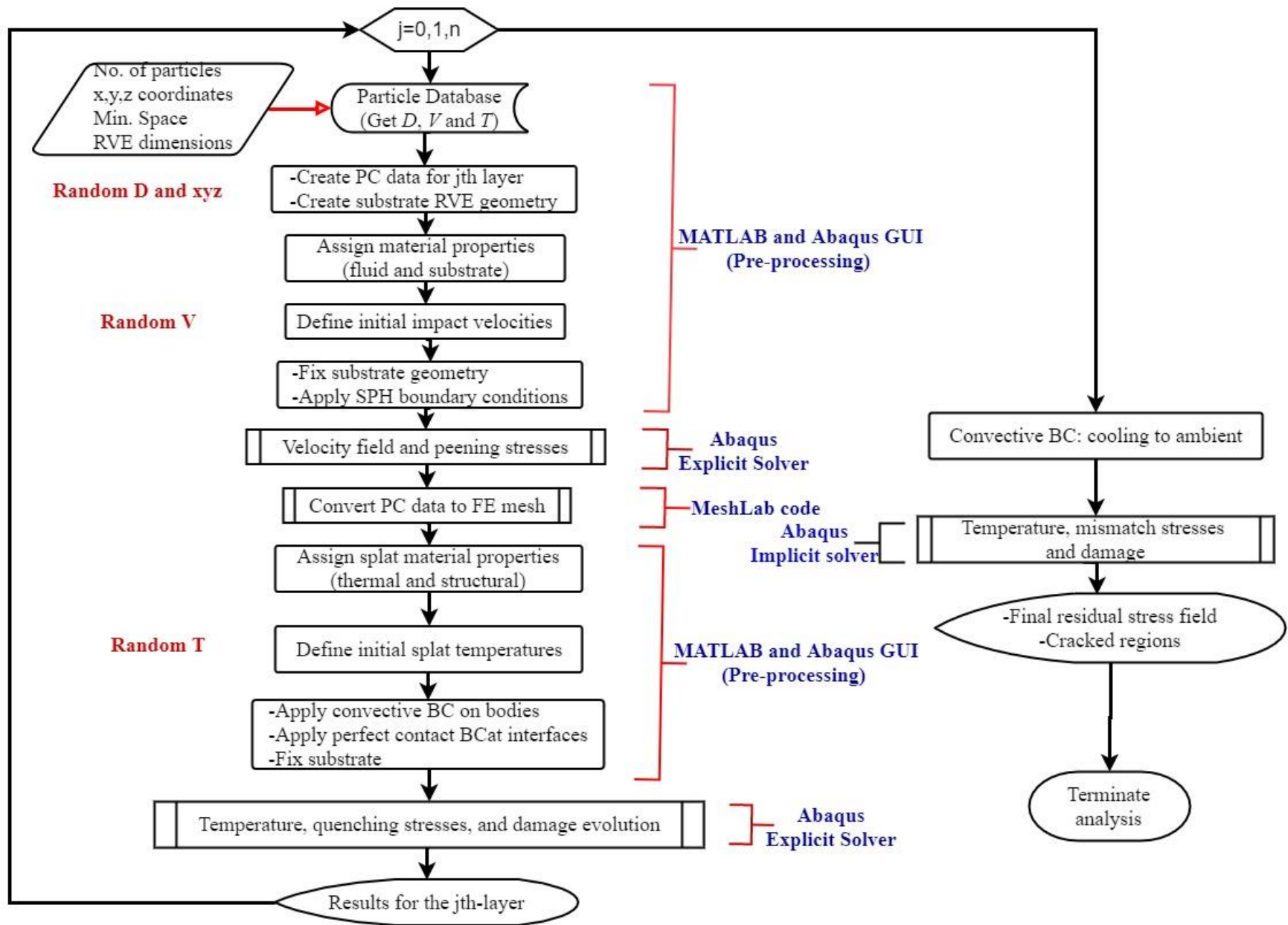


Figure 4-3: Flowchart for the numerical implementation of the proposed approach

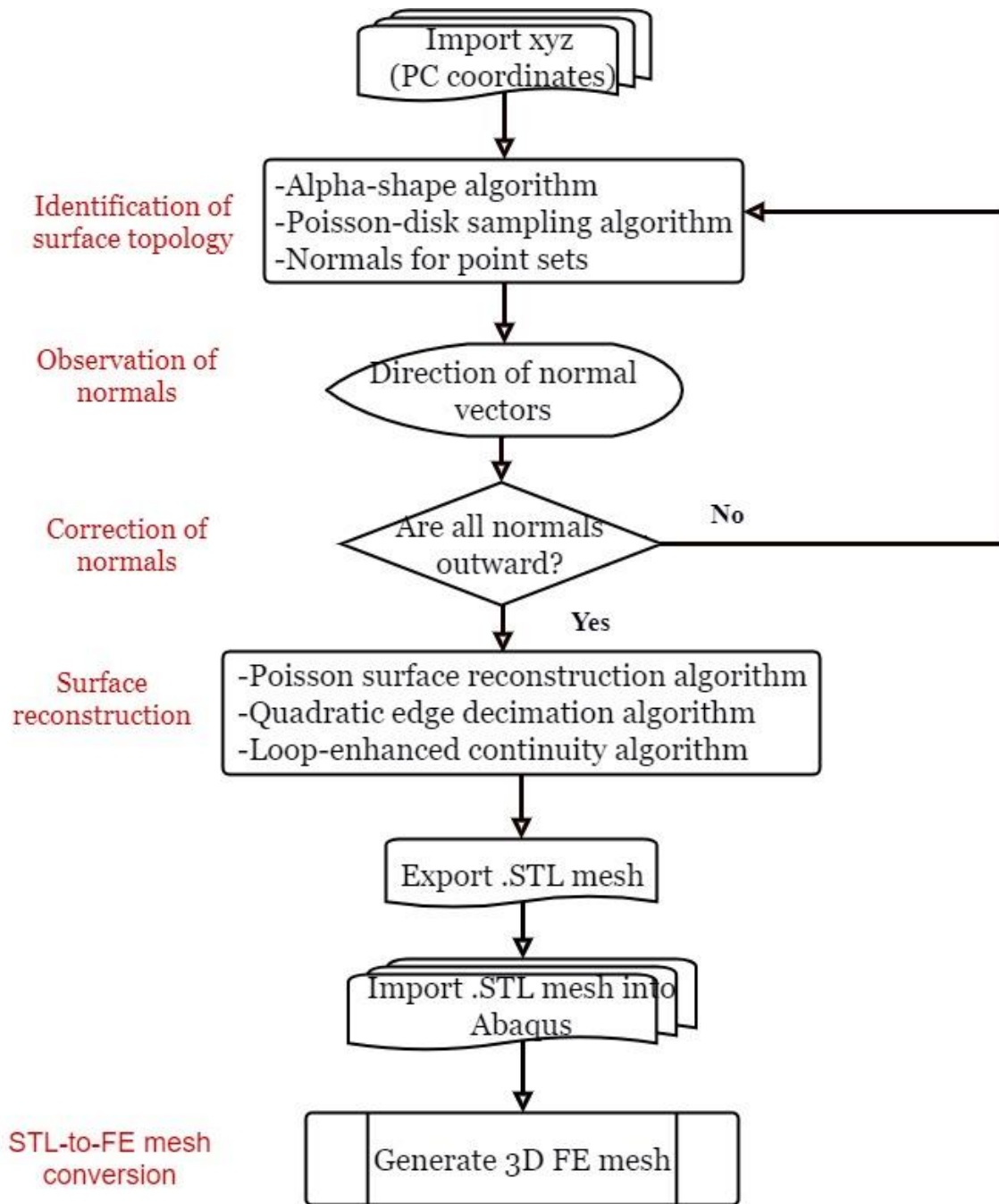


Figure 4-4: Flowchart for implementation of PC-to-FE conversion algorithms

4.5 Material properties and simulation parameters

Composite powder particles, containing same composition as that of YSZ and Ni-20%Al, are melted to droplet form before deposition. As droplets are considered as fluid; fluid properties

(i.e. density, viscosity, etc.) are required as main inputs to the deposition model. As the droplets are highly dense, bulk values of properties are used.

For the FEM, the materials of the coating and substrate are defined to have isotropic and temperature dependent structural and thermal properties. All properties used for the present study are all selected from the literature as shown in Table 4-1. It is difficult to get exact values of some properties for the droplet/liquid portion of coating. Therefore, reasonably estimates are obtained from the literature. The fluid properties of Ni-20%Al droplets are taken from the work of Zhang et al. [159]. While, the thermal and structural properties of the Ni-20%Al coating are taken from the works of Chen and Yueming [161] and Matthews et al. [162]. The fluid and phase change properties, mainly that of the liquid YSZ droplets, are all selected from previous data given by Zhang et al. [163] and Zhu et al. [164]. Elements within molten regions are made to have very low elastic modulus. Temperature-dependent structural properties of YSZ splat are selected based on previous works by Adams et al. [165] and Hayashi et al. [166]. The structural properties of the substrate are selected from the data provided by Cverna [167] and Zhu et al. [164].

Table 4-1: Material inputs data to simulation

Property	YSZ/ Ni-20%Al coating	301 Stainless Steel	
Fluid properties	Density, ρ (kg / m^3)	7900	
		5890/7850 @ liquid state	
		5890/8450 @ solid state	
	Viscosity, μ (kg / ms)	0.008/0.006	-
	Speed of sound, c_0 (m / s)	3000/3000	-
Dimensionless parameter, s	2.39/2.39	-	
Dimensionless parameter, Γ_0	0/0	-	

	Surface tension, γ (N / m)	0.5/1.350 @ liquid state 0.5/1.647 @ solid state	-
	Contact angle, δ (deg)	70/90	-
Phase change properties	Latent heat, L (J / kg)	$7.07 \times 10^5 / 2.92 \times 10^5$	-
	Specific heat capacity, c_p ($J / kg \cdot K$)	713/735 @ liquid state 580/595 @ solid state	477
	Thermal conductivity, k ($W / m \cdot K$)	2.32/69.2 @ liquid state 2.0/80 @ solid state	14.9
	Coefficient of thermal expansion (CTE), α ($^{\circ}C$)	9.68/16.3 $\times 10^{-6}$ @ 20 $^{\circ}C$	16.6 $\times 10^{-6}$ @ 100 $^{\circ}C$
		10.34/20 $\times 10^{-6}$ @ 1000 $^{\circ}C$	17.6 $\times 10^{-6}$ @ 300 $^{\circ}C$
		11/22 $\times 10^{-6}$ @ 2527 $^{\circ}C$	18.6 $\times 10^{-6}$ @ 500 $^{\circ}C$ 19.5 $\times 10^{-6}$ @ 700 $^{\circ}C$
	Heat transfer coefficient of air, h_{cv} ($W / m^2 K$)	20/20	20
Melting point	2527/1450 $^{\circ}C$	1455 $^{\circ}C$	
Structural properties	Elastic modulus, E (GPa)	170/200 @ 20 $^{\circ}C$	200/0.3 @ 700 $^{\circ}C$
		170/190 @ 200 $^{\circ}C$	0.2/0.4 @ 1400 $^{\circ}C$
		170/175 @ 400 $^{\circ}C$	
		170/160 @ 600 $^{\circ}C$	
		170/145 @ 800 $^{\circ}C$	
		170/120 @ 1000 $^{\circ}C$	
		170/3 $\times 10^{-3}$ @ 1450 $^{\circ}C$	
		170/3 $\times 10^{-3}$ @ 2000 $^{\circ}C$	
		160/3 $\times 10^{-3}$ @ 2522 $^{\circ}C$	
		3 $\times 10^{-3}$ / 3 $\times 10^{-3}$ @ 2532 $^{\circ}C$	
3 $\times 10^{-3}$ / 3 $\times 10^{-3}$ @ 3000 $^{\circ}C$			

Poisson's ratio, ν	0.21/0.3 @ 20 °C	200/0.3 @ 700 °C
	0.21/0.33 @ 1000 °C	0.2/0.4 @ 1400 °C
	0.21/0.4 @ 1450 °C	
	0.21/0.4 @ 2000 °C	
	0.21/0.4 @ 2522 °C	
	0.4/0.4 @ 2532 °C	
	0.4/0.4 @ 3000 °C	
Yield strength, σ_y (MPa)	2000/300	Johnson-cook parameters: $A = 310$, $B = 1000$, $C = 0.07$, $n = 0.65$, $\dot{\epsilon}_0 = 1/s$, and $m = 1$
Isotropic hardening modulus, H (GPa),	-/70	
Fracture strength, σ_f (MPa)	300/-	

CHAPTER 5

CHARACTERIZATION, MECHANICAL TESTS AND RESIDUAL STRESS MEASUREMENTS

In this section, discussion about procedures adopted for several experiments are discussed in detail. Experiments related to material characterization and mechanical tests were conducted to determine important findings about the microstructure and properties of several coating samples. Material characterization provides essential information about various microscopic features (such as interfaces, cracks, pores, inclusions, etc.), coating thickness, randomization of defects, and undulation of the coating surface and interface. Mechanical tests provide good estimates of effective coating structural properties such as hardness, elastic modulus and cohesion/adhesion strength. These are required as inputs to the hybrid computational model and hole drilling formulation for experimental residual stress estimation. The various experiments conducted include: optical microscopy, scanning electron microscopy (SEM), surface profilometry, micro-indentation and scratch test. The incremental hole drilling experiment is also conducted to estimate the residual stress profile developed along depth of coating samples. The results obtained from the experiment will be used to validate numerical results obtained from the hybrid model. As discussed previously, air-plasma sprayed ceramic (YSZ) and metallic (Ni-20%Al) coatings that are deposited on stainless steel substrate are selected for the present study.

5.1 Samples preparation and process parameters

As discussed in section 4.4., two types of standard (industrial) coatings materials, i.e. Ni-20%Al and YSZ, are considered for the present study. The Ni-20%Al coating was directly deposited on SS310. From practical point of view, YSZ coatings commonly crack upon direct deposition on SS310 substrate due to high residual stresses. Therefore, it was necessary to deposit thin NiCrAl bond coat layer on SS310 before the deposition of YSZ.

The stainless steel (SS310) was first cut into dimensions of 12 mm x 2.5 mm x 1.5 mm and grit-blasted with an alumina grit having an average diameter of 0.16 mm before coating deposition. Coating deposition was then carried out using Ni-20%Al, NiCrAl and YSZ coating powders of types Metco 404NS [168], Metco 443NS [159], and Metco 204NS-G[169] respectively. The Ni-20%Al feedstock contains chemically clad nickel having enclosed aluminum core with the chemical composition: 80 mol% Ni and 20 mol% Al. The coating powder is self-bonding and commonly used to provide oxidation and thermal shock resistance to surfaces. The NiCrAl feedstock contains aluminum-clad-nickel-chromium alloyed powders with the chemical composition: 69.5-59.5 mol% Ni, 15.5-21.5 mol% Cr, 4.0-8.0 mol% Al, 7.0 mol% others, 4.0 mol% organics. The coating powder is self-bonding and commonly used to provide oxidation and corrosion resistance to surfaces. While, the YSZ feedstock contains agglomerated and sintered 8 mol% yttria stabilized zirconia (YSZ) powders, mostly in the tetragonal phase. The powder is composed of 90.7-91.7 mol% ZrO₂, 7-8 mol% Y₂O₃, and 2.3 mol% others. This powder is mostly used for deposition of top coat layer in TBC system. Conventional DC plasma torch was used to deposit the coatings using process parameters shown in Table 5-1.

Table 5-1: Coating powder characteristics and process parameters

Process parameter	METCO 404NS	METCO 443NS	METCO 204NS-G
Nominal particle size (μm)	-90 +53	-125 +45	-125 +11
Apparent particle density (g/cm^3)	3	4	2.3
Morphology	Spheroidal	Irregular	Spheroidal
Manufacturing route	Chemical cladding	Mechanical cladding	Agglomerated
Number of passes	6	2-4	11 (thick)/ 6 (thin)
Deposition efficiency	70%	65%	75%
Spray rate (kg/hr)	2.0	2.5	
Stand-off distance (in)	5-6	5-6	2-3
Spray angle	60-90°	60-90°	60-90°
Powder feed rate (g/min)	23	30	40
Gun speed (in/min)	6-7	6-7	6-7
Deposition temperature (°C)	660	660	2480
Particle temperature, $N(\mu, \sigma^2)$	1754/178	1812/153	2716/194
Particle velocity, $N(\mu, \sigma^2)$, m/s	172/25	183/19	168/21
Final cooling rate (psi)	50	50	50
Initial substrate temperature (°C)	600	600	700

5.2 Material characterization and mechanical tests

As discussed previously, it is necessary to conduct several experiments to characterize the coatings and measure certain important properties which are required for numerical modeling as well as residual stress calculation based on hole drilling experiments. These experiments include: optical microscopy, scanning electron microscopy (SEM), surface profilometry, micro-indentation and scratch test. The procedure for the experiments is discussed in the following sections.

To characterize both the surface and cross-section of the coating, each coating sample was first cut into several smaller pieces using the metallography abrasive cutting machine. To minimize peel-up of coating layer, diamond coated wheel was used for the cutting operation. Then, the cross section samples were hot mounted (with pneumatic mounting press QualiMount-P, Qualitest, USA), grounded and polished to varying finish size. The polished samples were observed under high resolution optical microscope. After sputtering of surface with 20 nm diamond, SEM imaging of the sample cross section was done. The morphology and other features (e.g. pores, cracks, phases, interfaces, etc.) were identified in both optical micrograph and SEM image.

Basic mechanical properties of the coating samples were determined from microindentation test (with MicroCombi Tester, CSM instruments, Switzerland). The popular Oliver and Pharr method [170] was used to estimate the hardness and elastic modulus of the coating layer as expressed in Eq. (5.1)-(5.3). A Berkovich indenter was used to apply a normal load of 2N over dwell time of 10s at the loading and unloading rate of 0.2 N/min. The test was conducted at least ten times and the average value of the properties were estimated. The Poisson's ratios of the NiCrAl and YSZ sample were taken as 0.21 and 0.3 respectively.

The indentation hardness (H_{value}) is estimated by dividing the load with the projected contact area as expressed in Eq. (5.1).

$$H_{value} = \frac{P_{max}}{A_c} \quad (5.1)$$

Where, P_{max} maximum applied load and A_c is projected area of contact.

The elastic modulus is calculated from the contact stiffness (S) at maximum load. According to Sneddon [171], indenting an elastic half-space results in a solid of revolution. Thus, the effective elastic modulus (E_e) is obtained from Eq. (5.2) as:

$$S = 2\beta \cdot \sqrt{\frac{A_c}{\pi}} \cdot E_e \quad (5.2)$$

Where, $\beta = 0.0134$ for the indenter used and the contact stiffness (S) is obtained at the point of maximum load as:

Using the sample Poisson's ratio (ν_s), the elastic modulus of the sample (E_s) is estimated from:

$$E_e = \frac{1-\nu_s^2}{E_s} + \frac{1-\nu_i^2}{E_i} \quad (5.3)$$

Where, the elastic modulus (E_i) and Poisson's ratio (ν_i) of the indenter are 1141 *GPa* *GPa* and 0.07 respectively.

The surface roughness of the coating was measured using optical profilometer (ContourGT, Bruker, USA). 3D topographical image of the surface was obtained by scanning an area of 3.52 *mm*². As surface roughness varies from location-to-location, the images were taken at 4 different locations for each sample. Then, average values of arithmetic mean (RA), root-mean-square (RMS) and the peak-to-valley (PV) of the roughness were determined for each sample.

The adhesion of the coating to the metallic substrates was determined using scratch test using Rockwell C indenter of 100 μm tip radius. With an initial pressing load of 30 mN, the indenter was pulled along surface of the coating at a load rate of 0.1 N/s until reaching a

maximum applied load of 30 N. The test was conducted three times (for each sample) over a scanning length of 10 mm with a scratch speed of 2 mm/min. During the test, the normal load, penetration depth, acoustic emission, and the coefficient of friction (COF) were continuously measured and recorded. The critical load for the failure of the coating samples were determined from the experimental data.

5.3 Residual stress measurements using hole drilling method

The theory behind the hole-drilling experiment is that, drilling a small hole across depth of a stressed body results in relaxation of in-plane residual strains [172]. The relieved strains can be measured in many ways such as using optical interferometry, digital image correlation, strain gauge rosette, etc. Strain gauge rosette is commonly used due to its low cost, availability and ability to give direct strain measurements. As previously discussed in section 2.2, the strain gauge method has been widely used to estimate residual stresses developed in thermal spray coatings (TSCs). As the residual stress profile developed in these coatings is highly non-linear, the experiment requires that the drilling and strain measurements are done with incremental depths. In the current work, the conventional hole drilling set-up (manufactured by Vishay micro-measurements group) is used to measure residual stresses developed in coating samples as discussed in the following sections.

5.3.1 Procedure for the experiment

The experiment was conducted in several necessary steps which include the following:

1. **Surface preparation:** The surface of the coating samples was prepared according to the procedure given in bulletin B-129-8 [173] of the set-up manufacturer's manual. The top surface of each sample was first cleaned with a degreaser, M-prep conditioner-A and M-prep neutralizer 5-A. This helped to establish a strong bond between the strain gage and surface of the sample.

2. **Strain gauge bonding:** After successful preparation of the samples, the strain gage was bonded to the surface using M-bond 200 adhesive as explained in bulletin B-127-4 [174]. With the aid of sellotape, the gauge was first held at the exact position where it is required to be bonded. Then, a catalyst reagent which helps in strong bonding of the gauge was applied to the bonding area of the gauge and allowed to dry for 2 minutes. This was followed by the application of the adhesive to the bonding area and thump pressing the bonded gauge for several minutes to provide a void free interface. Finally, the sellotape was removed and the strain gauge was allowed to cure for several hours. The strain gage used for the present study is of type CEA-XX-062UM-120 (shown in Figure 5-1) which have gauge mean diameters of 5.13 mm and accommodates minimum/maximum hole size of 1.5/2 mm.
3. **Soldering of wires to strain gauge terminals:** The terminals of the strain gage were connected to the P3 strain gage indicator using lead wires and three-wire quarter bridge circuit. At other end, the lead wires were soldered to the strain gage terminals using a soldering unit (supplied by the Vishay group), after which a protective coating is applied to protect interconnection between wires during drilling. The soldering of wires to the strain gauge is very difficult due to miniature size of the terminals. Therefore, it is essential to use smaller soldering wire, optical lens and sufficient light to successfully carry out this task. Successful soldering operation on a strain gauge is shown in Figure 5-1(d).
4. **Attachment and alignment of the HD set-up:** The HD device was installed and fixed accurately above the strain gage according to the RS-200 Milling Guide [34]. The set-up was bonded with the help of the cement adhesive supplied by the company. The most important and difficult step is the alignment of the drill device cross hairs with the strain gauge center circle. For accurate measurement, it is

necessary to ensure that the point of intersection of the cross hairs coincides exactly with the center of the strain gage circle. This was achieved with the help of the microscope attached to the HD set-up.

5. **Drilling and recording of strain values:** The P3 strain indicator was first connected to a PC and then turned on. Due to the need for high cutting speed, an air turbine was used for the drilling operation. By pressing on the foot switch attached to the compressor, compressed air was supplied to the air turbine which rotates (the drill cutter) at around 200,000 rpm. Diamond-coated tungsten carbide cutters (shown in Figure 5-1(e)) with a diameter of 1.4 mm was used to drill through the strain gauge. It is essential to limit the drilling rotational speed to an optimum level (around 200,000 rpm) to minimize influence of cutting forces on strain readings. To minimize errors associated with shape of drill hole, each new experiment requires a new drill bit. To establish the zero depth, the material of the strain gage was removed by drilling a hole of 0.01-0.03 mm depth depending on initial position of the drill bit. After the establishment of the zero depth, the strain readings were reset to zero from the PC screen. Then, the hole drilling was started in increments of 20 μm and feed rate of 5 μm /minutes until attaining the depth at which the sensitivity limit of the gauge is reached. After reaching each increment, the strain readings could stabilize for couple of minutes before being recorded. However, for the ceramic YSZ coating, it was necessary to wait at least 10 minutes for strain readings to stabilize. This is due to overheating of the sample caused by its low thermal conductivity. After completion of drilling process, the drilled hole diameter was measured with an optical microscope that comes with the set-up.
6. **Estimation of residual stress profile using incremental strain readings:** As explained previously, the multilayered nature of coated samples necessitates the use

of finite element analysis to compute the calibration coefficients required for the estimation of residual stress profile. Therefore, the formulations required for this task are explained in the next section.

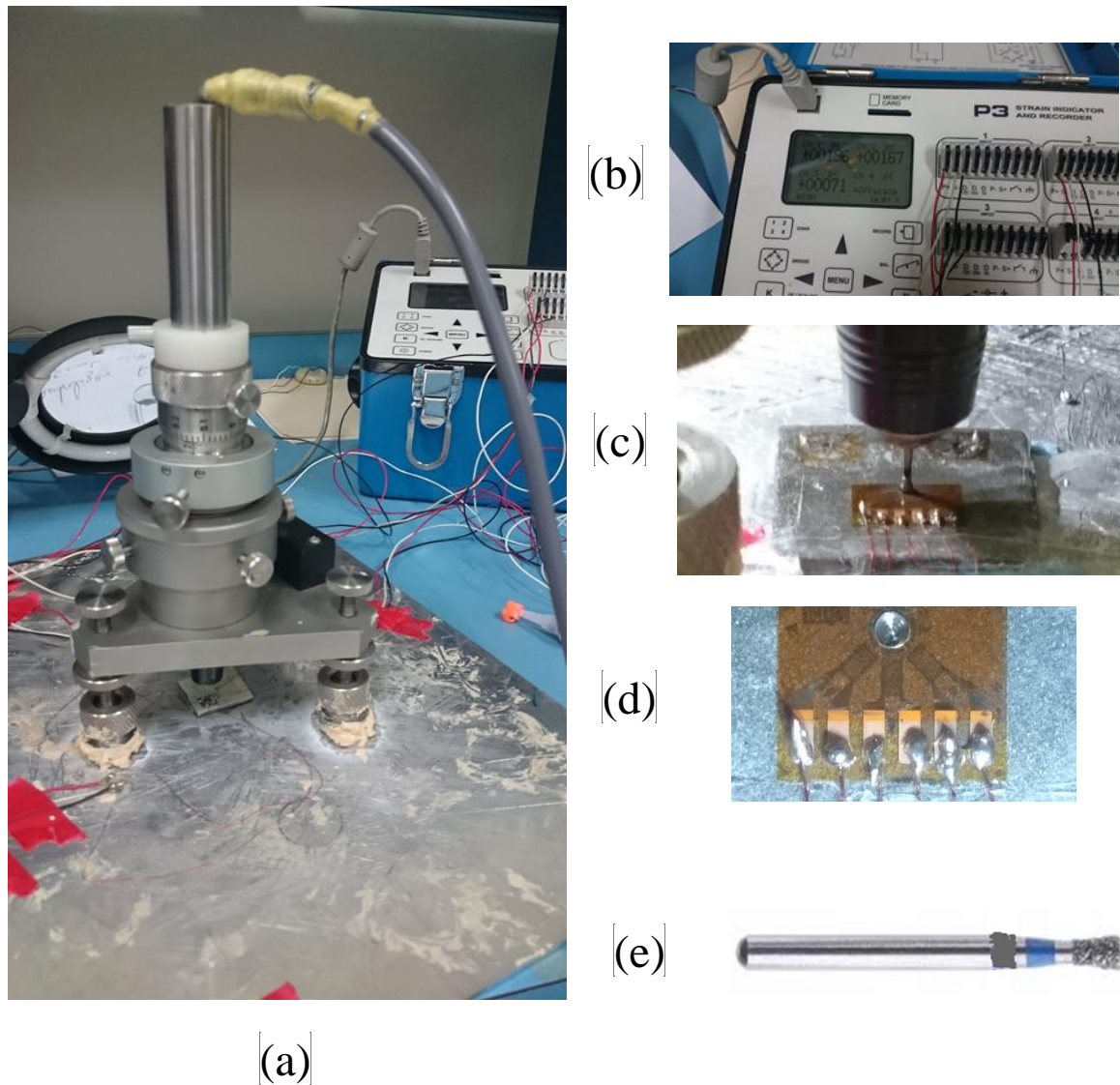


Figure 5-1: (a) Hole drilling set-up by Vishay micro-measurements (drilling YSZ sample), (b) strain gauge indicator, (c) drilling of NiCrAl coating sample, (d) bonded strain gauge having soldered wires.

5.3.2 Calibration of influence coefficients

Based on hole drilling residual stress calculation theory [172], proper influence (or calibration) coefficients are necessary for reliable estimation of through-thickness (in-plane) residual stress profile developed in coatings. Due to the heterogeneous nature of

coating/substrate system, the influence coefficients need to be determined from finite element analysis. The differential method [34] is commonly used to estimate the stress profile using incremental strain data obtained during the experiment. The method assumes that the surface deformation of strain gauge is the result of residual strain relaxation at a depth (or cutting increment). With smaller drilling increment and smoothed incremental strain data, the method has proven to be more effective than other methods in estimating residual stress profile developed in coatings as investigated by Wenzelburger et al. [117], Weidman et al. [175], and Obelode et al. [176].

The influence coefficient directly relates the measured surface (or gauge) strains with the nominal residual strains acting at each incremental depth. A three-dimensional (3D) finite element model for simulation of the hole drilling experiment was developed in ABAQUS/Standard environment. Transversely isotropic (effective) elastic moduli of the coatings required for the analysis were obtained from the micro-indentation tests. The Poisson ratios used were: 0.29 for NiCrAl and Ni-20%Al, 0.22 for Cr₂C₃-(Ni20Cr), and 0.21 for YSZ. The properties of the substrate (i.e. SS310) were taken from the literature Zhu et al. (2015). Utilizing symmetry, only a quarter computational model of dimensions 10 x 10 x 2.16 mm was considered. It was ensured that the domain is wide enough to have minimal effect of boundary condition on numerical results. The coating and substrate layers were made to have specific thicknesses, t_c and t_s , as measured experimentally from optical microscopy. The interface between the coating and substrate layers was assumed to be perfect. For high accuracy and consistency of results, a mapped mesh having high mesh density at the locations of the strain gauge and hole was used for the analysis (as shown in Figure 5-2 (c)). ABAQUS user-subroutine, USDFLD, was used for the simulation of the incremental drilling process whereby elastic modulus of drilled hole region was made very small using a field variable as indicated in Figure 5-3 (a) and 2 (b). Field variable of value 1

corresponds to drilled region. From the simulation, the change in nominal (gauge) strain and stresses with drilling depth was extracted and fed into a self-developed MATLAB code for the calculation of influence coefficients and residual stress profile using Eq. (5.4) - (5.8). The three terminals of the strain gauge provides direct measurements of in-plane strain components, i.e. two normal strains (ε_0 and ε_{90}) and one shear strain (ε_{45}) from which the corresponding in-plane residual stresses (σ_0 , σ_{90} and σ_{45}) can be calculated.

$$\mathbf{K}_1(z) = \frac{\frac{d\varepsilon_{x-FEM}(z)}{dz}\sigma_{x-FEM}(z) - \frac{d\varepsilon_{y-FEM}(z)}{dz}\sigma_{y-FEM}(z)}{\frac{1}{E_{c,s}}[\sigma_{x-FEM}^2(z) - \sigma_{y-FEM}^2(z)]} \quad (5.4)$$

$$\mathbf{K}_2(z) = \frac{\frac{d\varepsilon_{x-FEM}(z)}{dz}\sigma_{y-FEM}(z) - \frac{d\varepsilon_{y-FEM}(z)}{dz}\sigma_{x-FEM}(z)}{\frac{\nu}{E_{c,s}}[\sigma_{x-FEM}^2(z) - \sigma_{y-FEM}^2(z)]} \quad (5.5)$$

$$\sigma_{0^\circ}(z) = \frac{E}{(K_1(z))^2 - \nu^2(K_2(z))^2} \cdot \left[K_1(z) \frac{d\varepsilon_{0^\circ}(z)}{dz} + \nu K_2(z) \frac{d\varepsilon_{90^\circ}(z)}{dz} \right] \quad (5.6)$$

$$\sigma_{45^\circ}(z) = \frac{E}{(K_1(z))^2 - \nu^2(K_2(z))^2} \cdot \left[K_1(z) \frac{d\varepsilon_{45^\circ}(z)}{dz} + \nu K_2(z) \left(\frac{d\varepsilon_{0^\circ}(z)}{dz} + \frac{d\varepsilon_{90^\circ}(z)}{dz} - \frac{d\varepsilon_{45^\circ}(z)}{dz} \right) \right] \quad (5.7)$$

$$\sigma_{90^\circ}(z) = \frac{E}{(K_1(z))^2 - \nu^2(K_2(z))^2} \cdot \left[K_1(z) \frac{d\varepsilon_{90^\circ}(z)}{dz} + \nu K_1(z) \frac{d\varepsilon_{0^\circ}(z)}{dz} \right] \quad (5.8)$$

Where E is effective elastic modulus, ν is Poisson's ratio and $K_{1,2}$ are influence coefficients.

The principal (σ_1 and σ_2) and directional stresses (σ_x and σ_y) can be obtained from:

$$\sigma_{1,2}(z) = \frac{\sigma_{0^\circ}(z) + \sigma_{90^\circ}(z)}{2} \pm \frac{1}{\sqrt{2}} \sqrt{(\sigma_{0^\circ}(z) - \sigma_{45^\circ}(z))^2 + (\sigma_{90^\circ}(z) - \sigma_{45^\circ}(z))^2} \quad (5.9)$$

$$\sigma_{x,y}(z) = \frac{\sigma_1(z) + \sigma_2(z)}{2} \pm \frac{\sigma_1(z) - \sigma_2(z)}{2} \cdot \cos 2(\alpha - 45^\circ) \quad (5.10)$$

And principal angle is,

$$\alpha(z) = \frac{1}{2} \arctan \frac{2\sigma_{45^\circ}(z) - \sigma_{0^\circ}(z) - \sigma_{90^\circ}(z)}{\sigma_{0^\circ}(z) - \sigma_{90^\circ}(z)} \quad (5.11)$$

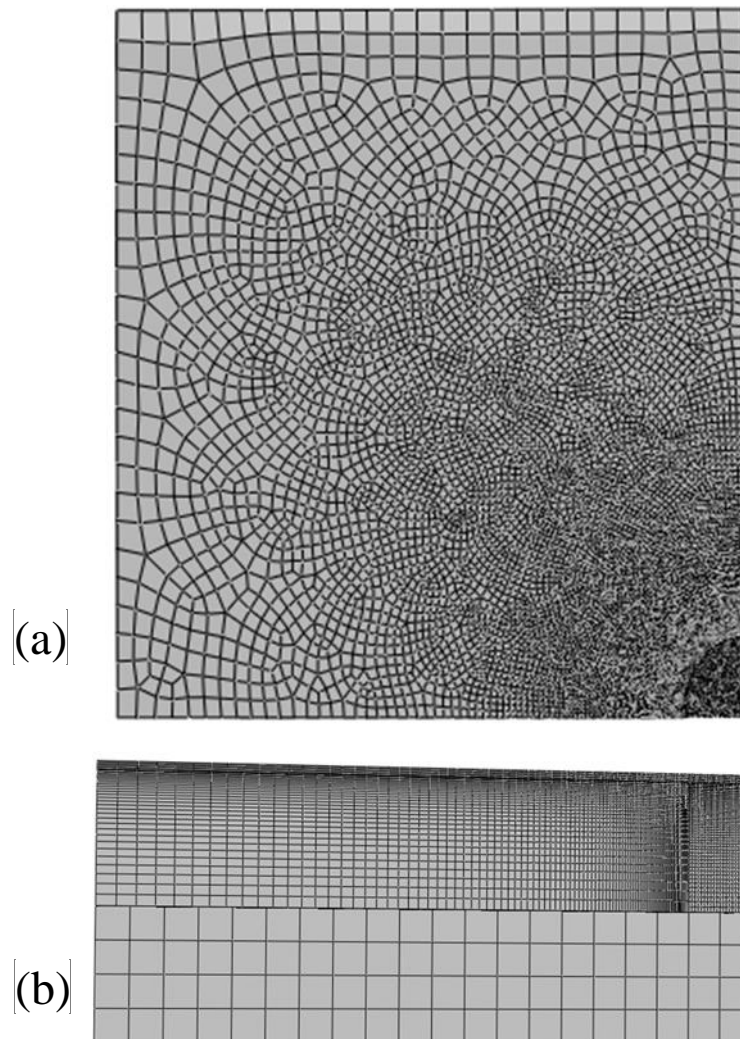


Figure 5-2: Mapped mesh used for hole drilling simulation: (a) top view, (b) side view

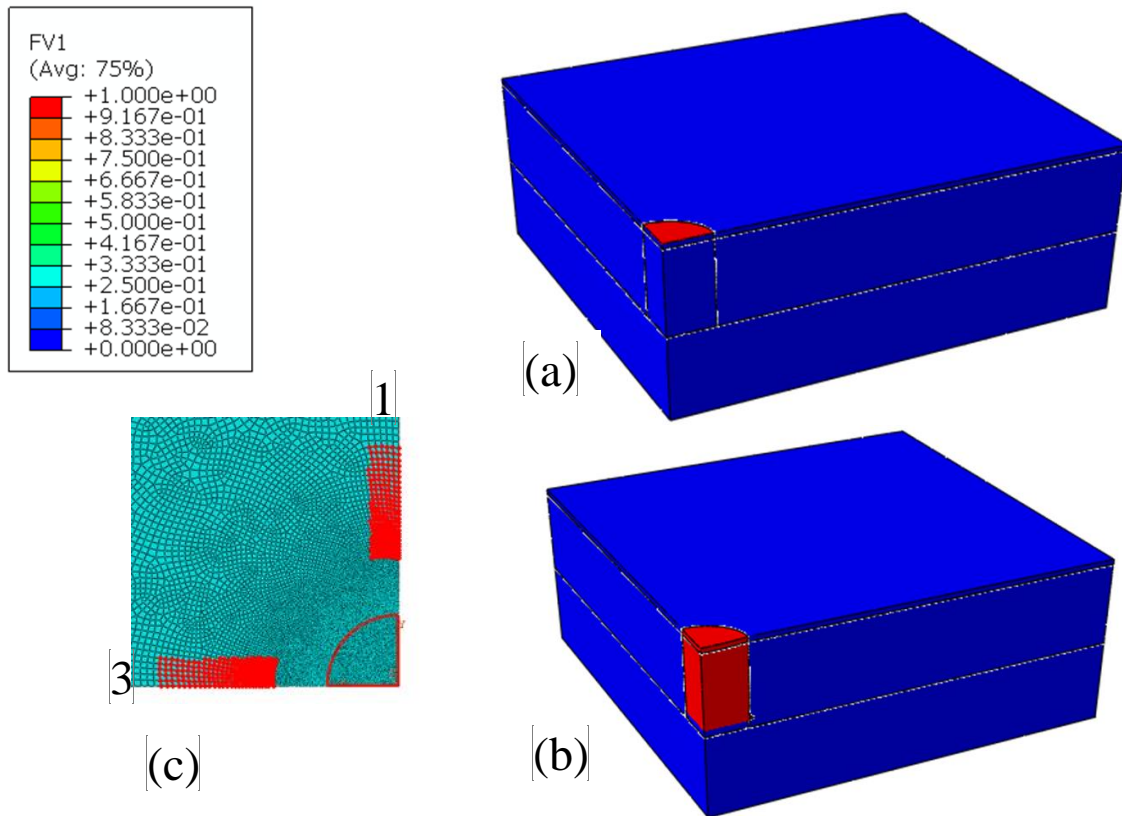


Figure 5-3: Computational simulation of hole drilling experiment: (a) at start of drilling, (b) after drilling, (c) mapped mesh used for analysis

5.3.3 Estimation of stress profile by Tsui and Clyne model

Table 3 shows the parameters required for the analysis of residual stress developed in the selected coatings. The elastic properties of the coating layers (i.e. E and ν) are selected from the micro-indentation tests. The coefficient of thermal expansion (CTE) of the layers are selected from the literature [166], [177]. Other parameters such as total coating thickness, number of depositions passes, particles deposition temperature, and substrate initial temperature are all selected from the coating process parameters given in Table 2. The quenching stress developed during coating deposition is estimated using the theoretical quenching stress model given in Eq. (15). According to recent discussions by Abubakar et al. [29], the theoretical quenching stress result in unrealistically high stress values as it does not account for several uncontrolled mechanisms (such as presence of internal defects, extensive plastic deformation, microcracking, and interfacial sliding) which often lead to the relaxation

of quenching stress. Therefore, it is necessary to reduce magnitude of the theoretical quenching stress by a reduction factor as previously done [178], [179]. Similarly, grit blasting of the substrate surface induces initial peening (compressive) stresses up to depth of about 200 μm within the substrate layer [180]. The peening stress can reach as high as -300 MPa depending on the severity of grit blasting process. However, during substrate preheating, the peening stress partially relaxes to lower values. Therefore, to be more realistic, we have added a reasonable peening stress of about -100 MPa to the stresses induced within the substrate layer.

$$\sigma_q = \zeta E_c \int_{T_s}^{T_d} \alpha_c(T) dT = \zeta E_c \cdot \alpha_c \cdot (T_d - T_s) \quad (15)$$

Where E_c is the effective elastic modulus of the coating as determined from indentation test, α_c is coefficient of thermal expansion, ζ is reduction factor which is taken as 0.1, T_p is the particles deposition temperature, and T_s is the initial substrate temperature.

Table 5-2: Parameters required for estimation of stress profile with Tsui and Clyne model

Parameter	SS310	NiCrAl	Ni-20%Al	Cr ₂ C ₃ - (Ni20Cr)	YSZ
Elastic modulus, E (GPa)	200	124	142	104	59
Poisson's ratio, ν	0.3	0.29	0.29	0.22	0.21
CTE, α ($1 \times 10^{-6} / ^\circ\text{C}$)	19	15	15	11	9
Number of passes, p	-	6	6	5	6

Layer thickness, t (mm)	2	0.16	0.16	0.12	0.28
Intrinsic quenching stress, σ_q (MPa)	-	225.43	258.16	143	
Initial peening stress, σ_p (MPa)	-100	-	-	-	-

CHAPTER 6

MICROSCOPY, EFFECTIVE PROPERTIES AND RESIDUAL STRESS PROFILE

In the current section, the results obtained from characterization, mechanical tests and experimental residual stress measurements are discussed. The work presented here has been submitted to Material Science and Engineering-A Journal.

The discussion starts with material characterization where the types and distribution of defects/discontinuities within the coating microstructure, coating surface morphology, and surface roughness are studied. This is followed by discussion about mechanical properties measured from indentation and scratch tests, i.e. hardness, elastic modulus and cohesion strength. Estimated values of the mechanical properties are linked to the information obtained from characterization of the coatings. Lastly, thorough discussion is made about the residual stress profile measured along the coating depth as obtained from the hole drilling experiments. The aim of the present study is to relate the results of microscopic studies with effective coating properties and residual stress profile.

6.1 Coating characterization

In Figure 6-1 to Figure 6-3, the cross-section views of the deposited coating layers are shown as obtained from optical microscope. It can be seen from the figures that, the coating layers exhibit highly non-uniform thickness, surface roughness, and porosity. It is found that the average thicknesses of the selected coatings are: 155 μm for Ni-20%Al, 160 μm for YSZ

having 40 μm thick NiCrAl bond coat (i.e. thin TBC specimen) and 280 μm for YSZ having 100 μm thick NiCrAl bond coat (i.e. thick TBC specimen). The thicknesses of the coatings vary due to use of different process parameters (previously shown in Table 5-1). Figure 6-1 to Figure 6-3 also shows that the coating microstructures are filled with the typical defects encountered in TSCs. It can be seen that the distribution of defects within the coating layer is highly non-uniform because of the random nature of the process. Identifiable defects from the microstructure include: pores, microcracks, interlamellar cracks, hard inclusions, and highly rough surface. Similarly, it can be seen that secondary (minor) phases emanate at random locations within the coating layers. Obviously, the material mismatch occurring at the interface of these secondary phases contributes to the formation of additional discontinuities/imperfections (such as cracks, pores, and interfaces) within the coating layer. Due to use of nanostructured agglomerated powder, the coating lamella structures are not clearly visible in the microstructure of YSZ topcoat layer of TBC.

In Figure 6-4 to Figure 6-5, the cross-section views are presented at higher resolution based on images obtained from SEM. For brevity, only selected sections of the microstructure are shown. The images clearly show the various imperfections formed within the coating layers. Secondary phases are more visible from the SEM images especially for the case of the Ni-20%Al coating and NiCrAl bond coat. Some secondary phases settle as hard inclusions that may be beneficial or detrimental to the integrity of coating layer. The coating lamella (or splat) structures are more visible in the Ni-20%Al and NiCrAl coatings due to effective spreading of metallic droplets (shown in Figure 6-4 and Figure 6-5). This is attributed to their high surface tension and ductility as compared to the materials YSZ coating. Consequently, during thermal spraying, the metallic droplets undergo less splashing, fingering, and break-up. Figure 6-4 and Figure 6-5 also show that pores exist at random locations within the microstructure of the coating layers. The microstructures contain both nano and micro-pores

with size range falling within 0.1-5 μm depending on the originating source and coating material. Due to their miniature size, the nano-size pores (mostly formed due to nucleation) have less significance on the mechanical behavior of the coatings. On the other hand, micropores immensely affect the coatings thermo-mechanical behavior. It is well established that [35], [181], large (major) micropores originate from unfilled interstices formed because of splats edge curl-up (in metals), ceramic microcracking, impact of semi-molten droplets, and high surface tension forces. While, small (minor) pores are formed because of droplets splashing, formation of satellite droplets or fingers, and oxidation. From image processing, the porosities of the deposited coatings were estimated to be 4.21% for NiCrAl, 4.54% for Ni-20%Al, and 15.98% for YSZ coatings. Therefore, the metallic coatings have lower porosity with most pores existing in elongated form. This is because of the high surface tension of metallic droplets and high ductility of the solidified coating layer. Due to deposition with powder particles of smaller size, the porosity in the Ni-20%Al coating is less than that of the NiCrAl coating. Also, the YSZ coating is more porous and inhomogeneous due to the low surface tension and brittle nature of YSZ. Contrary to what was observed for the case of the metallic coatings, the YSZ coating also exhibits globular and near-spherical pores. This might be attributed to the fact that the coating was deposited with highly structured nanocomposite agglomerated powder. Similar results have been previously observed by Soltani et al. [182].

Moreover, Figure 6-4 to Figure 6-5 shows the various cracks formed within the coating layers. They are mostly micro-scale cracks with size of about 5-20 μm . Two forms of cracks can be identified from the microstructure, i.e. inter-lamella (or interface) and through-splat (horizontal or vertical) cracks. The inter-lamellae cracks (formed at splat and coating interfaces) emerge due to splat-edge curl-up, buckling or extensive splat microcracking resulting from the high stresses formed during deposition (i.e. splats quenching). While the

through-splat (horizontal or vertical) cracks emerge because of high tensile (mismatch) stresses developed when the coating and substrate layers are cooled to room temperature. It is found that the NiCrAl and Ni-20%Al coatings contain very few or no cracks due to the high surface tension of metallic droplets and high ductility of solidified metallic splats. The relatively higher impact velocities and spray rate used to deposit such coatings can be another reason of lower crack intensity observed. On the contrary, the YSZ coating contains higher intensity of microcracks, obviously, due to the brittle nature of their ceramic constituent. The YSZ coating contains more of miniature (through-splat) cracks that emerge during the deposition process. As widely discussed in literature [183], the high tensile stresses are immensely relaxed by extensive microcracking. The microcracks in the YSZ layer emerge due to thermal shock attributed to the sudden solidification of sprayed (ceramic) material. Furthermore, shorter cracks are formed in the YSZ layer because of the coating was deposited with agglomerated nanostructured powder.

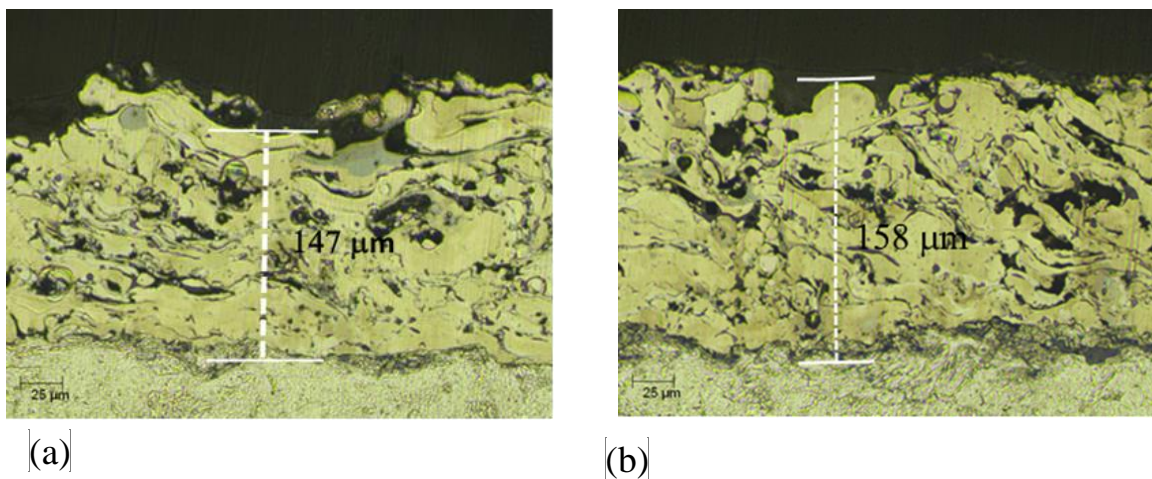


Figure 6-1: Optical micrograph showing cross-sectional view of Ni-20%Al coating: (a) & (b) shown at two different locations

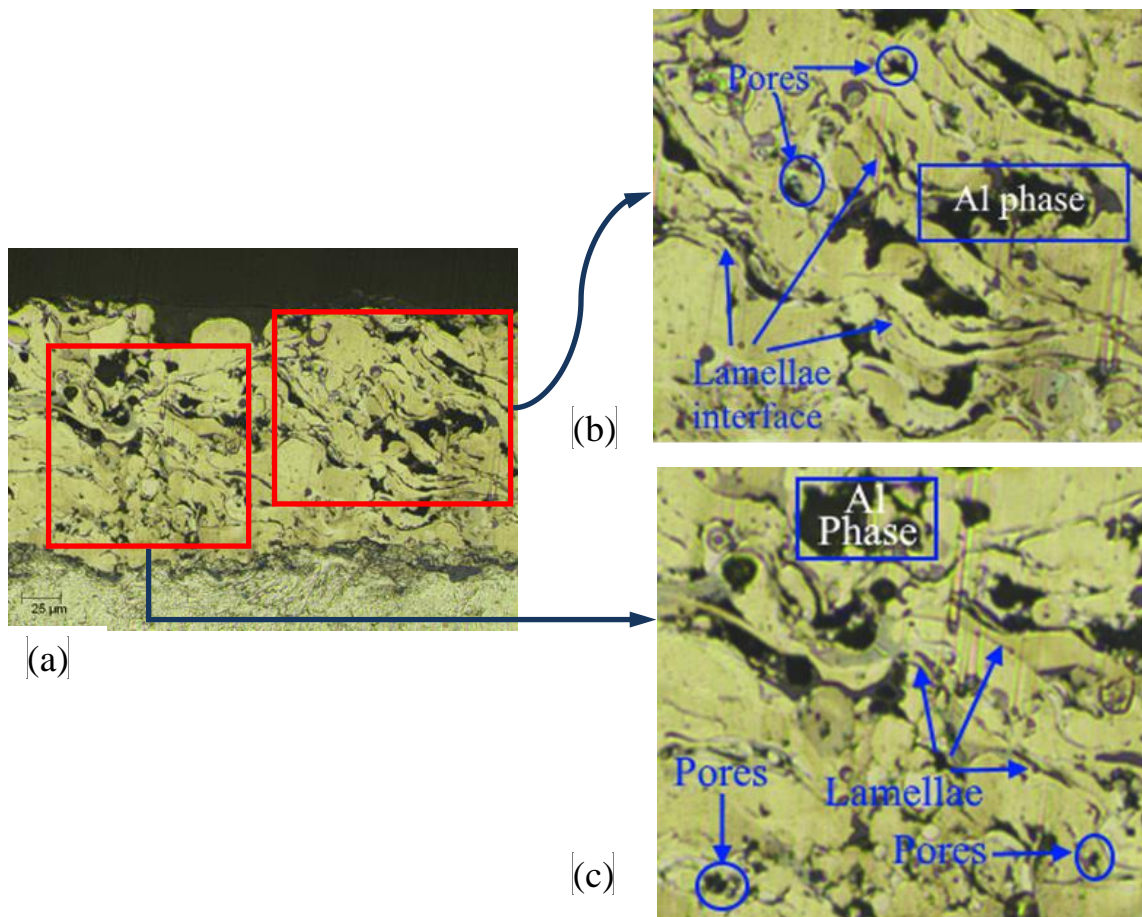
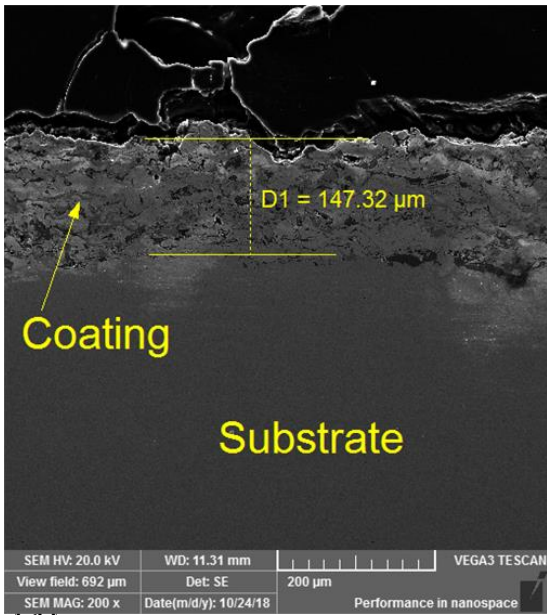
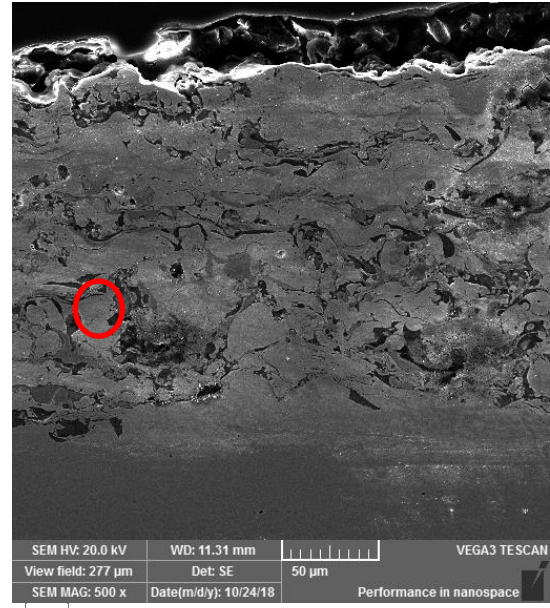


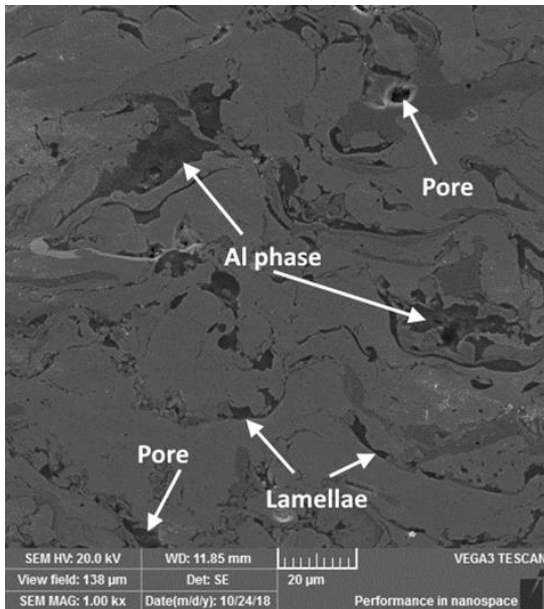
Figure 6-2: Real microstructure image of Ni-20%Al coating: (a) x500 magnification, (b) Zoomed region 1, (c) Zoomed region 2



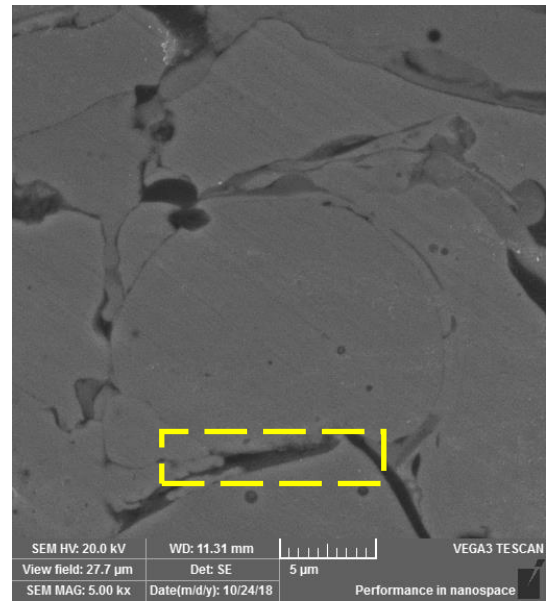
(a)



(b)

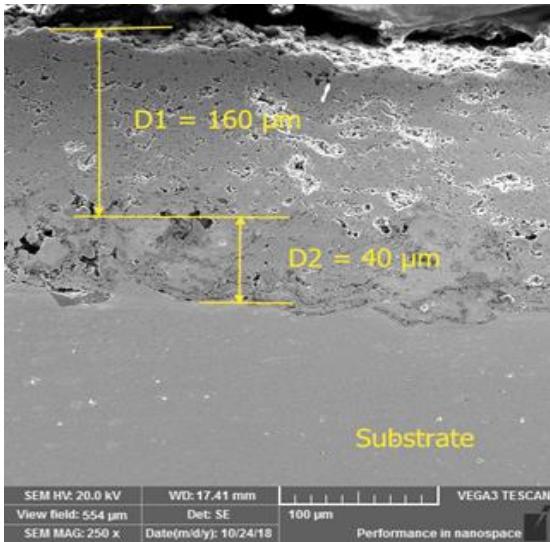


(c)

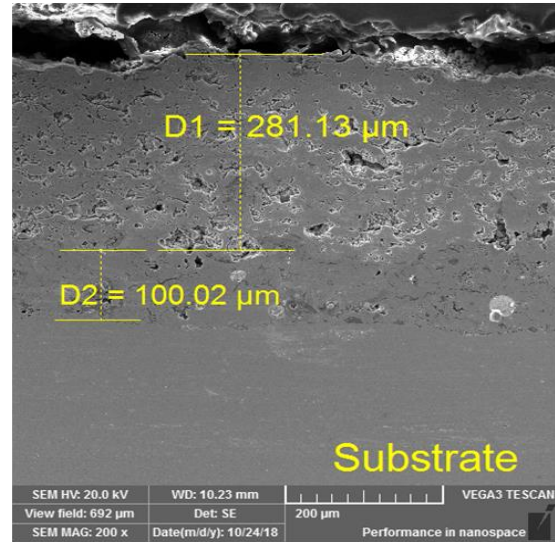


(d)

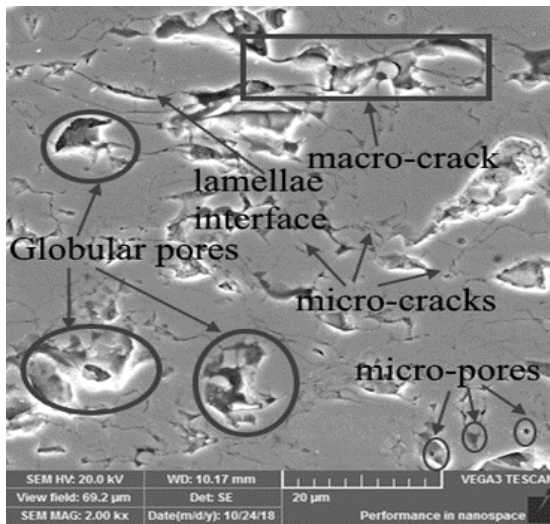
Figure 6-4: SEM micrograph showing cross-sectional view of Ni-20% coating layers showing: (a) total coating thickness and inhomogeneities at smaller magnification, (b)-(d) pores and interlamellar cracks at higher magnification



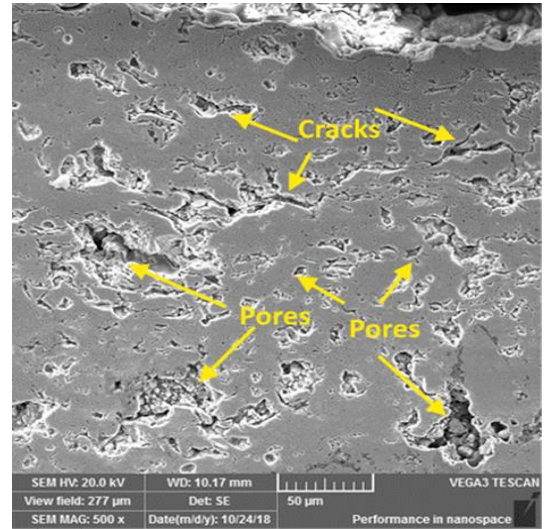
(a)



(b)



(c)

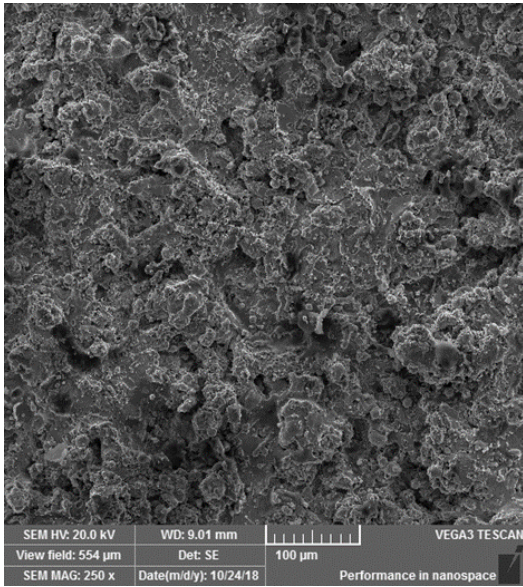


(d)

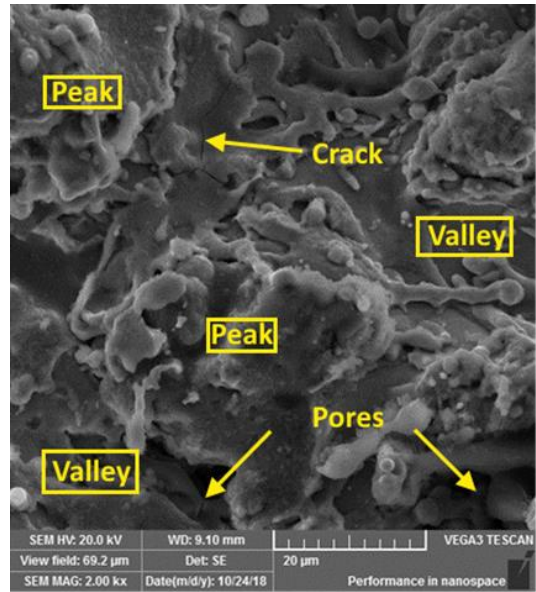
Figure 6-5: SEM micrograph showing cross-sectional view of coating layers showing: (a)-(b) thickness and inhomogeneities of the coating layers at smaller magnification, (c)-(d) cracks and pores at higher magnification

Figure 6-6 shows that the surface morphology of the coatings. Due to complex interaction resulting from the deposition (or spray) of multiple droplets, it is very difficult to identify the coating splat structures from the images. Rather, the surfaces are filled with large pores (or cavities) and undulations having significant variation in peak-to-valley heights. Therefore, the coatings surfaces are highly irregular and rough. The surface undulations are more visible for the case of the Ni-20%Al coating as observed in Figure 6-6 (a) and (b). This is because the metallic Ni alloy droplets exhibit higher surface tension and density as compared to the YSZ

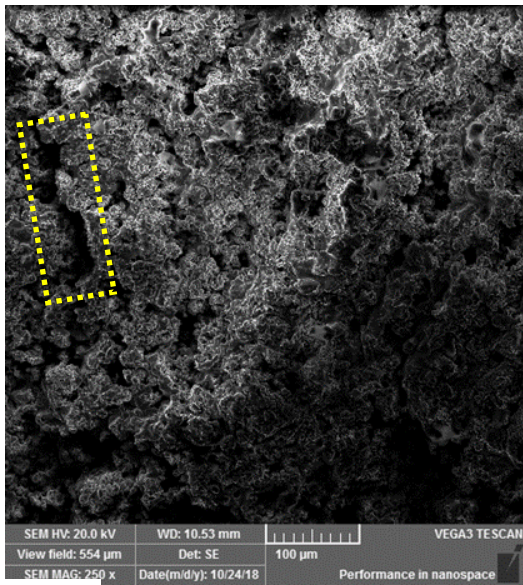
coating. Furthermore, several through-splat cracks can be identified from the surface of the YSZ coating due to their brittle nature as demonstrated in Figure 6-6 (c) and (d). As the surface roughness changes with location, roughness parameters were obtained at four different locations; thus, only average is reported here. Figure 6-7 shows a sample 3D topographical views of the selected coatings obtained after eliminating noise with Gaussian regression S-filter having short wavelength of 25 μm . It is found that the average peak-to-valley heights of the respective coating surfaces are: $72.0 \pm 2.6 \mu\text{m}$ for Ni-20%Al and $59.6 \pm 4.1 \mu\text{m}$ for YSZ. Table 6-1 shows the corresponding surface roughness parameters, i.e. arithmetic mean and root-mean-square surface roughness. It can be seen that Ni-20%Al coating has higher surface roughness as compared to the YSZ coating. This is because the Ni-20%Al coating was deposited with powder consisting of larger particles. Furthermore, it exhibits higher thermal conductivity; thus, incoming metallic droplets may not suitably conform with existing splat because of quick solidification and large plastic deformation occurring during splats quenching. However, for the YSZ coating, their lower conductivity results in heat entrapment; thus, better conformability is attained with deposition of new droplets. In addition to that, tensile (quenching) stress relaxation through microcracking of the ceramic coating cause the breakup of flattened splats into multiple (smaller) pieces, eventually leading to the low surface roughness observed.



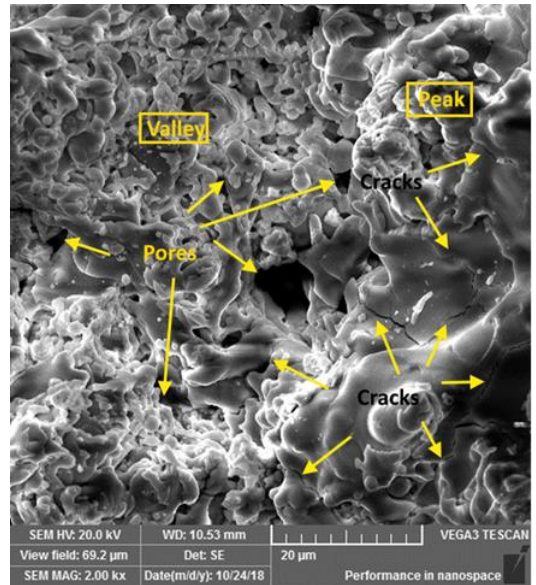
(a)



(b)



(c)



(d)

Figure 6-6: SEM micrograph showing surface morphology of the coating layer at low and high magnifications: (a)-(b) Ni-20%Al, (c)-(d) YSZ

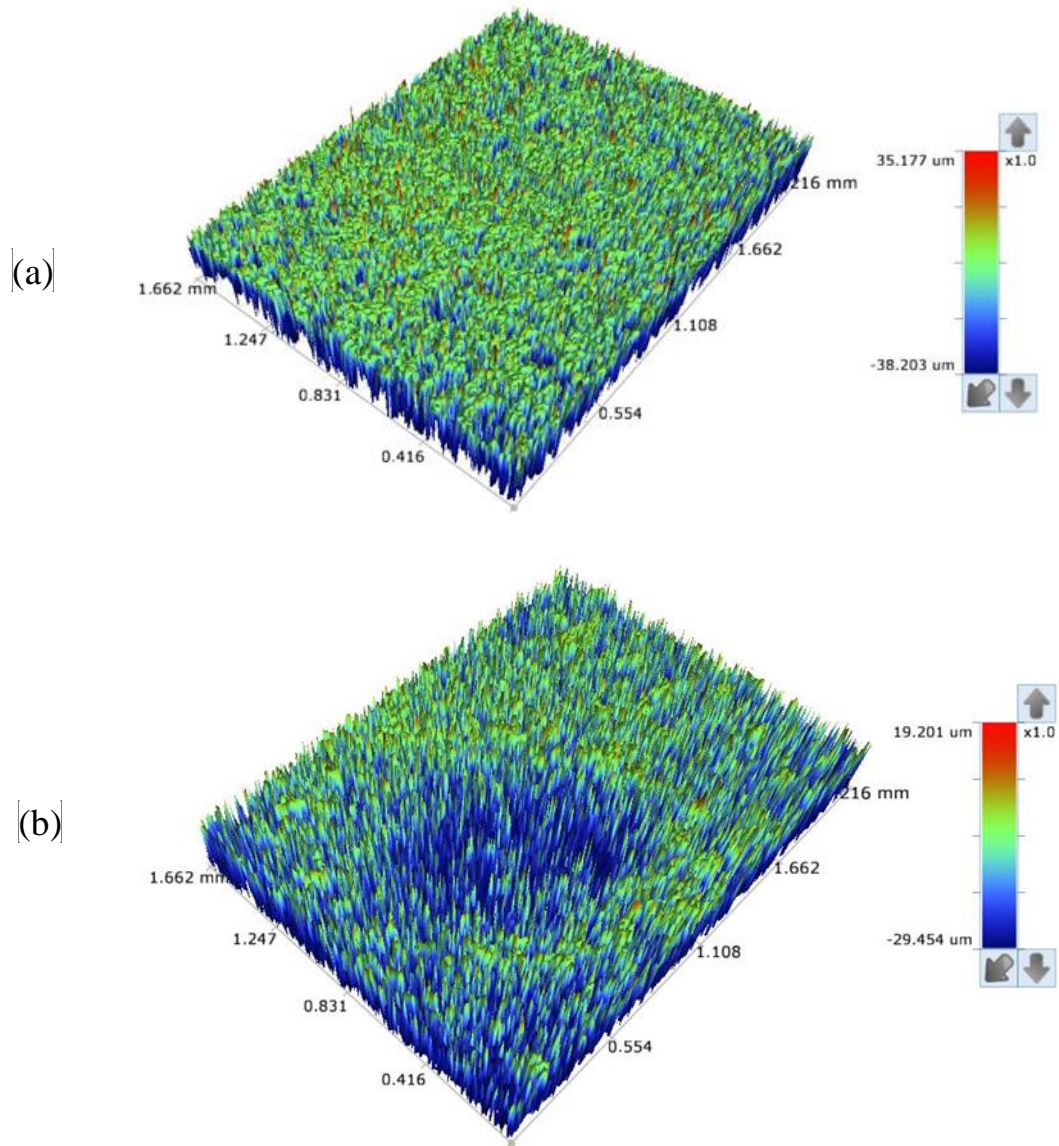


Figure 6-7: Surface roughness profile obtained for 3D optical micrograph: (a) Ni-20%Al specimen, (b) TBC specimen

Table 6-1: Surface roughness parameter values

Roughness parameter	Ni-20%Al	YSZ
Arithmetic mean, $R_a(\mu m)$	2.314 ± 0.046	2.322 ± 0.019
Root-mean-square, $R_q(\mu m)$	3.336 ± 0.065	3.146 ± 0.026
Peak-to-valley, $PV(\mu m)$	72.007 ± 2.630	59.612 ± 4.102

6.2 Mechanical properties obtained from microindentation

Figure 6-8 shows the loading-unloading curves obtained from the micro-indentation tests. Sample micrographs of indented locations are shown in Figure 6-9. By comparing Figure 6-8 (a) and Figure 6-8 (b), it can be seen that the micro-indenter penetrates deeper across the coating thickness as compared to the cross-section. This is true for all the coating samples considered here. This is because, after droplets impact, severely flattened disk-like structures (termed “splats”) having elongated grains are formed. Due to the nature of grains formed within splats as well as the presence of multiple elongated pores or horizontal (interlamellar) cracks, the deposited coating layers exhibit directionality of properties as observed in Figure 6-10. As shown in Figure 6-10, the hardness and elastic moduli of the respective coating layers are higher along the in-plane directions as compared to the thickness direction. Also, the Ni-20%Al coating exhibits higher stiffness, elastic moduli and hardness due to its dense nature as previously observed in Figure 6-4. While, the YSZ top coat has extremely low hardness and elastic modulus due to its high surface roughness and porosity as shown in Figure 6-5 and Figure 6-6.

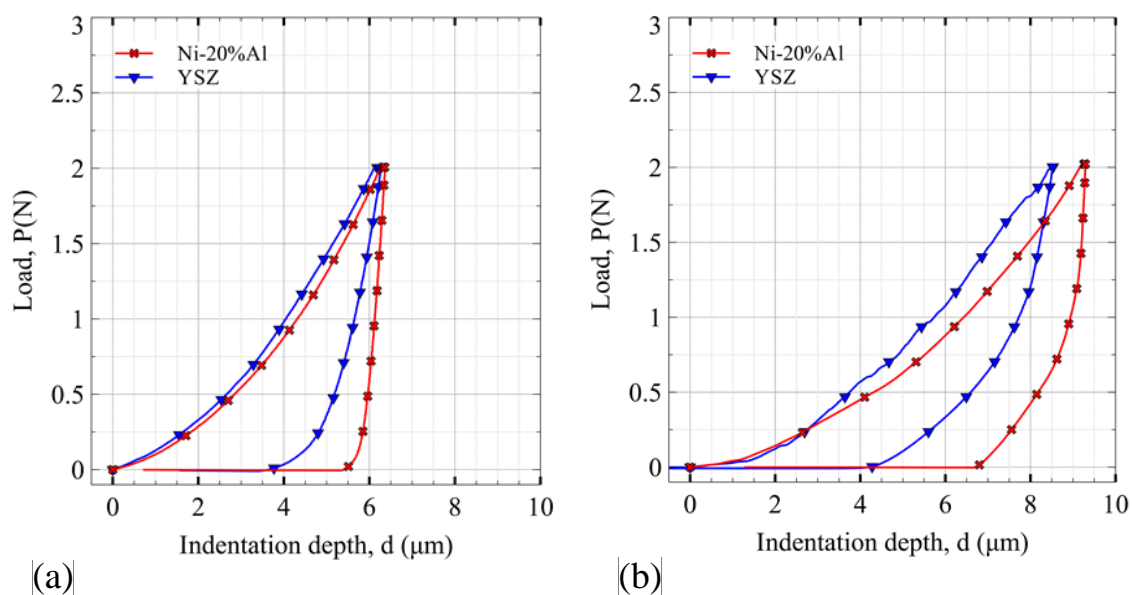
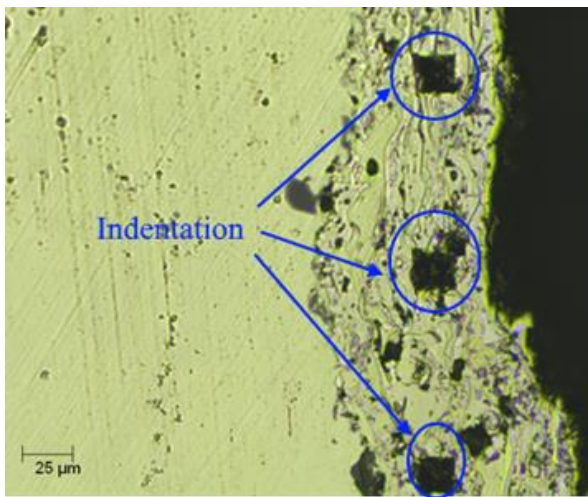


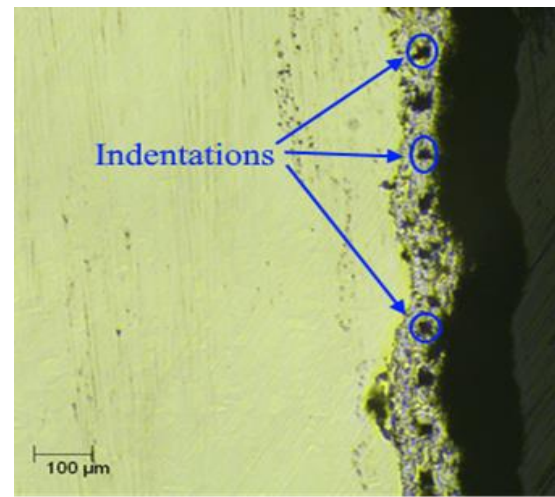
Figure 6-8: Loading-unloading curves obtained from micro-indentation: (a) test conducted on along cross section and (b) test conducted on surface (each curve is average of 10 experiments)

Table 6-2: Mechanical properties of coating specimens obtained from microindentation tests

Property	Ni-20%Al ¹	YSZ ¹	Ni-20%Al ²	YSZ ²
Indentation hardness, $H(GPa)$	3.062 ± 0.364	2.158 ± 0.041	1.370 ± 0.069	0.923 ± 0.014
Vicker's hardness, HV	289 ± 34.0	204 ± 4.0	139.7 ± 7.0	87 ± 1.3
Elastic modulus, $E(GPa)$	127.2 ± 11.9	54.5 ± 2.5	89.4 ± 5.7	28.7 ± 2.9
1: Test along cross section; 2: Test along surface				



(a)



(b)

Figure 6-9: Optical micrographs showing indented coating at: (a) 1000 magnification and (b) 200 magnification

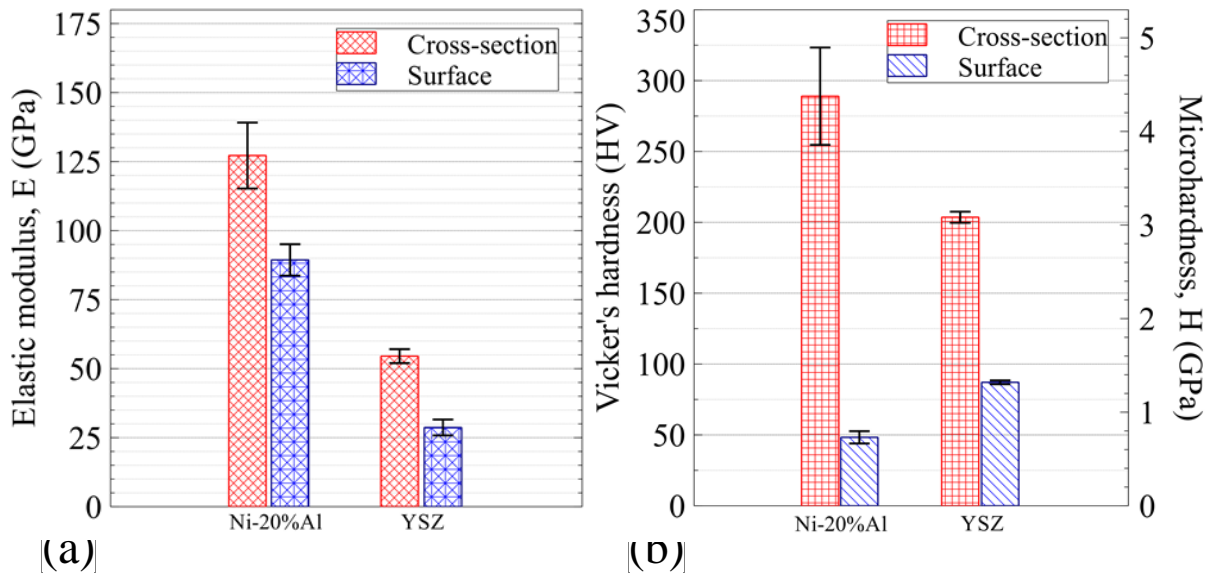


Figure 6-10: Effective coating properties obtained from nanoindentation: (a) Elastic modulus and (b) Hardness

6.3 Residual stress profiling with hole drilling method

Using finite element analysis, the influence coefficients required for effective estimation of residual stress depth profiling were computed. The effective properties of the coating layer were taken from the results of the micro-indentation tests. While, the SS310 substrate properties were taken from the literature values (previously given in Table 2-1). Calibration loads of 100 MPa and -50 MPa were applied on the outer boundaries along the x and y-axes respectively. The elastic strains and stresses corresponding to the deformation caused by the applied loads are shown in Figure 6-11 & Figure 6-12 for Ni-20%Al coating and Figure 6-13 & Figure 6-14 for TBC. The average (or nominal) strains and stresses developed within area of the gauge rosettes were used for the computations (as shown in Figure 6-15). As expected, it is found that the nominal shear strains and stresses developed within the coating layer are small and not needed during calibration. Figure 6-16 shows the calibrated influence coefficients for all the coating samples considered in present study. It can be seen that the curves are consistent with previous analysis by Gadow et al. [22] and Schuster and Gibmeier [184]. In addition, the present study considers orthotropic elastic properties during numerical

calibration of the influence coefficients. It can be seen from Figure 6-17, that the use of orthotropic properties strongly affects the influence coefficients, especially within the coating layer. This has been previously pointed-out by Weidman et al. [175] that, the orthotropic nature of the coating layer should not be neglected while calibrating the influence coefficients. Figure 6-18 shows the micro-strain readings (ε_1 , ε_2 and ε_3) obtained after each incremental drilling depth at the three strain gauge terminals. As commonly done in literature [175], the micro-strain relaxation is first fitted to polynomial of second order to avoid unwanted numerical fluctuations during residual stress estimation with the differential method. Thus, the micro-strains readings presented here are fitted to polynomial of third order in order to truly capture the distribution of residual strain across the depth of coating layers. It is found that the relaxation of residual strains changes with drilling depth. Repeatability of strain measurements within each coating material is investigated. It is found that the overall trend of strain measurements is similar, even though quantitative variations do exist between readings taken at different locations. This is because of high degree of inhomogeneity of the coating layers arising from high surface roughness, uneven distribution defects and complex interaction of process parameters as previously observed in Figure 6-1 to Figure 6-7. From Figure 6-18, it can also be seen that the values of the nominal strains are mostly negative within the Ni-20%Al coating layer. This indicates the presence of tensile residual stresses in these coatings. On the contrary, the YSZ coating develops compressive residual stress since the nominal strains in the coating layer are mainly positive. In all cases, non-linear strain profile was observed because of complex residual stress profile developed along the depth of the coating layers as previously predicted by Obelode and Gibmeier [176] and Back et al. [176].

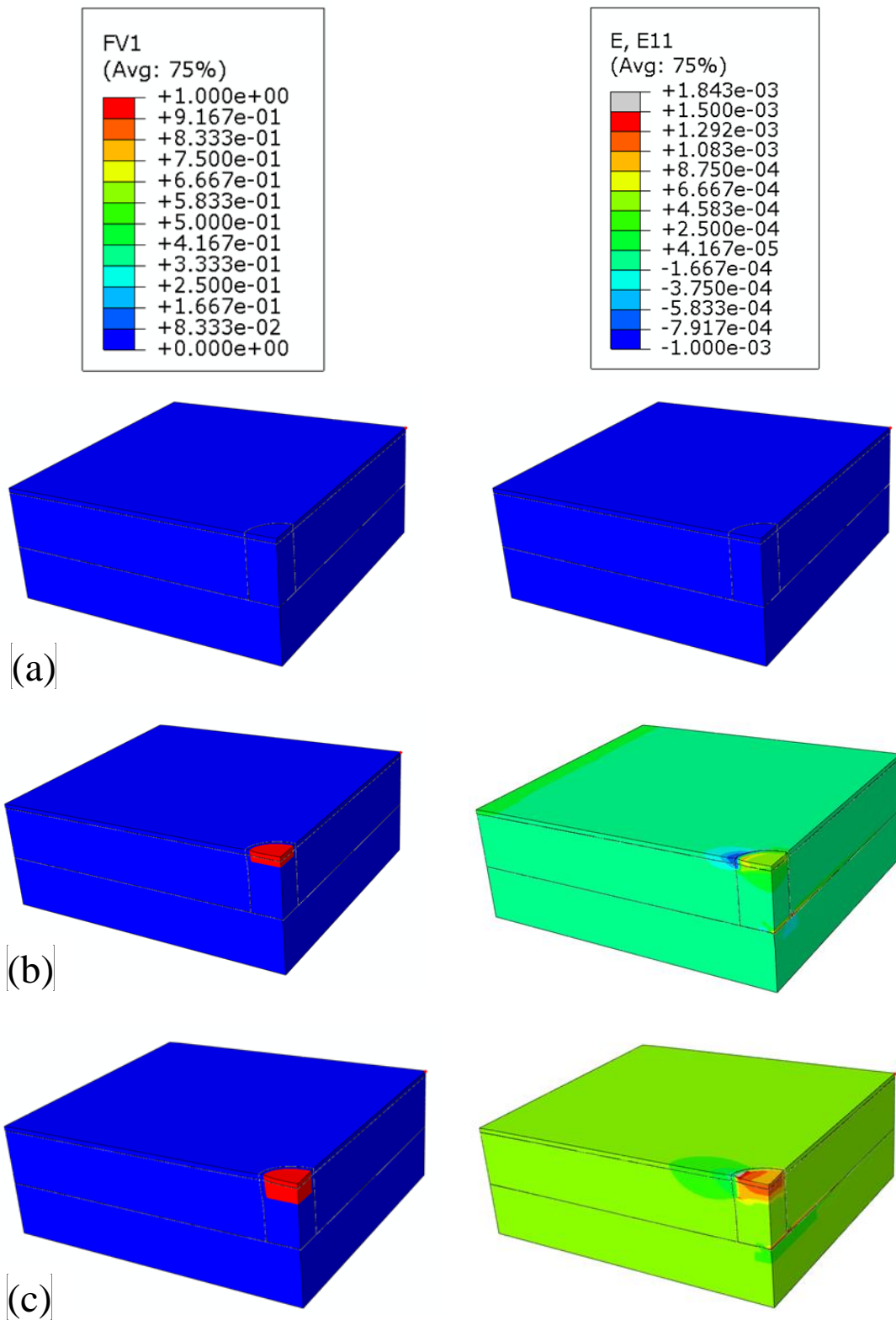


Figure 6-11: Variation elastic strain in x-direction during hole drilling process at depth of: (a) 0 μm , (b) 360 μm and (c) 800 μm .

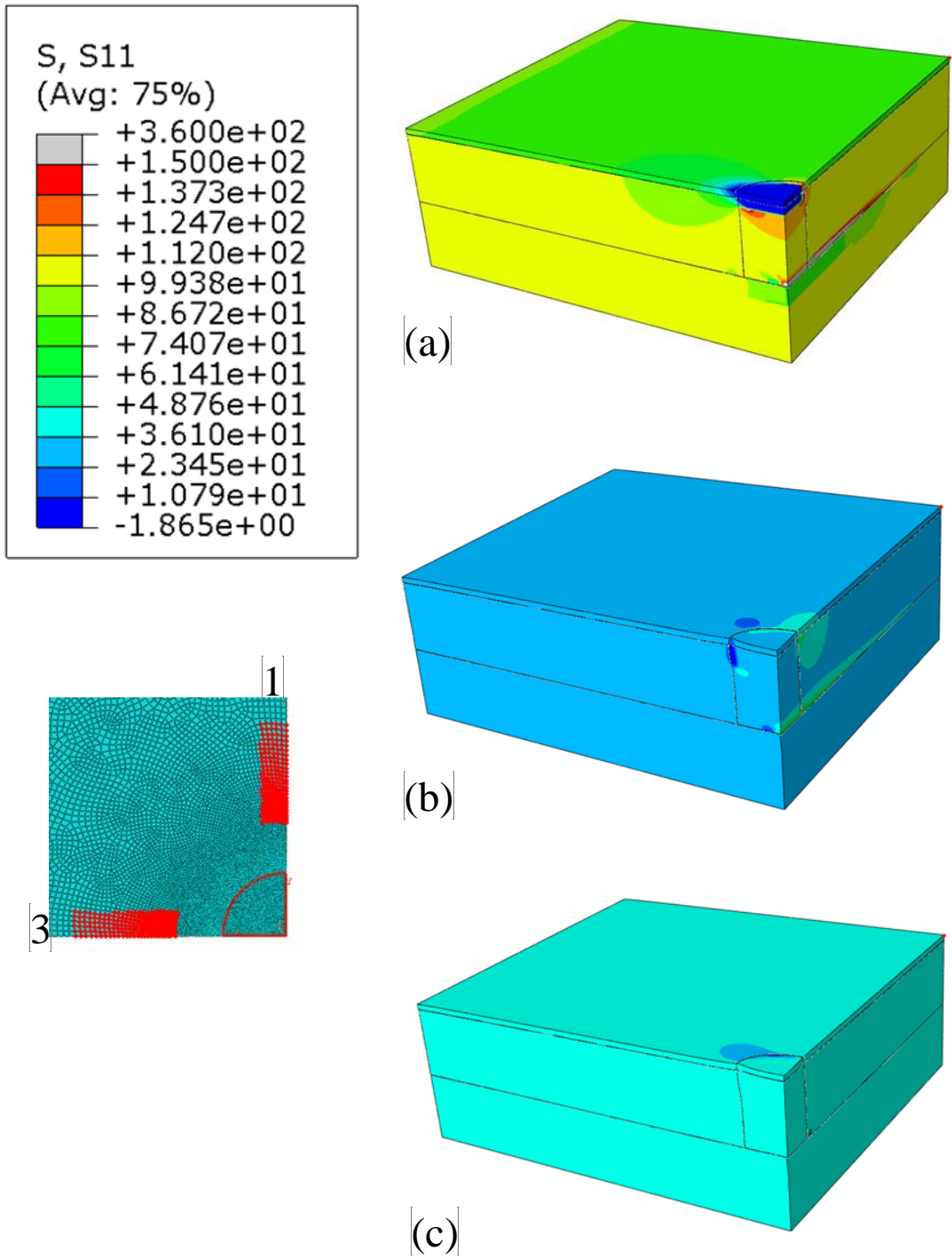


Figure 6-12: 3D plots of in-plane stress field developed during drilling: (a) normal stress in x-direction, (b) normal stress in y-direction and (c) shear stress in xy plane

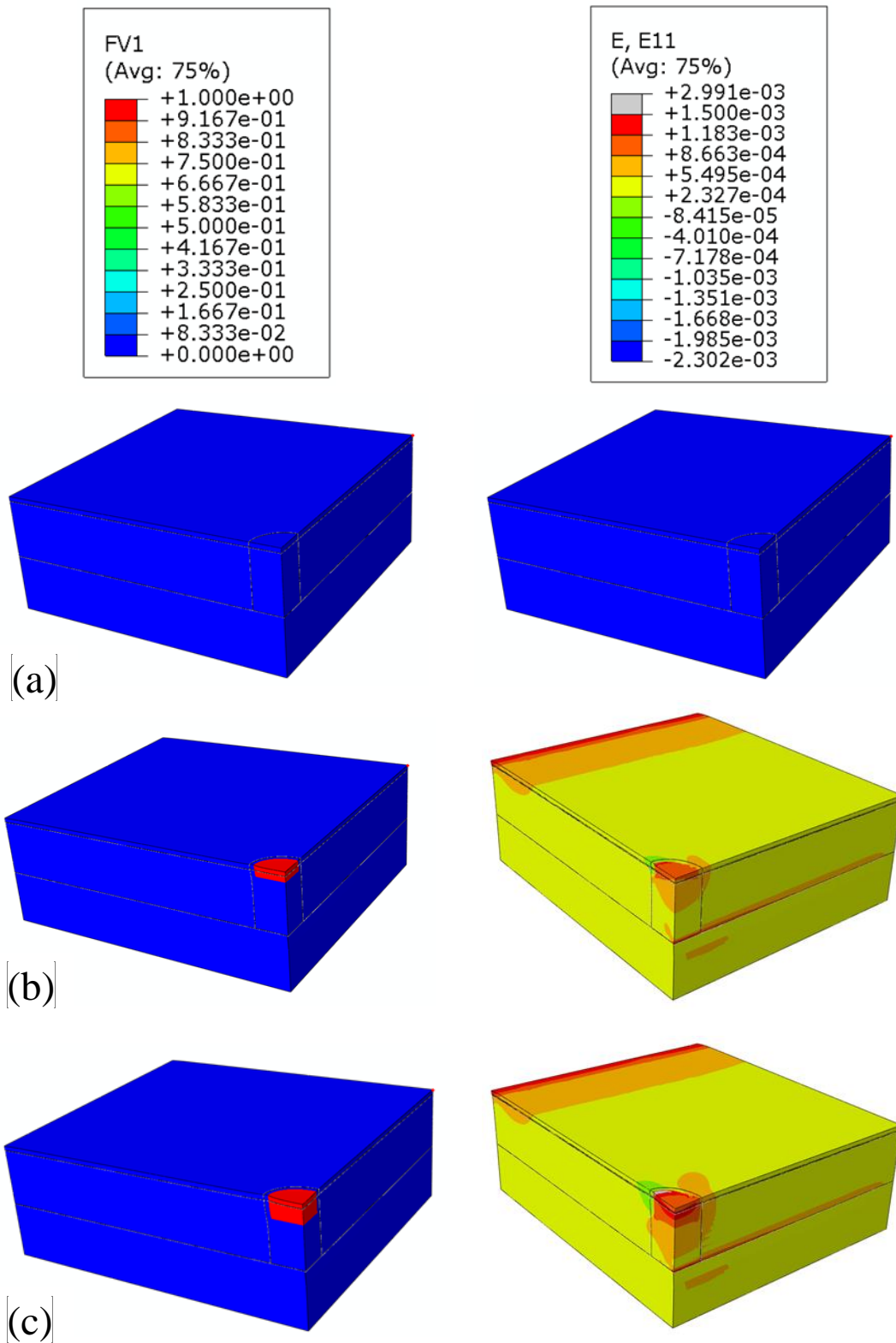


Figure 6-13: Variation elastic strain in x-direction during hole drilling process at depth of: (a) 0 μm , (b) 360 μm and (c) 800 μm .

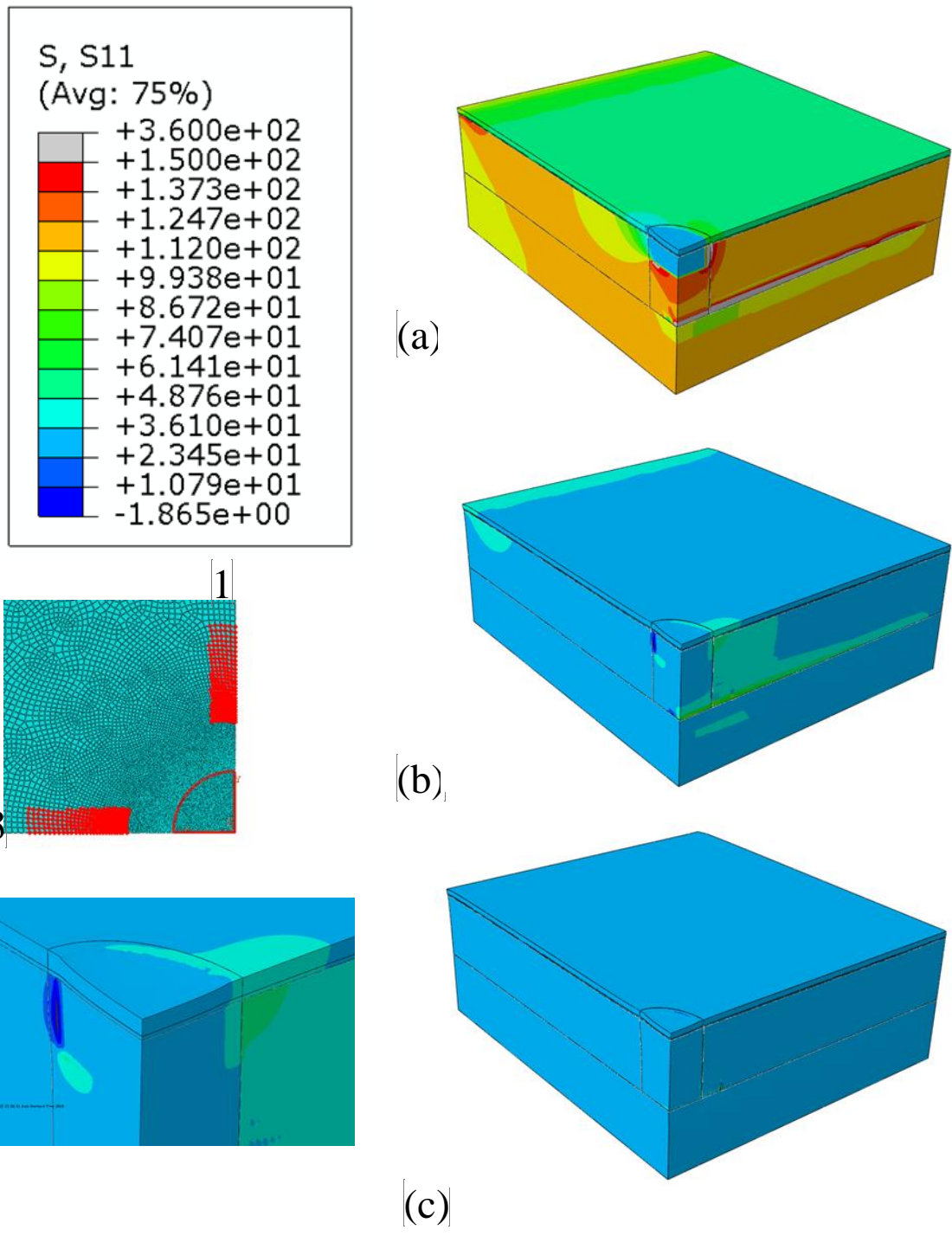


Figure 6-14: 3D plots of in-plane stress field developed during drilling: (a) normal stress in x-direction, (b) normal stress in y-direction and (c) shear stress in xy plane

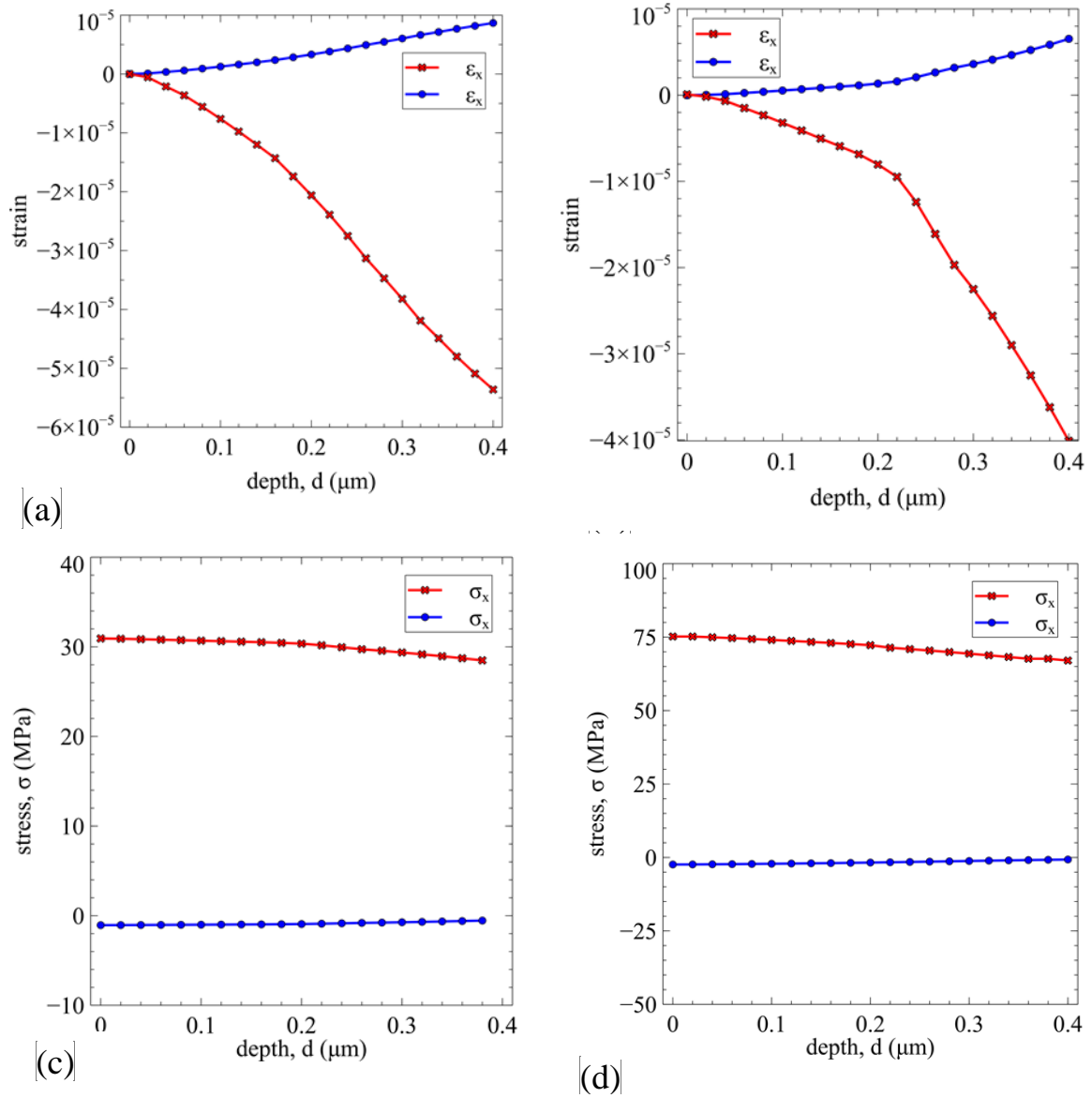


Figure 6-15: calibrated nominal strain and stresses developed in x and y directions: (a) & (c) for Ni-20%Al and (b) & (d) for TBC

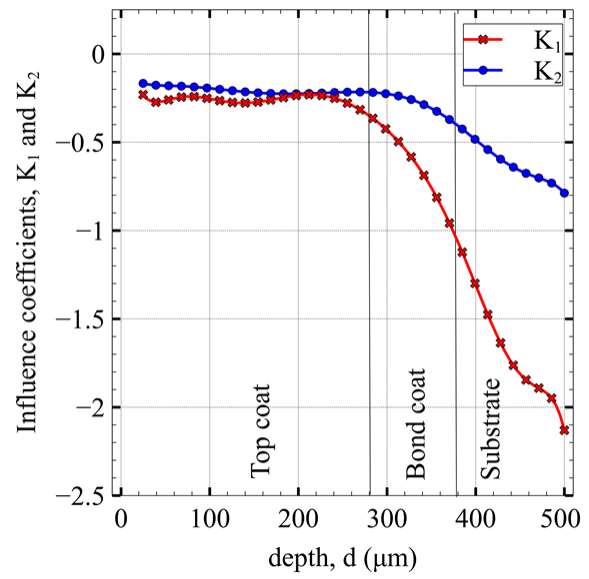
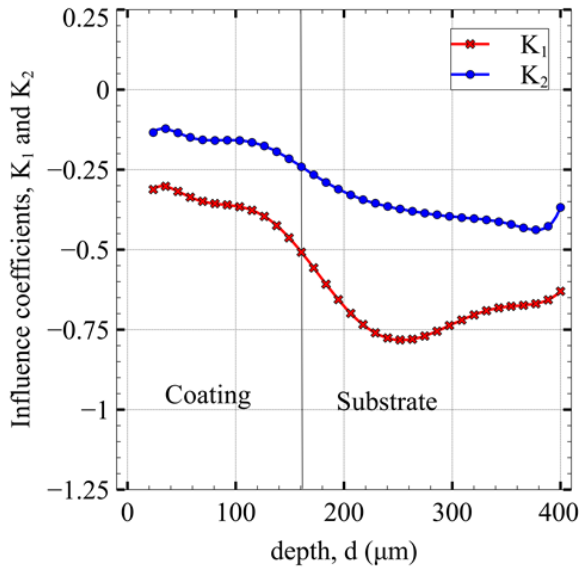


Figure 6-16: Influence coefficients used for calculation of stress profile: (a) Ni-20%Al and (b) TBC

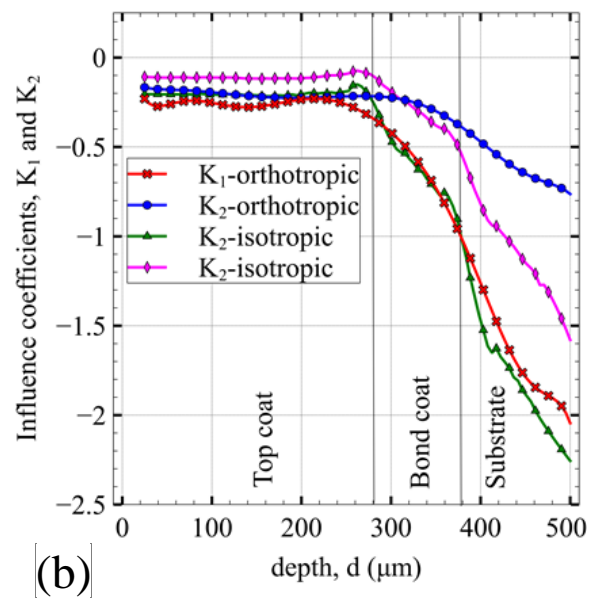
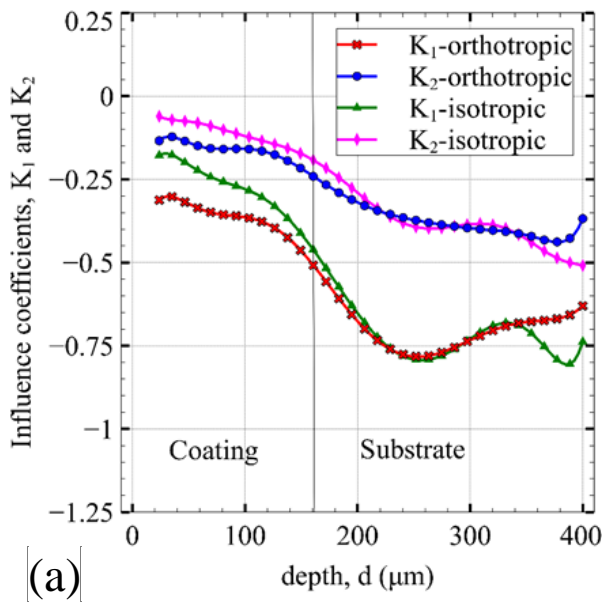


Figure 6-17: Effects of anisotropy on influence coefficients for: (a) Ni-20%Al coating and (b) TBC

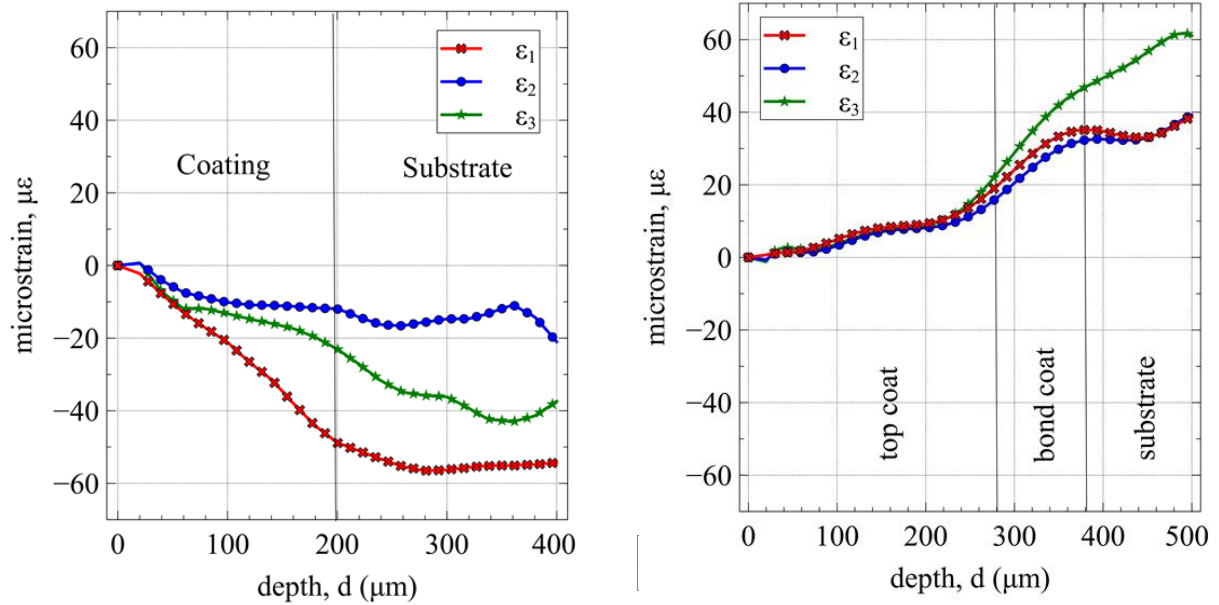


Figure 6-18: Micro-strain readings measured at each drilling increment: (a) Ni-20%Al and (b) TBC

Using the differential method [34], a MATLAB code was used to estimate the variation of residual stress across the depth of the coating layers. The measured micro-strain readings and calibrated coefficients were taken as direct inputs to the code as expressed in Eq. (5.6) - (5.8). Figure 6-19 shows the variation of the in-plane residual stresses across the depth of coating layers. It can be seen from Figure 6-19 (a) that, the in-plane normal stresses developed across the thickness of the Ni-20%Al coating are predominantly tensile and equi-biaxial. Similar results have been previously predicted by Sampath et al. [41] for HVOF sprayed Ni-20%Al coating. The tensile nature of stress state in the coating layer (i.e. around 0 to 200 MPa) is due to severe quenching action during solidification of the metallic splats as well as low compressive stresses attributed to the low structural mismatch between the coating and substrate layers. Similarly, the equi-biaxiality of the in-plane stresses as well as low shear stress state are expected, because the nature of thermal spray deposition is such that impacting droplets deform to form flattened disks (i.e. splats) that solidify from the edges to their centroid at the same rate. Thus, the layer-by-layer deposition of splats structures creates higher tendency for lateral expansion or contraction rather than distortion as discussed in our previous works [185], [186]. For plate-like structures like coatings, the development of very

low residual shear stress is expected. Thus, Figure 6-19 (a) shows that negligible shear stresses are developed within the coating layer. Furthermore, Figure 6-19 (a) shows that the experimental stress profiles predicted for the metallic coatings are comparable to that obtained using popular analytical model by Tsui and Clyne. The quantitative deviations that exist at some depths of the coating layer is due to negligence of temperature-dependence of elastic and plastic properties in the analytical model. Thus, it is expected that the analytical model over-estimates the residual stress profile.

For the TBC layer, Figure 6-19 (b) and Figure 6-20 (b) shows that compressive residual stresses (within range of 0 to -90 MPa) are mainly developed within the YSZ top coat. The compressive state transitioned to low tensile state within the NiCrAl bond coat layer. This is because the bond coat layer reduces the high mismatch in structural properties across the TBC interfaces. The compressive stress state developed within the YSZ layer is because of the low tensile (quenching) stresses and high compressive (mismatch) stresses developed after coating deposition. As previously discussed, the high tensile stresses developed after solidification of ceramic splats are immensely relaxed through emergence of multiple cracks as observed in Figure 6-5. On the other hand, the high compressive mismatch stresses are developed because the YSZ layer has very low elastic modulus and coefficient of thermal expansion (CTE) as compared to the bond coat and substrate layers (previously shown in Figure 6-10). Previously, Li et al. [53] measured the residual stress developed in the YSZ top coat with high energy synchrotron XRD and found that the compressive residual stress developed in as-received TBC sample can reach up to -200 MPa. But in the present study, it is found that the compressive stress does not go beyond -90 MPa. The deviation between the current results and the one that by Li et al. [53] is caused by several limitations of the hole drilling method such as its inability to capture out-of-plane normal residual stresses, its lower resolution which as well as development of additional cutting stresses during drilling. All

these problems are adequately captured by the expensive high energy synchrotron XRD method. Nonetheless, Figure 6-19 (b) and Figure 6-20 (b) shows that the experimental stress profile predicted for the TBC considered here compares very well with that obtained of the Tsui and Clyne analytical model. Furthermore, the results compares well to previous measurements conducted with the hole drilling method [19], [34], [187]. In fact, Valente et al. [34] and Guinard et al.[187] reported compressive stress values of reaching up to -70 MPa in the top coat, while Khan et al. [19] reported around -90 MPa. Also, the stress profile is found to be uniquely equi-biaxial with low shear stress state as observed for the case of the Ni-20%Al coating. Minor fluctuations are caused by the highly inhomogeneous nature of the ceramic top coat layer.

Figure 6-21 (a) and (b) compares stress profiles obtained with incremental strain readings taken at two different locations of the Ni-20%Al coating and TBC. This is done to confirm the established stress trend obtained along depth of coating layers. As previously found by Buchman et al. [65], it can be seen that both coating samples show identical trend of stress profile along depth with minor deviations emanating at several depths. The minor deviations are caused by several reasons such as randomization in coating process parameters (shown in Table 5-1) as well as significant variation in the thickness, surface roughness and density of the coating layer (previously shown in Figure 6-1 to Figure 6-7). Also, the highly non-uniform peening stresses developed during grit-blasting of the substrate layer affects the residual stress profile developed at several locations of the coating layer. Furthermore, Figure 6-21 (a) and (b) shows that the stress profiles developed within the metallic coating layer deviate more than that of its ceramic counterpart. From Figure 6-21 (a), it can be seen that the Ni-20%Al coating could have a standard deviation of 100 MPa at maximum. This is because of occurrence of highly localized plastic deformation during splats deposition. On the contrary, the TBC sample show good repeatability of measurements with minor deviations (at

interface) which is believed to be caused by the role played by plastic deformation of the substrate layer during coating deposition (shown in Figure 6-21 (b)). Thus, the standard deviation is 40 MPa at maximum which compares well to previous estimation by Buchman et al. [65] on alumina (ceramic) coating. Therefore, it can be said that residual stress profiles estimated here are acceptable within limits of hole drilling method. Figure 6-21 (c) and (d) shows the comparison of stress profile computed with orthotropic and isotropic influence coefficients. The TBC is least affected by orthotropy due to its brittle and highly porous nature (shown in Figure 6-21 (d)). Therefore, it can be said that isotropic material model can lead to reasonably accurate stress profile in highly porous and brittle coatings having lower elastic modulus. However, the use of isotropic material model affects the stress profile developed along depth of the Ni-20%Al coating to a large extent, which necessitates the use of orthotropic material model in computation of the influence coefficients for the estimation of residual in metallic coatings.

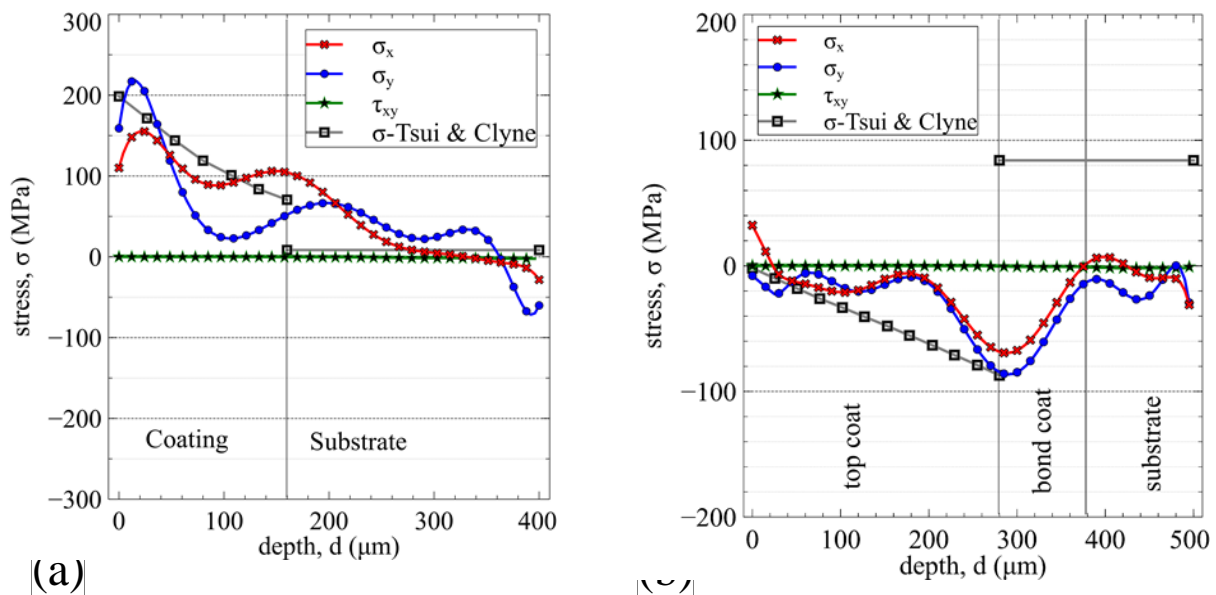
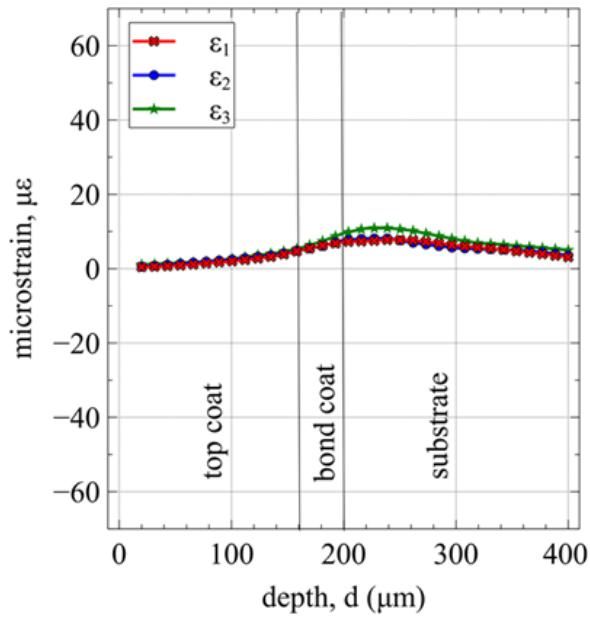
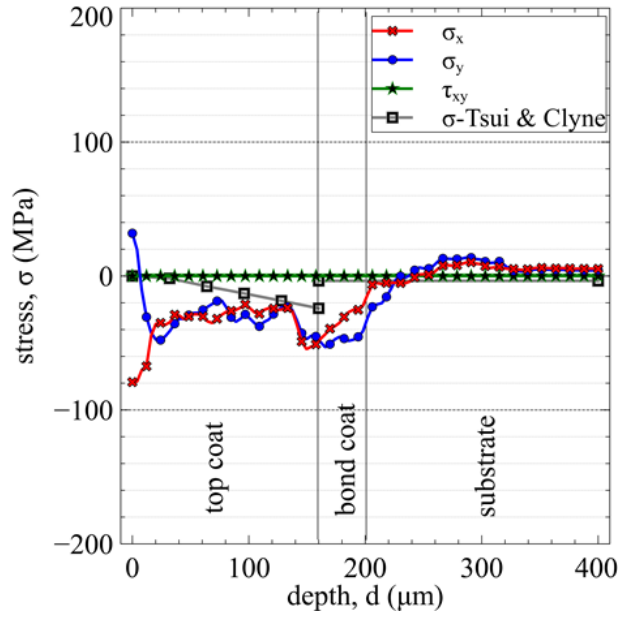


Figure 6-19: Residual stress profile developed along depth: (a) Ni-20%Al and (b) TBC (thick sample)



(a)



(b)

Figure 6-20: Results obtained from thin TBC sample: (a) Incremental strain reading and (b) Residual stress profile

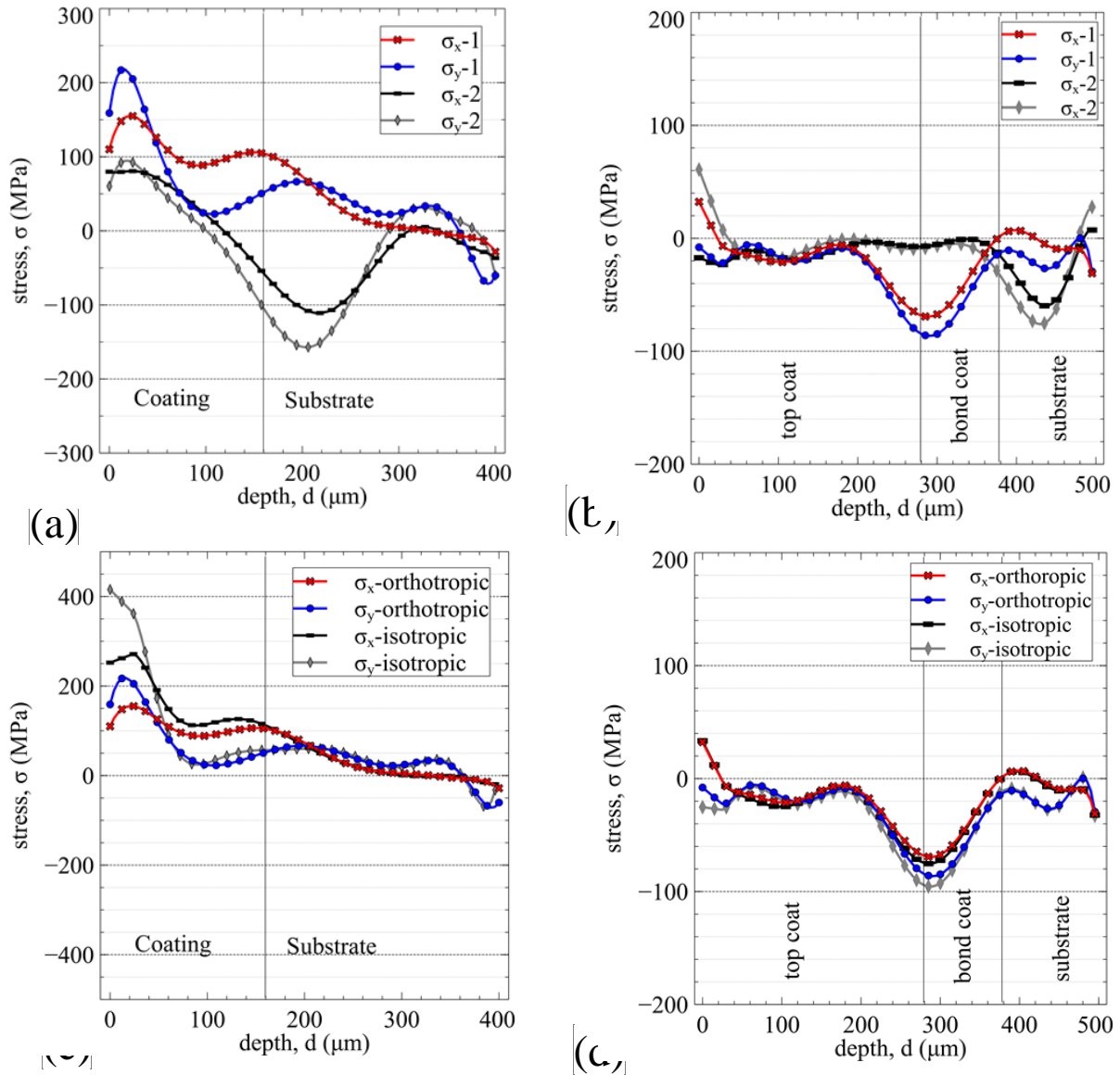


Figure 6-21: Stress profiles developed along depth showing: (a) repeatability for Ni-20%Al coating, (b) repeatability for TBC, (c) influence of orthotropy for Ni-20%Al coating, (d) influence of orthotropy for TBC.

6.4 Cohesive strength of the coatings

Figure 6-22 shows the critical load for the cohesive failure of the selected coatings as obtained from the scratch tests. From the figure, it can be seen that all the coating samples exhibit high cohesive strength. The Ni-20%Al coating has very high cohesive strength of about 26.5 N. Even though tensile residual stress is developed in the Ni-20%Al coating, it has high cohesive strength because it was deposited with a self-bonding powder (i.e. Metco 404NS [168]). On the other hand, the TBC has higher cohesive strength of around 29.5 N.

This high strength is due to the presence of compressive residual stresses within the topcoat layer as well as use of highly structured agglomerated powder that is an aggregate of nanoparticles.

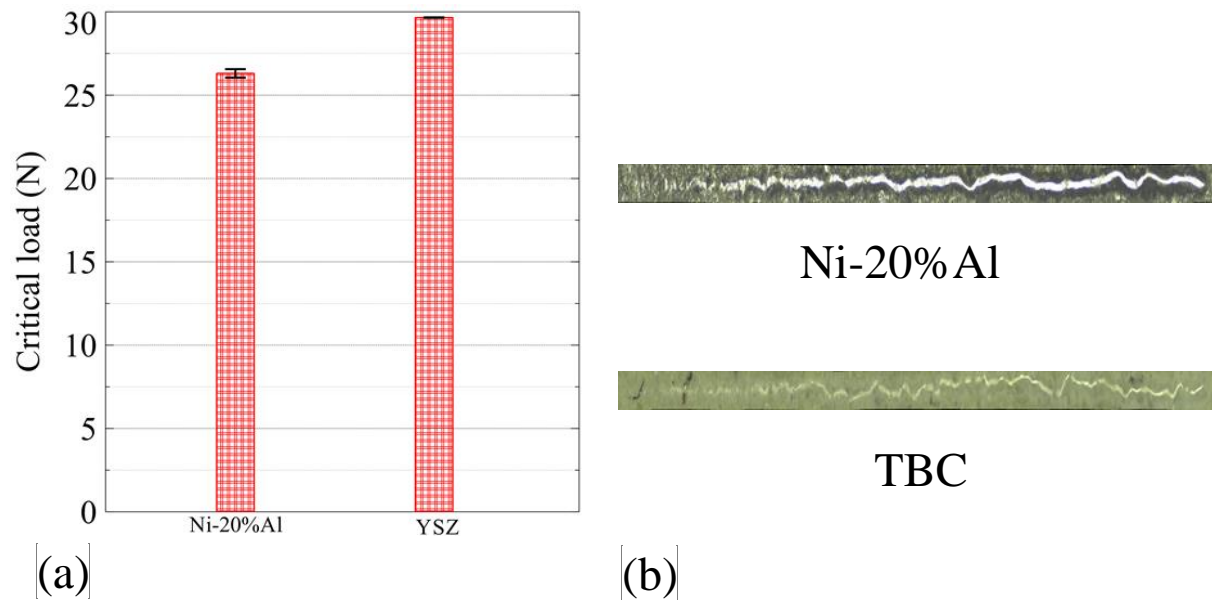


Figure 6-22: (a) critical load required for cohesive failure of coatings, (b) optical micrograph showing scratch track

6.5 Concluding remarks

In the current work, many experimental techniques have been used to collectively study the residual stress profile developed in thermal spray coatings. The coating samples were first characterized by performing various experiments involving optical and scanning electron microscopy, and surface roughness measurement. Then, the effective properties of the coatings were obtained from micro-indentation and scratch test. This detailed characterization and properties estimation enabled effective interpretation of the residual stress profile developed along the depth of coating layers. The residual stress profiles were estimated using the hole drilling method based on the differential method. The residual stress profiles were validated by comparing with results available in literature and the one obtained using the popular Tsui and Clyne analytical model. The following conclusions can be derived from the study:

1. The metallic Ni-20%Al coating has lower porosity, fewer micro-cracks and higher effective elastic modulus as compared to other coating material considered here. They mainly contain elongated pores.
2. The YSZ top coat have higher porosity, more micro-cracks and lower effective elastic modulus. They mainly contain globular and near-spherical pores as well as higher hardness due to their brittle nature.
3. The residual stress profile developed along depth of coating layers is highly non-linear, position-dependent as well as equi-biaxial. However, it was found that the stress profile results in a repeatable trend.
4. The metallic Ni-20%Al coating develop tensile residual stresses because of severe plastic deformation occurring during splats solidification (or quenching) as well as the low structural mismatch occurring between the coating and substrate layers.
5. The YSZ top coat develops compressive residual stress profile due to tensile stress relaxation and high structural mismatch between the coating and substrate layers. The stress profile was also found to fluctuate due to highly inhomogeneous nature of the topcoat layer.
6. As impacting droplets deform to form flattened disks or layers during thermal spraying, very low shear stresses are developed within the coating layers as expected.
7. The residual stress profile developed along depth strongly affects the cohesive strength or integrity of the coating layer. However, other properties related to diffusion kinetics and chemical compatibility equally play an important role in coating failure.

CHAPTER 7

SINGLE SPLAT ANALYSIS

In the present study, the hybrid computational approach is used to numerically predict temperature distribution and residual stress developed during deposition of single yttria-stabilized zirconia (YSZ) and Ni-20%Al droplets on stainless steel (SS310) substrate. The aim of the study is to assess the quality of results obtained with the hybrid approach and optimize its computational accuracy and efficiency. The work presented here has been published in Surface and Coatings Technology [185].

Firstly, discussion is made about the use of point cloud model to simulate single droplets impact and deformation on flat substrate. Based on results obtained from parametric study, investigation about the influence of common spray process parameters (such as droplet impact velocity, temperature and size) on splat formation is made. This is followed by demonstration of conversion from point cloud to finite elements with the use of point cloud processing algorithms previously discussed in Chapter 4. Finally, extensive discussion about the evolution of temperature and residual stress during splat solidification and post-deposition cool down is made. The predicted residual stress field developed in the single splats is validated by comparing with experimental and numerical results available in the literature.

7.1 Splat formation on point cloud

In the following sections, the point cloud model is used to study the phenomenon of splat formation (from inflight to final state) during deposition of single droplets.

7.1.1 Validation of point cloud deposition model

In order to validate the point cloud model, several test cases involving the impact of YSZ droplets were run and compared to results obtained from previous models/experiments. The single YSZ droplet considered for this study has initial size of 30 μm , initial impact temperature of 3000°C and several impact velocities. The droplet is deposited on stainless steel substrate having initial (pre-heated) temperature of 700°C. For the metallic droplet, a 54 μm size Ni-20%Al droplet having an impact temperature of 1455 °C and several impact velocities is sprayed on stainless steel substrate that is preheated to 400°C. It is found that, for the single droplet impact, numerical results converge with point cloud containing less than 212073 particles. Conventionally, results of droplet impact analysis are studied using the spread factor (i.e. ratio of splat diameter to droplet diameter). Figure 7-1 shows that variation of spread factor with initial impact velocity for the YSZ (ceramic) droplet. As shown in Figure 7-1, higher initial impact velocity results in higher splat spread factor, larger diameter and smaller thickness. It can also be seen from Figure 7-1 that, the spread factor and spreading time predicted with the current deposition model is comparable to that of Coupled-Eulerian-Lagrangian (CEL) approach [164] and previous experiments [188]. At high impact velocities, slight deviation exists between the current results and that of CEL due to the underestimation of the spread factor by meshless (SPH) scheme. Nevertheless, the SPH scheme is more feasible for numerical modeling of thermal spray deposition due to its high computational efficiency. The SPH scheme can even capture even more complex phenomenon like fluid splashing, satellite droplets, and fingers that are commonly encountered during the spray process (as shown in Figure 7-3). Similarly, Figure 7-2 shows the deformation of Ni-20%Al (metallic) droplet upon its impact onto a preheated stainless-steel substrate at 400°C. It can also be seen that the deformation pattern and spreading time of the Ni-20%Al droplet (after impact) is comparable to that of experiments and numerical

prediction by volume-of-fluid (VOF) method [189]. In all cases, the computational time (for single droplet) takes less than 10 minutes; using 30 cores of Intel processor, 56 GB RAM, and 2.0 GHz Dell workstation. Therefore, it is more feasible and suitable to model thermal spray process using point cloud (SPH) deposition model due to high computational efficiency.

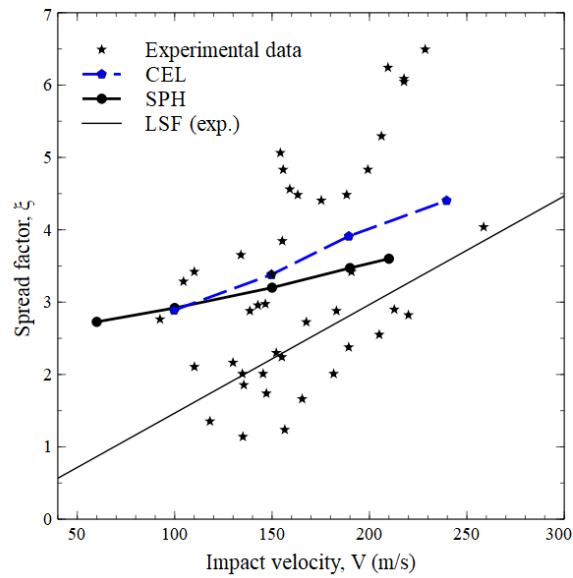


Figure 7-1: Comparison of spread factor variation with initial impact velocity for YSZ droplet as predicted by SPH (current results) and CEL/experiment (by Zhu et al. [164])

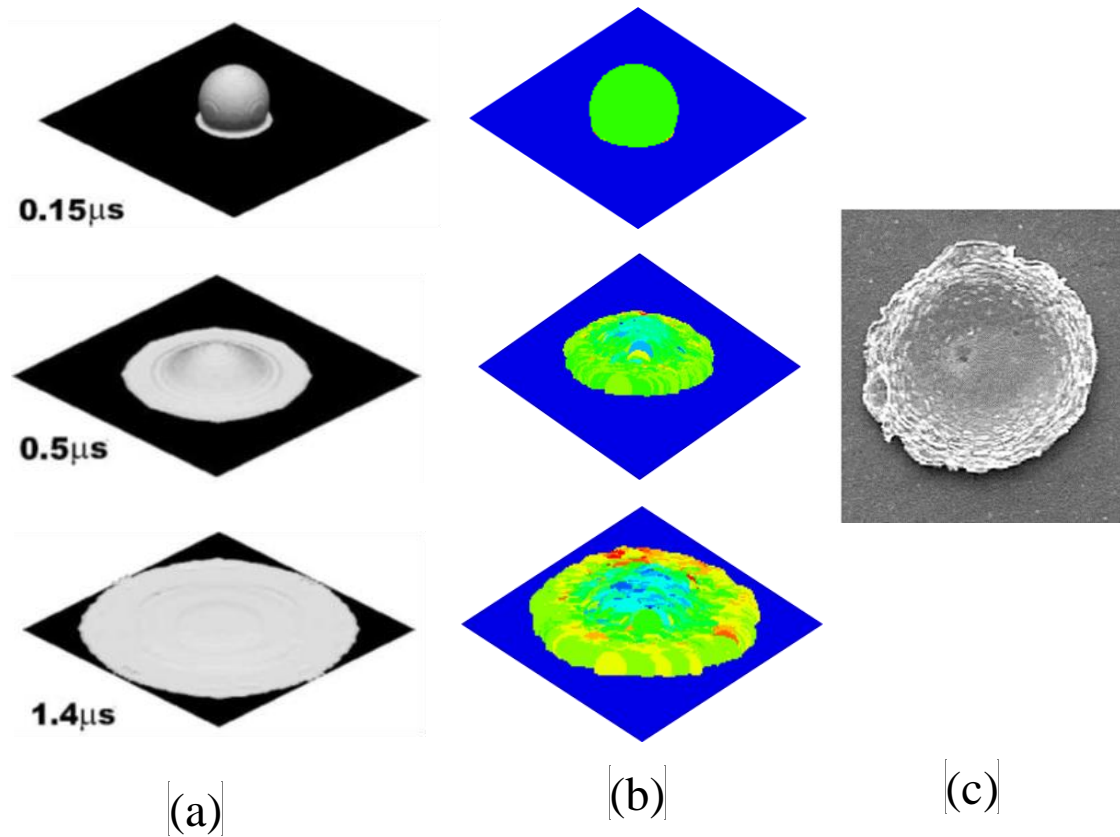


Figure 7-2: Ni-20%Al droplet deposited with initial impact velocity of 100 m/s obtained with: (a) volume of fluid (VOF) method [189] (b) current deposition model, (c) experiments (only final splat geometry shown) [189]

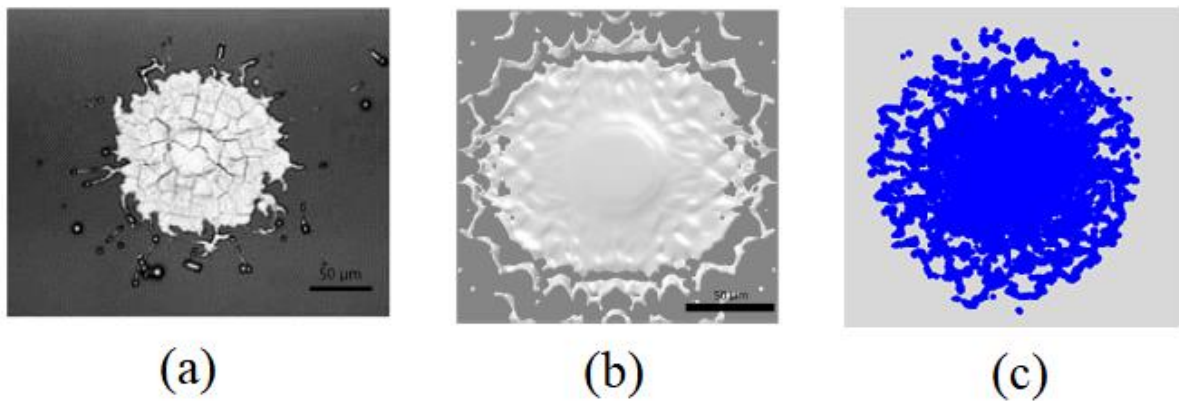


Figure 7-3: Qualitative comparison of results for YSZ droplet deposited with high initial impact velocity of 190 m/s; (a) experiments [188], (b) CEL model [164], (c) current SPH model.

7.1.2 Single droplet deposition

Using the point cloud deposition model, the impact and deformation of single YSZ and Ni droplets on stainless steel substrate has been simulated. The YSZ droplet is deposited with an initial impact velocity of 60 m/s, diameter of 30 μm, and temperature of 2535°C. Figure 7-4

shows the 3D deformation of the YSZ droplet from where it can be seen that the deformed shape of the impacting droplet is symmetrical and resembles the usual disk-like splat structure encountered during thermal spray process. As shown in the Figure, the droplet spreads-out during deformation until reaching the maximum spread factor. Figure 7-5 shows the evolution of velocity field magnitude (in 2D) during droplet deformation. As expected, a drastic reduction in velocity magnitude is observed from the initial value of 60 m/s to upon impact. During droplet spreading, it is observed that the magnitude of velocity field developed at the edges of the deformed droplet is higher than that developed at the center. Similar observation is made in Figure 7-6, which shows the evolution of velocity magnitude during deposition of Ni-20%Al droplets. Figure 7-7 shows that droplet spreading stops after reaching the maximum spreading factor. For the YSZ droplet, it stops after reaching the spreading factor of 2.3 (i.e. around 2.2 μ s). This corresponds to splat diameter and thickness of 69.75 μ m and 9.4 μ m respectively. While the Ni droplet stops after reaching maximum spreading factor of 2.7 (i.e. around 1.4 μ s). This corresponds to splat diameter and thickness of 159 μ m and 20.9 μ m respectively. In both cases, the size and shape of the splat compare well to that of previous studies. For APS process, the impact energy of droplets is considerably low and results in insignificant peening action. Thus, peening stresses are not displayed in the present analysis. However, it will be interesting in future works to use the proposed approach to consider the peening stresses as they significantly affect densification and residual stress distribution in coatings deposited by high energy process such as high-velocity-oxygen-fuel (HVOF).

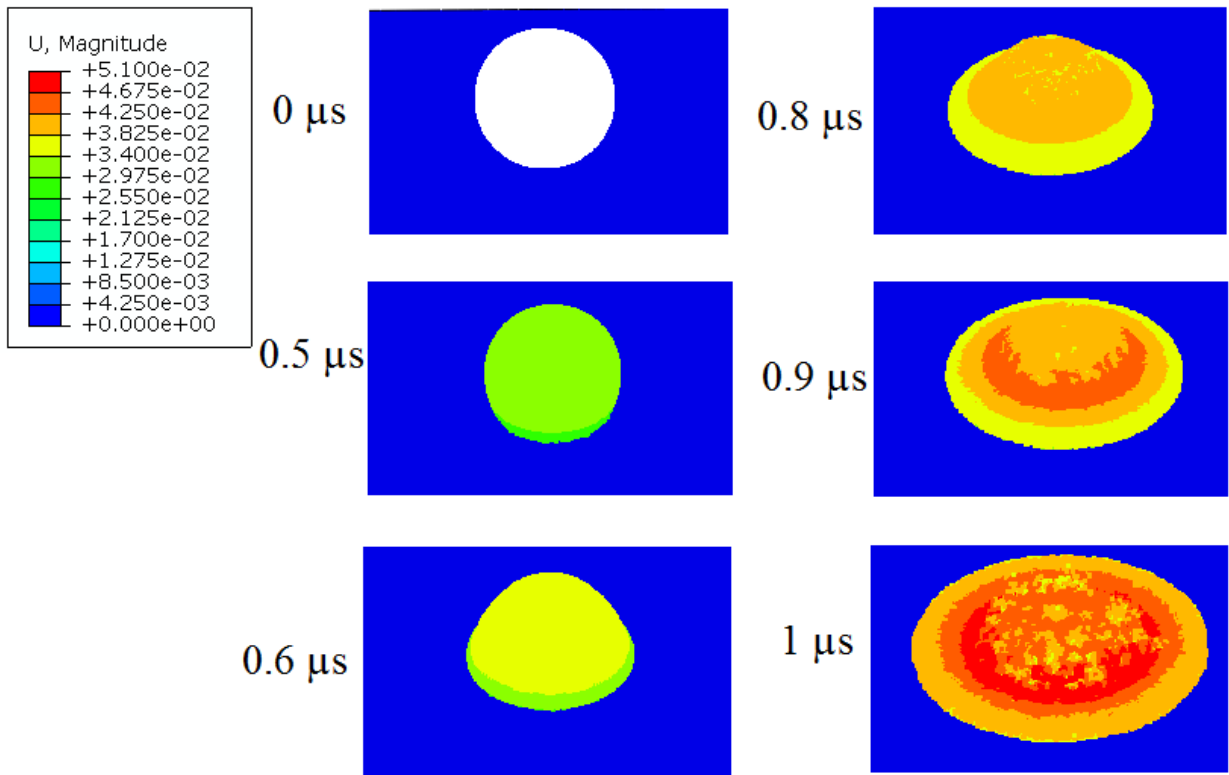


Figure 7-4: 3D displacement of YSZ droplet (mm) deposited with an initial impact velocity of 60 m/s

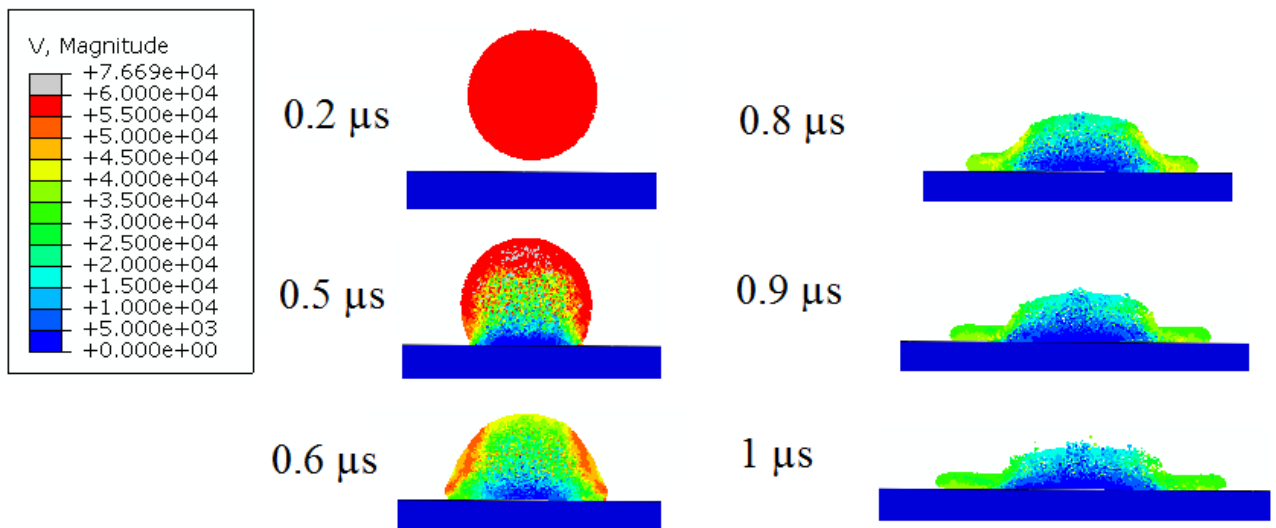


Figure 7-5: Velocity magnitude (mm/s) during deformation of YSZ droplet (in 2D) with initial impact velocity of 60 m/s

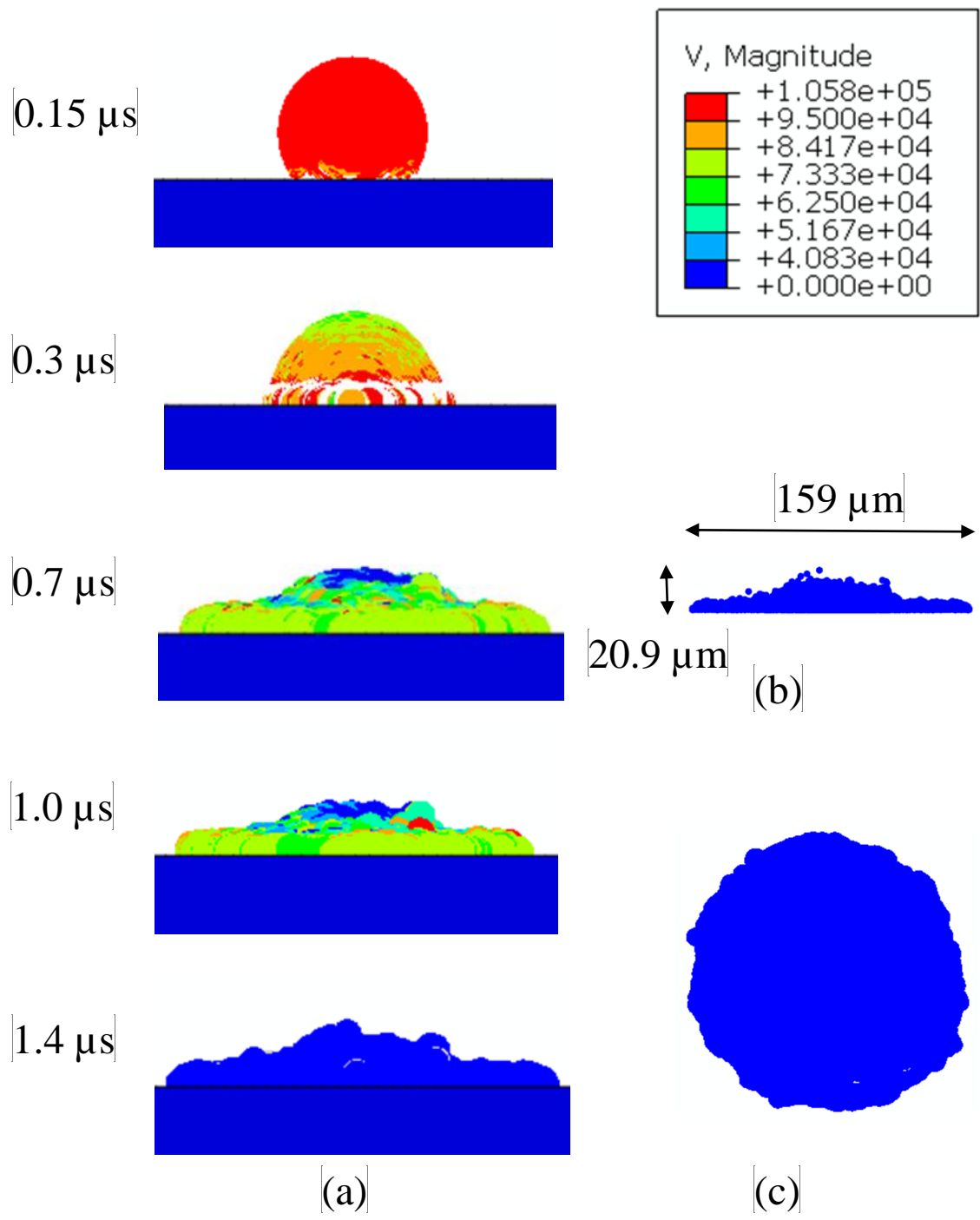


Figure 7-6: Splat formation process at various spreading time for Ni-20%Al droplet: (a)-(b) Side view, (c) top view

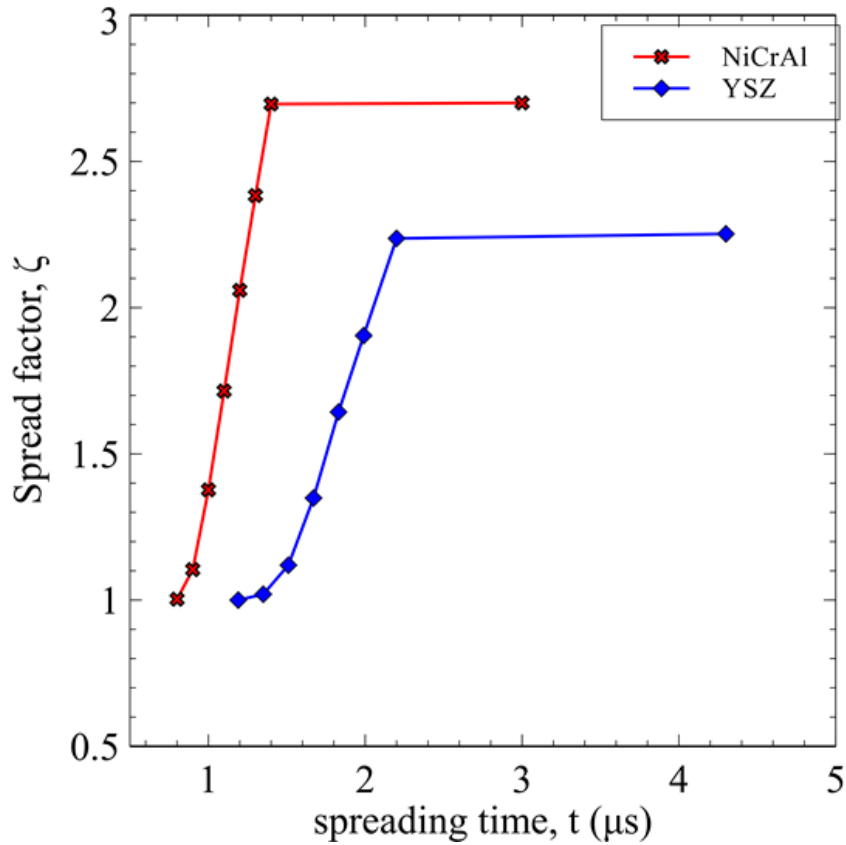


Figure 7-7: Temporal variation of maximum spread factor for the Ni-20%Al I and YSZ droplets considered in Fig. 24 and Fig. 25.

7.1.3 Effect of process parameters on splat formation

The prominent (process) parameters affecting the droplet deposition process are: droplets initial diameter, droplets impact velocity, droplets impact temperature, spray angle, spray path, and undulation of the target surface. In the present section, only discussion about the influence of initial droplet properties (i.e. size, impact velocity, and temperature) will be made. The influence of other factors is discussed in subsequent chapters as it is more relevant to multiple droplets deposition.

With all parameters being constant, the spread factor (i.e splat-to-droplet diameter ratio) may not significantly change with increase/decrease in initial droplet size. Even though, the size and shape of deposited splats are different for droplets of different sizes. Thus, larger droplets

result in thicker and wider splats, and vice versa. Smaller droplets often result in high porosity as they may not fit well into the various gaps, pores and rough substrate surface. On the other hand, larger droplets result in highly dense microstructure as it fit smoothly into all gaps (or voids) and undulation of the rough surfaces.

On the contrary, droplet initial impact velocity and temperature have an influence on the spread factor as demonstrated by Figure 7-8. Figure 7-8(a) shows that, for 60 μm YSZ droplet, increase in droplet impact velocity (or spray rate) results in significant increase in spread factor (or splat diameter) and decrease in splat thickness. However, as latent heat of fusion of YSZ is very high and its specific heat capacity is low, the droplet impact temperature does not have considerable effect on the Stefan number. This implies that the impact temperature has little effect on splat geometry. Consequently, the deposition model is calibrated to account for the minor influence of temperature using previous semi-empirical model [156]. This has tremendously saved computational time and memory. Similar trend is observed in Figure 7-8(b), it is shown that the spread factor (for the 54 μm Ni droplet) is strongly dependent on the impact velocity. However, the influence of impact temperature on the spread factor is more pronounced for the Ni droplet due to improved thermal properties. For metallic coatings, high peening (compressive) stresses are developed at high impact velocity.

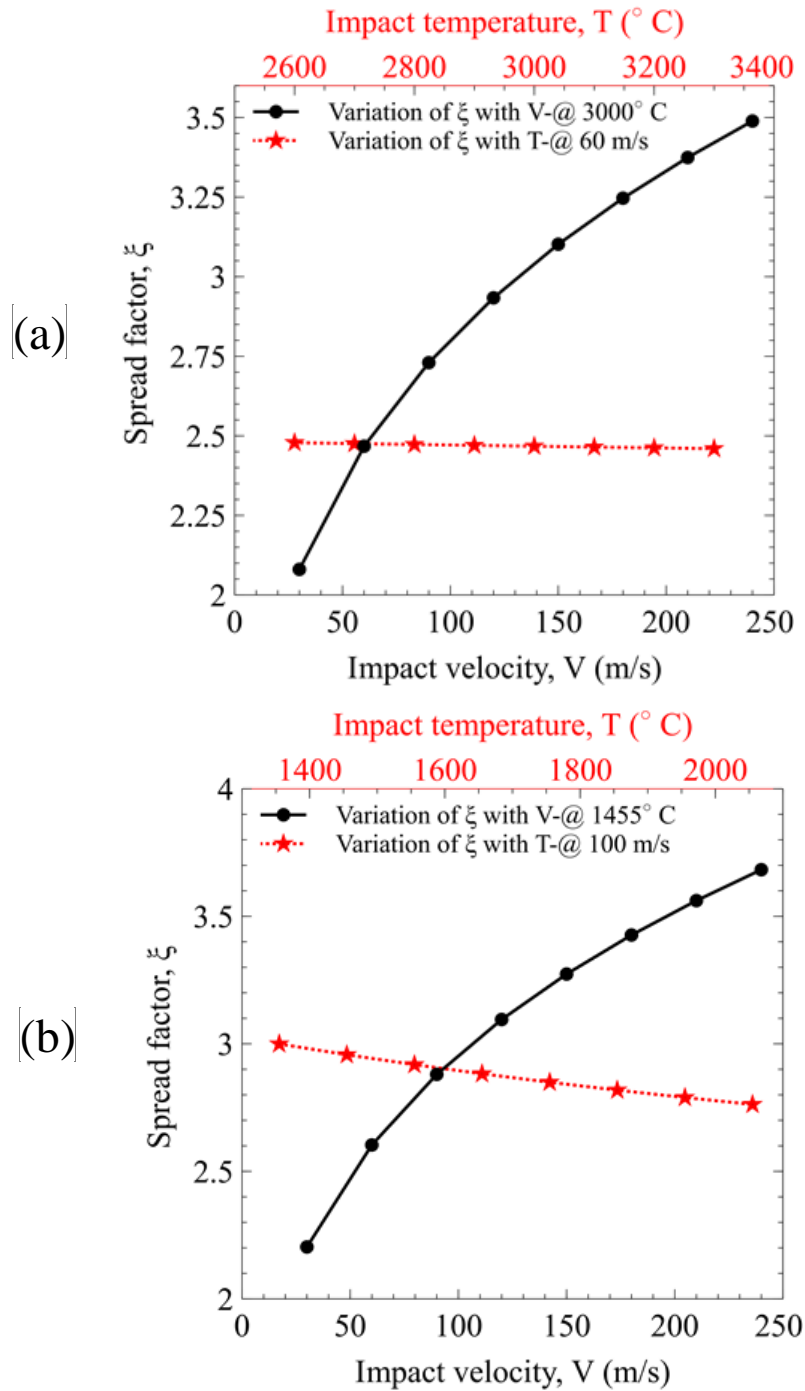


Figure 7-8: Influence of droplet impact velocity and temperature on spread factor for (a) 60 μm size YSZ droplet, (b) 54 μm size Ni droplet

7.2 Geometric modeling of splats

Using the point cloud deposition model, the splat formation process is adequately simulated. However, the point cloud data obtained at the last time step of deposition modeling need to be reconstructed into 3D FE mesh required for thermo-mechanical analysis. Due to the

intricate nature of splat geometry, the splat domains are meshed with tetrahedral elements using procedures discussed in section 4.2.2. Each splat domain is meshed with the required number of elements that will enable effective stress prediction at optimal computational cost. The average time required for the conversion is about 45 minutes per splat using 32 cores/64 GB RAM/2 GHz Dell workstation. It is found that the current process of converting the point cloud data into FE mesh works well for all type of splats regardless of how intricate their geometry might be as demonstrated in Figure 7-9 and Figure 7-10.

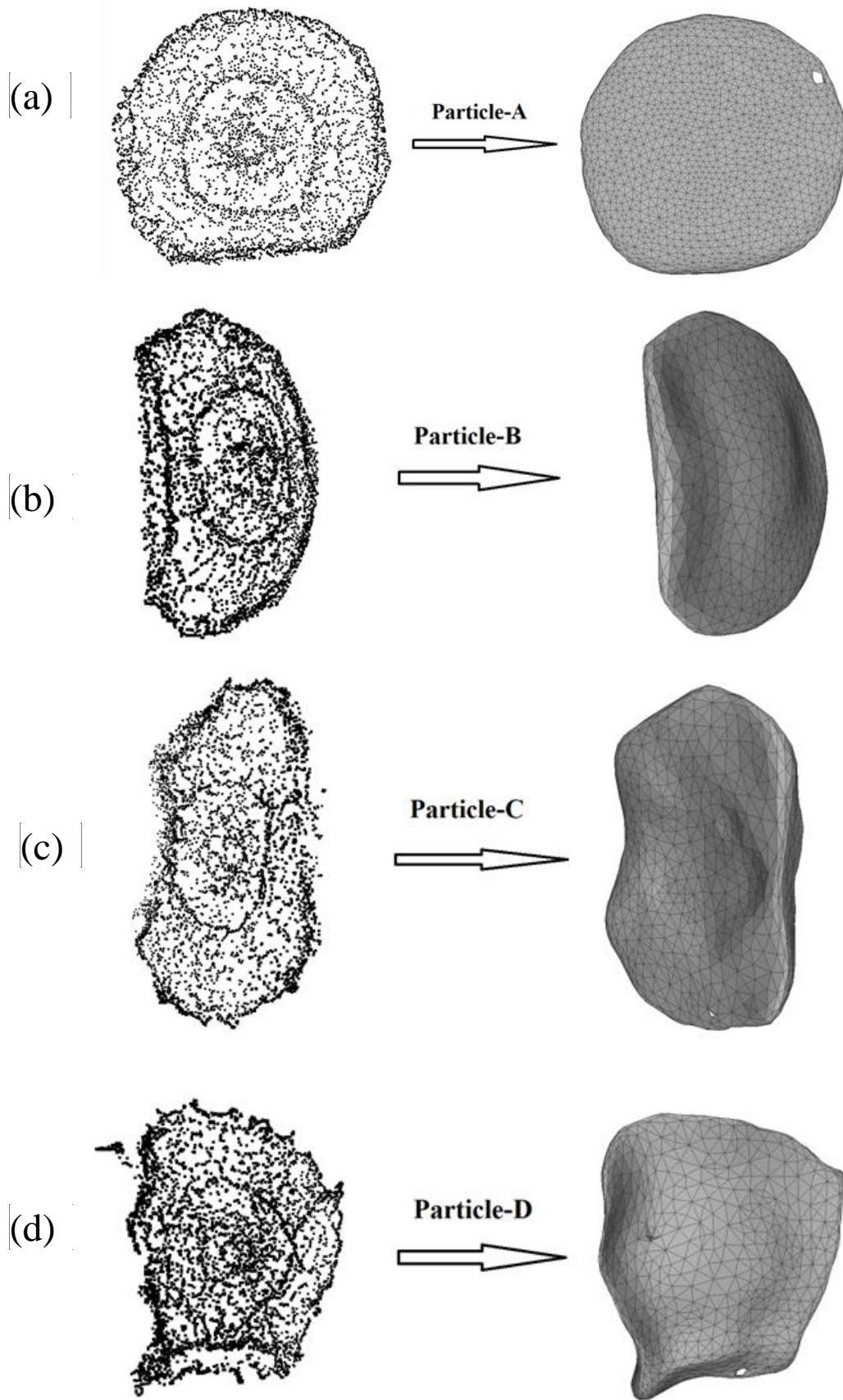


Figure 7-9: PC-to-FE mesh conversion for splats ((a)-(d)) of intricate shapes

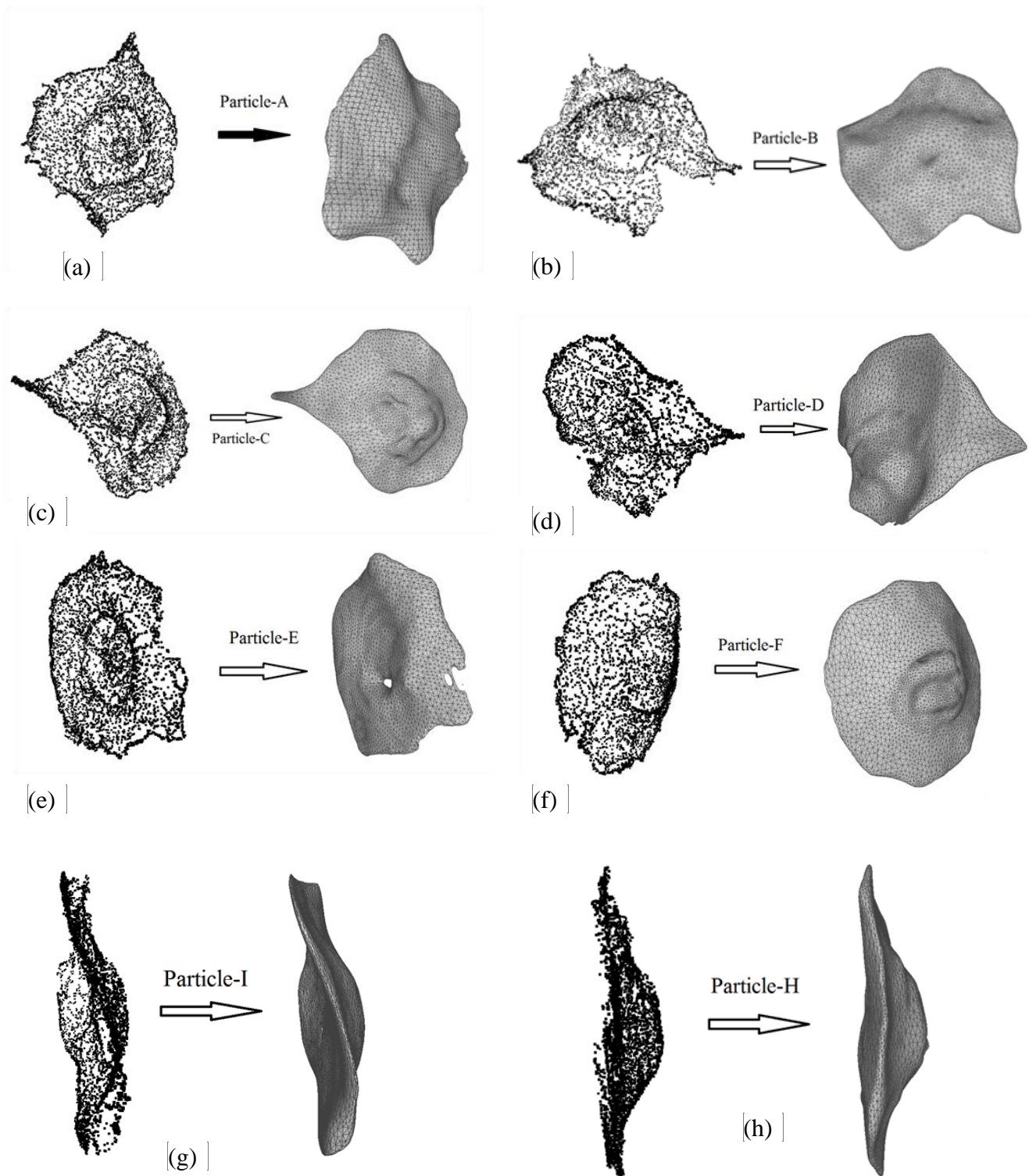


Figure 7-10: Conversion from PC-to-FE mesh for several splat geometries having various geometrical complexities

7.3 Thermo-mechanical analysis using FEM

7.3.1 Validation of numerical model

For the finite element model, several tetrahedral element sizes and time stepping settings are used to study the convergence and efficiency of the model. For simplicity, only the results obtained from two mesh sizes are presented here (as shown in Figure 7-11). Due to the nature of splats geometries, it is ensured that each splat contains a sufficient number of elements (only about 5-9 nodes) along its thickness to achieve numerical convergence of results at a less computational cost. To reduce computational costs further, automatic time stepping settings are used in all cases. As compared to the post-deposition regime, smaller time steps are used for the prediction of temperature and stresses developed during deposition. It can be seen from the Table 7-1 that, the maximum temperature and 1st principal stress values computed with the coarse mesh (consisting of around 11,725 elements) is reasonably close to that of the fine mesh (consisting of around 23428 elements) with considerable savings in computational time. Furthermore, the soft zone is defined to have a more considerable temperature difference (between solidus and liquidus point) of about 10 °C to reduce the numerical difficulties/costs associated with numerical modeling of phase change process with negligible effect on the results accuracy. Figure 7-12 has confirmed the convergence of numerical results where a negligible difference is observed in the values of temperature distribution and stress field developed along the axial and radial directions of the splat. Specifically, Figure 7-12 (c) and (d) shows that the deposition (quenching) stress field obtained with the explicit-dynamic FE scheme is very comparable to that of implicit-static FE schemes. The explicit scheme is more suitable for numerical prediction of the

deposition stresses due to the highly dynamic and nonlinear nature of thermal stresses developed during splat solidification. Implicit-static FE schemes often lead to prolonged simulation time due to convergence difficulties associated with the sharp variation in temperature during splat solidification. However, it was necessary to optimize the computational efficiency of the explicit scheme using mass scaling, an approach where the simulation run time is reduced by increasing the density of the (smallest) elements controlling the stable time increment. By tracking the variation of kinetic and internal energy during the analysis (shown in Figure 7-13 (a)), it is found that the results obtained with the default automatic mass scaling option of ABAQUS/Explicit are acceptable. This resulted in a simulation that is 3 times faster than that of an unscaled or sequential implicit model without compromise on results quality. It can be seen from Figure 7-13 (a) that, the kinetic energy is only a small fraction (less than 10%) of the internal energy throughout the explicit analysis. As demonstrated in Table 7-1, the computation of temperature and deposition stresses using the segregated solver, in which both energy and stress equations are solved simultaneously with weak coupling terms, is more efficient than the explicit scheme. This is because the problem is solved with sequential coupling without the need for reading temperature values (from an external file) at each increment.

As splat size falls within the microscale, it is not currently feasible to experimentally predict the temperature distribution and localized stresses developed during deposition of single splat. However, we found that the temperature distribution and solidification time of a single splat are in good comparison with that of previously discussed numerical models by Alavi et al. and Zhang et al. [163], [190]. To account for stress relaxation by microcracking and interfacial sliding in ceramic coatings, the deposition stresses are

calibrated to be low and tensile based on previous experimental data obtained by Shinoda et al. [191]. Upon cooling the coating to room temperature, additional high compressive (mismatch) stresses are developed. Consequently, the residual stress field developed within the ceramic layer is compressive as previously predicted both experimentally and numerically by Wu et al. [101] for thick YSZ coating. The values of residual stress predicted here falls within -100 to -150 MPa which qualitatively compares well to recent experimental results by Sebastiani et al. [178] for 30 μm alumina splat deposited on steel substrate at 200 °C. Sebastiani et al. predicted higher stress values (i.e., 200 to -300 MPa) for micro-cracked single (alumina) splat using FIB ring-core drilling within SEM chamber in conjunction with FEM analysis. Being more brittle than alumina, the YSZ splat is expected to develop lower compressive residual stresses as predicted by the current model. Further verification of the current results is done by comparing with that of previous analytical (elastic) model by Tsui and Clyne [99]. The analytical model was solved using coating and substrate elastic properties (given in Table 4-1), deposition (quenching) stress of 30 MPa and geometrical dimensions adopted for the simulation. It can be seen from Figure 7-13 (b) that, the residual stress profile compares well to that of the analytical model with minor deviations due to the necessary assumptions adopted in deriving the analytical model. Thus, the current results are in proper comparison to that of previous numerical and experimental studies.

Table 7-1: Mesh convergence test and analysis of computational time for single droplet analysis

	Thermal analysis				Structural analysis		
Stage	Mesh	C_t (min s)	T_{max} (°C)	Δt (s) Average (Min/Max)	C_t (mins)	σ_{p1} (MPa)	Δt (s) Average (Min/Max)
Deposition	Fine mesh ¹	386	2284	1.21×10^{-7} ($1 \times 10^{-13} / 1 \times 10^{-6}$)	5865	33.8	5.05×10^{-12} ($1.03 \times 10^{-12} / 8.96 \times 10^{-10}$)
	Coarse mesh ²	68	2284	2.81×10^{-7} ($1 \times 10^{-13} / 1 \times 10^{-6}$)	580	35.1	4.52×10^{-11} ($3.03 \times 10^{-11} / 1.22 \times 10^{-10}$)
	Explicit ²⁻¹						
	Implicit ²⁻²	68	2284	2.81×10^{-7} ($1 \times 10^{-13} / 1 \times 10^{-6}$)	1560	33.1	2.09×10^{-7} ($3.41 \times 10^{-13} / 4.12 \times 10^{-6}$)
	Weakly coupled ²⁻³	-	2284	-	470	33.3	1.52×10^{-6} ($1 \times 10^{-8} / 6.45 \times 10^{-6}$)
	Coarse mesh ³	27	2234	1.81×10^{-7} ($1 \times 10^{-13} / 6 \times 10^{-6}$)	270	47	1.52×10^{-9} ($1.03 \times 10^{-10} / 1 \times 10^{-9}$)
Post-deposition	Fine mesh ¹	72	25.2	4.05 ($1 \times 10^{-4} / 10$)	120	168	3.05 ($1 \times 10^{-4} / 10$)
	Coarse mesh ²	3	25.5	3.91 ($1 \times 10^{-4} / 10$)	160	162	2.68 ($1 \times 10^{-4} / 10$)
	Implicit ²⁻²						
	Weakly coupled ²⁻³	3	25.5	-	240	162	2.68 ($1 \times 10^{-4} / 10$)
	Coarse mesh ³	1	26.8	3.05 ($1 \times 10^{-4} / 10$)	180	140	3.05 ($1 \times 10^{-4} / 10$)
<p>1-Fine mesh: has 23,428 tetrahedral elements with 1.85 and 8.84 as average and worst aspect ratios respectively 2-Coarse mesh: has 11,725 tetrahedral elements with 1.93 and 11.23 as average and worst aspect ratios respectively 3-Coarse mesh: has 5,726 tetrahedral elements with 2.37 and 15.71 as average and worst aspect ratios respectively 2-1-Sequentially coupled explicit thermal analysis with automatic time stepping 2-2- Sequentially coupled implicit thermal analysis with automatic time stepping 2-3-Weakly coupled implicit thermal analysis with segregated solver dropping stress coupling terms *Substrate domain has about 169,787 high-quality triangular elements</p>							
<p>C_t -computational time, $\Delta T = 10$ °C; difference between solidus and liquidus temperature, T_{max} - maximum temperature, σ_{p1} -the maximum value of 1st principal stress, Δt -time step</p>							

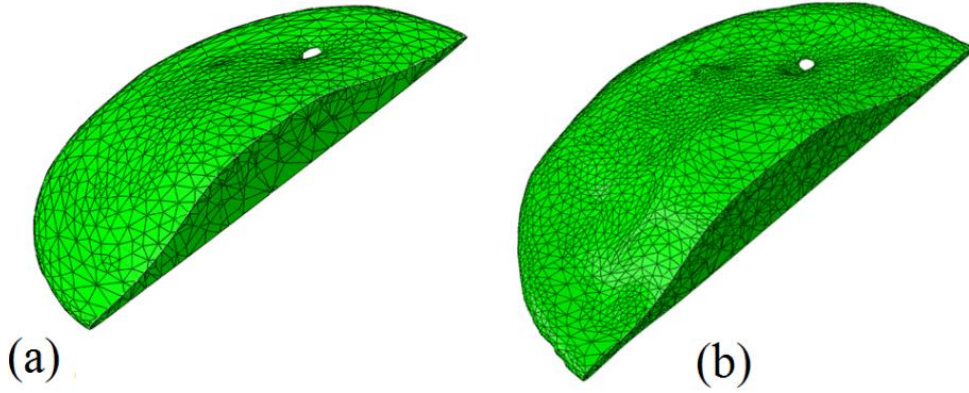


Figure 7-11: (a) Coarse mesh and (b) Fine mesh of single splat (sectional view)

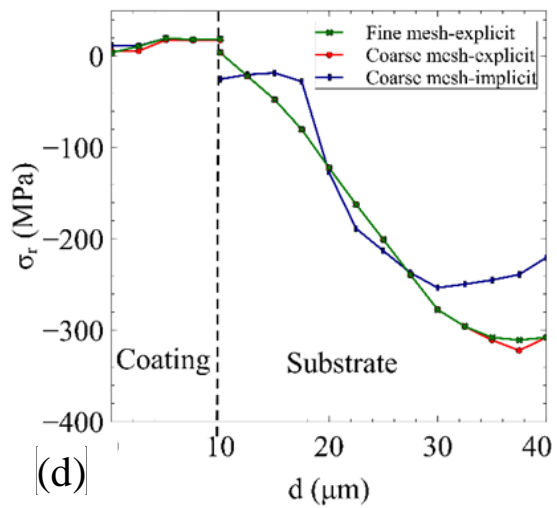
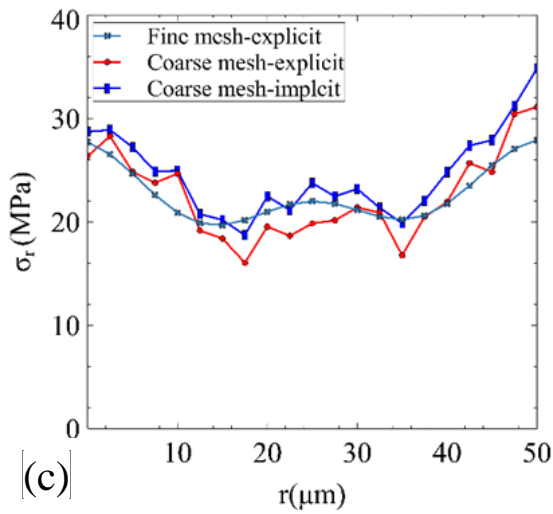
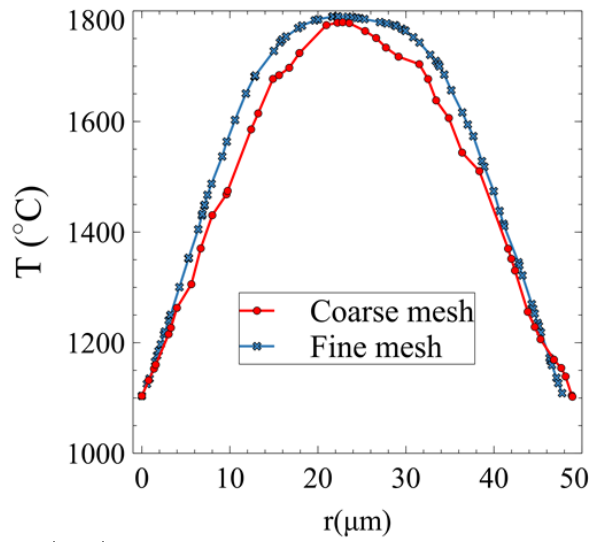
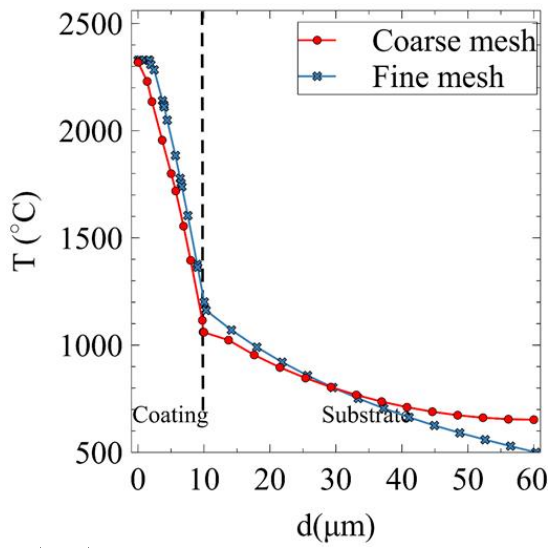


Figure 7-12: Convergence of numerical results: (a)-(b) temperature & (c)-(d) deposition stress

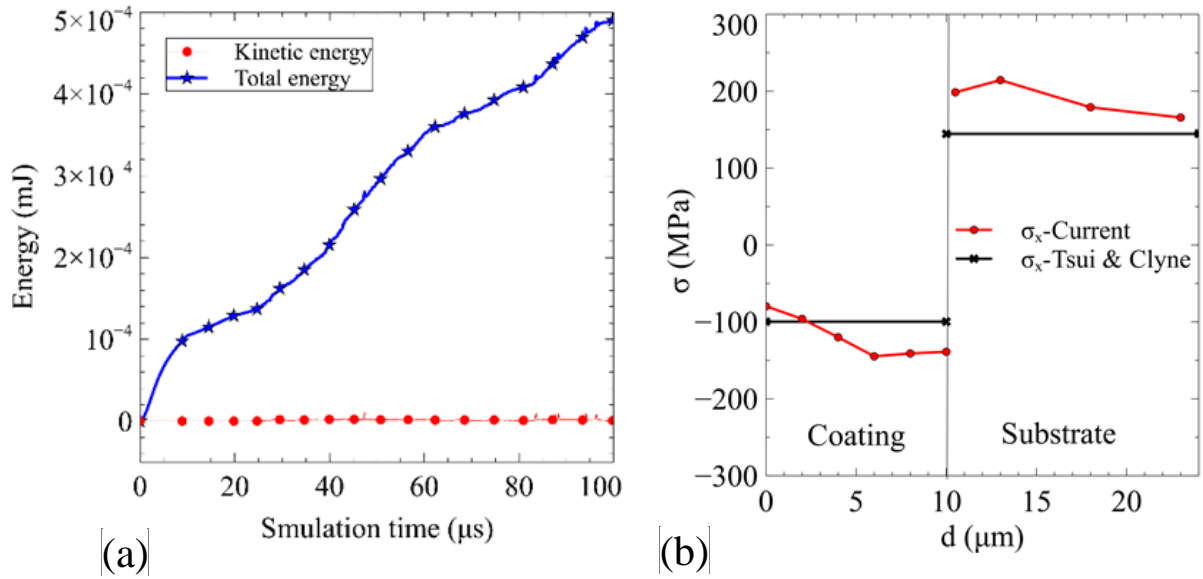


Figure 7-13: (a) variation of system energy with time & (b) comparison of stress profile to that of the analytical model

7.3.2 Numerical prediction of temperature distribution and residual stress field developed in single YSZ splat without consideration of microcracks

In this section, an elastic-perfectly plastic material model is used to predict residual stress developed in single YSZ splat deposited on stainless steel (SS310). High thermal stresses developed during splat solidification relax to a large extent through excessive microcracking attributed to thermal shock. Therefore, the use of an elastic-perfectly plastic model is necessary to restrain stresses to realistic values as measured experimentally. The results are discussed and compared with that of previous findings.

Using FEM, thermo-mechanical analysis has been carried out for the single splat deposit. Because of symmetry, the results of temperature distribution and residual stress field can

be explained in 2D with two axes (r, z) for the cylindrical coordinate system. Figure 7-14 (a) shows the temperature distribution developed during splat solidification. Heat lost by the splat domain is mainly through conduction; thus, the latent heat release during solidification immensely influence the temperature distribution within both splat and substrate. Figure 7-15 (a) shows the temperature profile developed along the depth of splat at its centroid. It can be seen from the figure that, the initial temperature of splat (about 2535 °C) approaches that of the substrate material (about 700 °C) due to solidification and heat conduction to the substrate. Also, the steep temperature gradient is developed at the coating-substrate interface due to the significant difference in initial temperatures of the coating and substrate. It is found that the solidification time of the YSZ splat is around 80 μ s which is within the typical range for ceramic oxides. This not only compares well with that of previous works but also confirms the common assertion that splat solidification time is two orders of magnitude higher than the droplet spreading time [101], [118]. Figure 7-15 (b) shows the temperature profile developed along the radial axis of splat at around 3 μ m above the substrate surface. Like the velocity field, it can be seen that the temperature profile is symmetrical along the radial direction due to nature of initial splat shape and its contact to the substrate. Also, it takes more time for the splat to solidify at thicker splat regions (i.e., close to the centroid) as compared to the thinner sections close to the edges. This is due to lower solidification rates in thicker regions. Figure 7-16 (a) shows the temporal variation of temperature at three points located at different locations on the surface of the splat. It can be seen that the temperature history of the three points differs considerably. This leads to variation in residual stress state of the coating at various regions of the splat. Therefore, the

temperature distribution predicted by the present model qualitatively captures the phase change process occurring during the typical thermal spray process.

Using the results of nodal temperature, thermal stresses were determined at each time step. Due to the nature of coating deposition, in-plane stresses and normal out-of-plane stress have considerably higher magnitudes as compared to other stress components. Thus, during our discussion, the emphasis is given to those stress values. Figure 7-15 (c) and (d) shows the radial (quenching) stress profile developed along the axial and radial directions respectively. It can be seen that, the variation of radial quenching stress along the radial direction is symmetrical and the overall trend looks similar to that of temperature profile displayed in Figure 7-15 (b). As calibrated using experimental data by Shinoda et al. [191], the deposition stress is tensile with reduced stress values ranging from 0 to 30 MPa depending on temperature and locations. The low stress values are due to stress relaxation in the ceramic material by microcracking and interfacial sliding as discussed previously. Thus, the calibration of the deposition stress to low stress values is currently necessary to account for these uncontrolled (or difficult-to-predict) processes. From the figures, it can be seen that the tensile stresses are lower near free surfaces such as top face and edges as expected. The low tensile stresses developed near the interface are due to high compressive stresses developed on the substrate side. Upon cooling the coating and substrate layers to room temperature, the coating develops compressive residual stresses (as shown in Figure 7-17). This is due to high mismatch in structural properties (e.g., CTE, elastic modulus, etc.) of the YSZ coating layer as compared to the stainless-steel substrate. Compressive stresses are helpful as they improve the coating adhesion strength. It is found that about 100 MPa and 150 MPa of compressive residual

stresses are developed at the surface and interface of the splat respectively. It can also be seen from Figure 7-17 (a) that, the compressive residual stresses developed at the near-interface region of the coating are balanced by corresponding tensile stresses developed on the substrate side. This high difference in stress values at the interface roughly indicates how good adhesion strength of the coating is. Consistent with common observation in the literature [29], Figure 7-17 (b) shows that equi-biaxial residual stress field is developed in the coating layer. Furthermore, higher compressive stresses are developed at the edges of the splat than at the center due to the thinness of the edges. Figure 7-16 (b) shows that the residual stress developed at the three different points (considered in Figure 7-16 (a)) are markedly different due to differences in their thermal history. Thus, temperature evolution plays a vital role in determining residual stress distribution in thermal spray coatings. Figure 7-18 shows the 3D residual stress field developed within the coating and substrate. The symmetrical nature of the stress field can be confirmed further from the 3D plots presented in Figure 7-18.

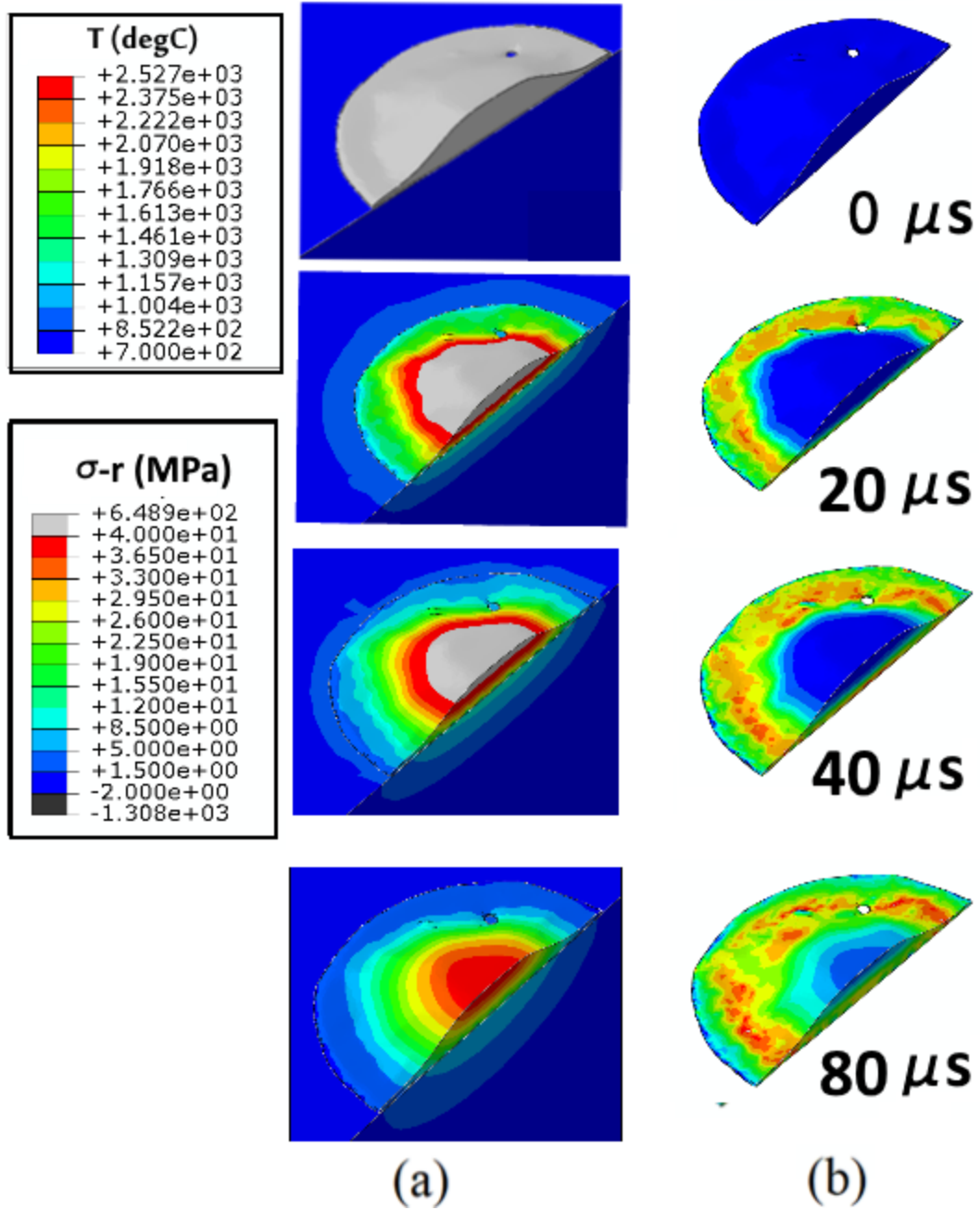


Figure 7-14: (a) Temperature evolution ($^{\circ}$ C) and (b) quenching stress (MPa) evolution during splat solidification

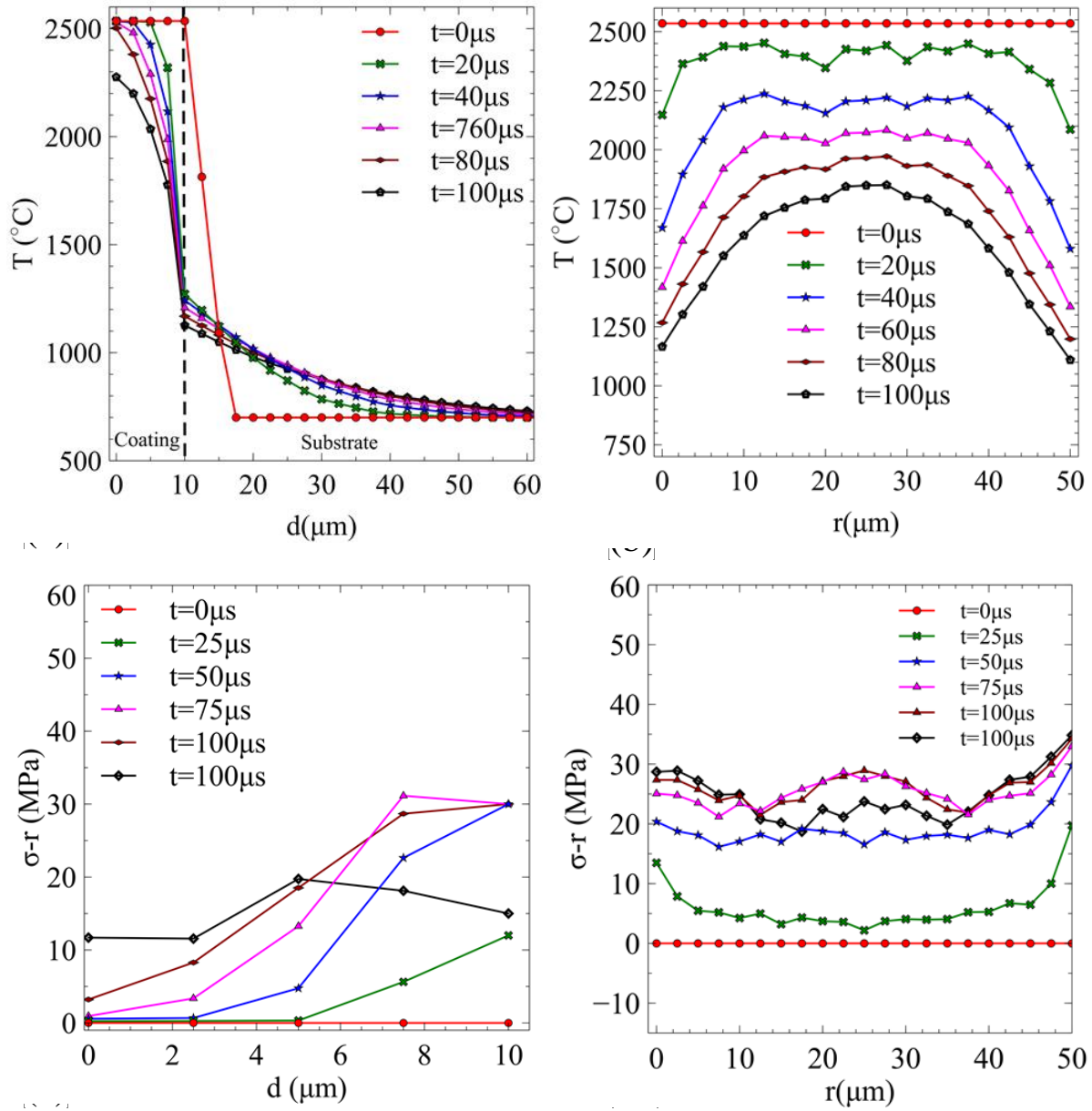


Figure 7-15: (a) temperature profile along depth at centroid, (b) temperature profile along radial direction at 3 μm above the surface of the coating, (c) radial deposition stress variation depth at the centroid, (d) radial deposition stress variation along the radial direction at 3 μm above the surface of the coating

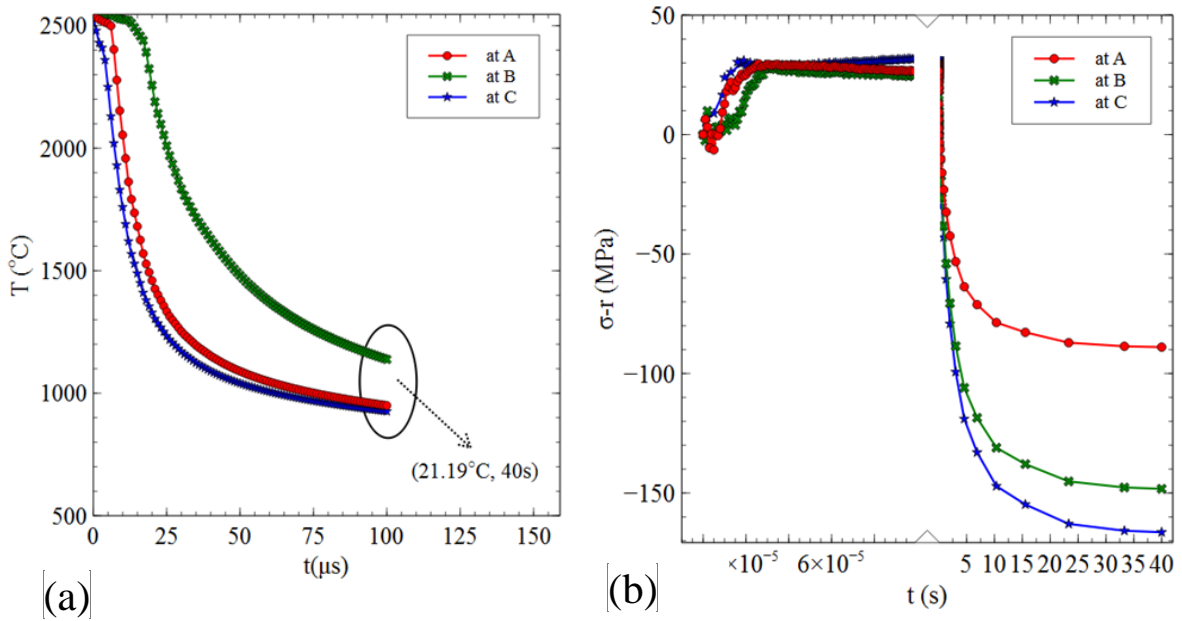


Figure 7-16: Temporal variation of (a) temperature, (b) stress at three points, A, B and C

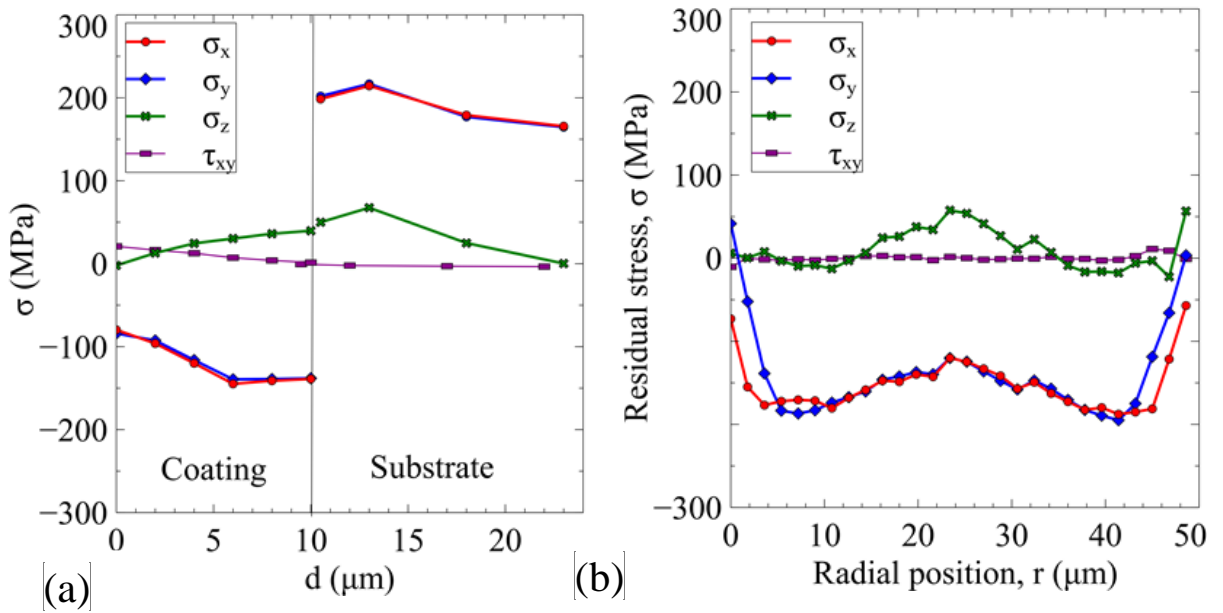


Figure 7-17: (a) Residual stress profile along the axial direction, (b) Residual stress along the radial direction

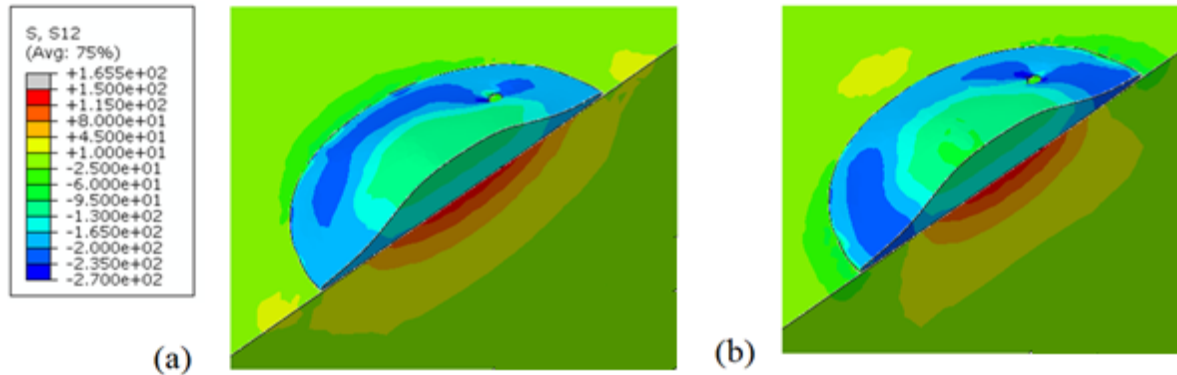


Figure 7-18: Residual stress developed in (a) x-direction and (b) y-direction for single splat analysis

7.3.3 Numerical prediction of temperature distribution, residual stress field and cracks formation in single YSZ splat

In section 7.3.2, an elastic-perfectly plastic material model was used to numerically predict residual stress in single YSZ splat deposited on stainless steel (SS310). The use of elastic-perfectly plastic model is necessary in order to restrain the development of unrealistically high stress values attributed to the brittle and stiff nature of YSZ ceramic. The high thermal stresses developed during quenching relax to a large extent through excessive microcracking caused by thermal shock. Therefore, in this section, a more realistic material model (i.e. the ceramic microcracking model) is used to model the thermo-mechanical behavior of the single YSZ splat. The same simulation parameters as that of the elastic-perfectly plastic model case are used for the analysis. The results are discussed and compared with that of previous findings.

Figure 7-18 shows the temperature distribution, quenching stress field, and microcracks formed after solidification of YSZ splats. It can be seen that, temperature of the YSZ splat, initially at 3000 °C, drops substantially as a result of conductive heat transfer to the

substrate. Thus, during heat transfer, temperature of the substrate rises continuously from 700°C up to about 1300°C. As compared to the elastic-perfectly plastic case, YSZ splat takes longer time (about 300 μ s) to fully solidify due to the obvious presence of microcracks. As expected, the cracked elements (denoting empty space) act like insulators due to their low thermal conductivity. Thus, more heat is entrapped within the cracked splat. Figure 7-18 (b) and (c) shows the quenching stress field and corresponding microcracks developed in the YSZ splat. The quenching stress field is represented in absolute form (i.e. von Mises equivalent) in order to clearly indicate cracked regions of the coating. According to Equation (4.19), crack initiates within an element when its value of equivalent tensile strain is equal to that of the ultimate cracking strain of the ceramic material (i.e. about 0.004). The cracks propagate in the direction of maximum principal strain as commonly adopted for ceramic materials. The stiffness of cracked elements diminishes to zero according to equation (4.18). Consequently, the quenching stress field predicted here have numerical values ranging from 0 to around 500 MPa depending on location within the splat. It is found that crack propagation stops after full solidification of the splat. Therefore, there is no visible difference between the contour plots of damage parameters at 300 μ s and 2000 μ s (as shown in Figure 7-18 (c)). Using the microcracking model, it is found that cracks initiate from the splat edges due to high stress concentration. Then, it propagates towards the center as previously observed experimentally [183]. Also, it is shown from Figure 7-18(c) that, the model captures through-thickness crack propagation which was previously observed from microscopic studies presented in Chapter 6. This indicates the robustness of the FE mesh reconstructed with the hybrid computational approach. As the simulated splat domain is

slightly thicker than that of Figure 7-20 (c), slight discrepancy occurs between the SEM image and simulated splat in terms of crack intensity and splat thickness. This is because the experimental splat was deposited at higher droplet impact velocity.

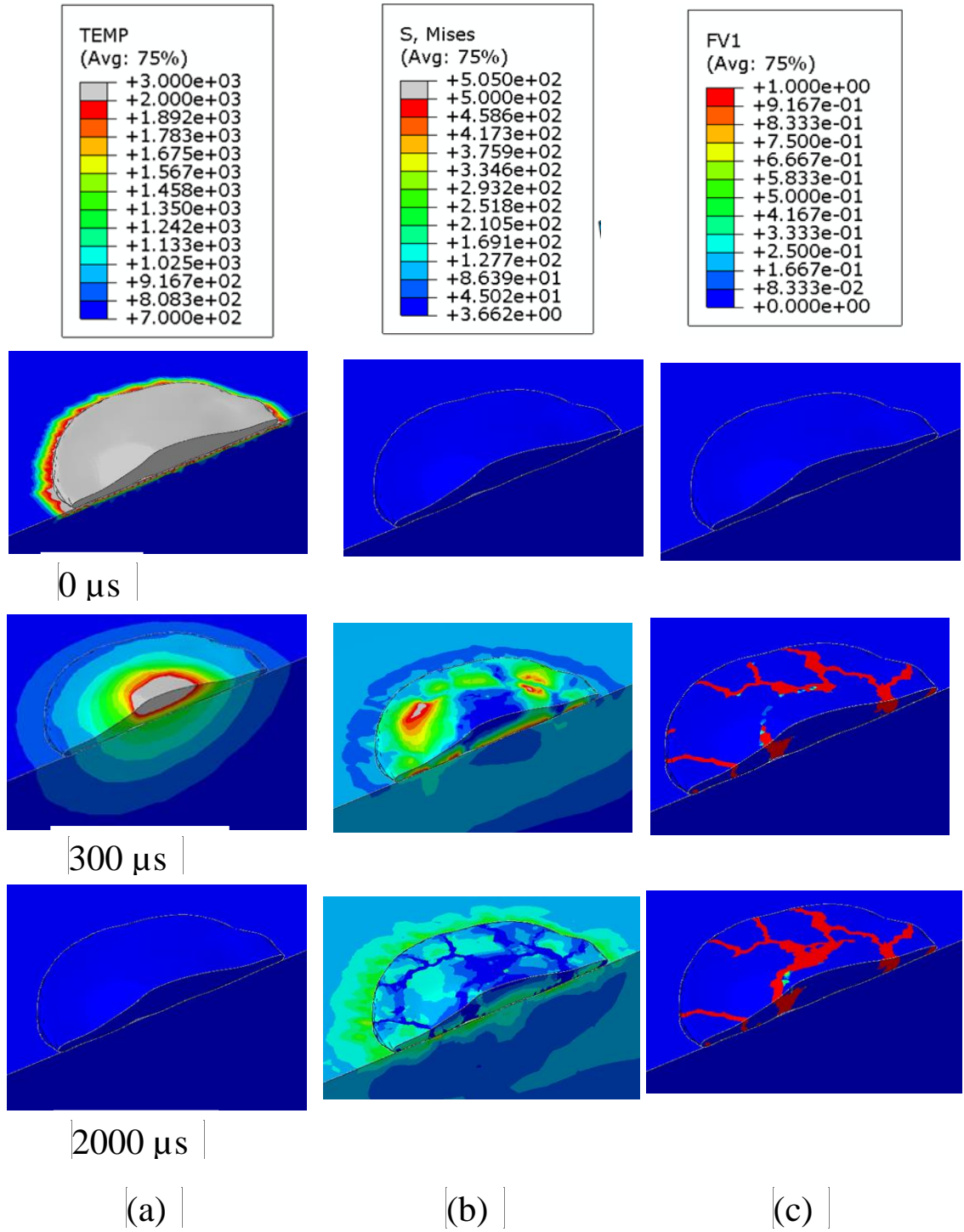
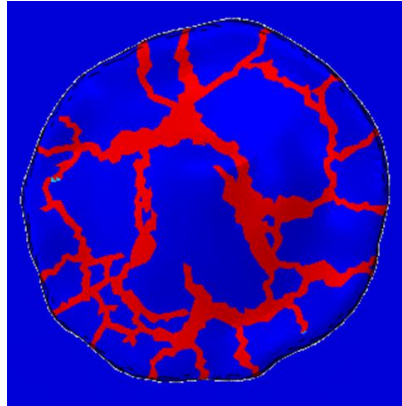
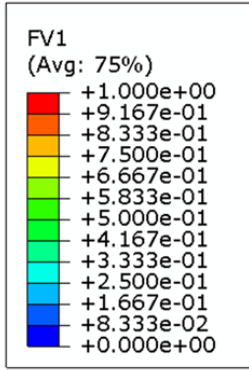
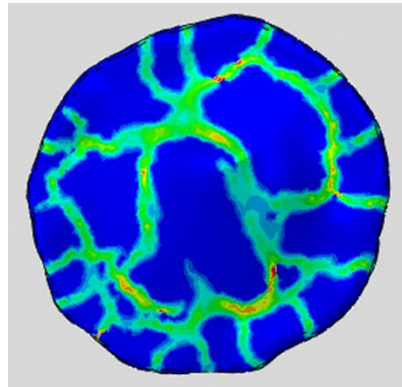
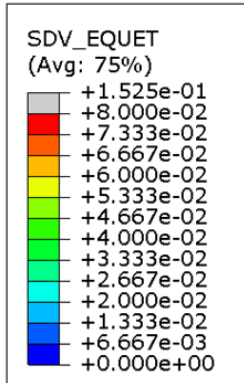


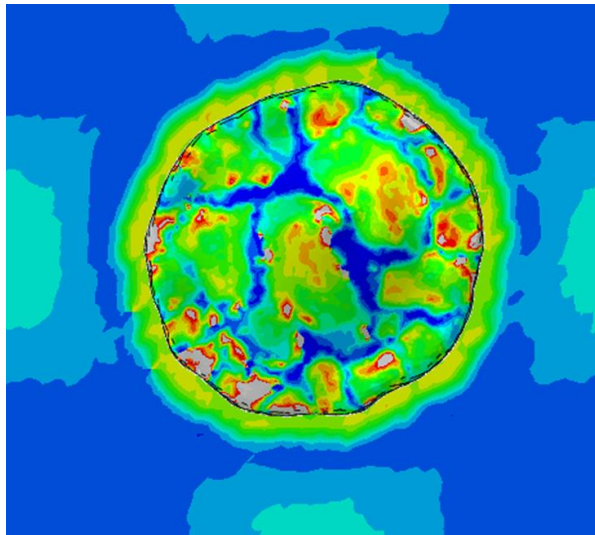
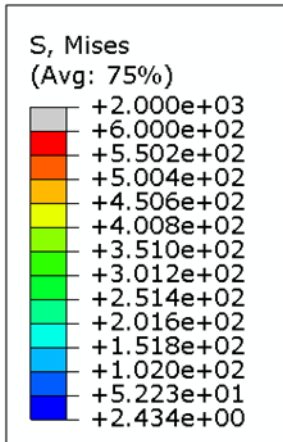
Figure 7-19: Cross section view of YSZ splat showing evolution of (a) temperature (°C), (b) von Mises quenching stress (MPa) and (c) damage parameter at 0, 300 and 2000 μs



(a)



(b)



(c)

Figure 7-20: Top view of splat showing final state of splat at room temperature: (a) cracked YSZ splat, (b) equivalent tensile cracking strain, and (c) von Mises residual stress

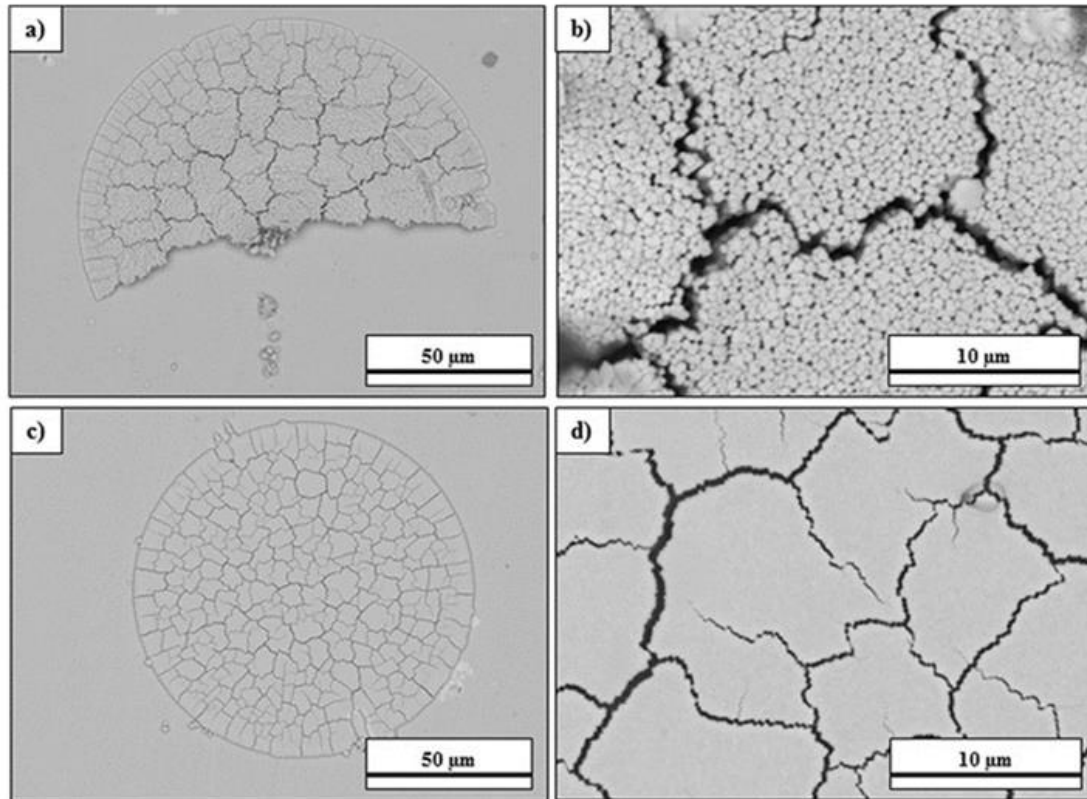


Figure 7-21: SEM images of cracked YSZ splat deposited on SS310 showing: (a) & (b) spalled splat deposited at low substrate temperature, (c)&(d) well adhered splat deposited at higher substrate temperature [183]

Figure 7-21 (a) shows the temperature profile developed along the radial axis of splat at around 3 μm above the substrate surface. Unlike with the elastic-perfectly plastic model, it can be seen that the temperature profile is not perfectly symmetrical due to presence of microcracks. The asymmetry is more vivid from Figure 7-21 (c) where it can be seen that, the stress fluctuates from near-zero to high tensile stress values. Figure 7-21 (c) also shows that radial stress increases first to high tensile values (of about 250-600 MPa) and then decrease to around 100-250 MPa towards end of deposition. This is due to combined effect of stiffness degradation during micro-cracking and splat supercooling. Figure 7-21 (b) and (c) shows the temporal variation of temperature and quenching stress developed

at three different locations. Due differences in both thermal and strain history, there exist differences in the residual stress developed at the three points (as clearly indicated by Figure 7-21 (c)). Moreover, the temporal variation of maximum principal stress at the three locations (considered in Figure 7-22(a)) is not only different, but also shows that the quenching stress is tensile and residual stress in compressive as observed for the elastic-perfectly plastic case. Therefore, both thermal history and crack formation affects the residual stress state of the coating layer. As expected, very low shear stress is developed in the coating layer as shown in Figure 7-22(b). This is because, thermal expansion and contraction are the predominant mode of deformation for splats deposited with thermal spray process. Figure 7-19 shows top view of the cracked YSZ splat after the coating and substrate are cooled to room temperature. From the figure, it is clearly visible that the cracks predicted with the microcracking model compare well with that of previous experimental work shown in Figure 7-20 (c) and (d) [183].

Figure 7-19(b) shows the equivalent tensile residual strain developed after the YSZ splat is cooled to room temperature. It can be seen that the cracked elements develop strain up to the critical state (i.e. 0.04) and have very low stress due to stiffness degradation as shown in Figure 7-19(c). It will have been more interesting to delete failed elements from the FE mesh to be more consistent with reality. However, the numerical difficulties and discontinuities associated with element deletion have made this task unrealizable.

For the elastic-perfectly plastic case, the residual stress was predicted to be compressive as previously shown in Figure 7-16. However, for the case of microcracking model, Figure 7-22(d) shows that residual stress fluctuates from tensile to zero and compressive state due to the presence of cracks. Specifically, the stress changes from -50 to 200 MPa

and -400 to 400 MPa along radial axis and depth respectively. There is no available information for experimental validation of predicted stress profile within the cracked YSZ splat. However, the values predicted fall within same range as that of recent experimental measurements for single (ceramic) alumina splat by Sebastiani et al. [178]. The present study is the first contribution where a microcracking damage model is used to predict residual stress and micro-cracking deposition of ceramic coating. The model gives detailed insight into the complicated mechanism of residual stress evolution in thermally-sprayed ceramic coatings. This is an important contribution considering the difficulties and uncertainties involved in experimental measurement residual stresses developed in ceramic coatings as previously discussed in section 2.2.

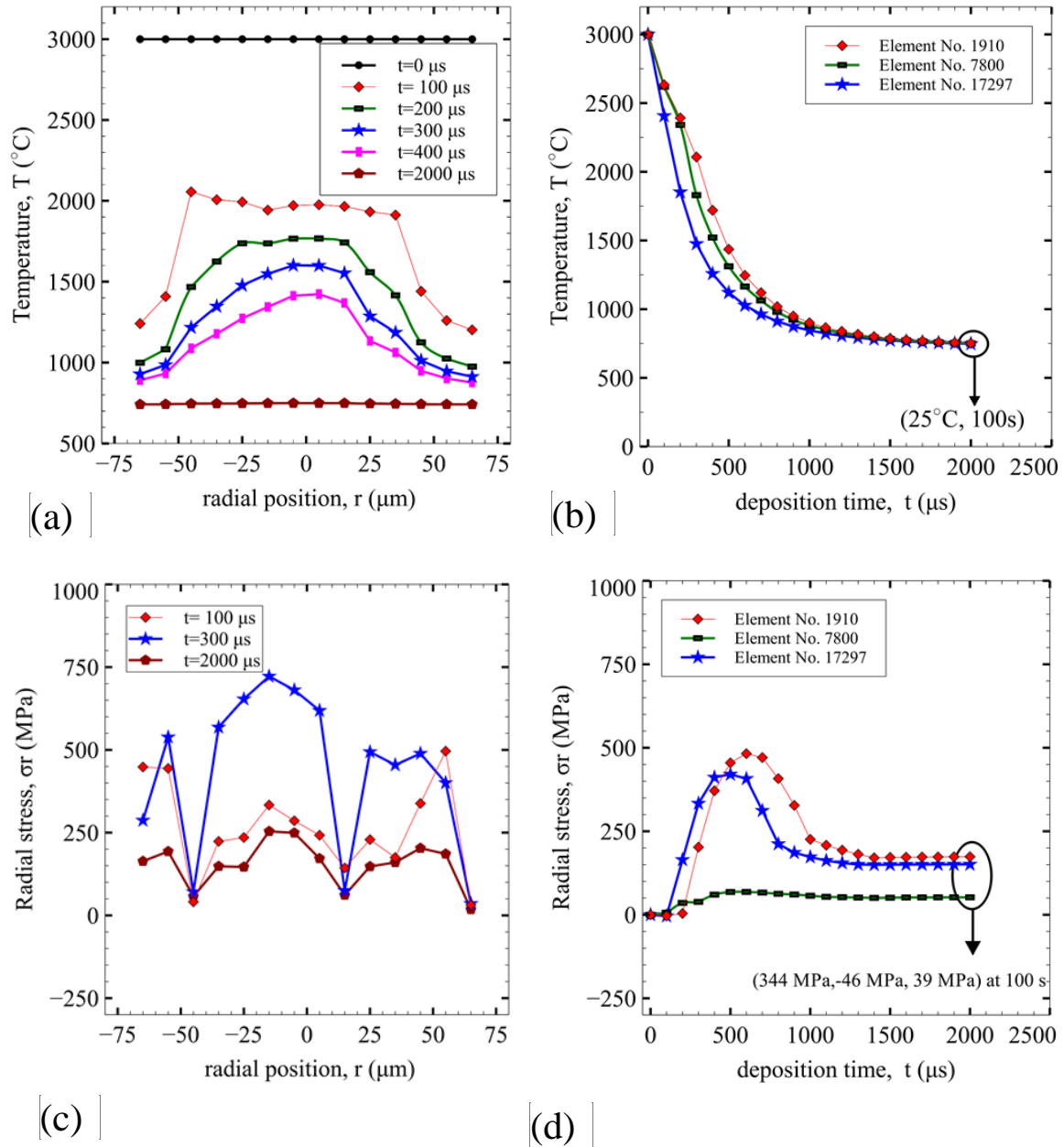


Figure 7-22: (a) Temperature profile along radius of splat, (b) temporal variation of temperature, (c) radial stress profile developed along radius of splat, and (d) temporal variation of radial stress ((a) and (c) were taken at 3 μm above coating interface, while (b) and (d) were taken at integration points of three elements)

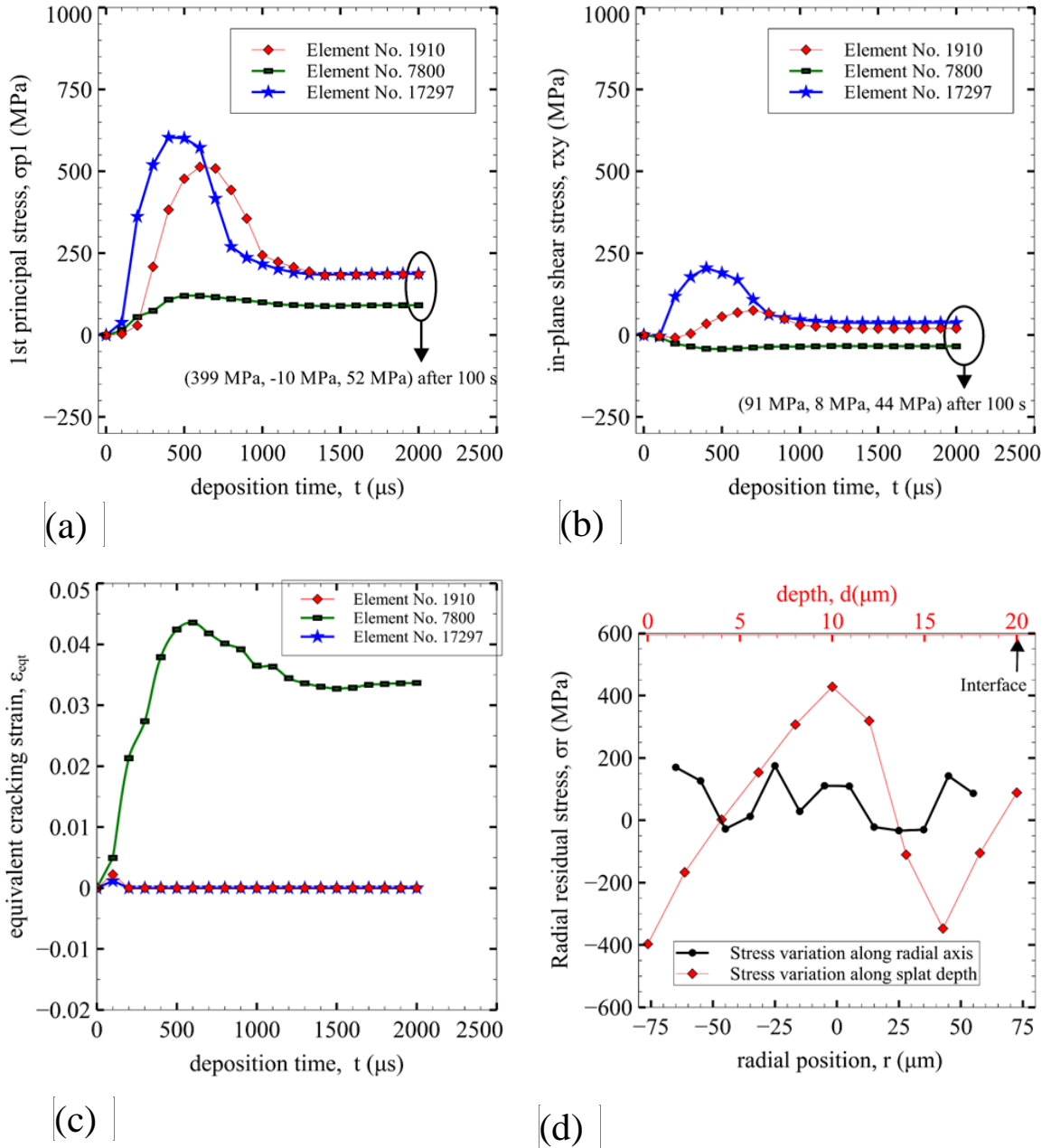


Figure 7-23: Temporal variation of (a) first principal stress, (b) in-plane shear stress and (c) equivalent cracking strain at integration points of three elements, (d) radial residual stress profile developed along radius and thickness of coating.

7.3.4 Numerical prediction of temperature distribution and residual stress field developed in single Ni-20%Al splat

In this section, the hybrid approach is used to predict temperature distribution and residual stress field developed in metallic Ni-20%Al splat deposited on SS310 substrate. The aim of the study is to demonstrate that, the hybrid approach can be used to predict stress formation in metallic coatings subjected to extensive plastic deformation. The multi-linear isotropic hardening model is used to model plastic deformation within the coating layer. The results are discussed and compared with that of previous findings.

Figure 7-23 shows the temperature distribution and quenching stress field developed during solidification of metallic Ni-20%Al splat. As shown in Figure 7-23 (a), molten Ni-20%Al splat having initial temperature of 1827 °C is deposited on SS310 substrate which is preheated to 600 °C. From Figure 7-23 (a), it can be seen that, the molten Ni-20%Al splat solidifies after about 100 μ s, i.e. within same range of solidification time for the YSZ splat. Also, it is found that, the metallic Ni-20%Al splat undergoes extensive plastic deformation due to high thermal stresses developed during solidification as shown in Figure 7-23 (b). Thus, the equivalent plastic strain variable fluctuates due to differential thermal history associated with the intricate nature of the splat geometry. The largest value of equivalent plastic strain is around 0.03. Figure 7-23 (b) shows the von Mises stress developed after quenching of the Ni splat. As predicted for the ceramic counterpart, the quenching stress fluctuates due to differential plastic deformation. However, in this case, it fluctuates only within tensile stress range (i.e. 200-300 MPa) due to low mismatch in structural properties of the coating and substrate layers [29].

Figure 7-24 (a) shows the temperature profile developed along the radial axis of splat at around 3 μm above the substrate surface. As in the case of YSZ splat, the temperature profile is symmetrical and temperature values drops splat solidification. Figure 7-24 (b) shows the von Mises quenching stress profile developed along the splat radial axis. Unlike in the temperature profile, the quenching stress field is not symmetrical due to variation in plastic deformation within the splat domain. It is found that, quenching stress developed in the Ni-20%Al splat is tensile in nature and fairly comparable to previous research work by Sebastiani et al. [178]. However, Sebastiani et al. predicted quenching stress of about 150 MPa which is lower than the 250 MPa average predicted with the hybrid approach. This is because of uncertainties associated with the adoption of certain necessary assumptions as well as the difficulty to get the exact value of certain properties.

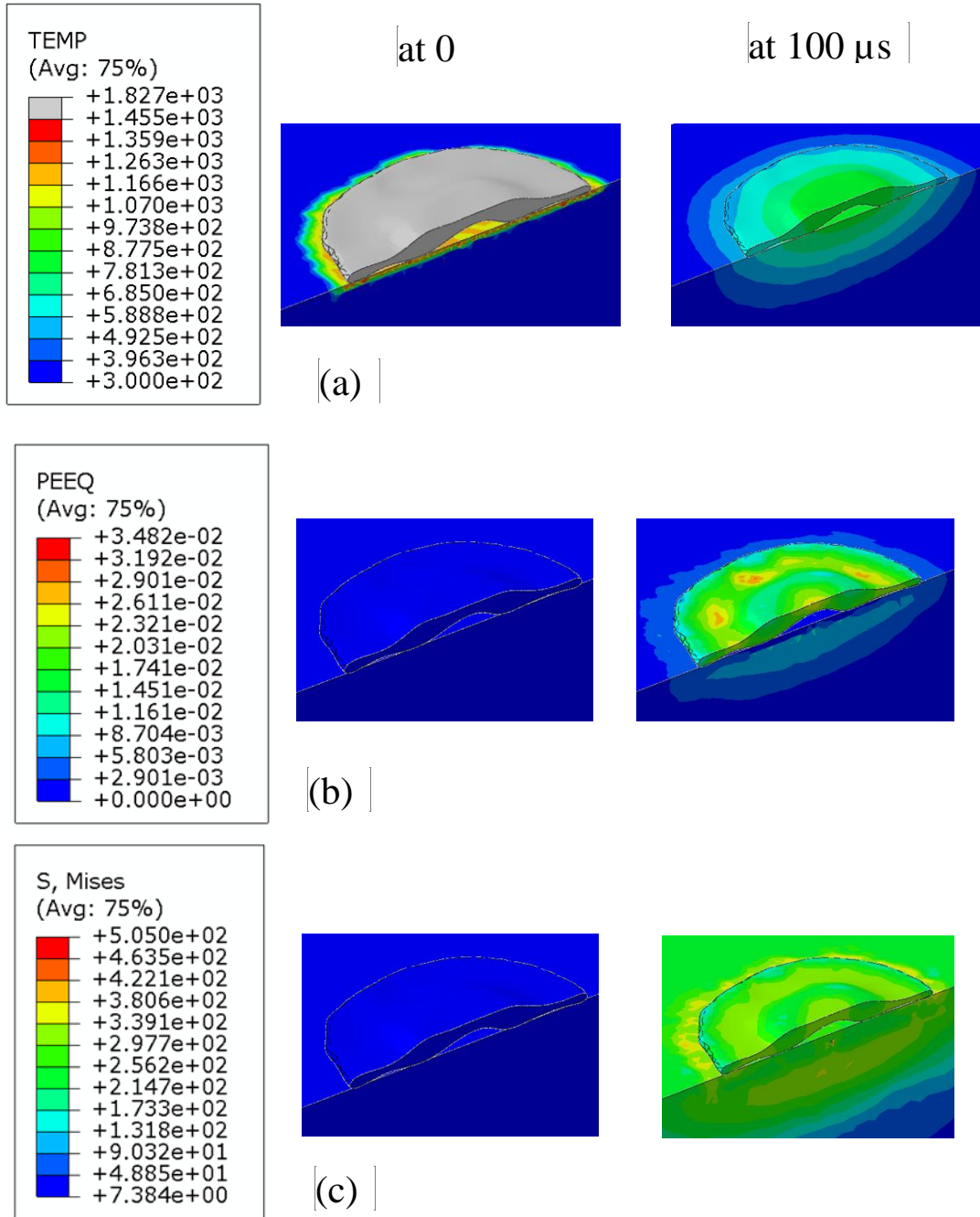
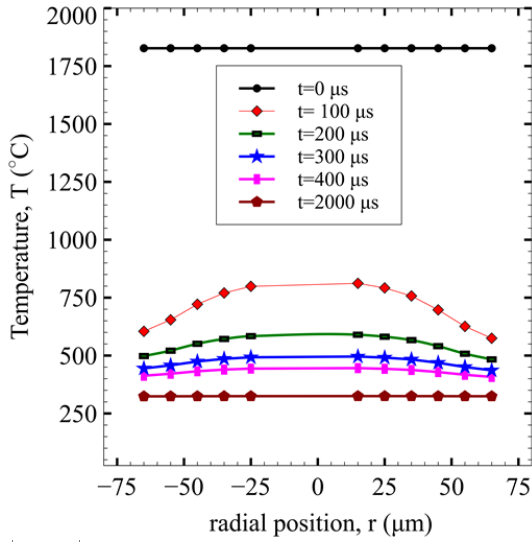
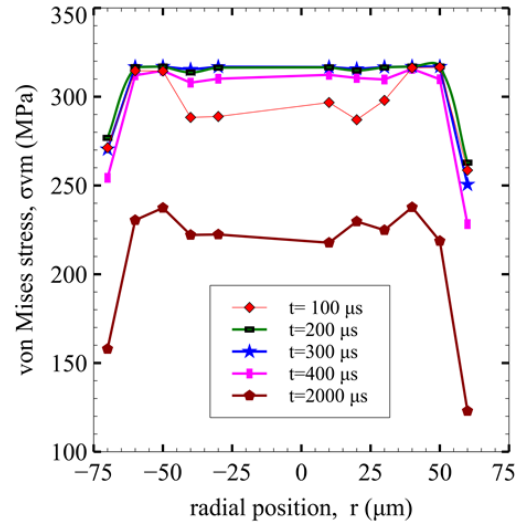


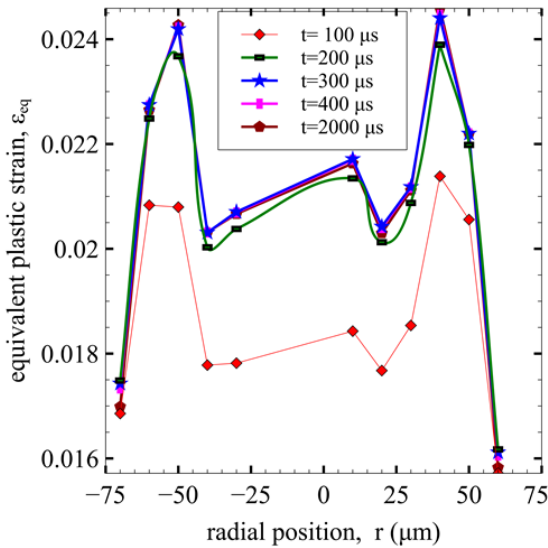
Figure 7-24: Cross section view of Ni splat showing evolution of (a) temperature (°C), (b) equivalent plastic strain and (c) von Mises quenching stress before and after solidification (i.e. at 0 and 100 μs)



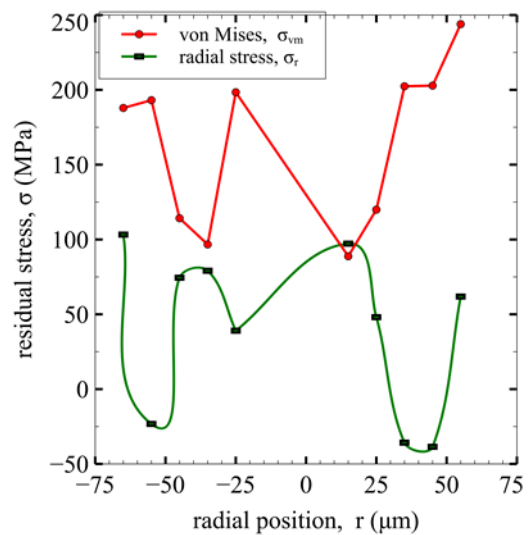
(a)



(b)



(c)



(d)

Figure 7-25: (a) Temperature profile along radius of splat, (b) temporal variation of temperature, (c) radial stress profile developed along radius of splat, and (d) temporal variation of radial stress ((a) and (c) were taken at 3 μm above coating interface, while (b) and (d) were taken at integration points of three elements)

Due to small difference in structural properties of the coating and substrate materials, the compressive mismatch stresses are low. Thus, the final residual stress state of the coating extremely depends on the quenching stresses developed during splat solidification. Figure

7-24 (d) shows that the von Mises and radial residual stress profile developed along radial axis of the coating falls within 100-250 MPa which is not up to both the quenching stress and yield strength of the material. This implies that the magnitude of high tensile quenching stresses reduces due to additional compressive (mismatch) stresses developed when the coating is cooled to room temperature. Figure 7-24 (d) also shows that the radial stress falls within -50 to 100 MPa. These values conform well to previous experimental measurements by Sebastiani et al. [178] in which they predicted the residual stress to be tensile and around 100 MPa. Due to the occurrence non-uniform plastic deformation and complex strain history, the residual stress varies significantly within the splat domain. Therefore, residual stress fluctuation observed in Figure 7-24 (d) is not unexpected. This is further demonstrated in Figure 7-25 which shows the 3D plot of equivalent plastic strain and von Mises residual stress field developed within the Ni splat layer.

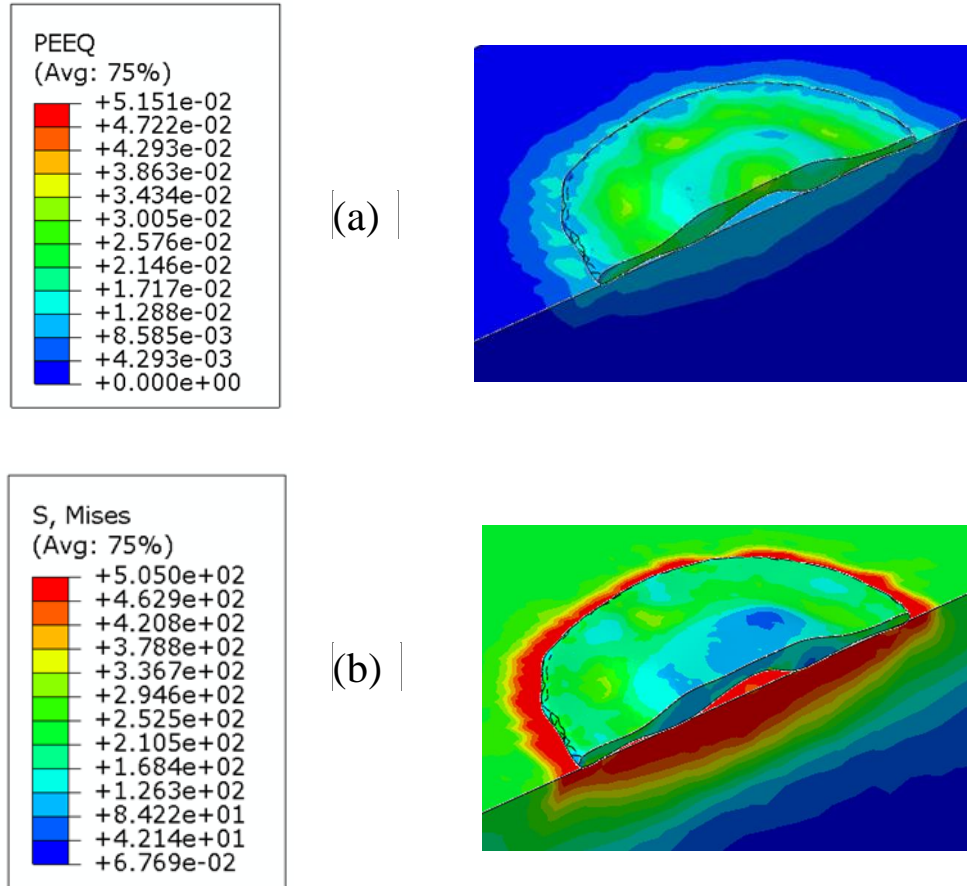


Figure 7-26: Cross section view of Ni splats final distribution of: (a) equivalent plastic strain & (b) residual stresses after cooling to room temperature

7.4 Concluding remarks

In the present study, the new hybrid approach which couples point cloud and finite elements has been used to numerically predict the residual stress developed in single YSZ and Ni-20%Al splats deposited on stainless steel. From the analysis conducted, the following conclusions can be made:

- the proposed approach relates deposition process parameters with microstructure evolution and residual stress development in thermal spray coatings.

- the approach gives more realistic temperature distribution due to the inclusion of splat solidification apart from convective heat loss to the environment during analysis.
- the approach has captured the strong dependence of residual stress on thermal and strain history. Consequently, the high tensile stresses developed during splat quenching reduce to lower tensile or even compressive stresses due to the addition of mismatch stresses developed after the post-deposition stage.
- as observed experimentally, the hybrid model predicts that the ceramic YSZ coatings develop very high tensile quenching stresses that change to compressive state upon cooling to room temperature. These high tensile (quenching) stresses partially relax to lower stress state due to microcracking attributed to thermal shock. On the other hand, the metallic Ni-20%Al coatings develop very high tensile stresses and undergo substantial yielding during quenching. But the stress state remains tensile even after post-deposition cool down due to low structural mismatch between the metallic coating and substrate.

Therefore, the current approach can be used to model the evolution of coating microstructure (containing various form of defects or imperfections) and residual stress in TSCs. Discussion about this possibility is made at length in Chapters 8 and 9. The approach is applicable to a variety of spray processes such as plasma spray, high-velocity-oxy-fuel, detonation gun, and cold spray.

CHAPTER 8

MULTIPLE SPLATS FORMATION, INTERACTION AND RESIDUAL STRESS EVOLUTION

In the present study, the hybrid computational approach is used to model multiple splats formation, their interaction and evolution of residual stress during the thermal spray process. The work has been published in Journal of Thermal Spray Technology [186].

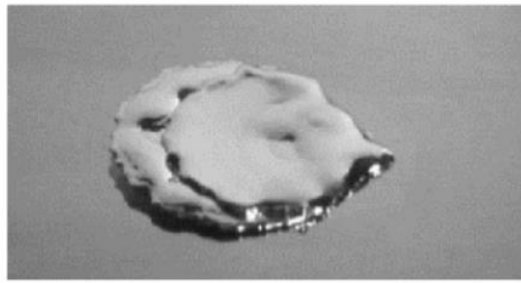
In the current work, multiple YSZ droplets (or splats) are deposited on SS310 stainless steel. The same constitutive models used in Chapter 7 are considered here for the finite element analysis. The model is first used to study temperature distribution and residual stresses developed in few multiple interacting splats. Based on results obtained from such studies, the same model is used to numerically predict temperature distribution and residual stress developed in multilayered coating deposited to certain thickness. The predicted residual stress profile is validated by comparing with experimental results obtained from hole drilling experiment and results available in the literature.

8.1 Splat formation on point cloud

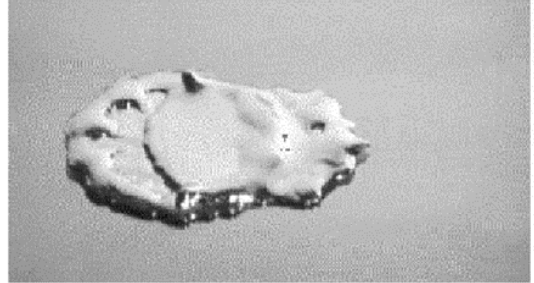
Due to the complicated nature of the spray process, common reason tells us that droplets interact with one another in a complex fashion during deposition. Based on previous experimental studies by Ghafouri-Azar et al. [181], interaction of droplets with their nearest neighbors is possible in four ways (as demonstrated in Figure 8-1). In most cases, the profound effect of this interaction is seen on the splat geometry. Thus, the aim here is

using the point cloud model to study multiple splats interaction rather than single droplet impact and spread.

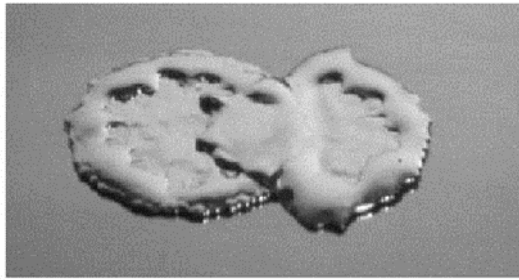
Figure 8-2 shows that the point cloud model effectively captures the geometry (i.e. shape and size) of two droplets which have direct or indirect interaction with each other. Figure 8-2 (b)-(d) shows that complicated splat geometries result due to complex interactions of the droplets during impact. From Figure 8-2 (b), it can be seen that two neighboring droplets push one another at an interface, thus resulting in distortion and complicated splat geometry. Figure 8-2 (c) and (d) demonstrates this further where it is shown that interaction of nine neighboring droplets results in splats having various forms of geometrical complexities. The splat interfaces are vividly shown from the Figures (in red). Figure 8-2 (d) and Figure 8-3 shows that the splat geometry is also affected by interaction of droplets with the target surface. It can be seen that, undulation of the target surface severely affects splats formation. Incoming droplet develops a concave structure as it deposits directly on unto a pre-deposited splat as shown in Figure 8-3(a). While, Figure 8-3 (b) shows that incoming droplet develops both concave and convex structure since only part of it deposit on pre-deposited splat. In practice, the adhesion of the coating to the substrate is often improved by roughening the substrate surface through processes such as shot-peening, sand-blasting or roller burnishing. Therefore, it is further shown in Figure 8-4 that the hybrid approach is robust in numerically predicting splat shape resulting from deposition of droplets on highly rough surface. This is important considering the significant role played by surface roughness on the final residual stress state of coatings.



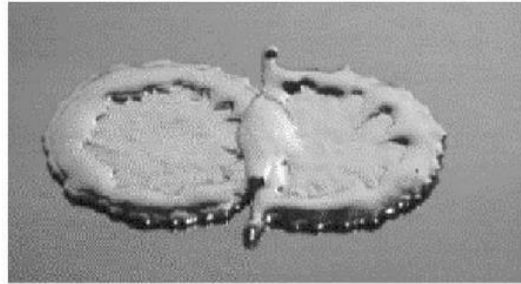
(a)



(b)



(c)



(d)

Figure 8-1: Possible scenarios for the interaction of two Ni droplets initially having offset of: (a) 1 mm, (b) 2 mm, (c) 3 mm, and (d) 4 mm

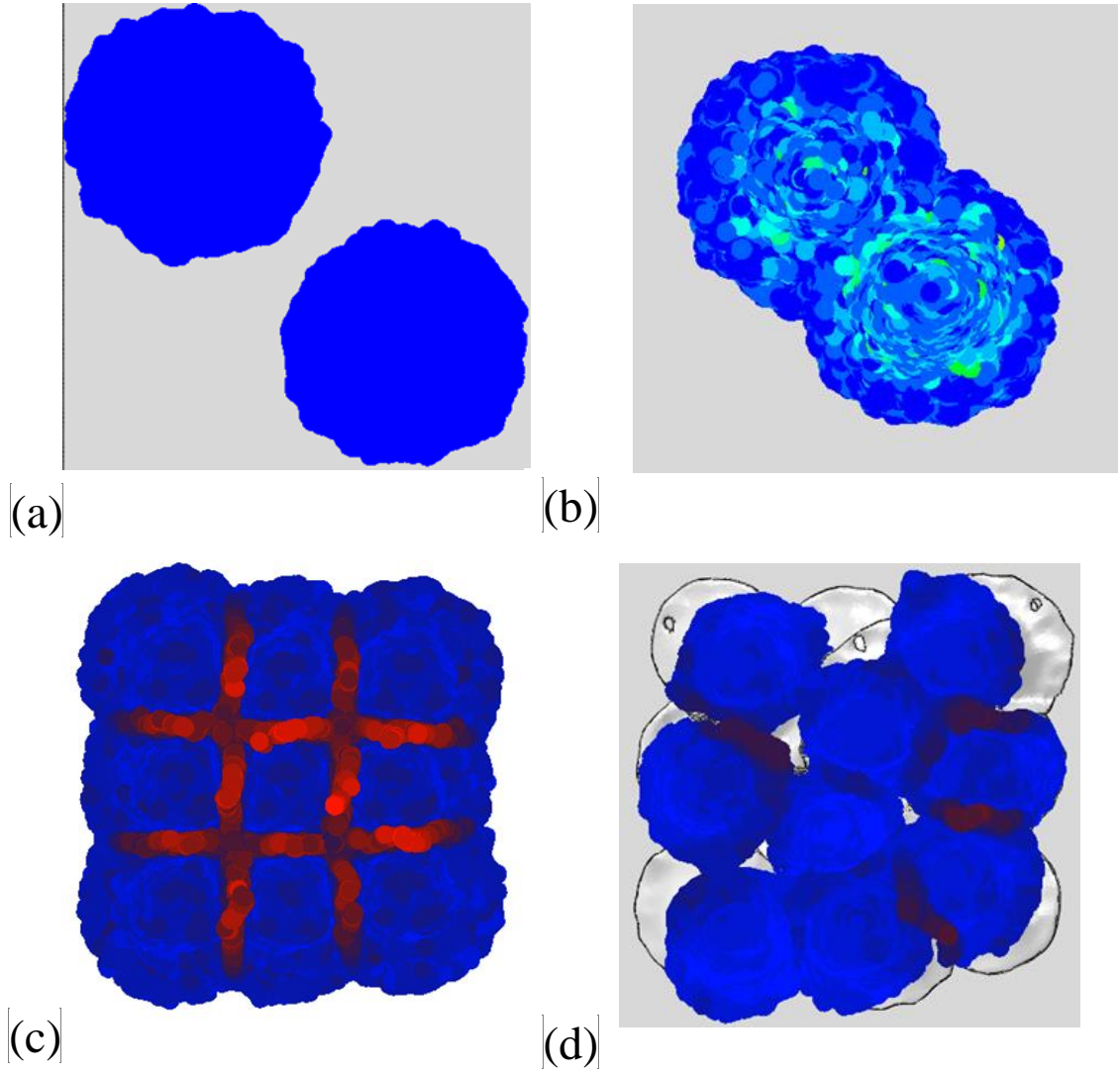


Figure 8-2: Demonstration of multiple droplets interaction: (a) two far YSZ droplets, (b) two near-by YSZ droplets, (c) nine near-by YSZ droplets (first layer), (d) nine near-by YSZ droplets (third layer)

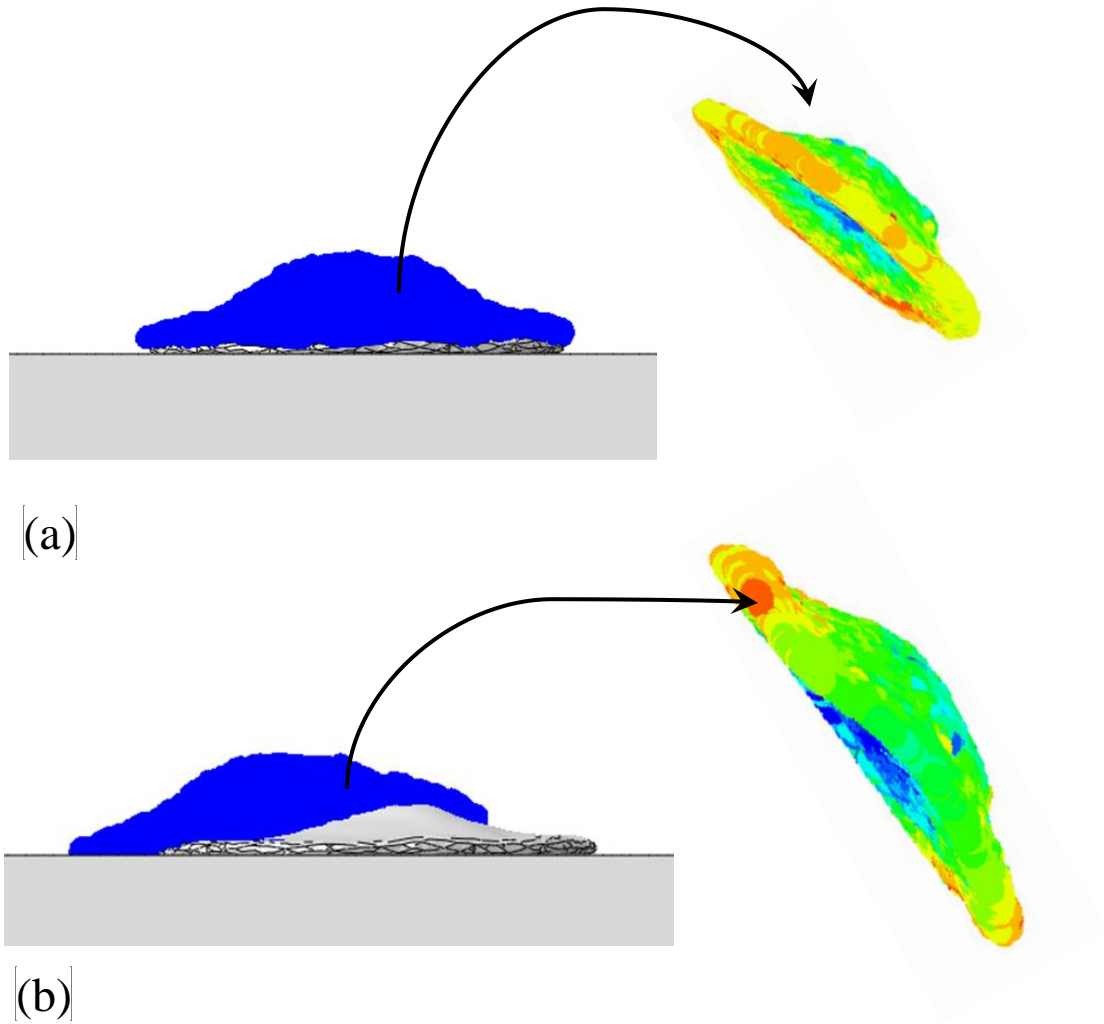


Figure 8-3: Droplet impact on pre-deposited splats: (a) new splat formed directly on top of old splat, (b) new splat formed half-way on top of old splat

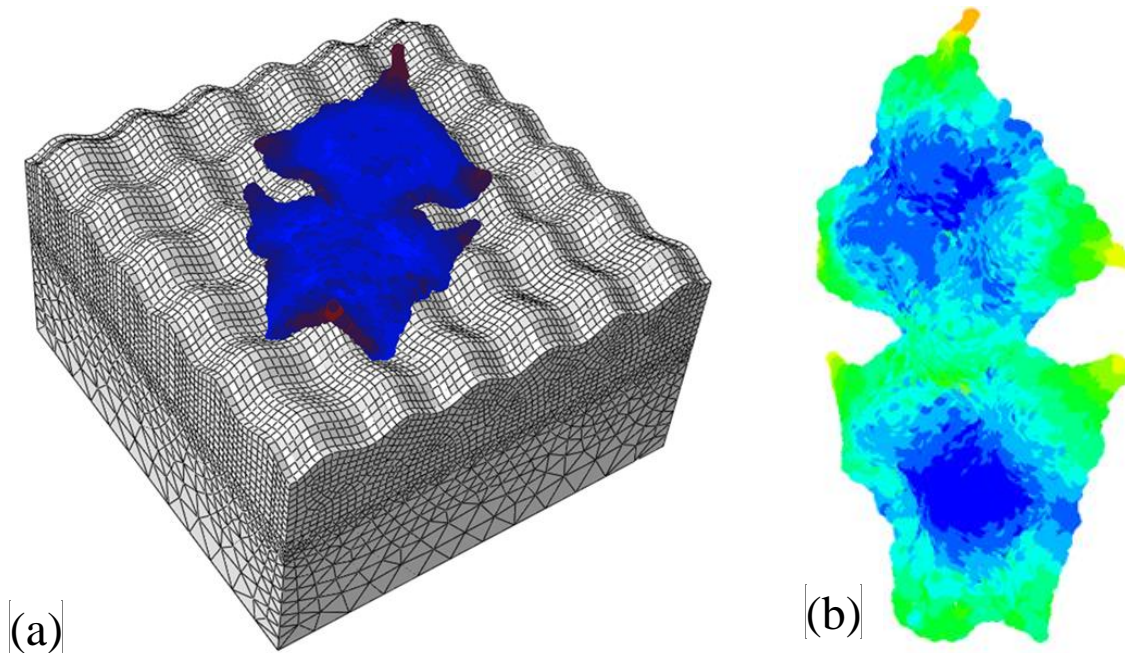
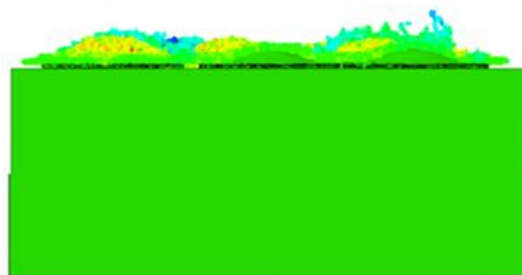
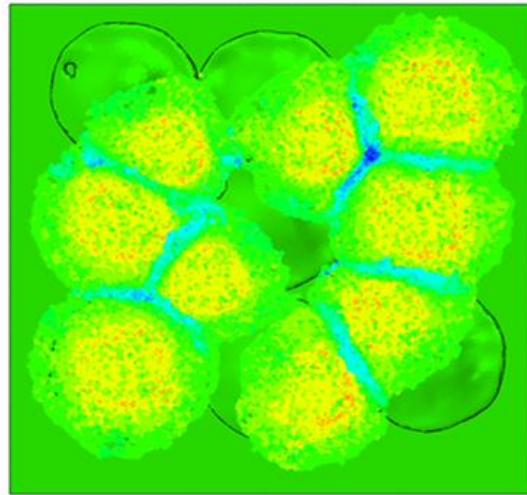
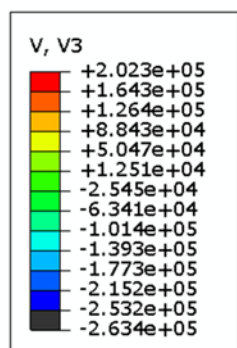


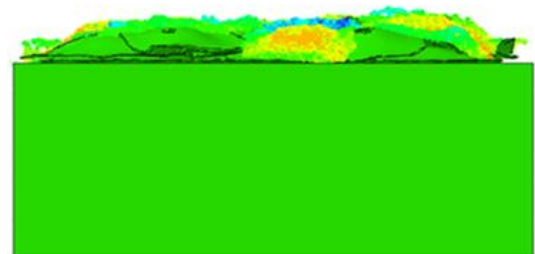
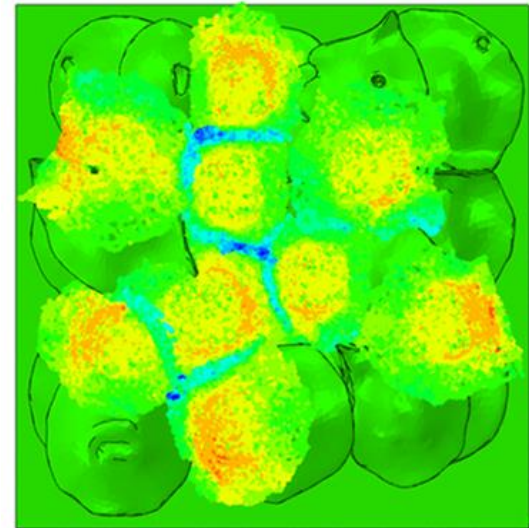
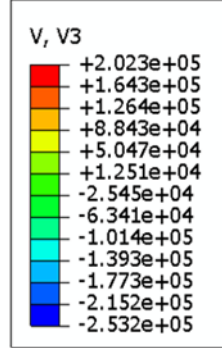
Figure 8-4: Droplet impact on rough surface: (a) splats geometry formed after deposition on bond coat, (b) zoomed view of splats interface formed

Using statistically-defined initial conditions (given in Table 2-1), the deposition of nine YSZ droplets and their interactions are modeled using the point cloud model. The computation is carried out layer-wise up to the 5th layer of droplets deposition. For brevity, only results of the second and fourth layer will be presented here. Figure 8-5 (a) and (b) shows the variation of the velocity component in the z-direction during the deposition of the second and fourth layer (each consisting of nine droplets). As in single droplet deposition, the velocity of each droplet reduces from its initial value to smaller values due to droplet-substrate and droplet-droplet interactions. Due to the low impact energy of air-plasma sprayed droplets, peening stresses are not considered here. Thus, the pre-deposited splat and substrate layers are modeled as rigid bodies in order to improve computational efficiency of the model. The average spreading time for the droplets is

found to be about 1 μs which is comparable to times reported in previous studies [163], [190]. The average spread factor, diameter, and thickness of the simulated splats are found to be 3.47, 79.2 μm and 4.2 μm respectively. The size and shape of deposited splats are found to be strongly influenced by their interaction with nearby droplets; thereby resulting in complex splat geometries. Consequently, the resulting splat shape is non-symmetrical and irregular in most cases. It is found that the point cloud model can be adequately used to study the interaction of process parameters and the discontinuities or imperfections (such as pores, cracks, and other complex geometrical features) encountered in TSCs.



(a)



(b)

Figure 8-5: Velocity magnitude after multi-droplet deposition for (a) second layer and (b) fourth layer

8.2 Simulation of coating microstructure in form of FE mesh

Upon completion of multiple droplets deposition in layers, the geometry of each splat is reconstructed using the various algorithms described in section 4.2.2. The geometry is first represented in the form of STL (or surface) mesh before its conversion to 3D linear tetrahedral mesh. Through stacking of multiple splats, a numerical coating microstructure with good overlap at splats interface is developed as shown in Figure 8-6 and Figure 8-7. It is found that, meshing splat bodies in ABAQUS results in higher computational efficiency and minimize numerical issues (arising due to poor elements) as compared to when it is done elsewhere. Also, grid-independence test was carried out to ensure that the level of mesh refinement is sufficient for numerical convergence at moderate computational cost. The average size of elements within each layer is demonstrated in Table 8-1 (in form of average edge lengths). The criteria for mesh quality are that, ABAQUS accepts any tetrahedral element that have shape factor of at least 3×10^{-3} , face corner angle within 5 and 170 and aspect ratio of at most 10. Upon preliminary checks, it is found that the mesh generated with current approach passed the overall criteria despite the presence of discontinuities (as demonstrated in Table 8-1). Even deleting the very few elements that failed the some of the criteria makes no difference in terms of results quality. The approach adopted here is more suitable and flexible as compared to the popular image-based finite element approach. Apart from having finite elements of higher quality, it is developed based on standard codes available in literature. Thus, it does not involve tedious noise cleaning and re-processing of microstructure images. The approach can also be used to study the process-dependence and layer-wise build-up of temperature and residual stress during the spray process.

Table 8-1: Information on tetrahedral element size and quality

Layer name	First	Second	Third	Fourth	Fifth
# Splats	9	9	9	9	9
# Elements	124,591	90,499	60,418	96,119	60,432
# Nodes	31,314	19,566	15,965	20,335	16,317
Shape factor < 0.0001: Average/worst/# Elem.	0.6085/2 x 10 ⁻² /0	0.5721/1 x 10 ⁻⁵ /1	0.5973/4 x 10 ⁻⁶ /4	0.5668/1 x 10 ⁻¹⁰ /6155	0.6/1.1 x 10 ⁻⁴ /0
Min angle < 5: Average/worst/#Elem.	36.17/7.97/0	35.93/4.83/0	35.69/3.42/1	36.12/5.00/1	35.81/4.35/1
Max angle > 170: Average/worst/#Elem.	91.56/150.90/0	91.95/168.65/0	92.39/170.21/1	91.64/163.76/0	92.03/169.27/0
Aspect ratio > 10: Average/worst/# Elem.	1.75/6.14/0	1.77/8.93/0	1.80/10.23/1	1.76/8.79/0	1.78/7.43/0
Average min. edge length (µm)	1.65	1.82	2.13	1.76	2.19
Average max. edge length (µm)	2.81	3.23	3.66	3.00	3.76
#Elem.: number of elements that failed the criteria-					

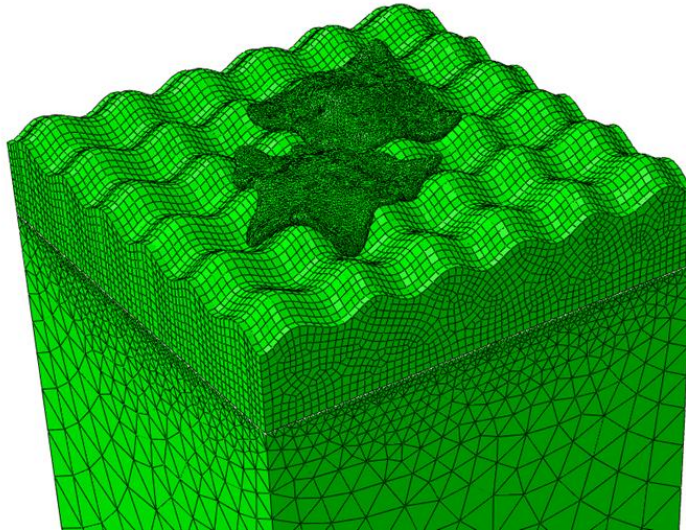
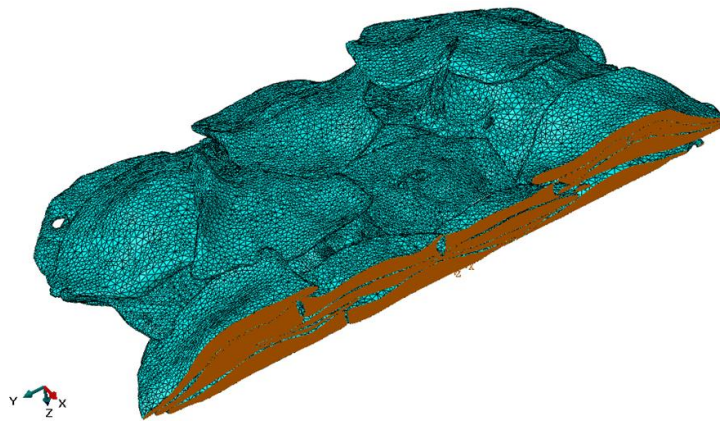
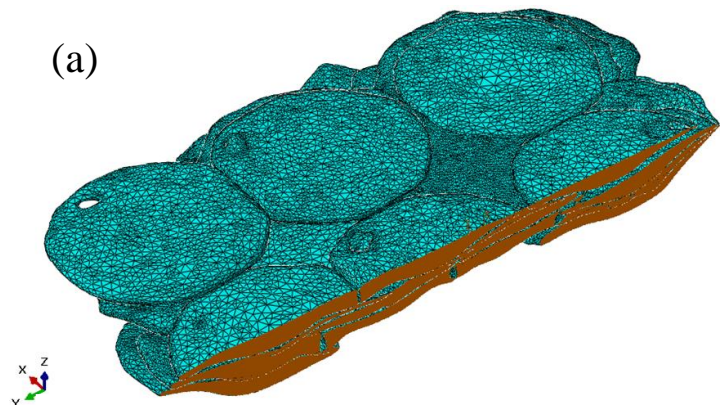


Figure 8-6: FE mesh for interacting splats deposited on rough target surface



(a)



(b)

Figure 8-7: 3D tetrahedral FE mesh of splats deposited in five layers

8.3 Numerical prediction of temperature distribution, residual stress and microcracks in multiple YSZ splats

Apart from their interactions while in fluidic state, deposited droplets do have thermal and structural interaction during solidification and resulting deformation. This form of interaction occurs at a time scale higher than that of droplet impact and spread; thus, they are not captured by the current deposition model. Therefore, in this section, the thermal and structural interactions of multiple YSZ splats are studied using finite element analysis. The analysis was conducted using the ceramic microcracking material model adopted for the single YSZ splat discussed in section 7.3.3.

Figure 8-8 shows temperature distribution and quenching stress field developed after the solidification of the two far-away splats (previously shown in Figure 8-2 (a)). Even though the splats have no direct fluid interaction, it can be seen that, the temperature distribution and solidification rate of one splat affects that of the other (as shown in Figure 8-8(b)). The region in-between the splats develop high temperature that affects their solidification rate. Figure 8-8(c) shows the corresponding quenching stress field induced after the splats has fully solidified. It can be seen that, von Mises stress goes as high as 300 MPa at several regions of the coating. Due to the adoption of microcracking model, relaxation of stress to as low as 50 MPa at cracked regions (as shown in Figure 8-8(c)). It can also be seen that, higher stresses are induced in-between the splats due to structural interaction. Figure 8-8(d) shows the corresponding microcracks formed after solidification. It can be seen that, radial cracks that propagates from the edges to center are developed as previously observed for the case of single splats.

For the case of directly-interacting splats, Figure 8-9 shows the temperature distribution and quenching stress field developed after solidification. It can be seen from the figure that, the two droplets solidify as if they are one body because of strong thermal interaction. Consequently, solidification time of the splats is less than that of the case considered in Figure 8-8 (a). Figure 8-9(c) shows that the strong structural interaction occurring between the splats severely affect the final quenching stress field developed. This is more visible from Figure 8-9(d) where it is shown that crack formation is severely affected by the structural interaction.

Figure 8-10 shows the temperature distribution developed after sequential deposition of two splats with zero offset distance. The first splat was allowed to supercool to the initial substrate temperature (around 700°C) before the deposition of second splat. Figure 8-10(a) shows that the two splats are under perfect thermal contact and have direct thermal interaction. Thus, top region of the first splat was reheated to its melting point upon its contact with the second one. The second splat took longer time to solidify (i.e. more than 2000 μ s) due to lack of direct contact with the highly conductive substrate. Similarly, interaction of two sequentially deposited splats with an offset of 0.05 mm is demonstrated in Figure 8-10(b). It can be seen that, due to misalignment of splat interfaces, the top splat requires longer time to completely solidify as compared to the case considered in Figure 8-10(a). Figure 8-11 shows the corresponding quenching stress field developed after the solidification of the interacting splats. It can be seen that, the high stresses developed during splat solidification relaxes at several regions due to the presence of microcracks. Figure 8-6 shows that the complex mesh resulting from the deposition of droplets on rough substrate surface. It can be seen that, the splats solidify

after about 400 μs which is nearly the same time predicted for the case of flat substrate (shown in Figure 8-8). This shows the robustness of the hybrid approach in capturing stresses developed at multi-material interface. Figure 8-13 shows that stresses of opposite sign (i.e. tensile and compressive) are developed at the hills and valleys of the rough surface. This is because as hills expand, the valleys contract. This further complicates the stress field developed near the coating-substrate interface. Equally, Figure 8-13 shows that the stress relaxation occurs within the splats deposited on rough substrate due to the presence of microcracks. However, Figure 8-14 shows that, with same the mechanisms of crack formation, cracks propagate in different direction in those splats as compared to the case shown in Figure 8-9.

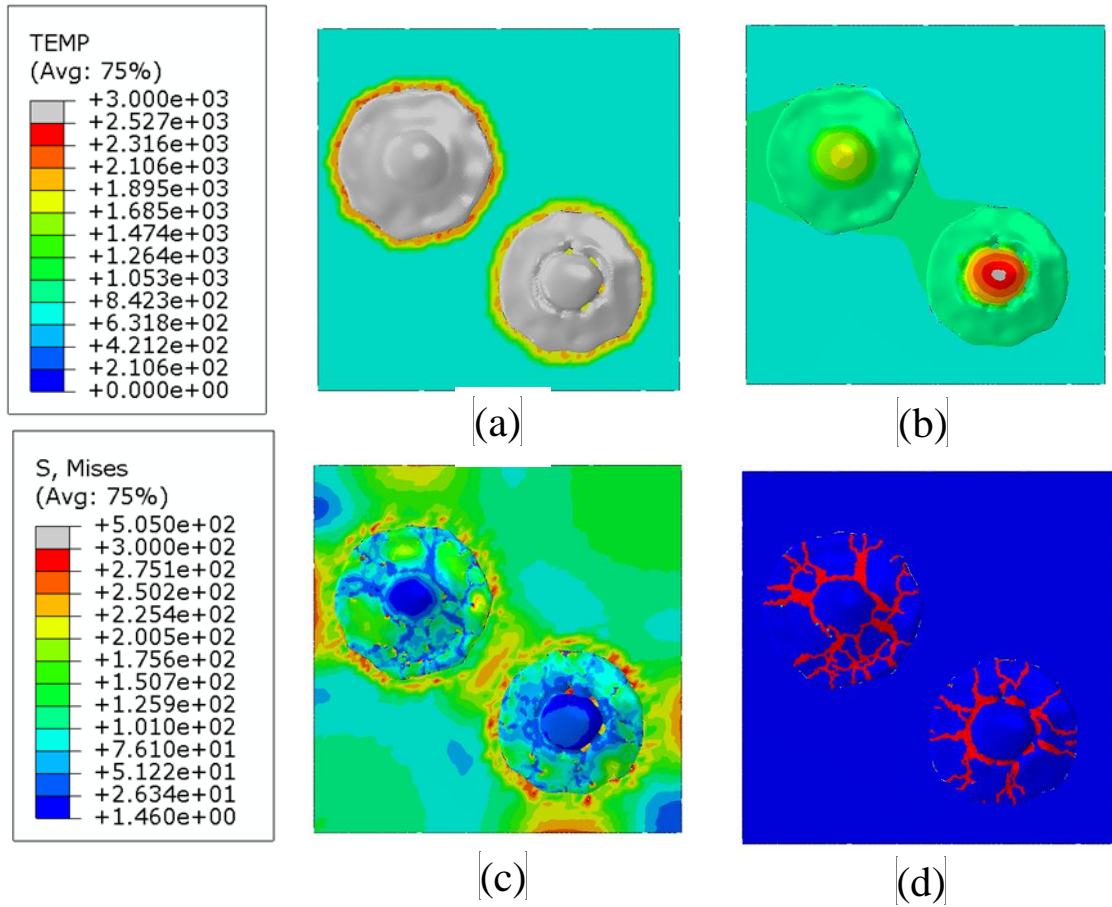


Figure 8-8: Top view of two far away splats: (a) before solidification starts, (b) after solidification (at 500 μ s), (c) quenching stress, (d) formation of microcracks

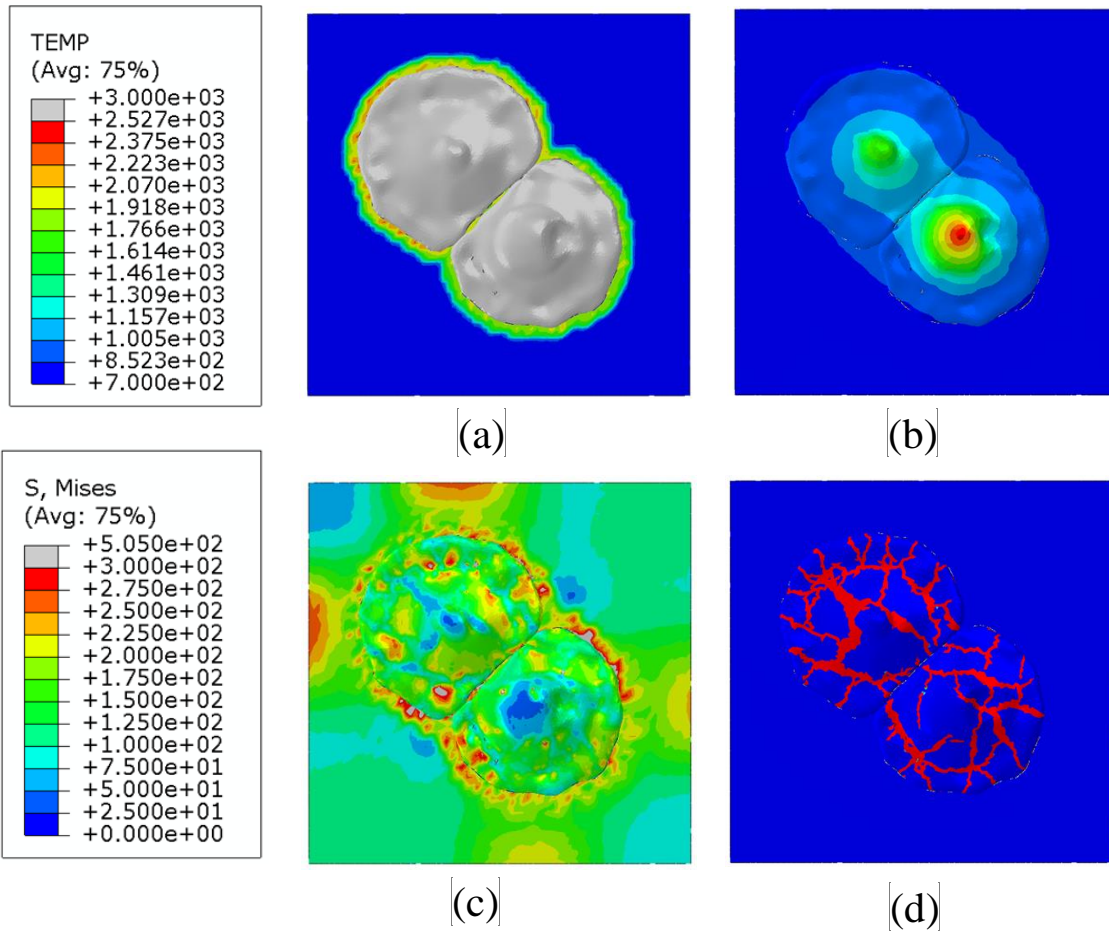


Figure 8-9: Top view of directly touching splats: (a) before solidification, (b) after solidification (at 400 μ s), (c) quenching stress, (d) formation of microcracks

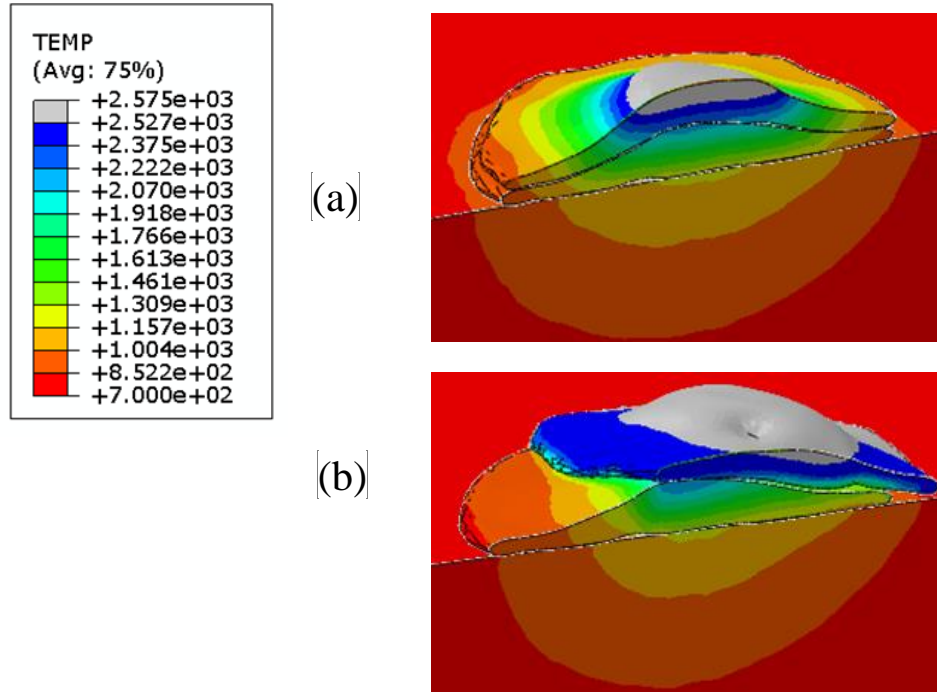


Figure 8-10: Temperature distribution after solidification of two interacting splats after 4000 μ s: (a) one directly on top of the other and (b) two droplets having offset of 0.05 mm.

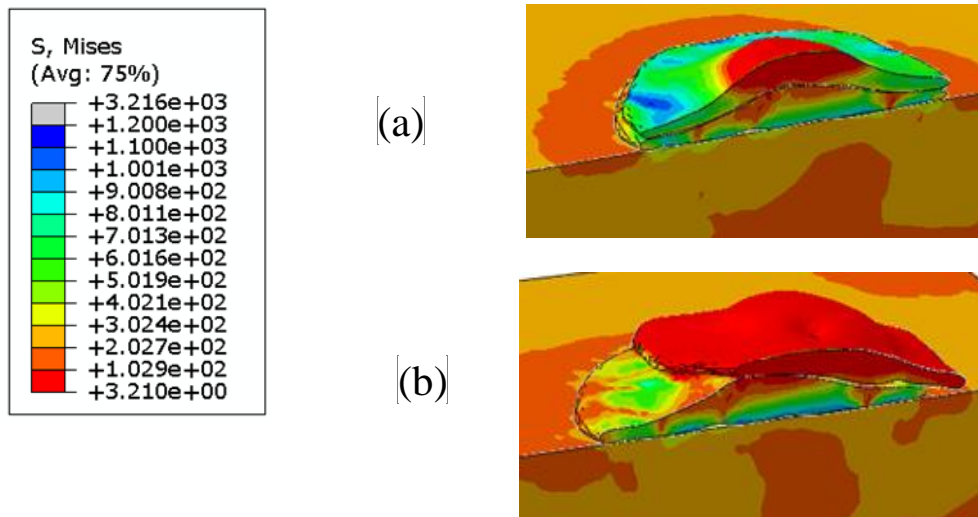


Figure 8-11: Quenching stress after solidification of two interacting splats after 4000 μ s: (a) one directly on top of the other and (b) two droplets having offset of 0.05 mm.

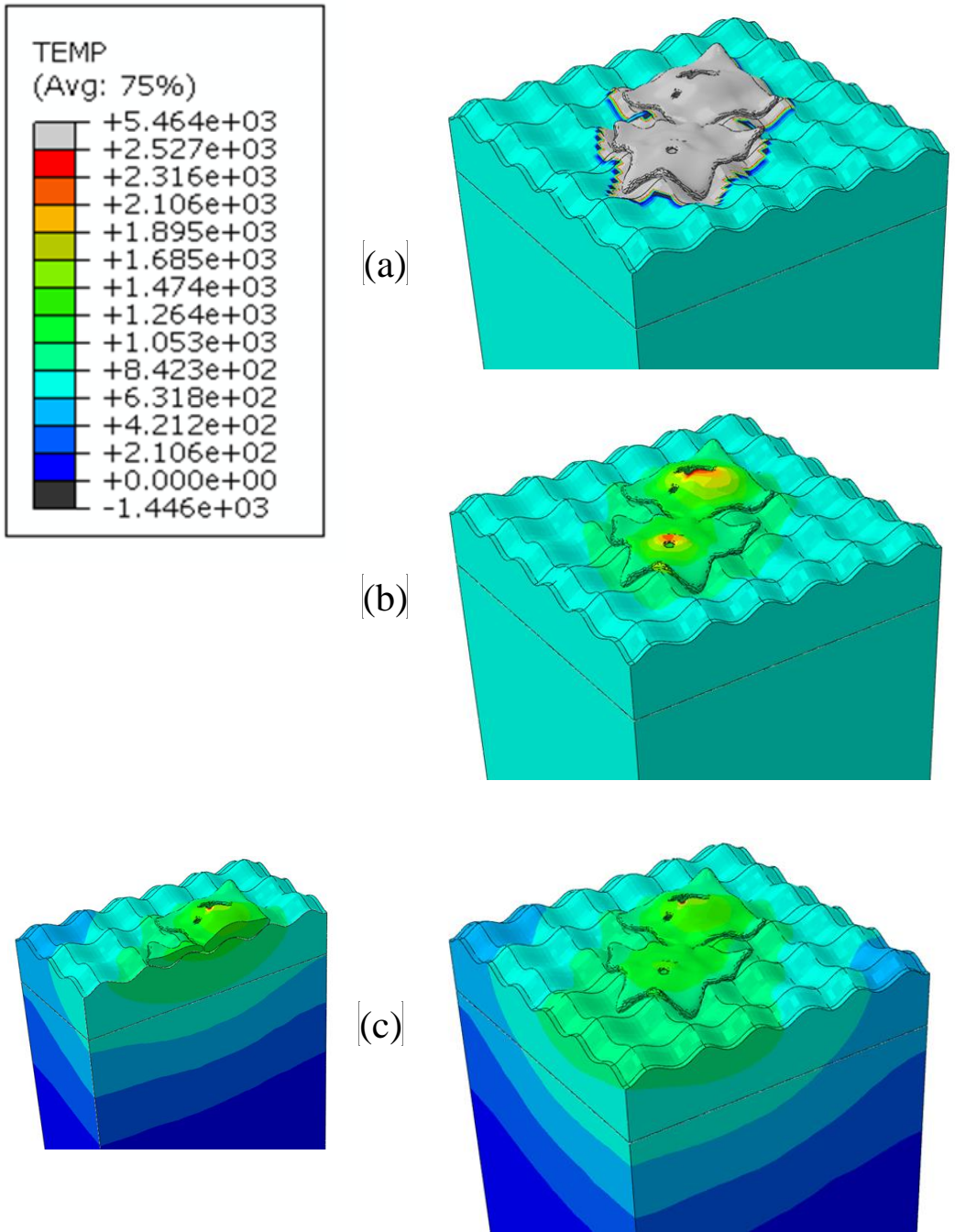


Figure 8-12: Temperature distribution during solidification of interacting splats that impact on rough target surface after: (a) 0 μs , (b) 400 μs , and (c) 2000 μs

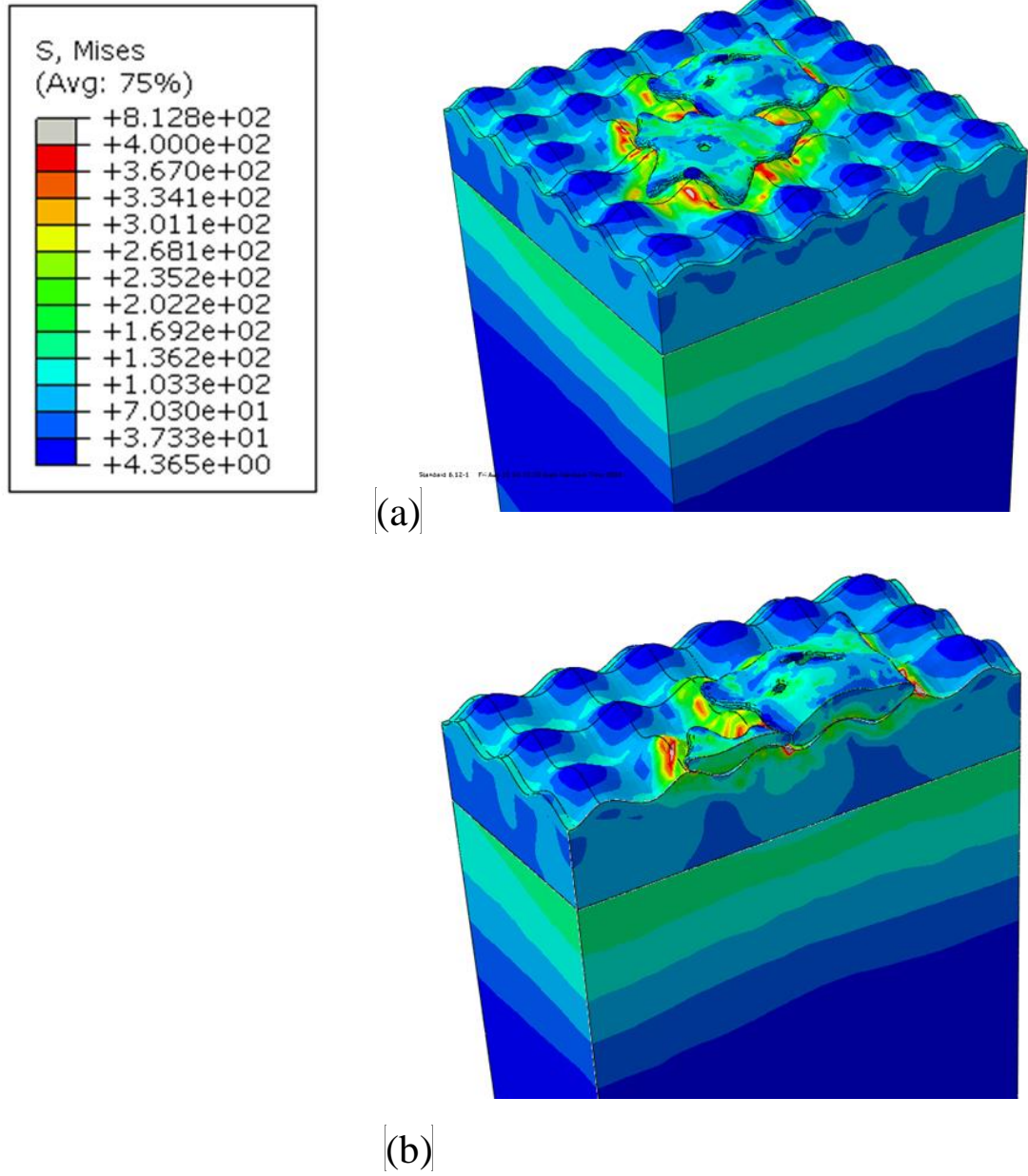


Figure 8-13: Quenching stress field during solidification of interacting splats that impact on rough target surface after: (a) 0 μs , (b) 400 μs , and (c) 2000 μs

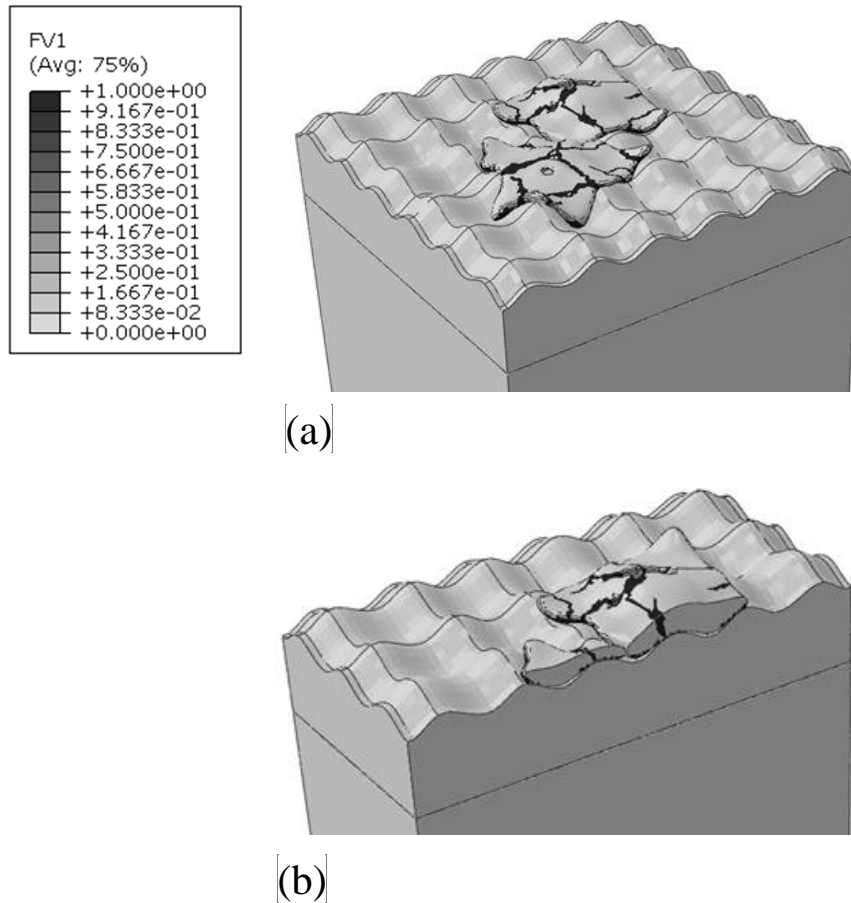


Figure 8-14: Microcracks formed during solidification of interacting splats that impact on rough target surface:
 (a) isometric view and (b) cross section view

8.4 Numerical prediction of temperature distribution and residual stress developed in multilayered YSZ coating

Using the numerical setting used for the few splats analysis, the hybrid model is run for multiple layers of YSZ splats deposited in five steps using 30 cores of Intel processor, 56 GB RAM, and 2.0 GHz from Dell workstation. Each layer consists of 9 droplets that are deposited on the SS310 substrate as previously shown in Figure 8-5. For simplicity, the elastic-perfectly plastic model (previously used in section 7.3.2) is used to restrict deposition stresses to low values caused by cracking of YSZ ceramic. The substrate

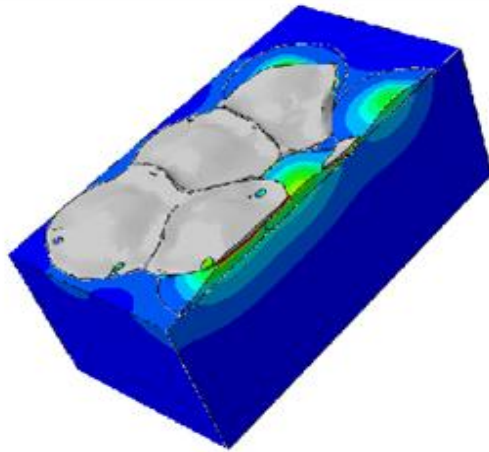
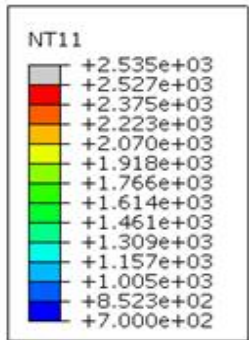
dimensions are selected based on the volume required for proper dissipation of the heat during the process. Any form of heat transfer during droplet flight is neglected. According to the usual practice, the substrate material is pre-heated in order to reduce deposition stresses and improve coating adhesive strength; thus, the substrate layer is assigned a fixed constant temperature of 700°C. The predicted residual stress profile has been validated qualitatively by comparing with the results of hole drilling experiments. The numerical efficiency of the developed model is tracked and optimized by monitoring both computational time and the results accuracy (as shown in Table 8-2).

Table 8-2: Analysis of computational times for multi-layer analysis

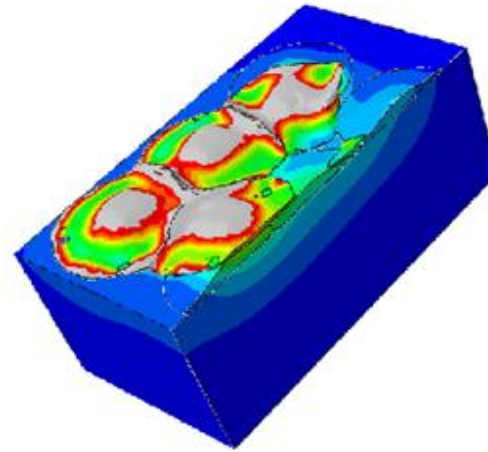
	Layer	No. of splats	No. of elements	Total computational time (hours)	Average time step size	T_{\max}	$\sigma_{p1} - \max$	Total time
Deposition	1	9	36745	7	1e-9	2532	32 MPa	100 μ s
	2	18	83745	12.2	1e-8	2566	33 MPa	150 μ s
	3	27	144163	15.83	5.2e-8	2551	34 MPa	200 μ s
	4	36	240282	23.57	2e-5	2549	34 MPa	250 μ s
	5	45	300714	33.55	1e-4	2563	32 MPa	350 μ s
Post-deposition	5	45	300714	0.67933	10	20.08	315 MPa	40 s

8.4.1 Temperature distribution

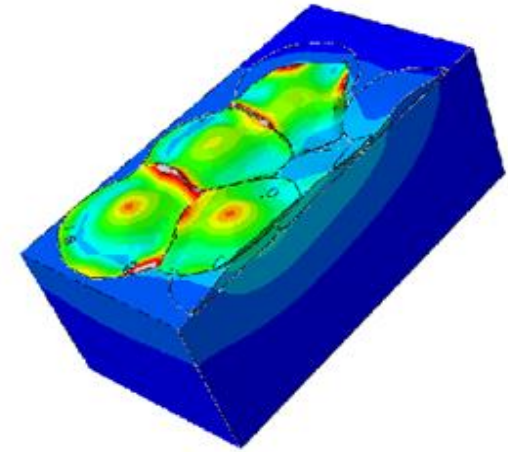
Figure 8-15 (a) and (b) shows the temperature distribution developed after the deposition of second and fourth layer respectively. The figures show that the newly deposited splat layer (in gray) start to solidify after its contact with the pre-solidified coating layers. The prediction of temperature distribution for the first and second layer is more computationally demanding due to the steep gradient developed near the interface. It is also found that, the solidification rate of a given splat is immensely affected by its interaction with its nearest neighbors. Consequently, partial re-melting of pre-solidified splats (due to contact with new splats) is observed in certain regions. Thus, the numerical results predicted here show that temperature distribution is not only complex but highly dependent on many factors such as geometrical complexity, number of layers deposited, solidification rate, quality of contact and other factors which should be considered for effective prediction of residual stress evolution.



0 μ s

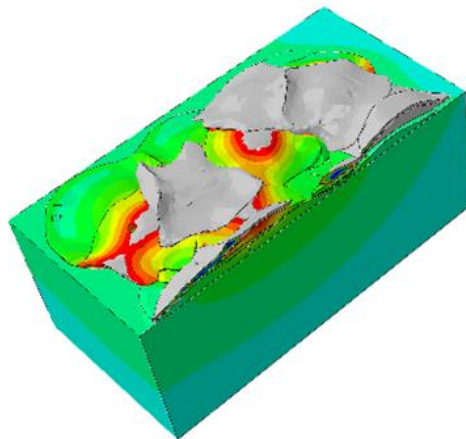
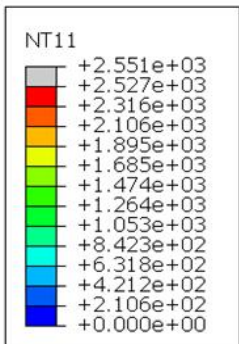


50 μ s

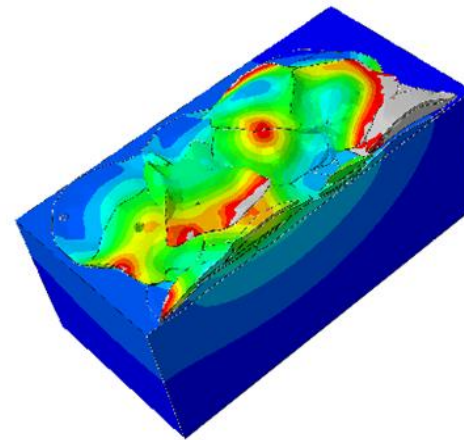


150 μ s

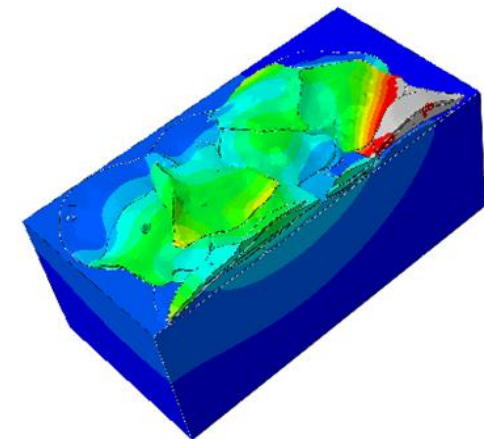
(a)



0 μ s



80 μ s



250 μ s

(b)

Figure 8-1: Evolution of temperature after deposition of (a) second layer and (b) fourth layer

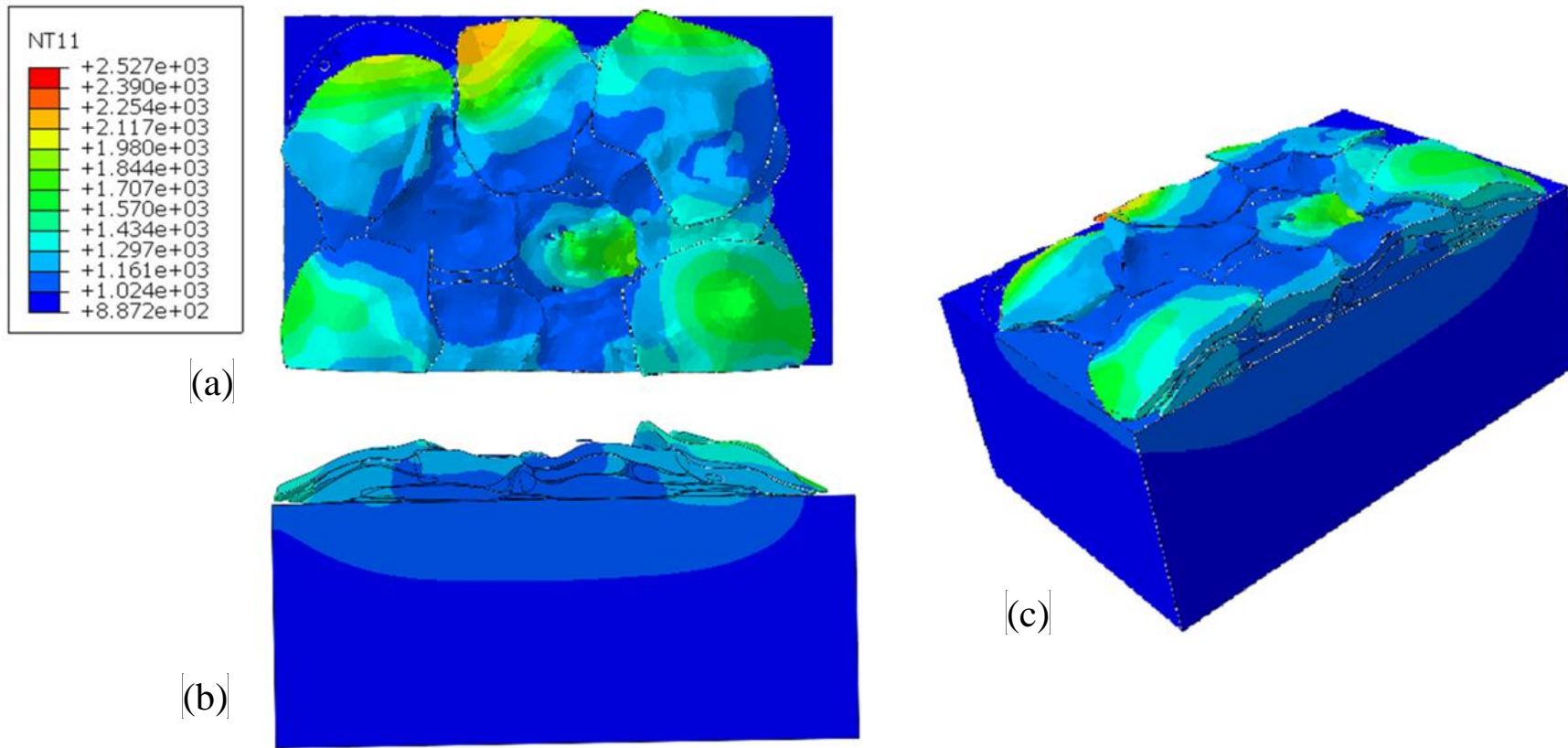


Figure 8-16: (a) Top view, (b) side view, and (c) cross-sectional view of temperature distribution developed after deposition of 5th layer

As shown in Figure 8-17, five points are selected for quantitative analysis of temperature and stress profiles developed along the thickness of coating layer. Figure 8-18 shows the variation of temperature along the thickness direction after solidification of the fifth splat layer. As observed experimentally, the coating layer has a variable thickness due to undulation resulting from interaction of multiple splat layers (shown in Figure 8-18 (a)). Thus, the simulated microstructure has a larger thickness (around 15-30 μm) at points A, C, and D as compared to points B and E (5-10 μm). Figure 8-18 (b) shows that the high-temperature gradient developed along the thickness of coating decreases with increase in coating thickness; thus, resulting in decrease of solidification rate with the deposition of more splat layers. Figure 8-18 (c) and (d) show the variation of temperature during the deposition of the fifth layer at points C and E. It can be seen that, the temperature of the coating layer drops from melting point to lower values during deposition, while that of the substrate rises. There is a sharp drop in temperature at some regions within the coating layer due to the presence of pores or cracks. Consequently, the temperature profile varies from point to point because of the influence of complex geometrical features on temperature distribution.

Figure 8-19 (a) shows the variation of temperature along the width and length of the coating. The thermal gradient developed along those directions is far lower as compared to that along the thickness direction. Consequently, it is expected to have less stress variation along that direction. Figure 8-19 (b) shows that the thermal history of three different points (A, B and E) located at different layers is not only different but highly random due to the complex nature of the process. As observed from the Figure, the temperature at those points overshoots to higher values after a certain time due to several

cycles of reheating caused by the deposition of new splat layers. It is expected for the coating layer to develop complex residual stress field within the coating microstructure due to the strong dependence of temperature with location and process history.

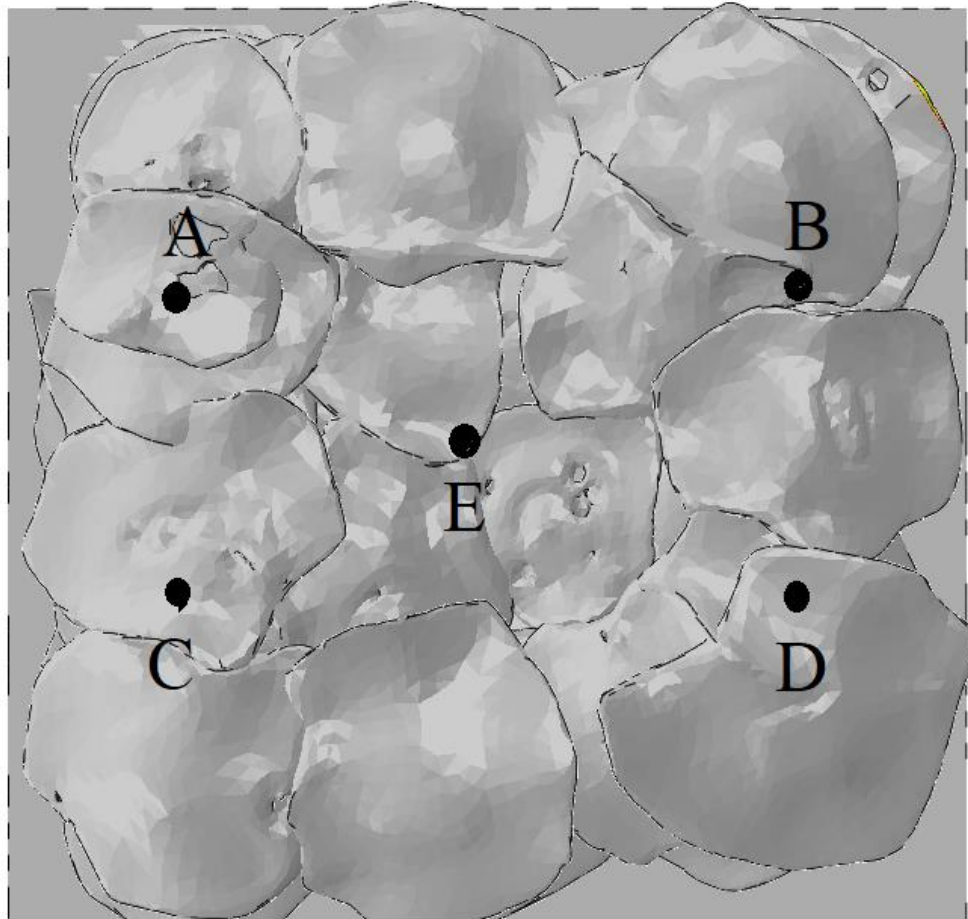


Figure 8-17: Five points selected for the analysis of results

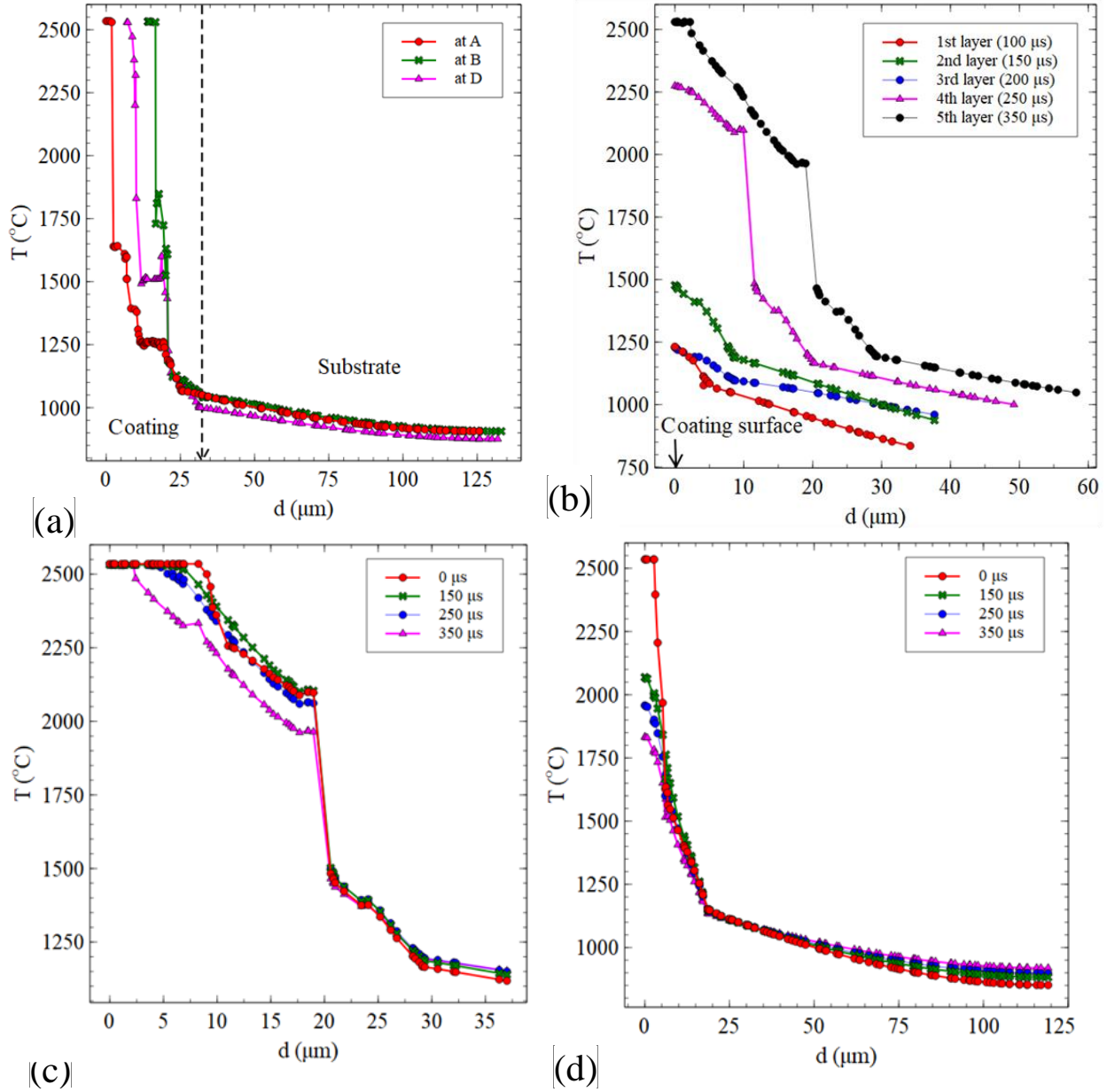
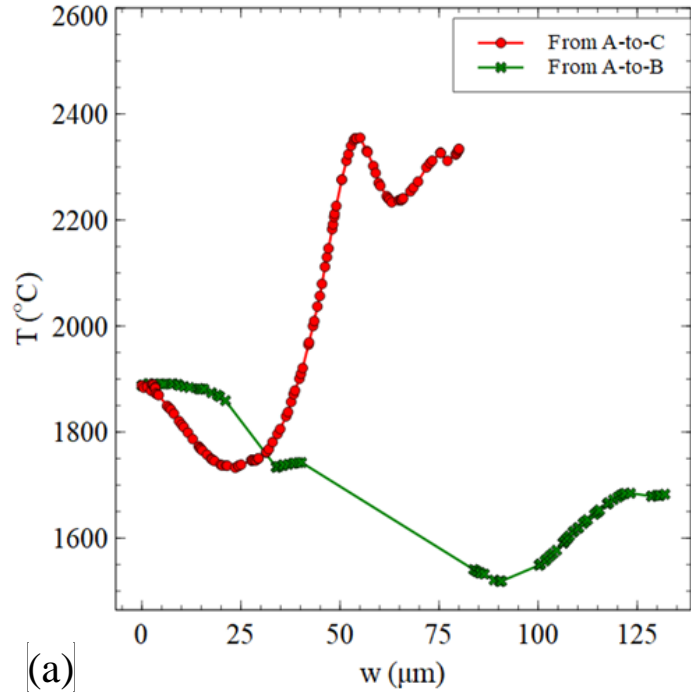
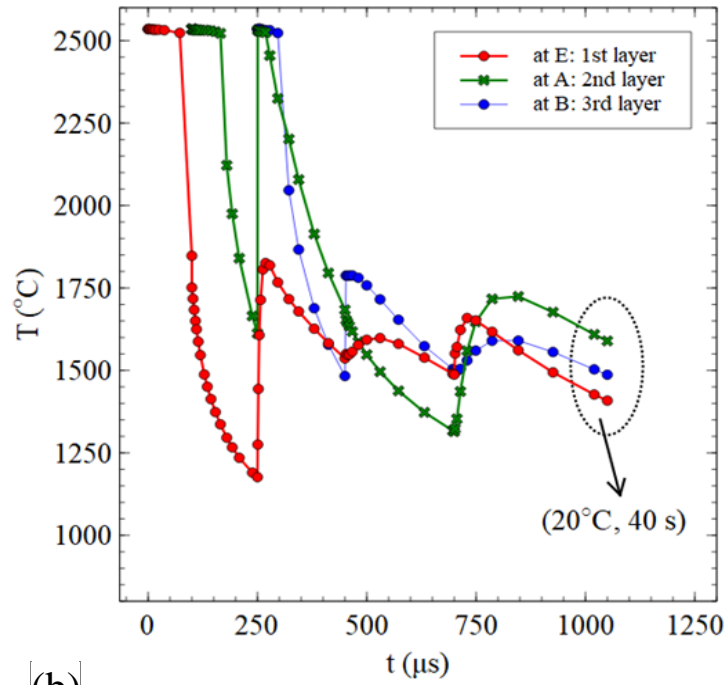


Figure 8-18: Temperature profile developed along depth after deposition of 5th layer, (b) Temperature profile developed along depth after deposition of 1st-5th layer, (c) Evolution of temperature during deposition of 5th layer and (d) Evolution of temperature during deposition of 5th layer



(a)



(b)

Figure 8-19: (a) Variation of temperature along width and length of coating, (b) Thermal history of three different points from start of deposition to end of cool-down

8.4.2 Residual stress evolution

The evolution of residual stress was computed using temperature solution obtained at each time step. Figure 8-20 (a) and (b) show the corresponding quenching stresses developed after the solidification of the second and fourth layer respectively. At the beginning of solidification, deposited splats have near-zero stress values since they are in molten state. However, during solidification, all solidified regions of the coating develop tensile quenching stress with low magnitude of about 30MPa. This low magnitude is attributed to the restriction of stress values with the use of elastic-perfectly plastic material model. This is commonly done to consider stress relaxation by microcracking and interfacial sliding within the ceramic coating layer (as found in previous works [21], [24], [29], [101]). However, unlike with the previous models, quenching stresses predicted here display an uneven field distribution having fluctuation of stress values because of process-dependence and presence of discontinuities. Similar observations can be made with the fifth layer as demonstrated in Figure 8-21 (a). Moreover, the quenching stresses influence the final stress state of the coating layer despite its small magnitude. As demonstrated by Figure 8-21 (b), the von Mises residual stress field shows that very high residual stresses of about 300 MPa are developed at various critical regions within the coating microstructure. The residual stress field is dominated by post-deposition stresses due to the large difference in coefficient of thermal expansions (CTEs) of coating and substrate layers.

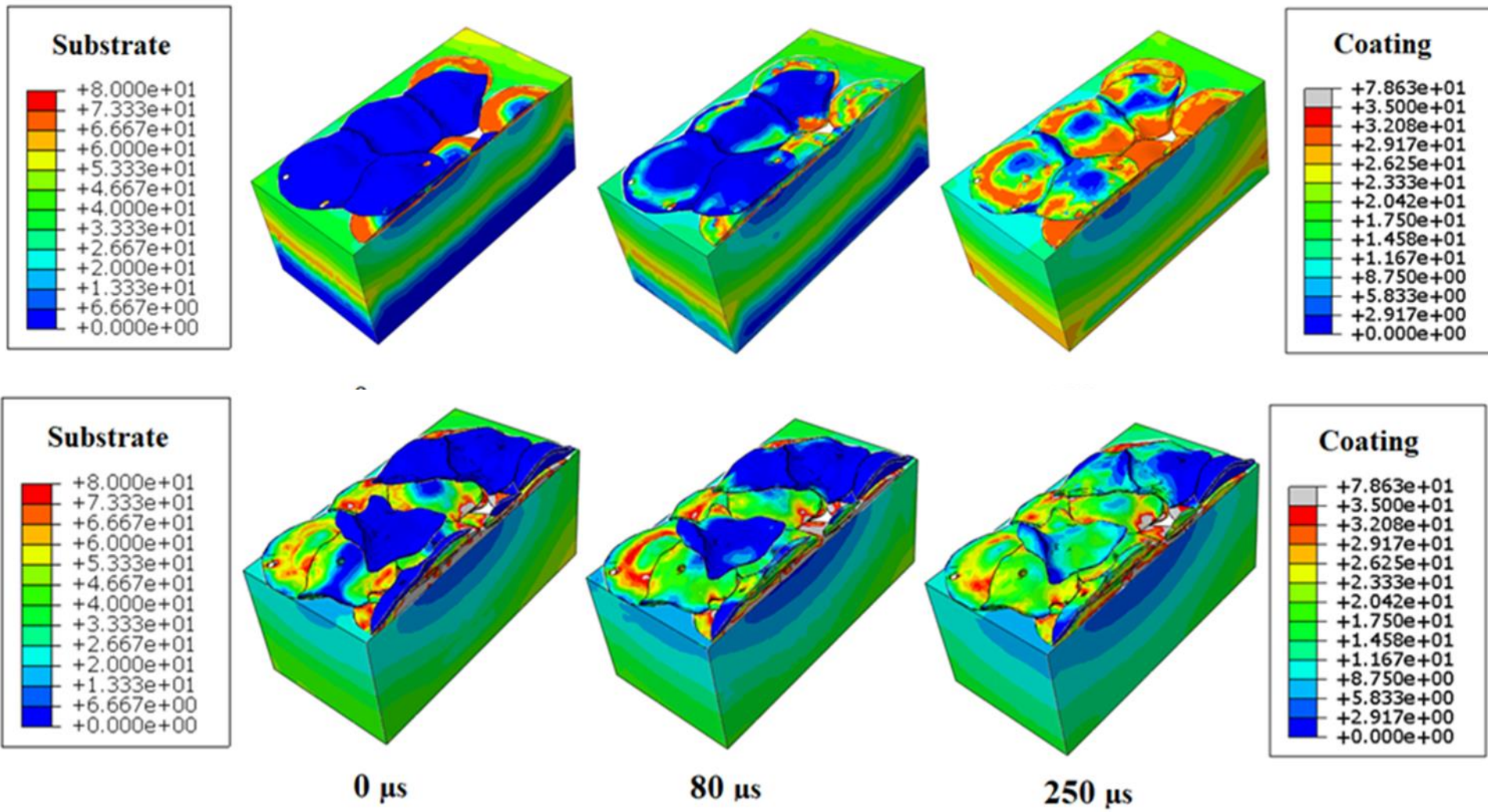


[Figure 8-2: Quenching (von Mises) stress field developed after deposition of (a) second and (b) fourth layer]

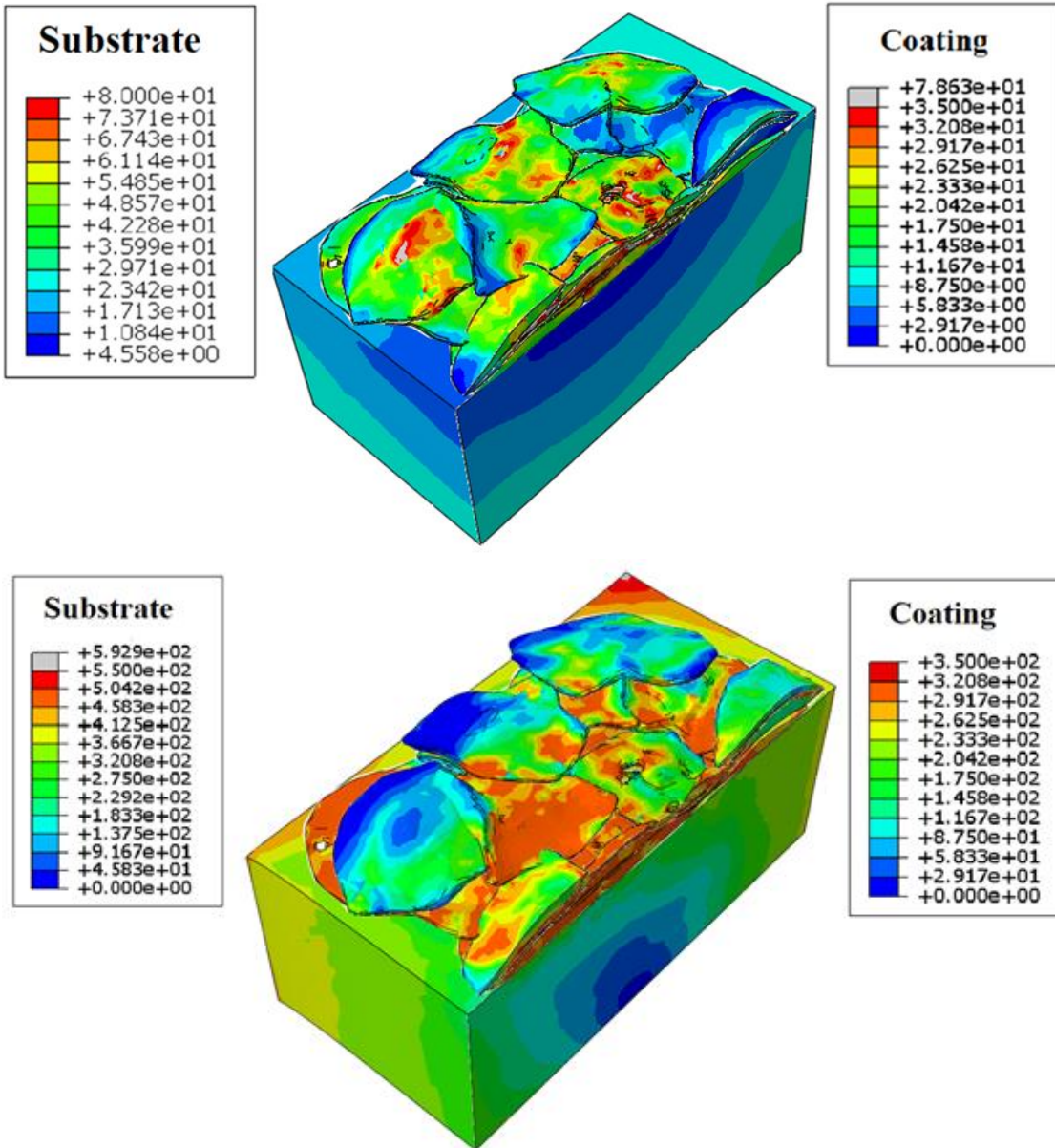


Figure 8-21: Cross-sectional view of von Mises stress field for (a) deposition stress and (b) residual stress in five-layer coating in: (a) x-direction, (b) y-direction

For analysis of results, emphasis is given to in-plane normal stresses due to their significance on coating lifetime. Figure 8-22 (a) and (b) shows the variation of biaxial in-plane deposition and residual stresses developed along the coating thickness. As observed in previous results by Buchmann et al. [65], the in-plane stresses (acting in x and y

directions) are equi-biaxial ,in the sense that, they are almost equal in terms of both magnitudes despite acting in perpendicular directions. This has also been observed from the results of our hole drilling experiment (shown in Figure 8-24). The equi-biaxial nature of the stress profile is attributed to the nature of coating deposition. The coating is usually deposited in a layer-by-layer (or pass-by-pass) manner such that temperature gradient is more predominant along the thickness direction. However, as observed experimentally, minor differences occur between the two orthogonal stress profiles due to the presence of discontinuities (or imperfections) within the coating layer. Figure 8-22 (a) and (b) show that the quenching (deposition) stress developed after splat solidification is tensile with low values attributed to stress relaxation by microcracking and interfacial sliding as previously stated when discussing Figure 8-20. Despite its low magnitude, the quenching stress influences the nature of final residual stress profile especially at the near-interface region of the coating layer.

It is well established in the literature [29] that, ceramic coatings develop very high compressive post-deposition (mismatch) stress because of their low CTE as compared to the underlying substrate. Consequently, compressive residual stress is developed in ceramic coating layer due to the dominance of mismatch (compressive) stresses over the low quenching (tensile) stresses. Thus, the residual stress profiles shown in Figure 8-22 (a) and (b) display equi-biaxial compressive stress values that increase with depth of coating layer. Also from the figures, it can also be seen that the residual stress profiles are fairly comparable to results obtained with Tsui and Clyne analytical model [99] for a coating layer deposited in 5 steps. The inputs to the analytical model were: elastic properties given in Table 4-1, intrinsic (quenching) stress of 30 MPa, and same

geometrical dimensions as used in numerical simulations. As elastic material model with temperature independent material properties was used to derive the analytical model, it is observed that deviation exists between the results obtained analytically and numerically especially at regions close to the interface. The analytical model overestimates the residual stress profile due to the assumptions made during derivation. Thus, for more realistic residual stress prediction, it is necessary to consider the non-linear material behavior of the coating and substrate layers. For ceramic coating layer, the presence of pores and microcracks considerable affects the residual stress profile. For metallic coatings, plastic deformation influences the stress profile more than pores and cracks. In all cases, it is essential to model the steel substrate layer with robust material model that considers plastic deformation with proper strain hardening criterion. The high compressive residual stress developed near the coating interface improves the adhesion strength of coating layer. As found in previous studies [99], [101], Figure 8-22 (a) and (b) shows that the compressive residual stress developed within the coating layer is balanced by corresponding tensile stresses on the substrate side due to mismatch of structural properties at the coating-substrate interface. Specifically, Figure 8-22 shows that the in-plane residual stresses developed at the interface (in x/y directions) are -110/-130 MPa and 310/370 MPa on coating and substrate side respectively. The large difference between the two interfacial stresses (in terms of magnitude and direction) signifies the influence of residual stresses on the adhesion strength/lifetime of coatings. The equibiaxial compressive stresses (shown in Figure 8-22) are very comparable to the results of our hole drilling experiment and that of previous studies [65], [99], [101], [102], [192]. As demonstrated in Figure 8-24, the current stress results fall within the expected range

of stress values based on experimental measurements conducted with incremental hole drilling set-up. It is not possible to quantitatively match the numerical and experimental stress profiles due to obvious stochastic presence of defects and limitations of developing samples with only 35 μm -thick coating deposits considered for the numerical simulation. In future works, the numerical framework presented here shall be used to predict the evolution of residual stress in simulated coating layer having more realistic thickness.

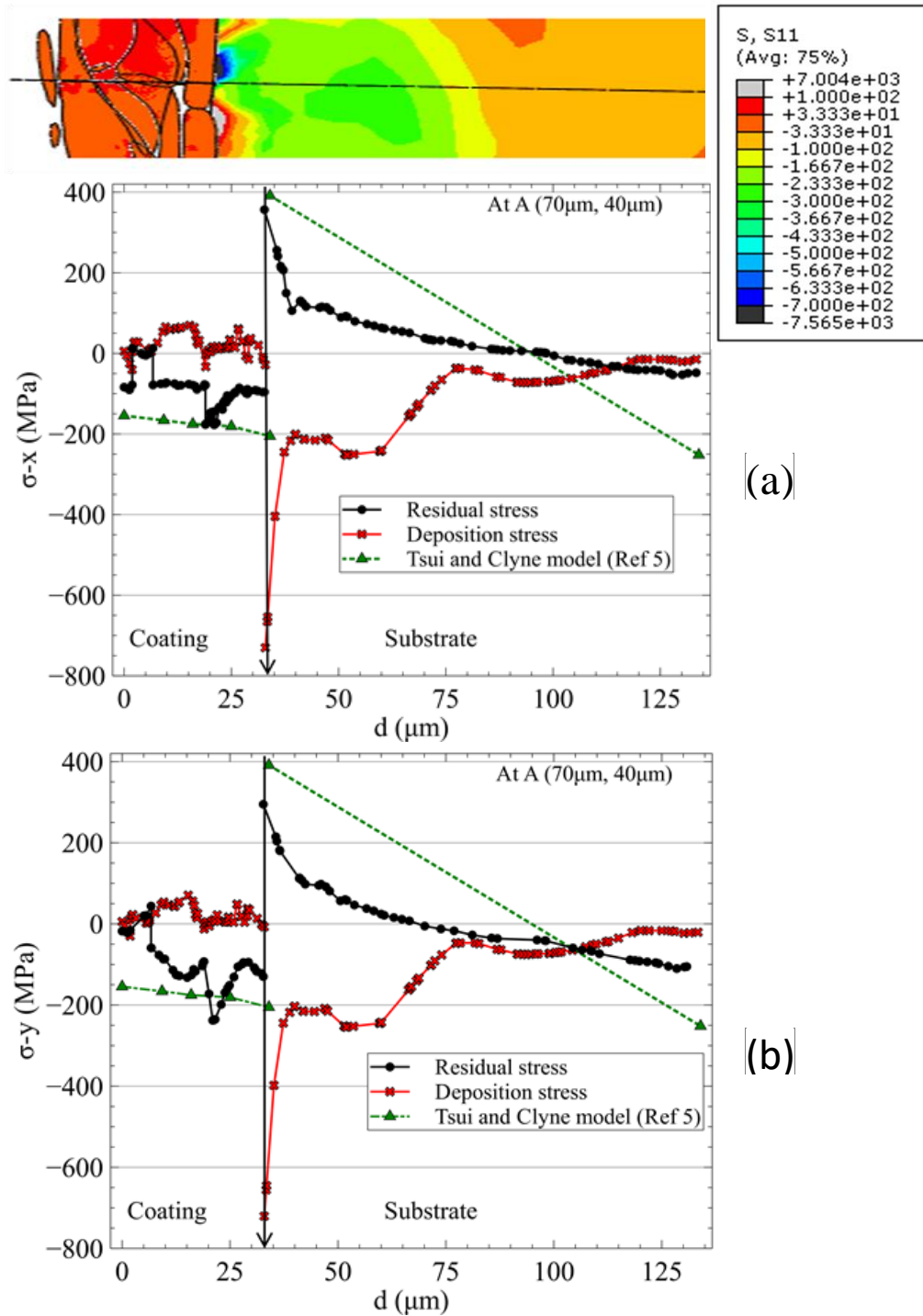


Figure 8-22: Bi-axial in-plane stress profiles at A: (a) stress in x-direction, and (b) stress in y-direction

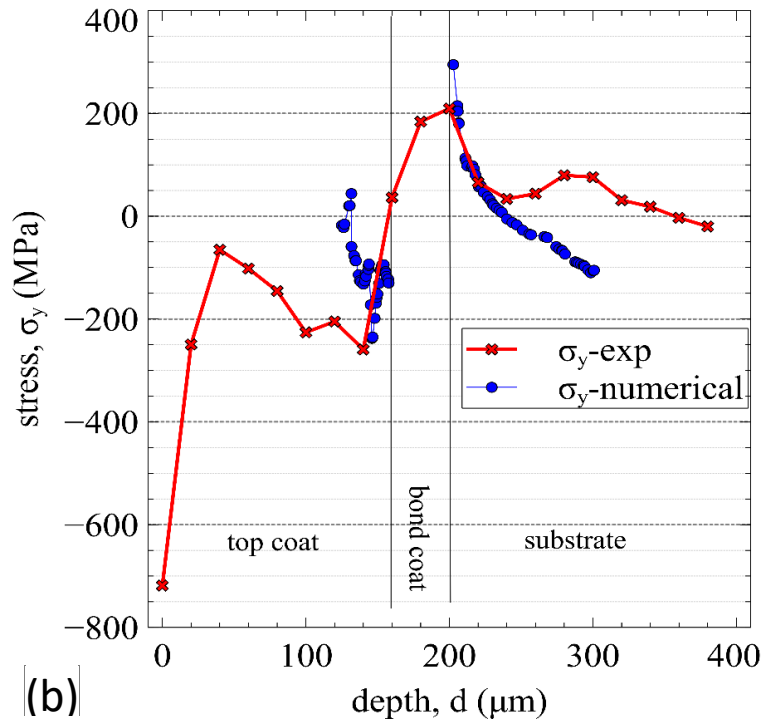
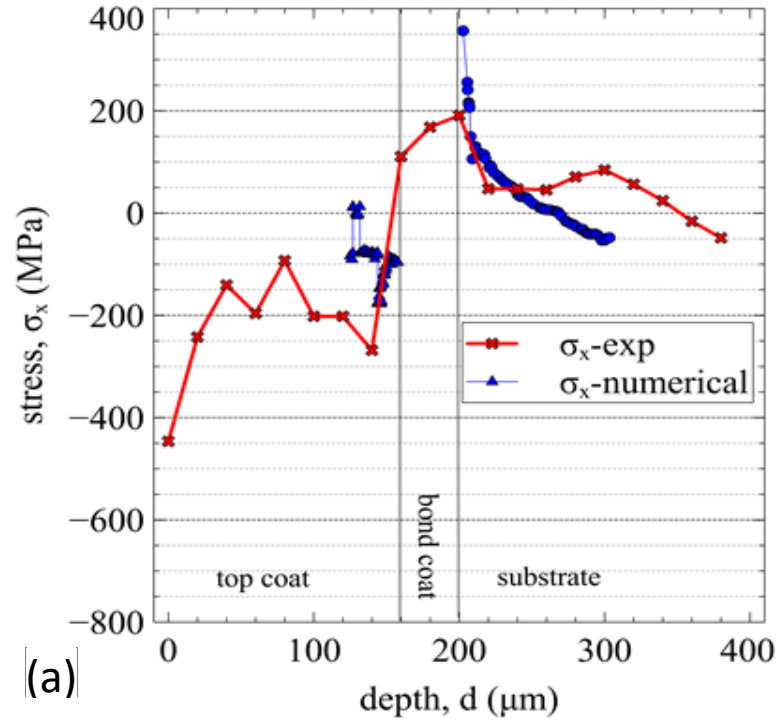
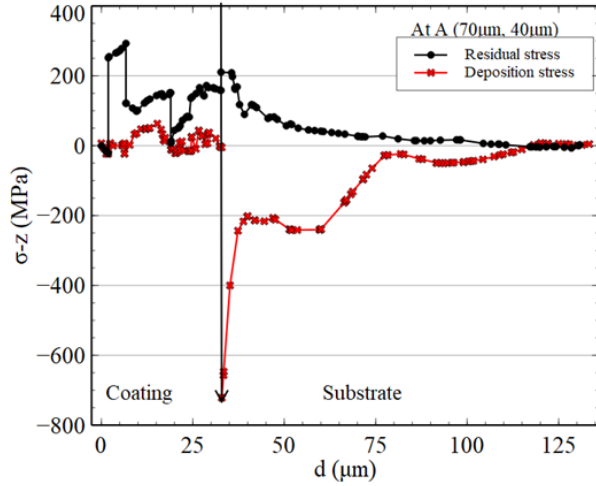
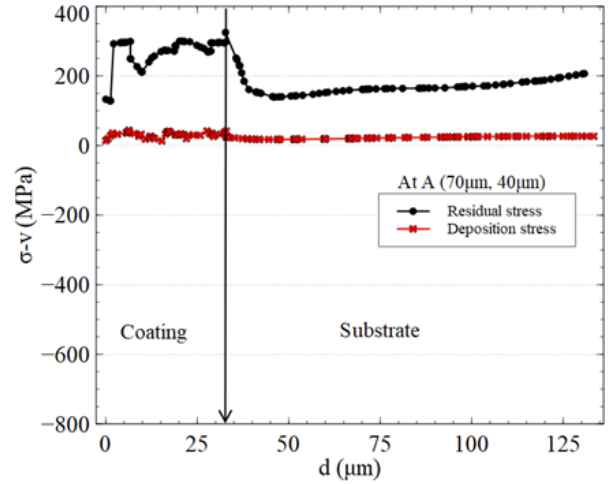


Figure 8-23: Comparison of residual stress profile (at A) with experimental results: (a) Stress in x-direction and (b) Stress in y-direction

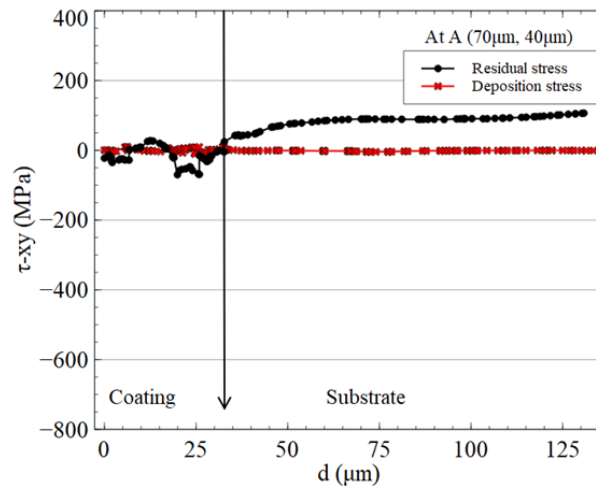
Figure 8-25 shows the variation of other stress components along the thickness of the coating and substrate layers at point A. The normal (out-of-plane) residual stress acting in the z-direction is considerably high and tensile especially at regions near the interface (as shown in Figure 8-25 (a)). The difference between the in-plane stresses developed at the interface on coating and substrate sides is small as compared to that of the equi-biaxial stresses explained previously. Consequently, the coating is weaker with loadings in z-direction than in other directions. As further confirmed by Figure 8-25 (b), it can be observed that the various stress components add up to result in higher von Mises stress variation along the coating thickness. The developed shear stresses are found to be very low with the xy-shear residual stress being the highest (shown in Figure 8-25 (c)). The maximum principal stress, shown in Figure 8-25 (d), seems qualitatively like the normal stress component in the z-direction. A similar observation is made at other locations as shown in Figure 8-25 to Figure 8-28. Figure 8-29 (a) shows that, despite the low temperature gradient along the width/length of coating layer, there exists fluctuation of stresses to within same range of values due to obvious presence of discontinuities at random sites within the coating microstructure. The expansion and contraction of the substrate are tracked (at base) during splats solidification (i.e. second regime) and post-deposition cooldown (i.e. third regime) respectively (as shown in Figure 8-29 (b)). As expected, substrate expansion during splats solidification is not very significant due to localization of heat near the interface. However, during post-deposition cooldown stage, the substrate contracts considerably due to rapid decrease in temperature throughout the substrate layer.



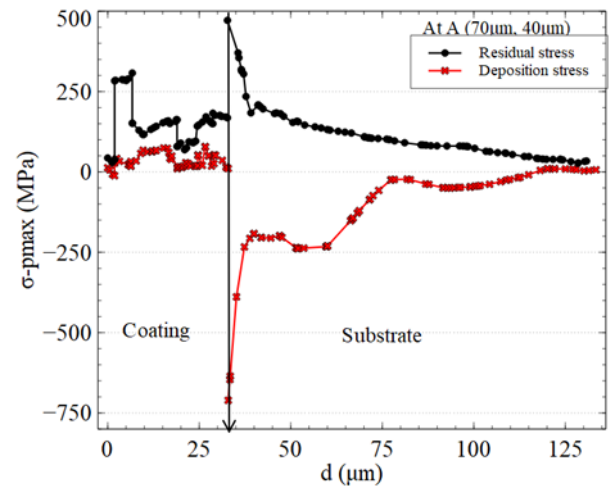
(a)



(b)

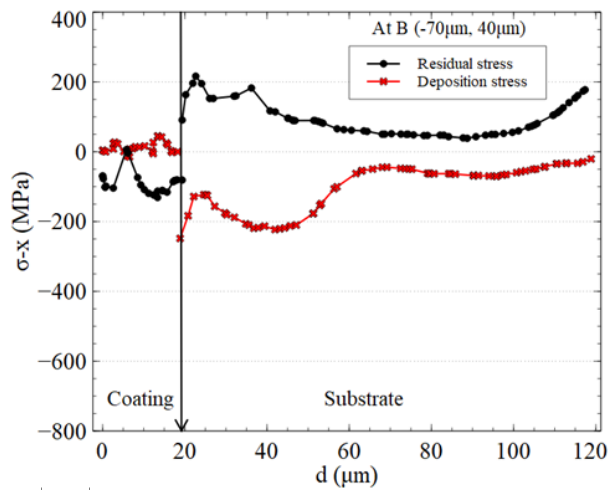


(c)

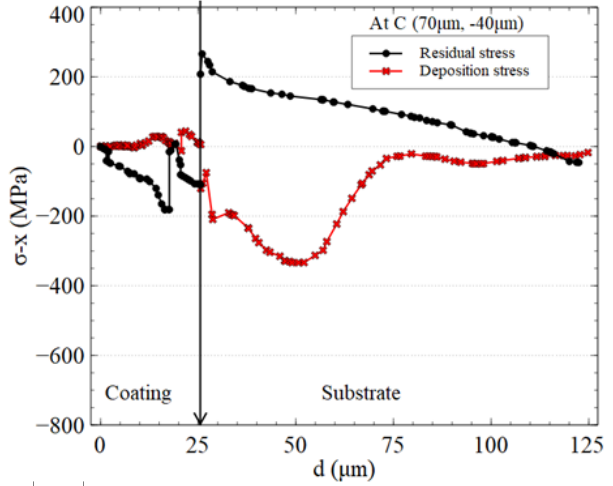


(d)

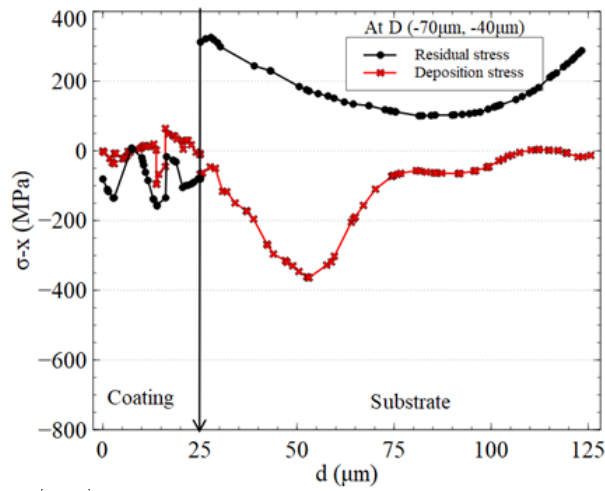
Figure 8-24: Comparison of stress profiles developed along point A: (a) in-plane normal deposition and residual stresses (acting in the z-direction), (b) von Mises deposition and residual stresses, (c) shear deposition and residual stress profile (acting in the xy-direction), and (d) maximum principal deposition and residual stress profile



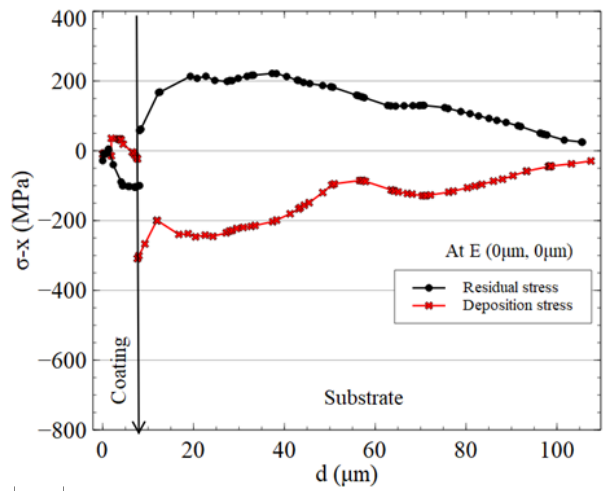
(a)



(b)

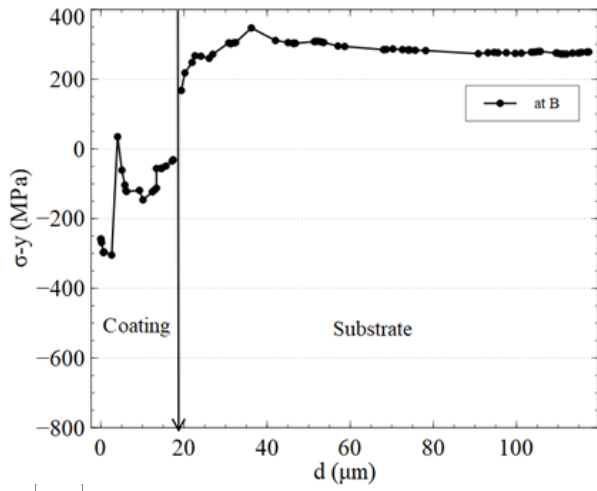


(c)

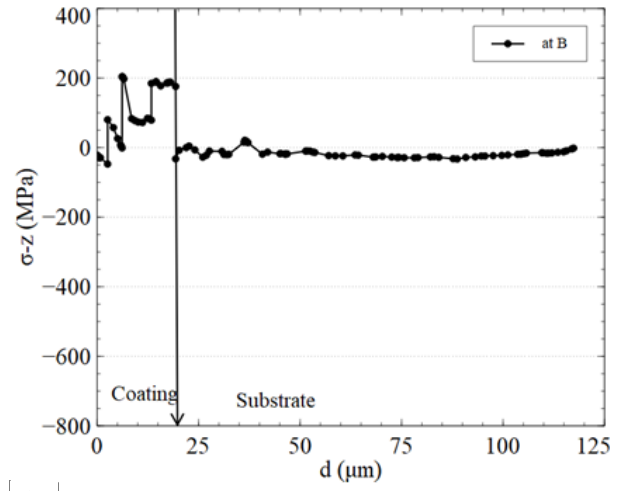


(d)

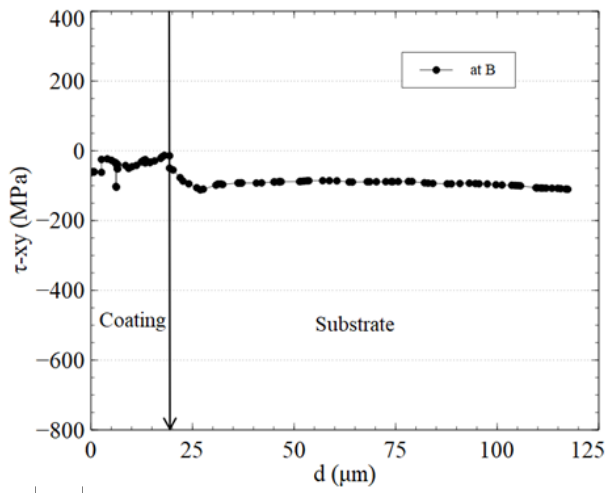
Figure 8-25: Comparison of bi-axial in-plane stress profiles (acting in the x-direction) developed along various points: (a) B, (b) C, (c) D, (d) E



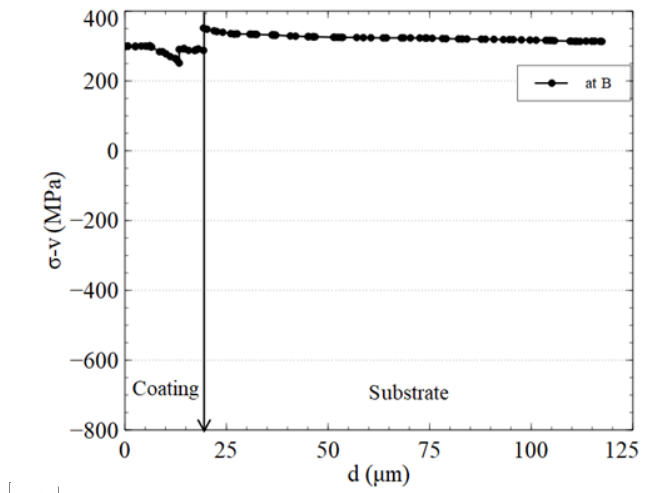
(a)



(b)

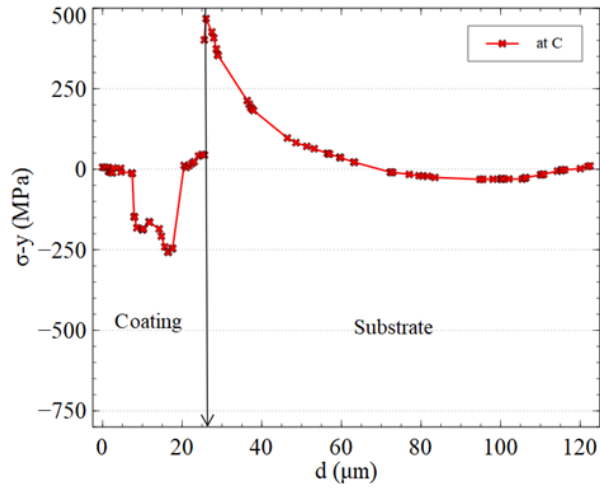


(c)

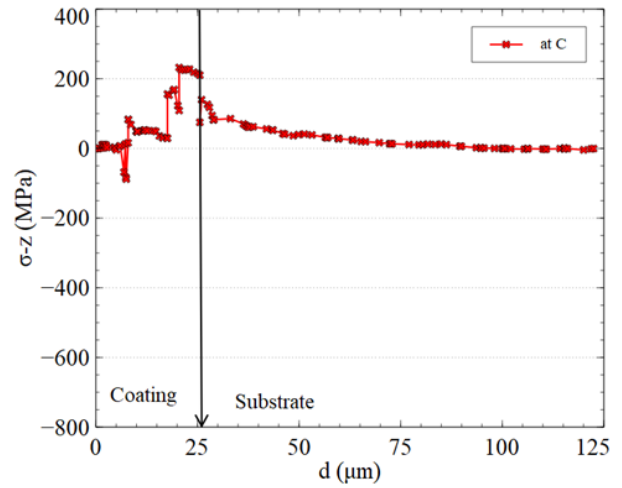


(d)

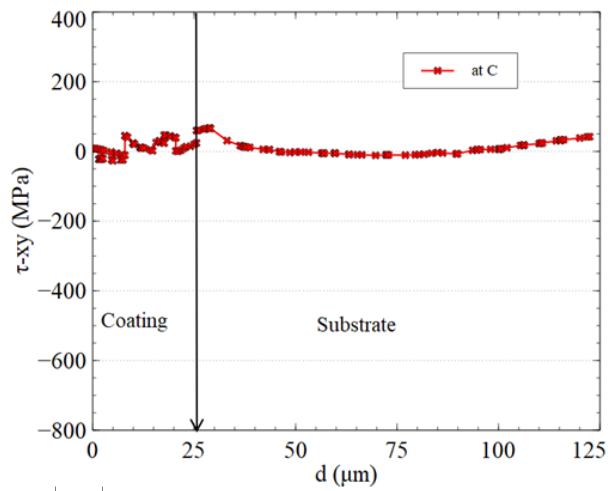
Figure 8-26: Comparison of residual stress profiles at point B: (a) in y-direction, (b) in z-direction, (c) shear in xy-direction, (d) von Mises



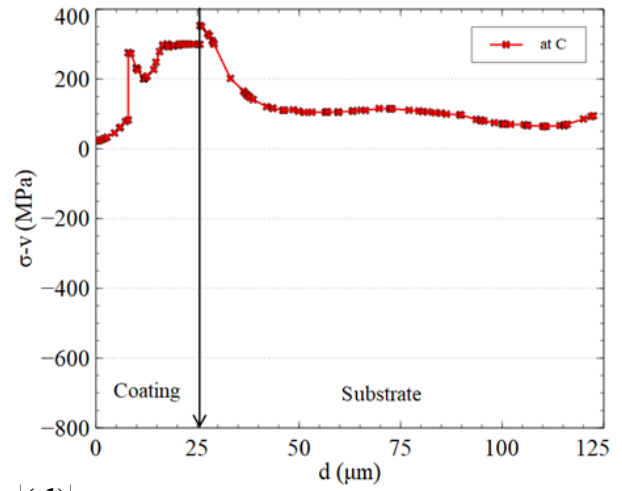
(a)



(b)

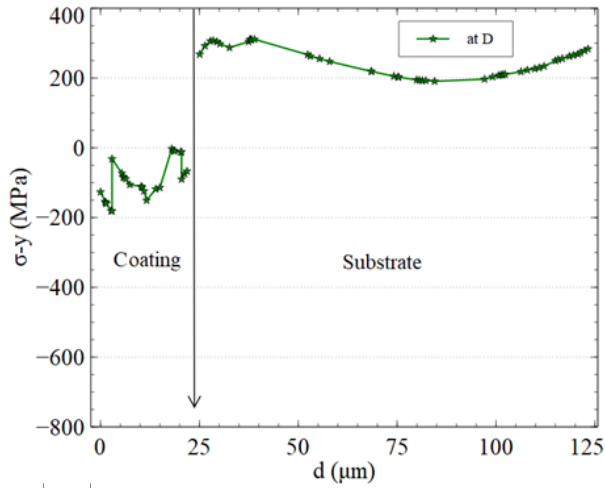


(c)

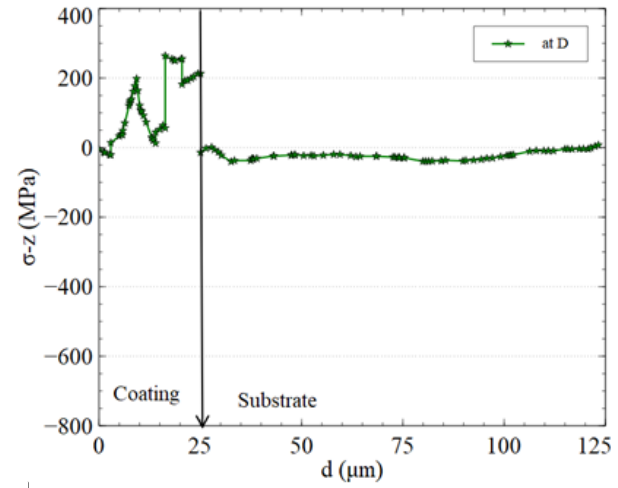


(d)

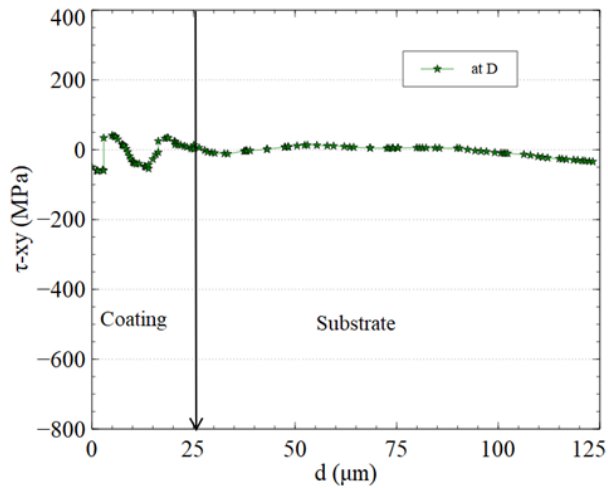
Figure 8-27: Comparison of residual stress profiles at point C: (a) in y-direction, (b) in z-direction, (c) shear in xy-direction, (d) von Mises



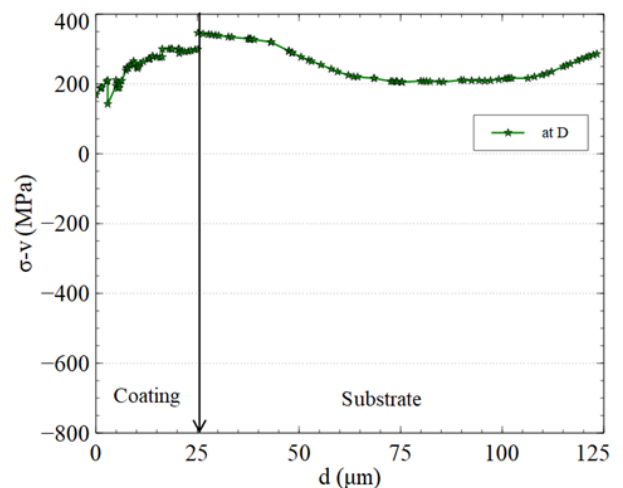
(a)



(b)

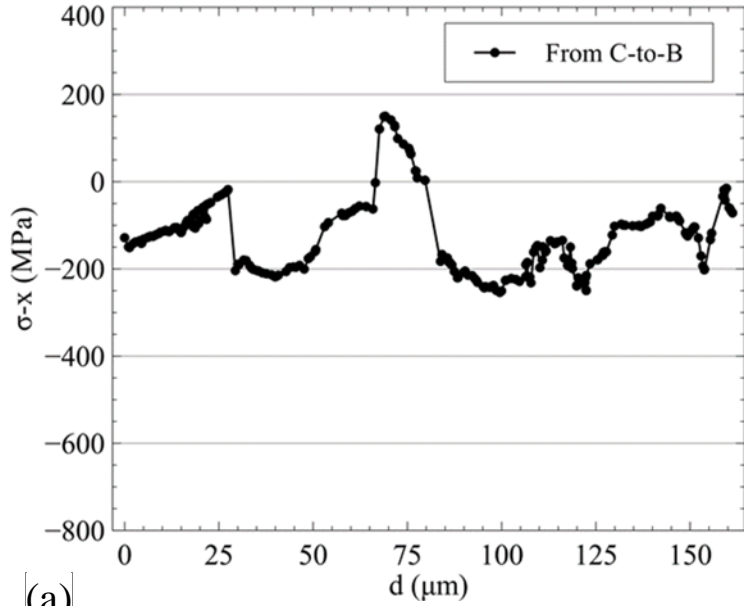


(c)

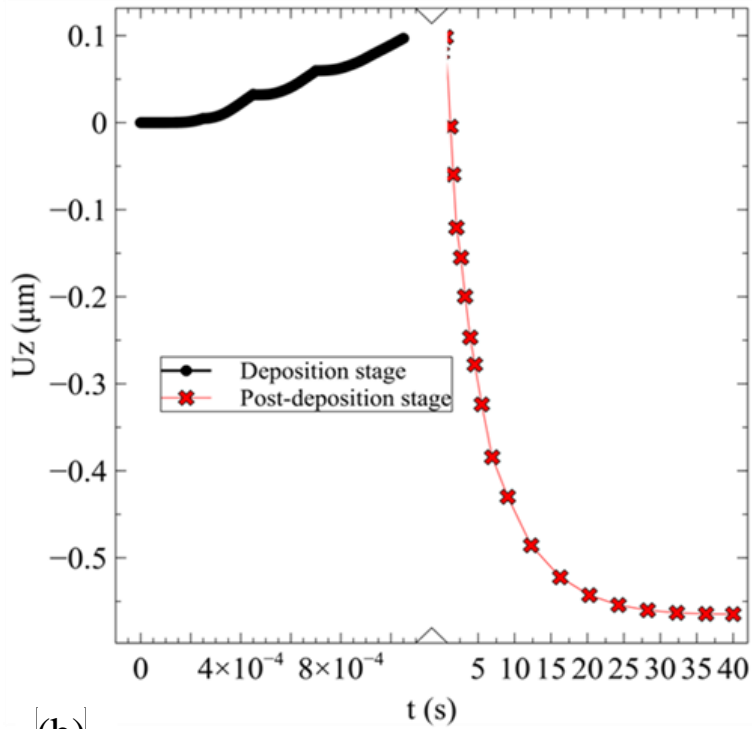


(d)

Figure 8-28: Comparison of residual stress profiles at point D: (a) in y-direction, (b) in z-direction, (c) shear in xy-direction, (d) von Mises



(a)



(b)

Figure 8-29: Bi-axial in-plane residual stress profile (acting in the x-direction) from C-to-B at 10 μm above interface, (b) Downward displacement of coating-substrate layers (in positive z-direction) during deposition and post-deposition stage.

8.5 Numerical difficulties commonly encountered with the splat-by-splat model

The splat-by-splat (or layer-by-layer) analysis discussed in section 8.3 has given us more insight on the feasibility of using the hybrid model to predict residual stresses developed in TSCs. The analysis involved residual stress computation in five layers of splats deposited up to average thickness of about 30 μm . The results can be used for advanced analysis with focus on detailed investigation of mechanism for residual stress development in coatings. However, the coating samples described in section 7.1 have a minimum thickness of about 130 μm . Due to thickness dependence of residual stress, there is need to run the hybrid model up to about 25 splat layers to effectively predict residual stress developed in the coating. Based on the results obtained, we found that the computational resources required for such task are enormously high. First, the number of degree of freedoms increase drastically resulting into solving billions of equations. With the need to have fine mesh for convergence of solution near the various sharp features (or stress concentration regions), the issue of computational time is even more worrisome. Furthermore, an attempt was made to numerically predict residual stress and microcracks during deposition of five-layer YSZ coating (as done for the case of single splats). However, several computational difficulties such as convergence problem due to element distortion, extremely smaller time increment, and instability of solution were encountered. Therefore, there is need for development of an effective strategy of modeling the stresses up to the full coating thickness. This can only be achieved by reducing the number of stress concentration regions through merging of splat interfaces as discussed in Chapter 9.

8.6 Concluding remarks

In the present study, the new hybrid computational approach has been used to model multiple splats interaction and residual stress evolution in YSZ coating deposited on stainless steel (SS310). With a five-layer model, it has been shown that, the approach can predict evolution of coating microstructure that contains various imperfections which lead to local variation of residual stresses. The following conclusions can be derived from the work:

- multiple splats interaction affects not only the resulting splat geometry but also the temperature distribution and residual stress field.
- the undulation of the target surface affects the residual stress field developed in the coating layer especially near the interface.
- the use of realistic process parameters leads to a more reliable estimation of residual stresses. As observed experimentally, we have predicted a residual stress profile that is non-linear along the length and thickness of the coating. Specifically, it is found that the discontinuities such as pores and cracks lead to local stress relaxation in various regions within the coating layer. The relaxation of the residual stress field weakens several regions within the coating which can serve as a source of damage initiation while in active service.

Therefore, the modeling approach proposed here will be helpful in future works related to process optimization and quality assessment in TSCs. After further improvement of the proposed approach, it will pave way for new openings on residual stress and failure analysis in TSCs.

CHAPTER 9

EFFECTIVE PREDICTION OF RESIDUAL STRESS IN MULTILAYERED COATINGS

As discussed in section 8.5, the numerical prediction of residual stress developed in thick coatings with the layer-by-layer model is very intensive. Computational time is prolonged due to large number of degree of freedoms (or high mesh density) resulting from the presence of hundreds of splat interfaces, sharp reentrant features and other high stress concentration regions. Therefore, in the present section, the hybrid model is extended to the case of thick coatings to optimize computational time without compromise on quality of results. This is necessary if the model is to be used for the design of coatings.

For real thermal spraying, deposition is done pass-by-pass whereby multiple droplets are sprayed unto the substrate surface simultaneously. Each deposition pass is often composed of 3-5 splat layers (i.e. about 25-35 μm thick) which are subjected to similar thermal cycle. Therefore, it is more realistic to merge the interfaces of splats sprayed during each pass as done with the new scheme developed here. The new scheme is used to numerically predict residual stress and damage in the thick ceramic (YSZ) and metallic (Ni-20%Al) coatings considered in chapter 6. The temperature distribution developed during solidification are first predicted. Then, the residual stress and damage developed after the deposited coating and substrate layers are cooled to room temperature are

predicted. The results obtained from the analysis are found to be in good comparison with that of hole drilling experiments presented in chapter 6.

9.1 From point cloud to merged-mesh model

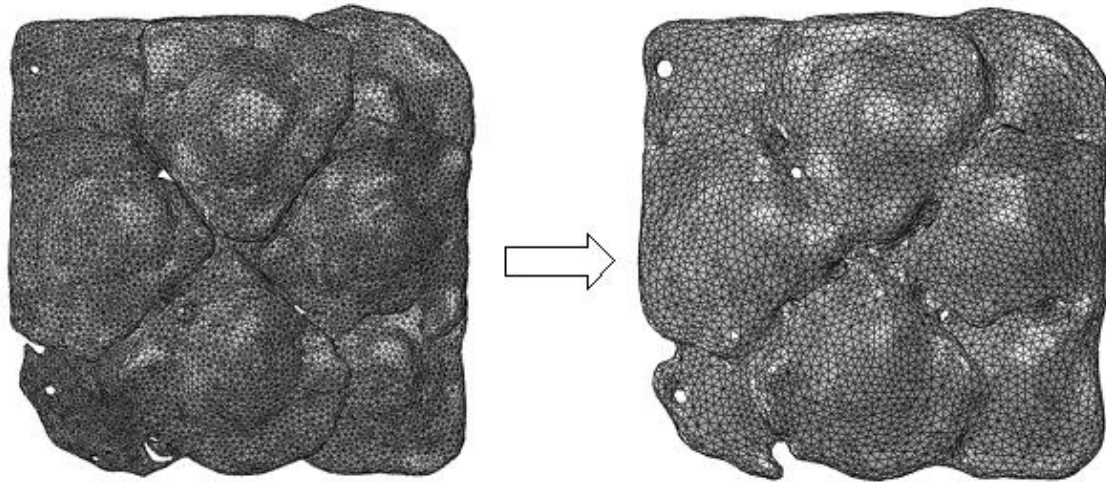
As done in chapter 8, the point cloud model is first used to deposit multiple layer of droplets on the substrate surface. Splats formed within each layer are converted to meshed domains using the methodology discussed in section 4.4. The deposition-conversion cycle is done up to 3-5 layers until reaching the thickness of a typical coating pass. Then, the various interfaces of the corresponding splat domains are merged such that the number of interfaces and discontinuities are reduced (for each pass). This is valid assumption because, during each pass, there is partial re-melting of pre-solidified splats. Therefore, the process model needs to be simplified further to that of pass-by-pass modeling to achieve more realistic results.

Figure 9-1 to Figure 9-4 demonstrates the conversion of combined splat meshes into a single pass mesh. It can be seen that, splat mesh interfaces are effectively merged after the conversion while still retaining the various sharp corners, holes, gaps and other imperfections present in the coating microstructure. This conversion is achieved using the surface-to-volume mesh algorithm (available in Meshmixer). Further demonstration of the conversion is shown in Appendix, Figure A1-A4. Some of the computational advantages of the pass mesh model includes: reduction in number of DOF (e.g. from average of 2,213,605 to 446,904 DOF. as shown in Table 9-1), improvement in overall element quality (or aspect ratio) and increase in time increments for convergence of Newton iterations. Therefore, the multi-pass model is more effective in predicting the

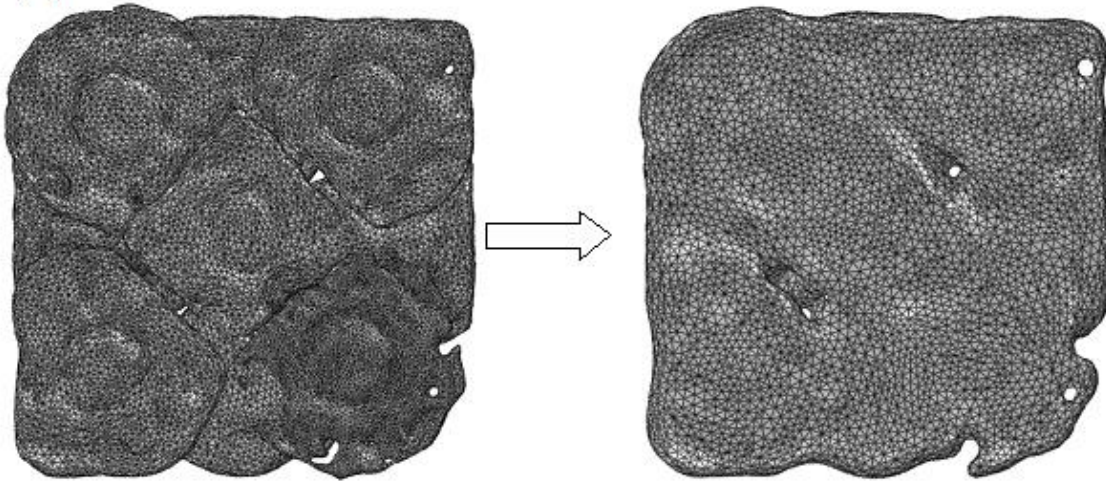
evolution of temperature, residual stress and damage in TSCs. Thus, the multi-pass model can be used carry out extensive study of the relationship between process parameters, coating microstructure and residual stress in TSCs.

Table 9-1: Comparison of degree of freedoms (dof) of layer-by-layer mesh with that of merged mesh

S/N	Pass name	No. of droplets deposited	No. of dof. in layer-by-layer mesh	No. of dof. in merged mesh	Average thickness (μm)
1	Pass-1	14 (in 3 layers)	532,008	112,347	35
2	Pass-2	10 (in 3 layers)	450,247	98,756	27
3	Pass-3	15 (in 4 layers)	690,675	120,456	42
4	Pass-4	12 (in 3 layers)	540,675	115,345	32
Total			2,213,605	446,904	136



(a)



(b)

Figure 9-1: Conversion to merged mesh for Pass-1: (a) top view and (b) bottom view (LEFT-layer-by-layer mesh, RIGHT-merged mesh)

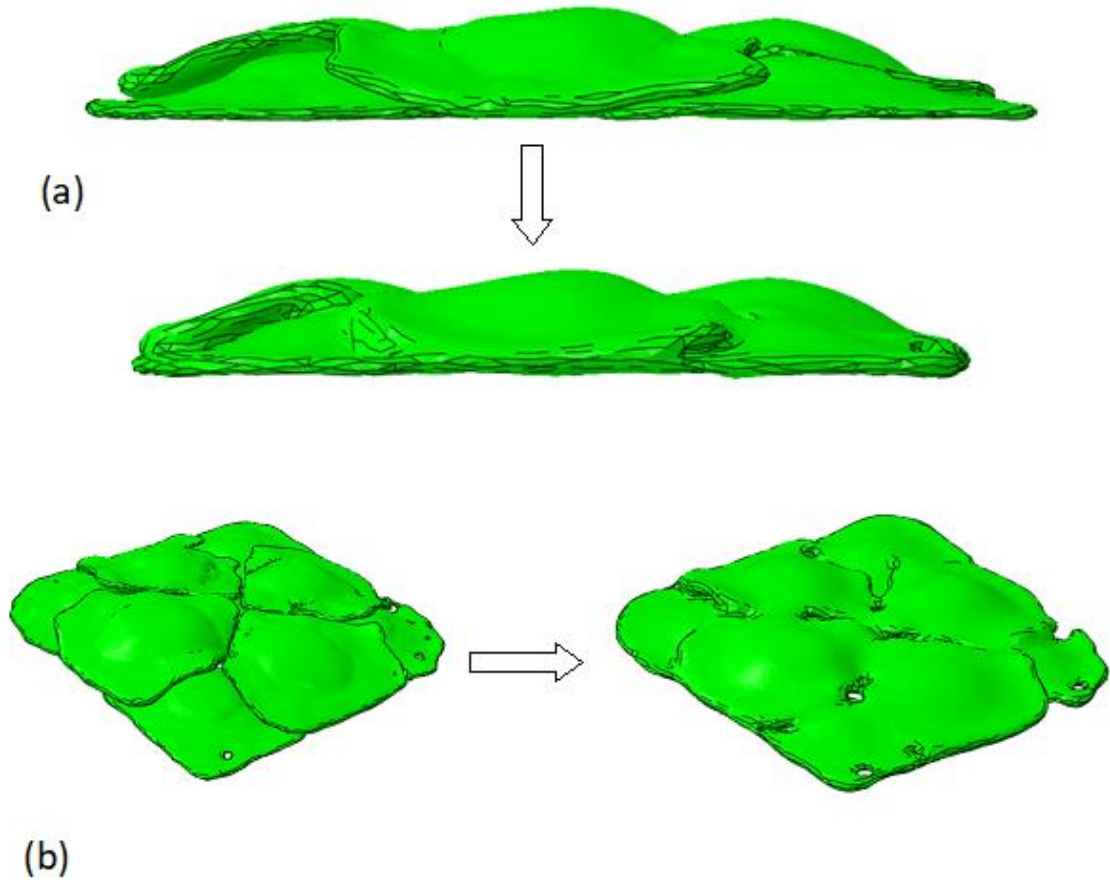
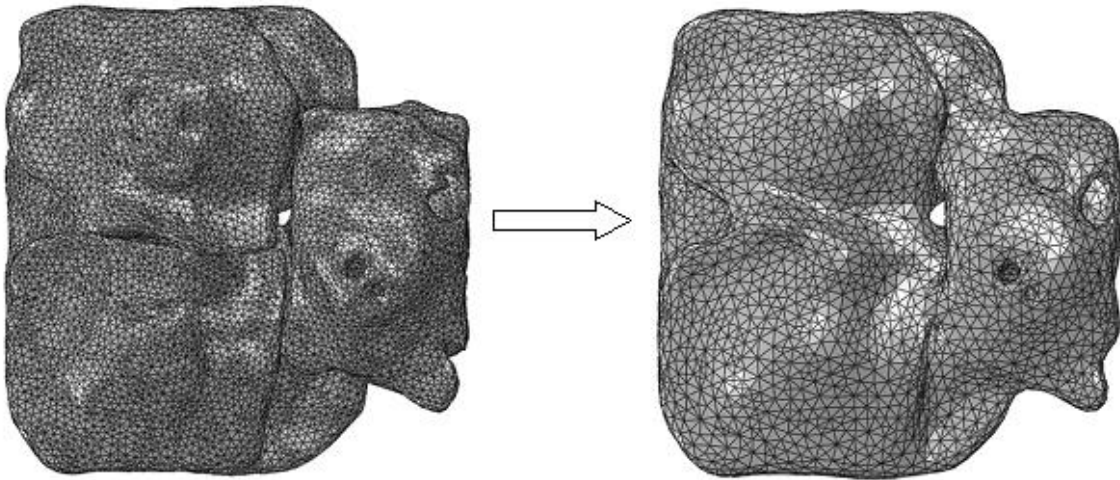
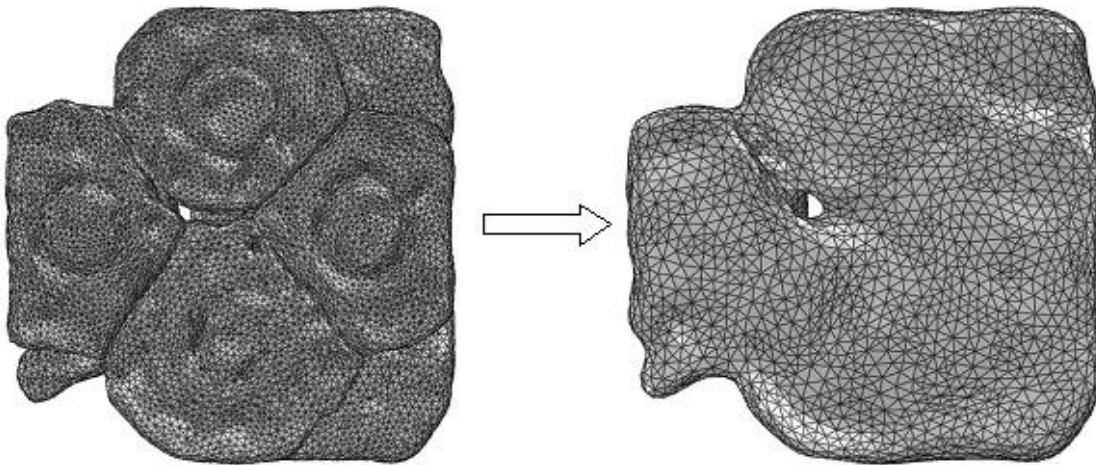


Figure 9-2: Conversion to merged mesh for Pass-1: (a) side view and (b) isometric view (TOP-layer-by-layer mesh, BOTTOM-merged mesh)



(a)



(b)

Figure 9-3: Conversion to merged mesh for Pass-2: (a) top view and (b) bottom view (LEFT-layer-by-layer mesh, RIGHT-merged mesh)

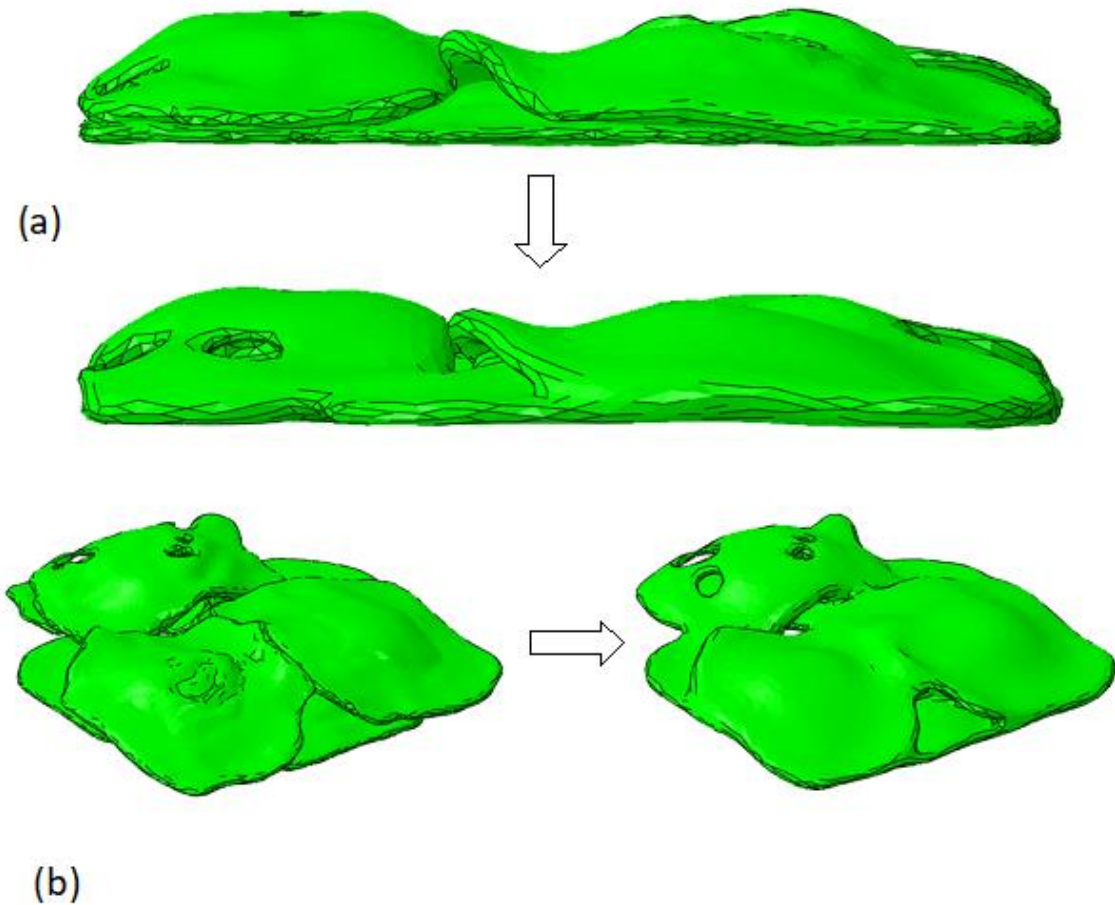


Figure 9-4: Conversion to merged mesh for Pass-2: (a) side view and (b) isometric view (TOP-layer-by-layer mesh, BOTTOM-merged mesh)

Using the new scheme developed here, the growth of coating microstructure is simulated up to 4 passes. Each pass is consisting of 3-5 splat layers deposited using random values of initial droplet properties previously given in Table 5-1. The average thickness of pass is within 25-35 μm . This is consistent with the actual pass thickness for the real coating samples. During the real spray process, controlling the coating thickness is often difficult due to the complex interaction of sprayed droplets; thus, resulting in the high surface roughness observed experimentally (presented in Chapter 6). From Figure 9-6, it can be seen that the high surface roughness previously predicted with the multilayered model is still retained with the multi-pass model despite the merging of splat interfaces. Also, the

figure shows that the simulated coating microstructure, conventionally known as the representative volume element (RVE), contains the various defects or discontinuities that were typically observed experimentally (presented in Chapter 6). The coating RVE has an average thickness of about $140\ \mu\text{m}$ and the surface is filled with random features corresponding to the rough surface observed experimentally. The deposition is numerically controlled such that the planar dimensions of the RVE (i.e. width and length) are almost equal to that of the substrate dimensions, $300\ \mu\text{m} \times 300\ \mu\text{m}$. It is important to note that, the substrate dimensions were optimized through repetitive finite element analysis (not shown here).

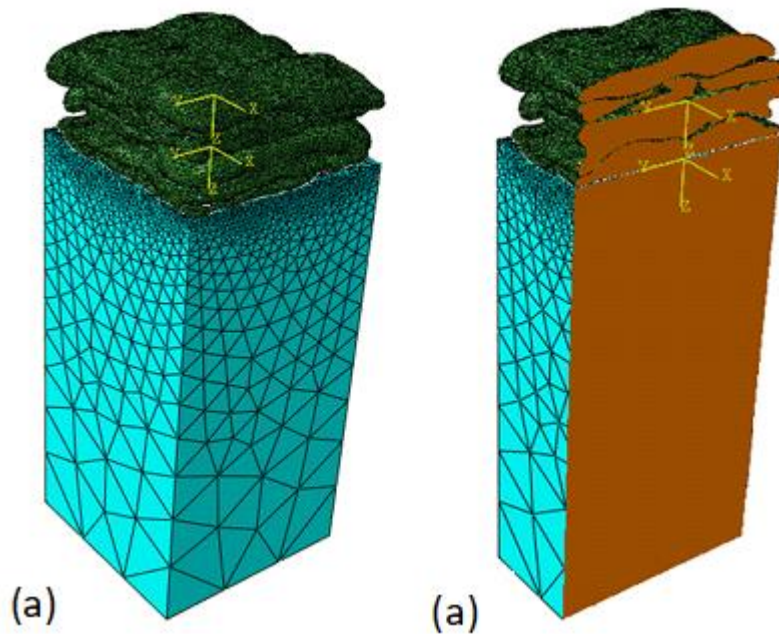


Figure 9-5: (a) 3D view of simulated coating microstructure, (b) 3D cross sectional view of simulated coating microstructure

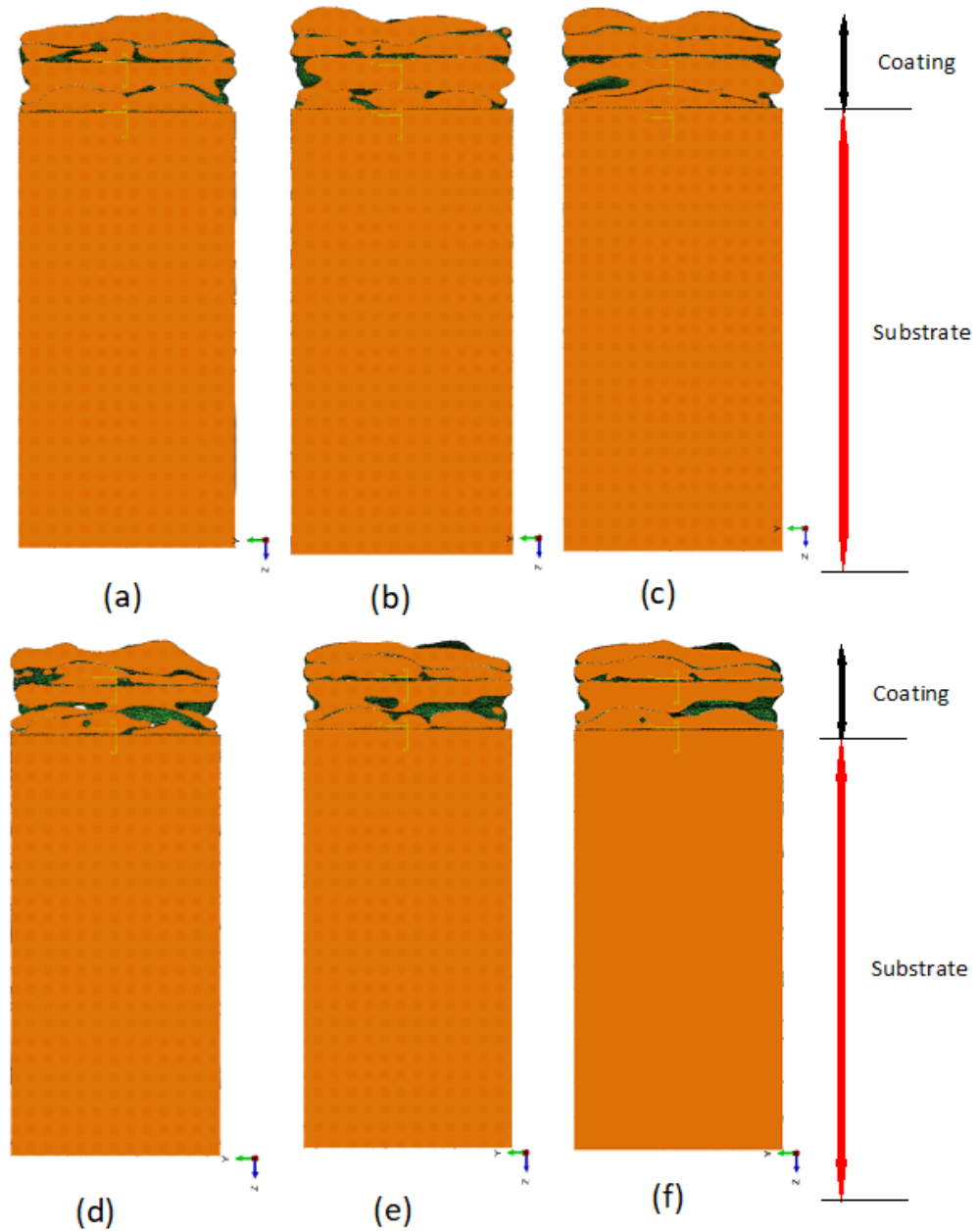


Figure 9-6: Cross sectional views of simulated coating microstructure at the cut planes along: (a) $x=125$ mm, (b) $x=100$ mm, (c) $x=74$, (d) $x=-75$, (e) $x=-100$, and (f) $x=-125$.

9.2 Numerical prediction of temperature distribution and residual stress developed in conventional YSZ coating deposited on SS310

In this section, the multi-pass model is used to predict the evolution of temperature and residual stress during the deposition of YSZ coating on SS310 stainless steel (based on four passes). To simplify the complexity of analysis, the thin bond coat interlayer is not considered for the analysis. This is valid considering that the properties of the metallic NiCrAl coating are not very different from that of the metallic substrate. After conducting several analyses, it is found that the temperature distribution in the coating layer homogenized very fast such that each pass can be made to have uniform initial (deposition) temperature. The substrate is assumed to be preheated to about 700 °C as adopted for the multilayered analysis considered in Chapter 8.

9.2.1 Temperature distribution

Figure 9-7 and Figure 9-8 shows the cross-section view of temperature distribution developed during solidification of the coating layer for first and third passes respectively. The first and third passes are considered to have initial deposition temperatures of 2700 °C and 2839 °C respectively. Even though the splat interfaces are merged, it can be seen from the figures that the temperature distribution developed during solidification of the coating layer is as complex as what was predicted with the multilayered analysis. As expected, the solidification starts immediately a given pass is deposited. Similarly, most of heat energy is transferred to the substrate through conduction. Convective heat transfer to the surrounding is essential for faster numerical convergence, but it has less influence on temperature distribution. As observed with the multilayered model, solidification rate decreases with number of deposited passes due to the accumulation of heat and reduction

in thermal gradient. It is also found that solidification process influences the temperature distribution due to latent heat release as observed with multilayered model. However, the solidification times predicted with the pass mesh are shorter than that of cumulative time predicted with the multilayered mesh, even though the final distribution of temperature are very comparable. This signifies enhancement in computational efficiency of the hybrid approach with the multi-pass model.

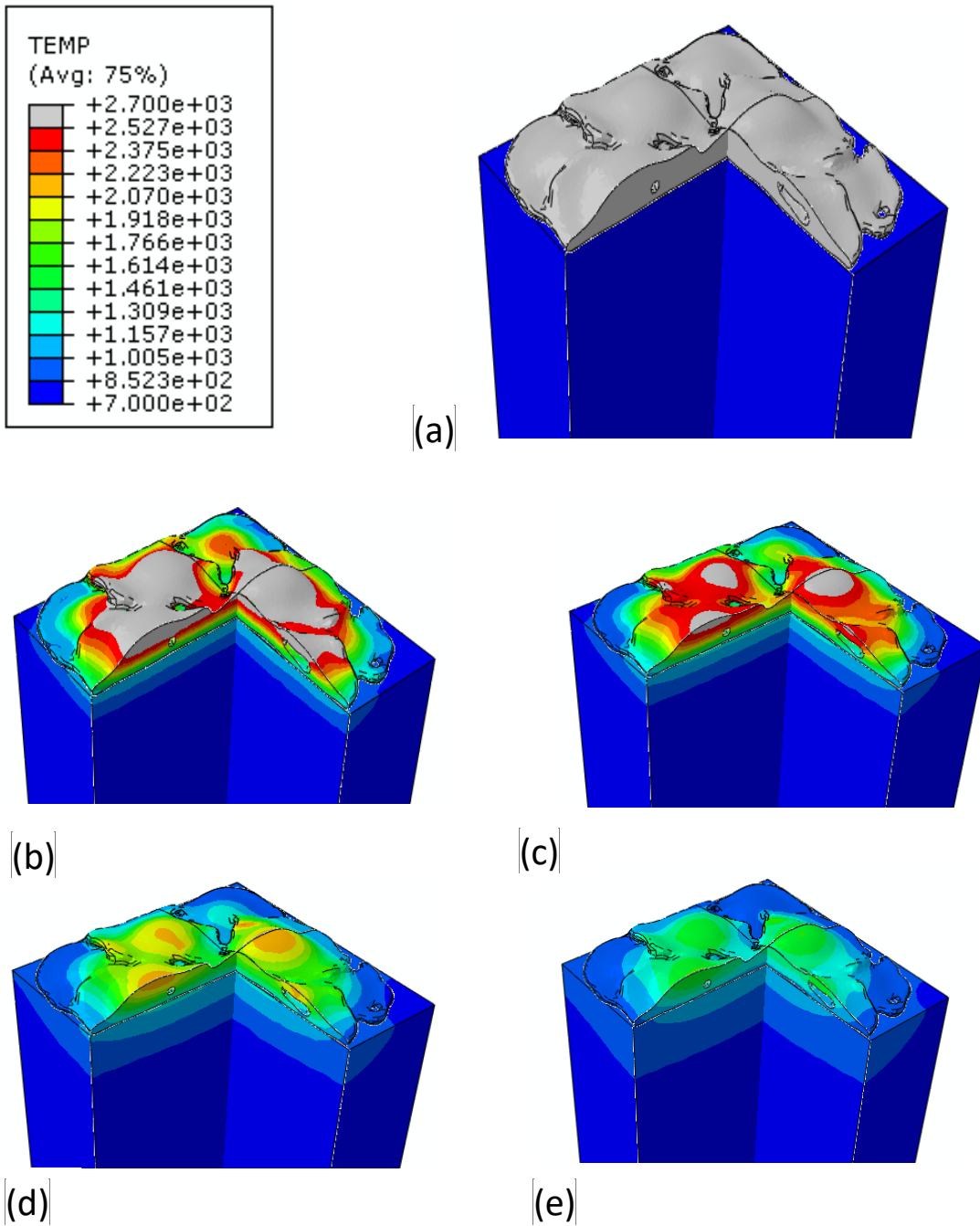


Figure 9-7: Temperature distribution (°C) developed during solidification of first pass of YSZ coating: (a) at 0 μ s, (b) at 100 μ s, (c) at 200 μ s, (d) at 400 μ s, and (d) at 500 μ s, and (e) at 1000 μ s

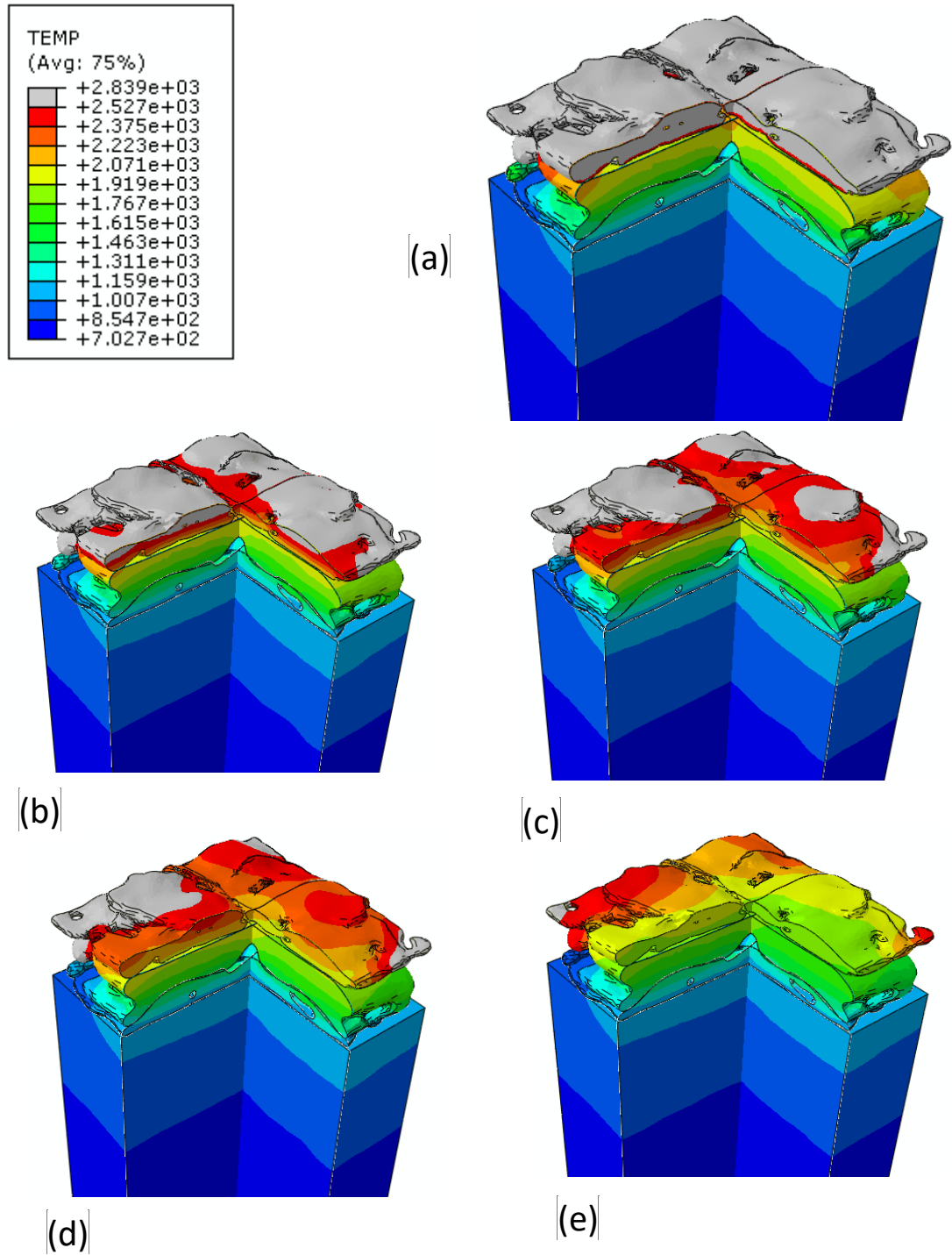


Figure 9-8: Temperature distribution ($^{\circ}\text{C}$) developed during solidification of third pass of YSZ coating: (a) at $4000\ \mu\text{s}$, (b) at $5000\ \mu\text{s}$, (c) at $5500\ \mu\text{s}$, (d) at $6000\ \mu\text{s}$, and (d) at $7000\ \mu\text{s}$, and (e) at $9000\ \mu\text{s}$

Figure 9-9 shows several 2D cut views of temperature distribution developed along the depth of coating and substrate layers. Despite the initial uniform temperature imposed on

deposited passes, the figure shows that non-uniform temperature distribution is developed within the coating layer. As discussed previously, the accumulation of heat at several regions occurs because of blockage of pathways for heat transfer caused by the presence of several discontinuities such as pores, elongated gaps and cracks. Consequently, temperature difference within the coating layer can reach as high as 1000°C depending on location. This large difference in temperature results in severe distortion; thus, inducing residual stresses and significant cracking of the coating layer. Like the multilayered model, five points, A to D, are selected for quantitative analysis of temperature distribution developed within the coating layer as shown in Appendix, Figure A5. Figure 9-10 (a) shows the temperature distribution developed across the depth of coating and substrate layers at the location of the selected points. It can be seen that, the thickness of the coating layer differs with location as observed experimentally and predicted with the multilayered coating model. This is attributed to the large surface roughness of the coating layer. Consequently, the temperature profiles developed across the depth of selected points are not only different but immensely affected by the high coating surface roughness as well as presence of internal defects as shown in Figure 9-9. Furthermore, by comparing Figure 9-10 (a) with (b), it can be seen that, the temperature gradient developed across the coating thickness is higher than that across its width. Figure 9-10 (c) and (d) also show that the thermal history of three points selected at different locations differs considerably as previously captured with the multilayered model. Therefore, the multi-pass model can capture the dependence of the temperature and residual stress on process history. As shown in Figure 9-10 (c), the rise in temperature after certain time is due to reheating of pre-solidified coating pass caused by

the deposition of new passes. Also, Figure 9-10 (d) shows that even points within a given pass (i.e. at topmost pass) have different thermal history due to presence of discontinuities.

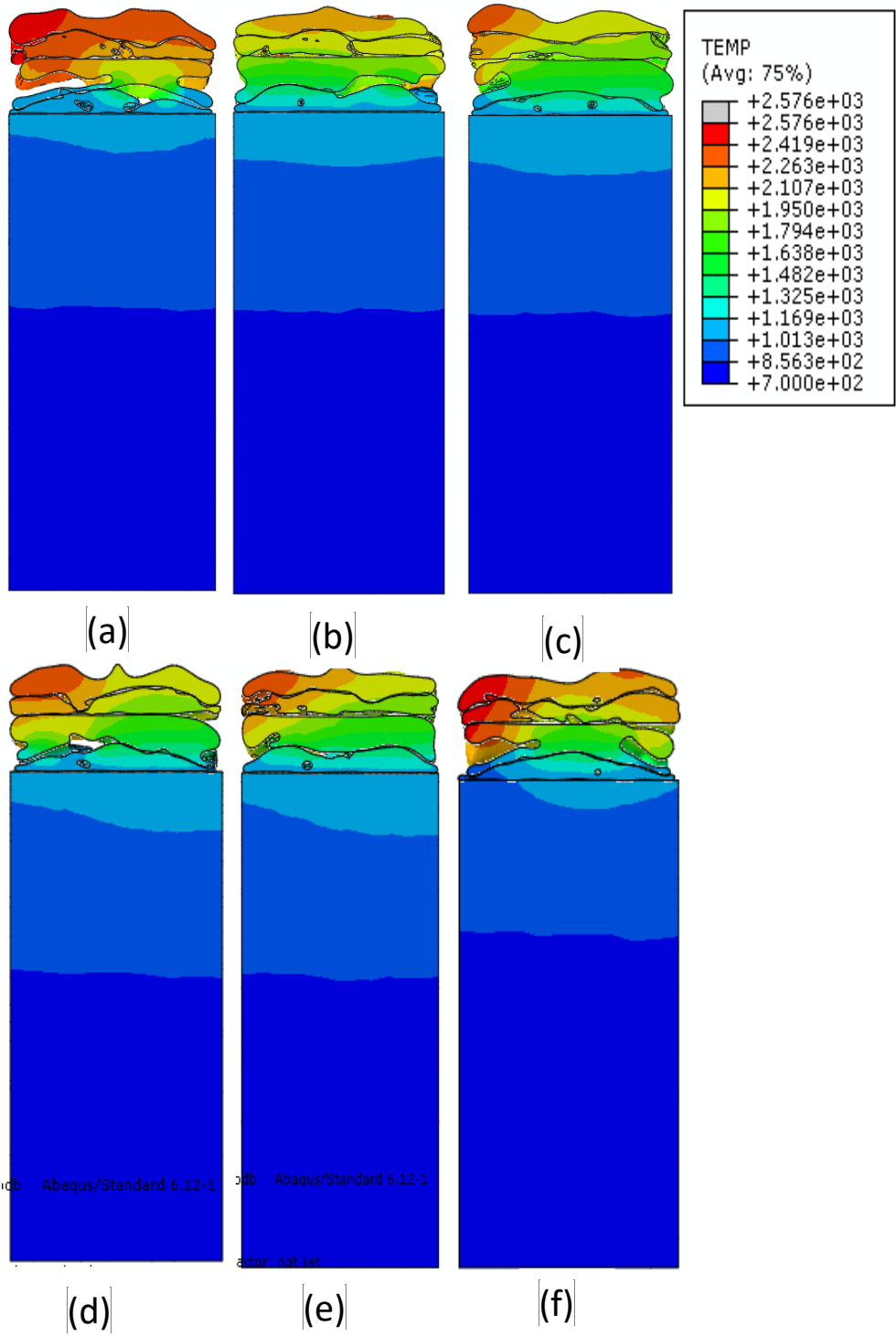


Figure 9-9: (a) to (f)- Temperature distribution (°C) at the selected cross sections after complete solidification of fourth pass of YSZ coating

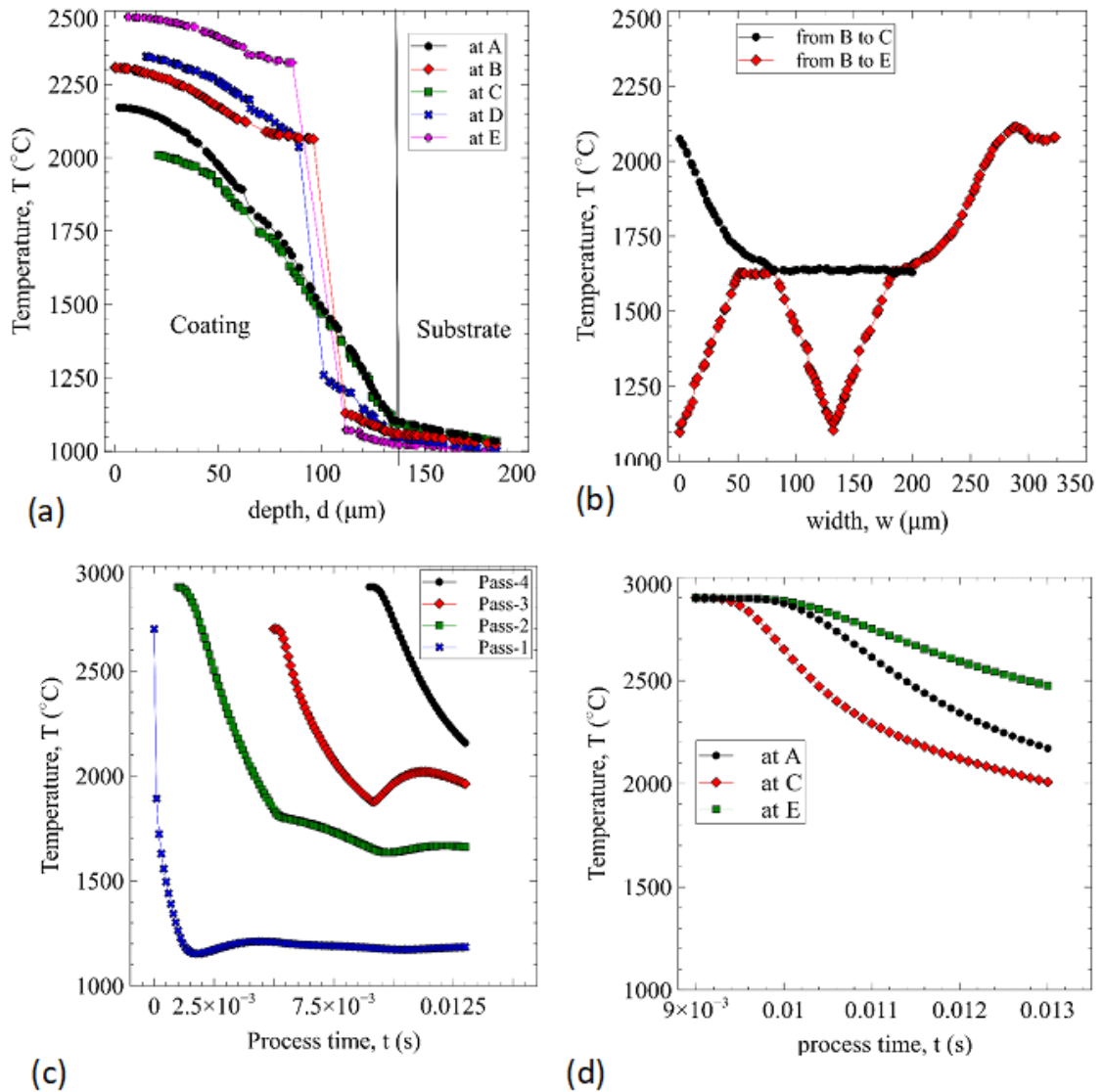


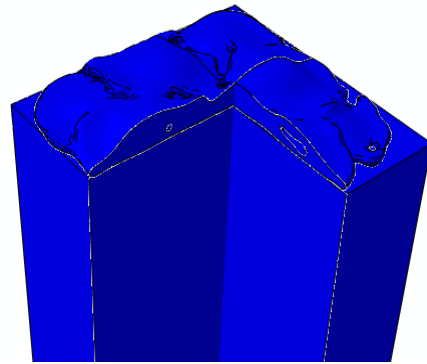
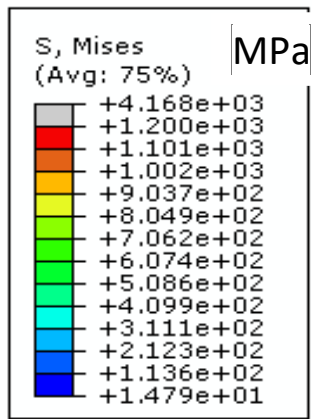
Figure 9-10: (a) Temperature profile along depth at points A, B, C, D and E, (b) Temperature profile along width of coating middle section, (c) Temporal variation of temperature points within specific passes during deposition, (d) Temporal variation of temperature at points A, C and E on coating surface

Therefore, based on obvious similarities in trend of results, it can be said that the temperature distribution predicted with the multi-pass model is comparable to that of multilayered model. The only difference is that, there is no much fluctuation of temperature along the coating depth and length due to the presence of fewer splat interfaces and discontinuities in the pass mesh. Thus, the severity of internal defects is

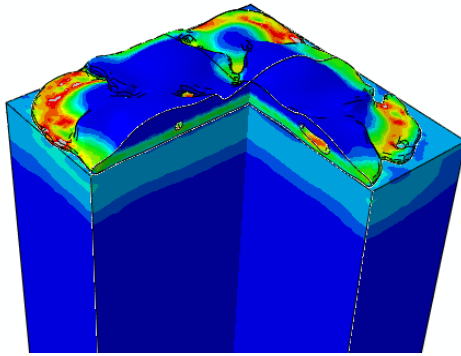
partially compromised, but with computational advantages which makes the model a viable numerical tool for design of TSCs.

9.2.2 Residual stress evolution

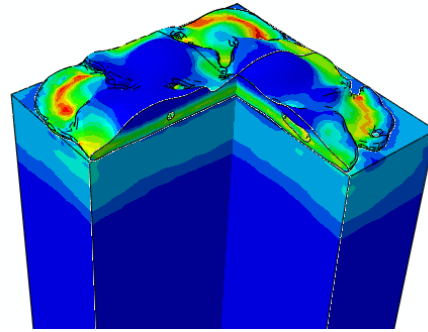
The temperature distribution obtained at each time step was used to predict thermal stresses developed during coating deposition. Figure 9-11 (a) and (b) shows the quenching (or deposition) stress field developed after the solidification of the first and third passes respectively. It can be seen that, a highly non-uniform quenching stress field is developed at solidified regions of coating layer. However, the quenching stresses relax at later stage due to the evolution of microcracks. As shown in Figure 9-11 (a), the model predicted that the von Mises quenching stress can reach as high as 1.2 GPa during the early stage of deformation. The high stresses developed are due to the brittle nature of YSZ. However, with the presence of micro-cracks, the value reduces to within range of 100 to 450 MPa. Furthermore, it is found that higher quenching stresses are developed during solidification of the first pass as compared to the third pass (shown in Figure 9-11 (a) and (b)). This is due the steep temperature gradient developed near the coating-substrate interface as previously observed for the case of the multilayered model. Figure 9-13 shows the 2D cross sectional view of quenching (von Mises) stress and damage parameter developed in the coating layer. The non-uniformity of the stress field is more obvious from the 2D plots. Higher stresses and crack intensities are developed within the first pass due to the steep temperature gradient developed. This has been observed by many in previous microscopic studies [21], [24], [29].



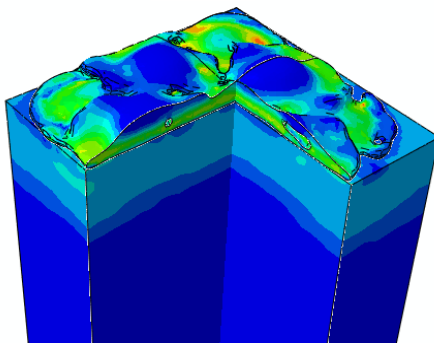
(a)



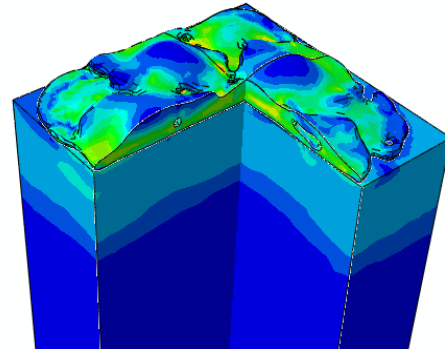
(b)



(c)



(d)



(e)

Figure 9-11: Quenching (von Mises) stress field developed during solidification of first pass of YSZ coating: (a) at 0 μ s, (b) at 100 μ s, (c) at 200 μ s, (d) at 400 μ s, and (d) at 500 μ s, and (e) at 1000 μ s

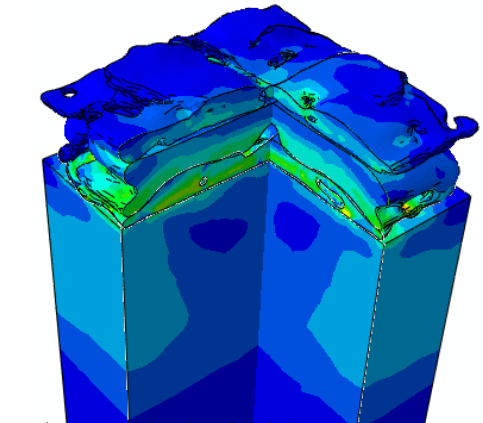
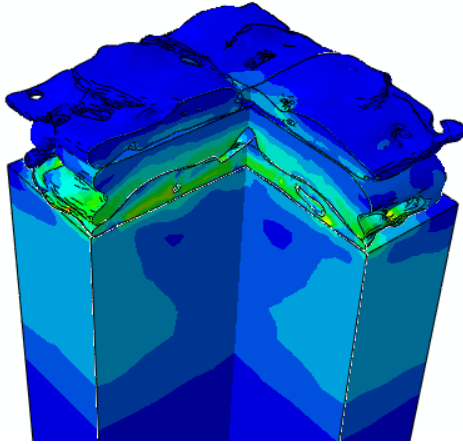
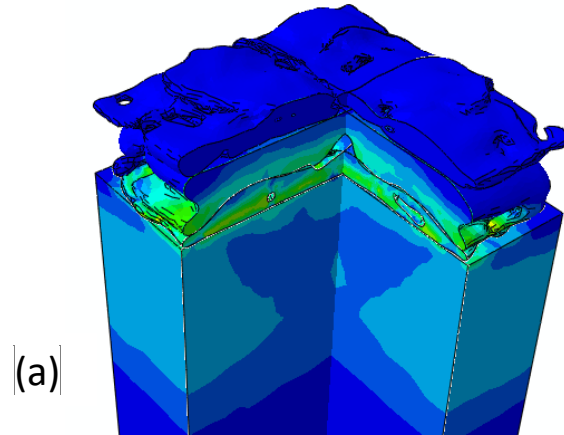
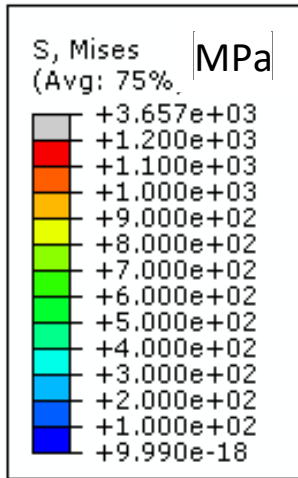


Figure 9-12: Quenching (von Mises) stress field developed during solidification of third pass of YSZ coating: (a) at 4000 μs, (b) at 6000 μs, (c) at 9000 μs.

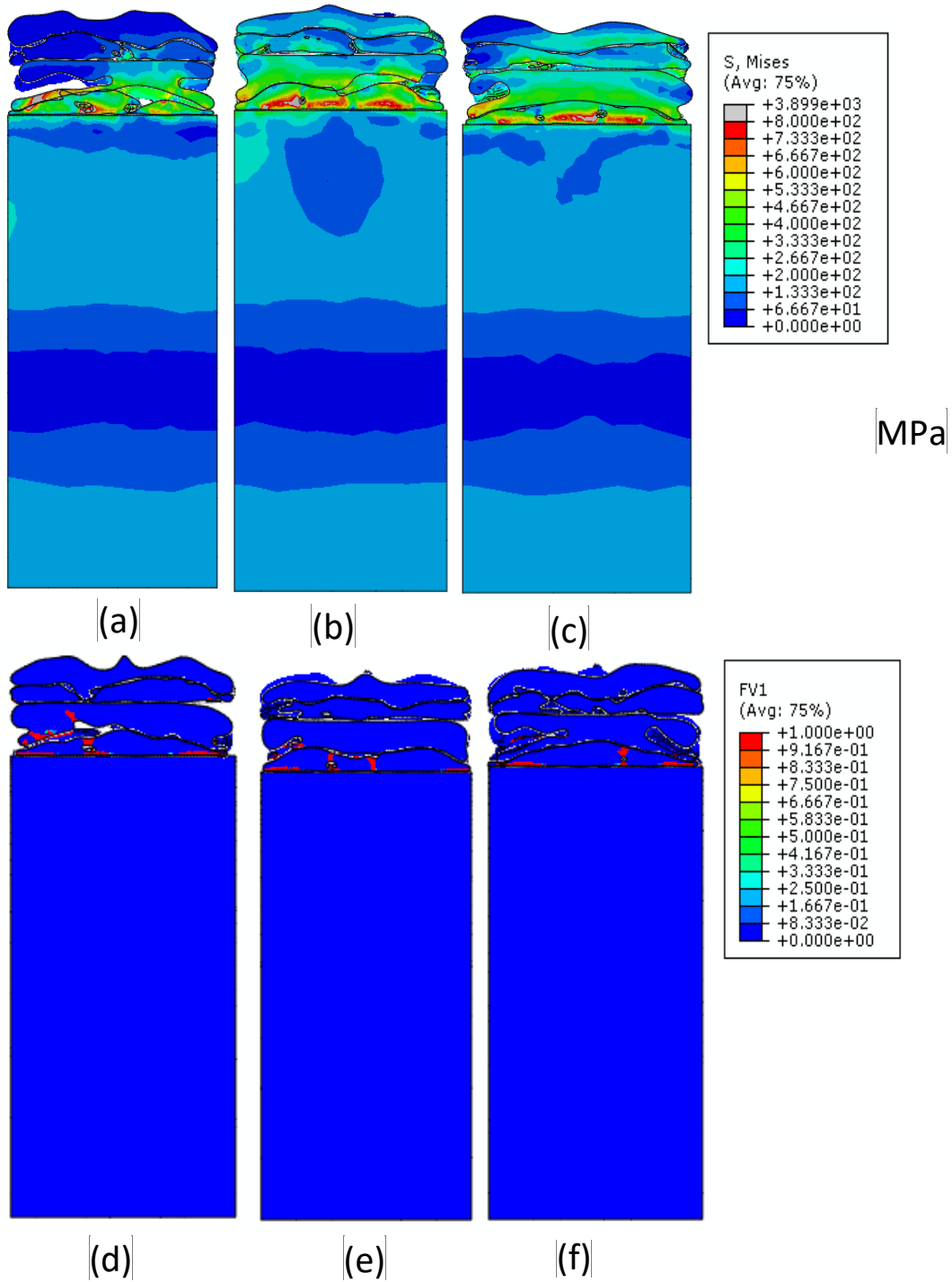


Figure 9-13: Temperature distribution at the selected cross sections after complete solidification of fourth pass of YSZ coating

For analysis of results, emphasis will be given to in-plane normal stresses due to their significance on coating lifetime. As observed for the case of multilayered model, Figure

9-14 (a) to (d) shows that the in-plane normal quenching (deposition) stresses are tensile and compressive within the coating and substrate layers respectively. As explained by many, this is attributed to the shrinkage of coating layer and simultaneous expansion of substrate layer during splats solidification. However, after cooling the deposited coating to room temperature, the curves reverse directions in which compressive and tensile residual stresses are developed in the coating and substrate layers respectively. This reversal of trend from tensile to compressive state is due to development of high compressive (mismatch) stresses developed when coating is cooled to room temperature (as observed in previous studies [21], [24], [29]). The tensile quenching stresses developed in the coating layer fluctuates within range of 100-450 MPa depending on location. This fluctuation is caused by the formation of microcracks as well as the presence of internal defects within the coating layer. Consequently, stress fluctuation is observed in all stress plots. Similarly, by comparing Figure 9-14 (a) and (b), it can be seen that the normal stress developed in x-direction along point A slightly differs from that developed along point B. This is due to the obvious difference in strain history at those points. Furthermore, Figure 9-14 shows equally that the in-plane normal residual stresses (acting in x and y directions) are equibaxial and compressive in nature as measured experimentally and predicted with the multilayered model. The magnitude of residual stresses falls within range of values predicted with the multilayered model. Thus, compressive residual stresses that fluctuates from 0 to -300 MPa are developed in the coating layer. Cracked regions of coating layer develop near-zero residual stress values. Also, stress values are roughly two times higher than that of experimental residual stress measurements. This is because, unlike with the hole drilling experiments, the numerical

model can capture the high stresses developed near localized regions or discontinuities present in the coating layer. As observed for the case of quenching stress field, the compressive residual stresses are balanced by the tensile stresses developed in the substrate layer. The slight deviations observed between the bi-axial stress profiles is due to presence of discontinuities resulting from imperfections within the simulated microstructure. This has been extensively discussed in previous research works [21], [24], [29]. Similar to previous predictions with the multilayered model, Figure 9-14 shows that the compressive residual stress developed near the coating interface is balanced by corresponding tensile stresses on the substrate side. The equi-biaxial compressive stresses (shown in Figure 9-14) are fairly comparable to the results of the hole drilling experiment (previously shown in Figure 7-18) and that of previous numerical and experimental works [65], [99], [101], [102], [192].

Figure 9-15 shows the variation of other stress components along the thickness of the coating and substrate layers. The contour plots of those stress components and displacement fields are shown in Appendix, Figure A6-A8. It can be seen from Figure 9-15 (a) that, the normal (out-of-plane) residual stress acting in the z-direction is low and tensile. Quantitatively, the value is lower than the one predicted with the multilayered model. This is possibly due to the large thickness of the coating considered here. As in-plane normal stresses are both compressive, the tensile nature of the out-of-plane stresses is expected and attributed to stress triaxiality. As the drilling process is done along the z-direction, it is not possible to measure the normal out-of-plane residual stress using the hole drilling method. However, the quantitative validation of the in-plane stresses has suffice validating the residual stress field presented here. Also, Figure 9-15 (b) shows that

the in-plane shear quenching and residual stresses (in xy plane) are considerably lower as observed from the hole drilling experiment. While, Figure 9-15 (c) shows that the von Mises equivalent of residual stress across the coating thickness is high and within range of the magnitudes of normal stresses.

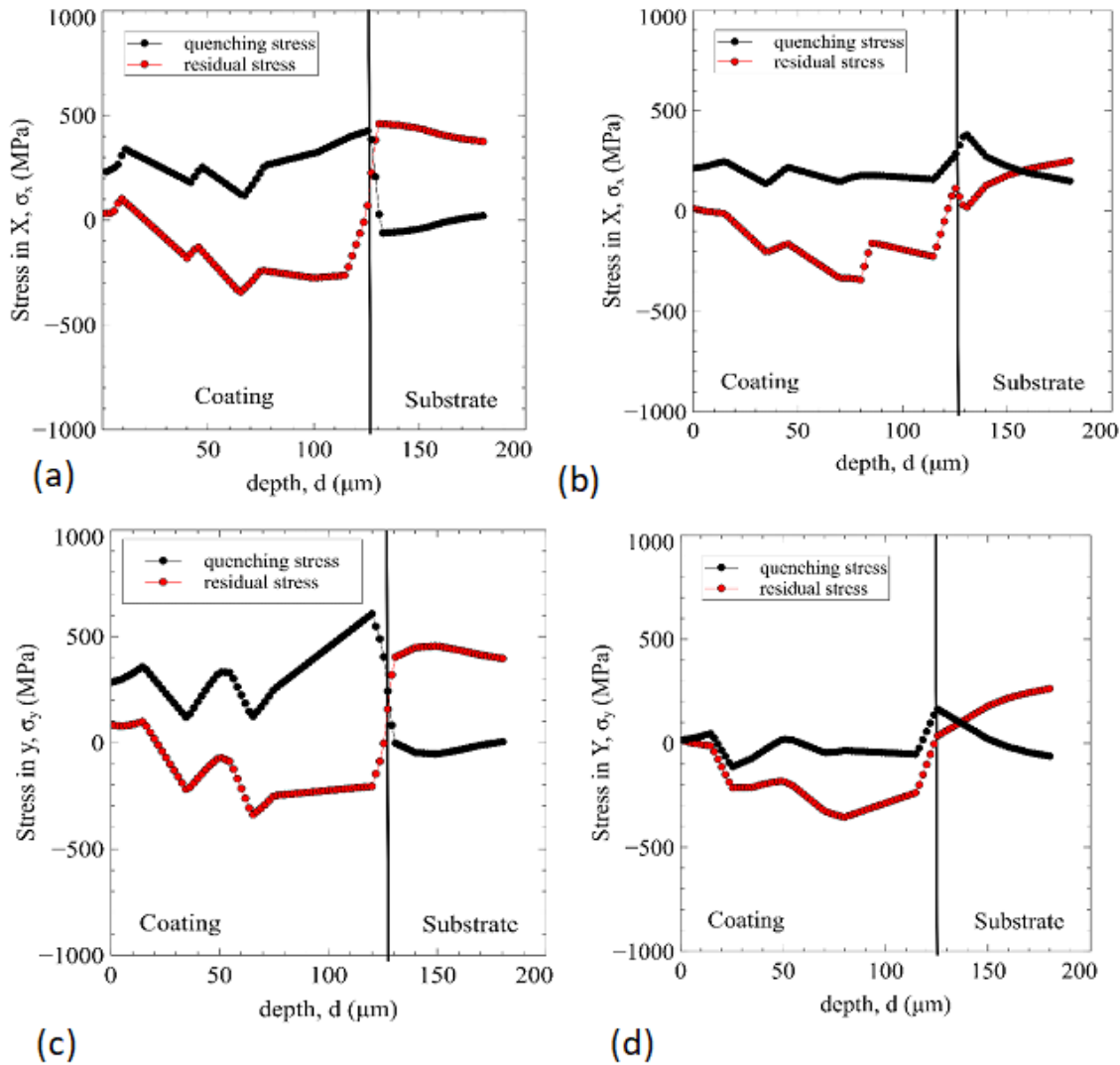


Figure 9-14: Quenching and residual stress profile along depth of coating: (a) Stress in X-direction at A, (b) Stress in X-direction at B, (c) Stress in Y-direction at A, and (d) Stress in Y-direction at B

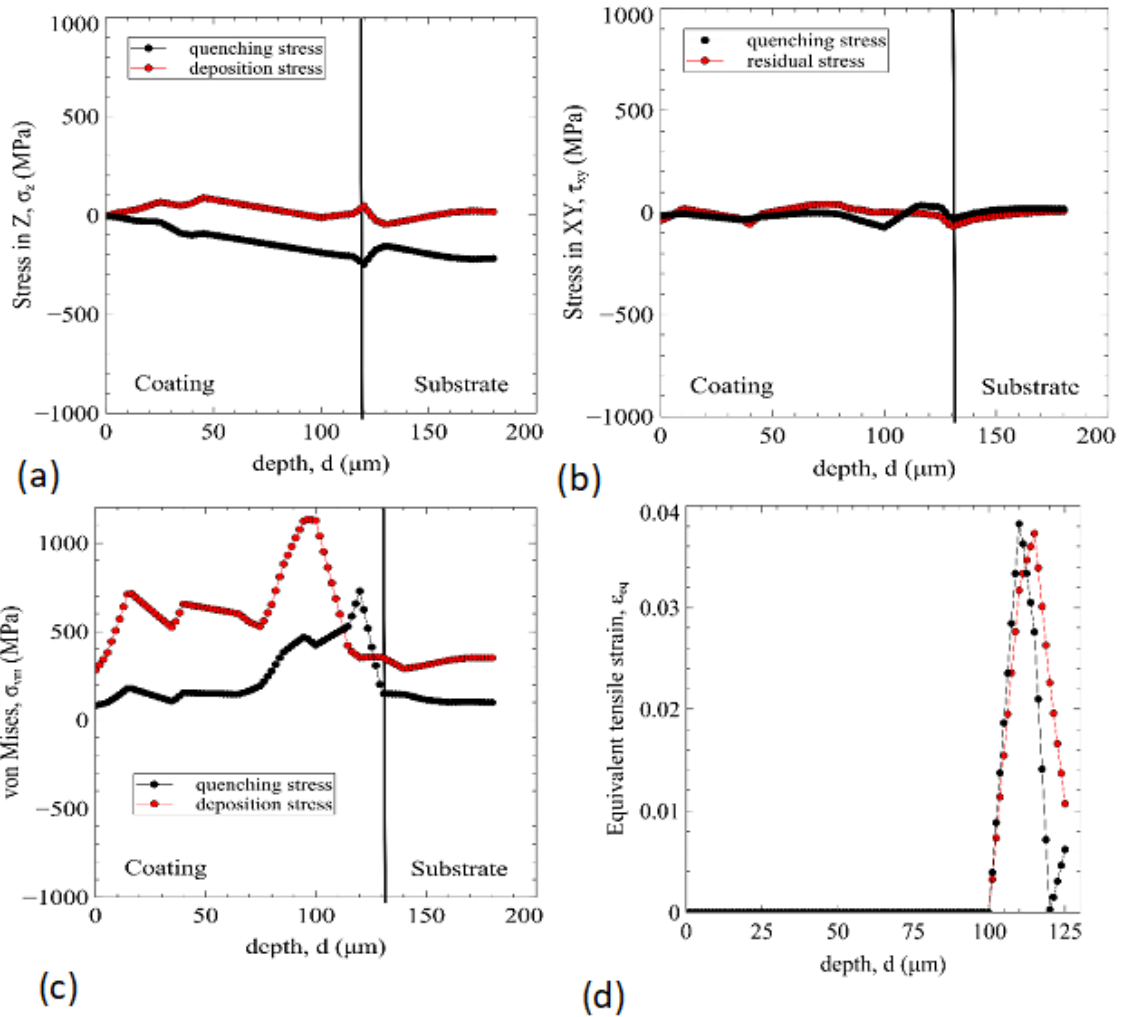


Figure 9-15: Quenching and residual stress profile along depth of coating: (a) Stress in Z-direction at A, (b) Stress in XY-direction at A, (c) von Mises stress at A, and (d) Equivalent tensile strain at A

9.3 Numerical prediction of temperature distribution and residual stress in conventional Ni-20%Al coating deposited on SS310

Similarly, the multi-pass model is used to predict temperature distribution and residual stress field developed in the Ni-20% Al coating layer deposited on SS310 stainless steel. The coating layer was deposited in 3 passes up to thickness of about 110 μm. A uniform initial temperature is randomly assigned to each pass layer and the substrate was preheated to 600 °C.

9.3.1 Temperature distribution

Figure 9-16 shows the cross-section view of temperature distribution developed during solidification of the coating deposit. Similar to observations made for the case of YSZ coating, non-uniform temperature distribution is developed within the coating layer. Even though the ceramic coating discussed in section 9.2 has larger initial difference of coating and substrate temperatures, it is found that the solidification rate of the metallic coating is higher leading to higher heat transfer rate to the substrate. This is because of the high thermal conductivity of the metallic coating as compared to its ceramic counterpart. As found with the ceramic YSZ coating, the solidification rate reduce with number of passes due to reduction in thermal gradient. Figure 9-17 shows the several 2D cut views of temperature distribution developed along the depth of coating and substrate layers. As in the case of the ceramic coating, the presence of discontinuities within the coating layer has resulted in a highly non-uniform temperature distribution. However, thermal gradient developed in the Ni-20%Al coating layer (shown in Figure 9-17) is not as severe as that of the YSZ coating discussed in section 9.2. This is because of the high thermal conductivity of the Ni-20%Al layer. Consequently, the metallic coating is not expected to distort or crack significantly during deposition as will be shown in next section.

For through analysis, the evolution of temperature is tracked at several points within the coating layer. For the purpose of comparison, the same locations as that of the YSZ coating are considered for the analysis. As observed with the ceramic YSZ coating, Figure 9-18 (a) shows that temperature profiles developed along the five points (considered in section 1.2.1) are different due to variation in coating thickness, internal defects and thermal history. Similarly, the temperature gradient developed along the

coating thickness is higher than that along its width (as shown in Figure 9-18 (b)). Also, the thermal history of several points within the coating layer are different and temperature rise can be spotted at different points within pre-solidified pass due to deposition of new passes (shown in Figure 9-18 (c) and (d)).

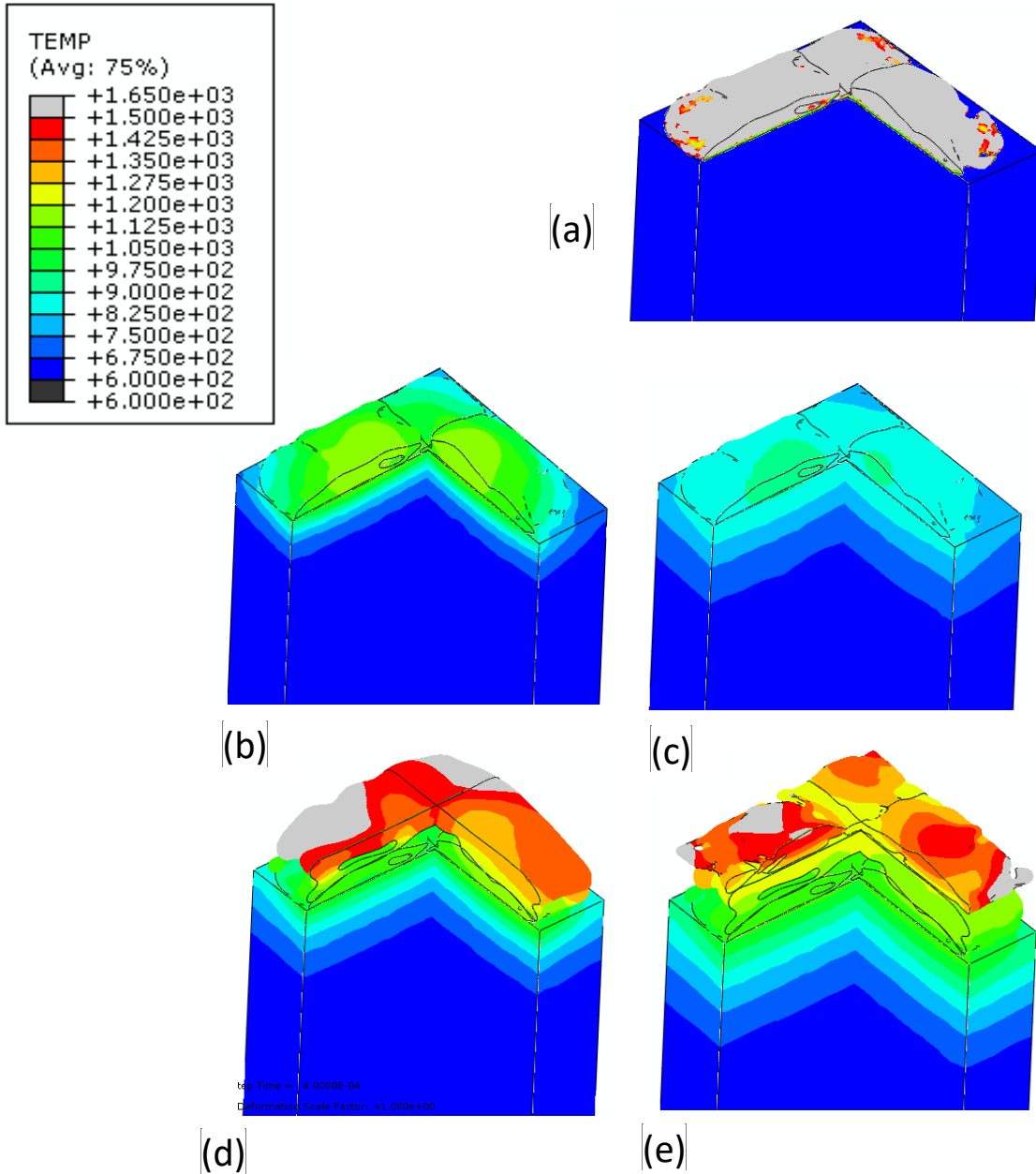


Figure 9-16: Temperature distribution ($^{\circ}\text{C}$) developed during solidification of Ni-20%Al coating: (a) first pass at $0 \mu\text{s}$, (b) at first pass at $100 \mu\text{s}$, (c) first pass at $500 \mu\text{s}$, (d) second pass at $1300 \mu\text{s}$, and (e) third pass at $2100 \mu\text{s}$

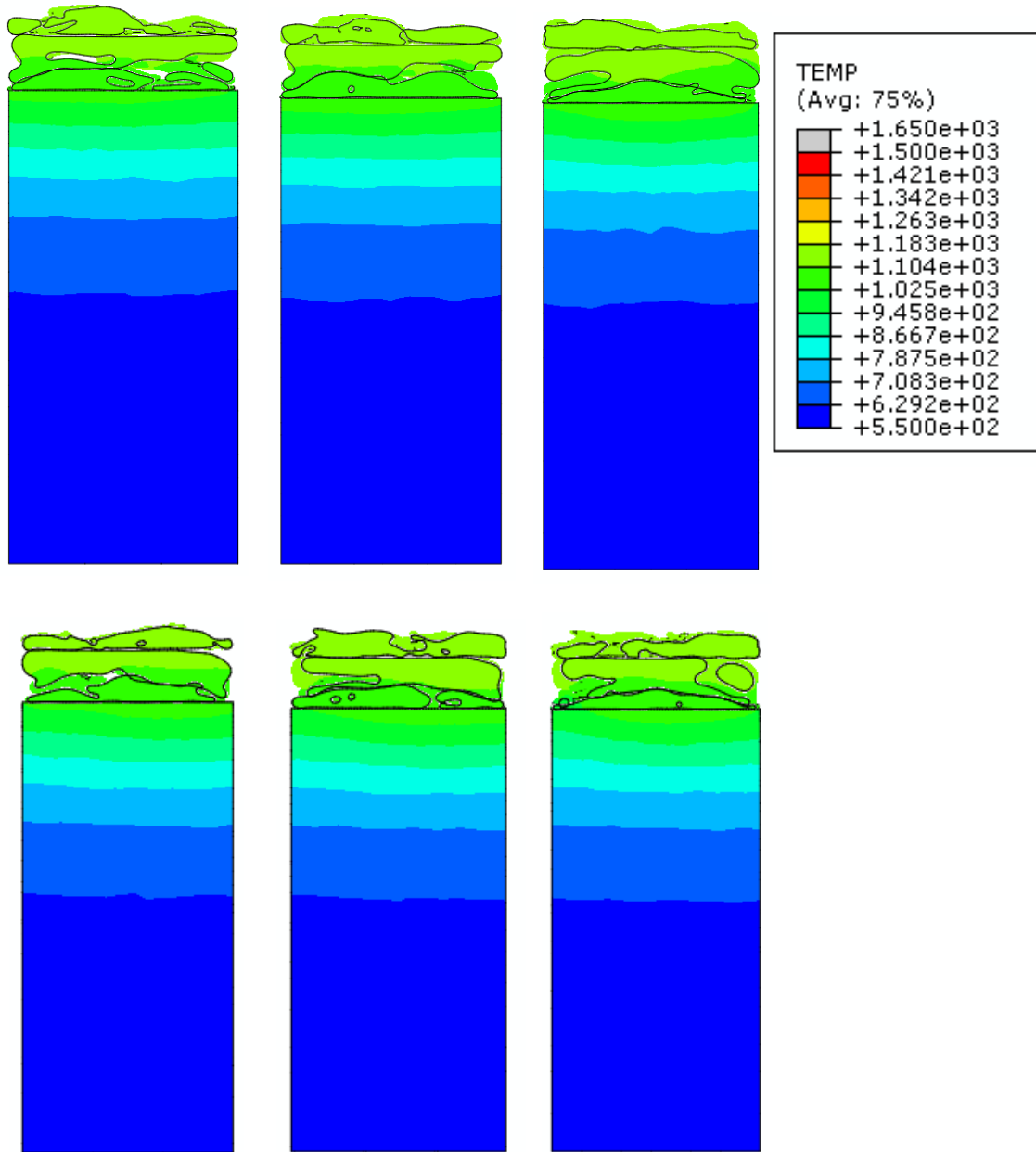


Figure 9-17: (a) to (f)- Temperature distribution (°C) at the selected cross sections after complete solidification of fourth pass of YSZ coating

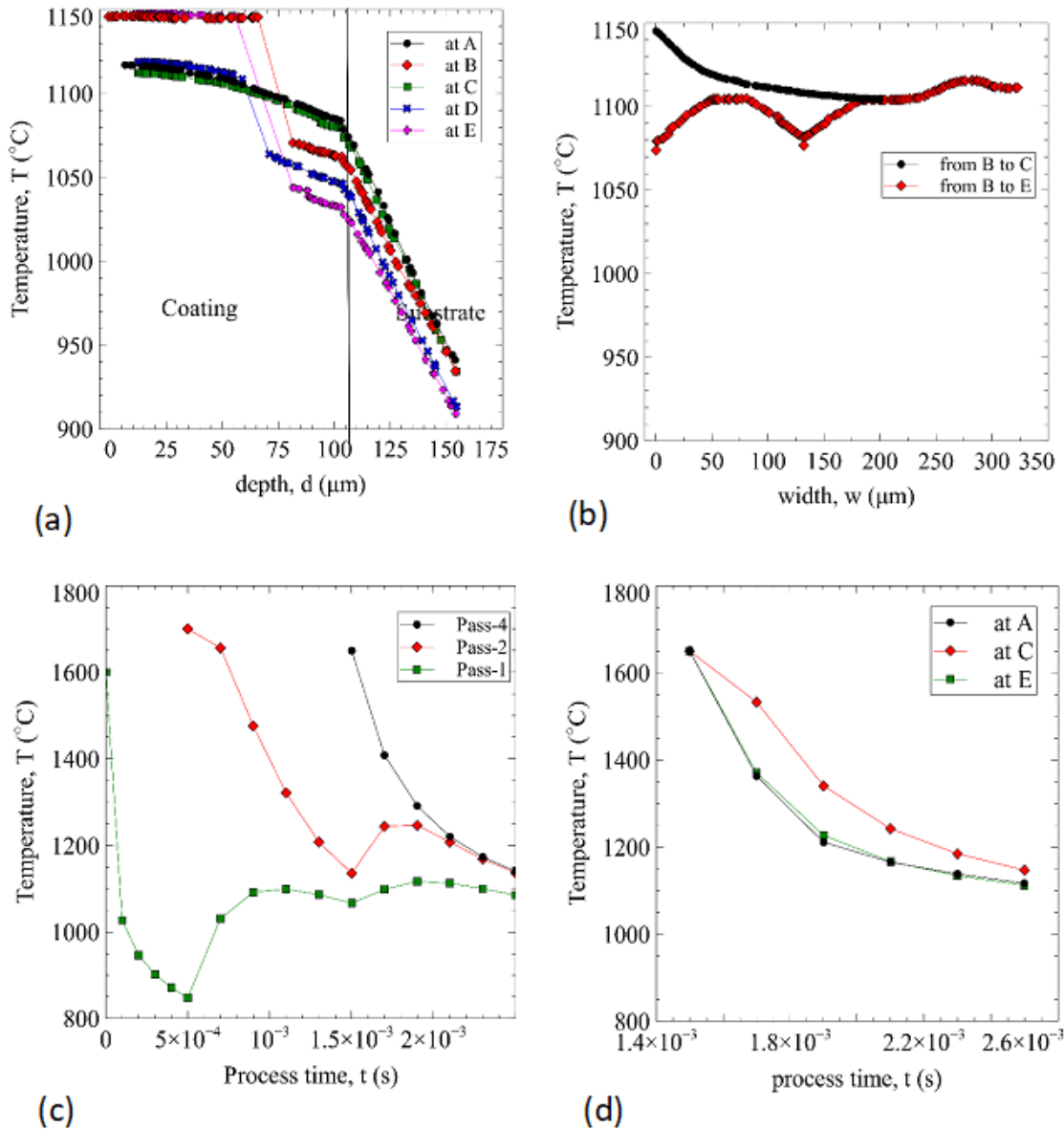


Figure 9-18: (a) Temperature profile along depth at points A, B, C, D and E, (b) Temperature profile along width of coating surface, (c) Temporal variation of temperature points within specific passes during deposition, (d) Temporal variation of temperature at points A, C and E on coating surface

9.3.2 Residual stress evolution

The temperature solution obtained at each time step was used to compute the evolution of residual stresses developed in the Ni-20%Al coating. Figure 9-18 shows the corresponding quenching stresses developed after the solidification of the first, second and third passes. Similar to the case of ceramic coating, it can be seen that the quenching

stress field developed is highly non-linear due to the complex temperature distribution developed during the process. However, the quenching stress developed in the Ni-20%Al coating layer is considerably lower as compared to that of the YSZ coating. This is because of the ductile nature of the Ni-20%Al coating layer as well as the lower temperature gradient developed during its deposition. As shown in Figure 9-18 (a)-(e), the model predicted that the von Mises (quenching) stress has reached values of plastic range (i.e. around 350 MPa) depending on location. Also, the quenching stress developed within the first deposition pass is considerably higher as compared to that of the other passes due to the steep temperature gradient developed near the coating interface. Figure 9-20 shows the 2D cross sectional view of stresses and plastic strain developed in the coating layer. The high non-linearity of the stress field developed is obvious from the 2D plots. It can also be seen that, the high stresses developed within the first pass has resulted in substantial plastic deformation near the coating interface. Thus, the interface region is the most critical point for damage assessment in coatings.

Contrary to what was predicted in YSZ coating, Figure 9-21 (a) to (d) shows that the in-plane normal quenching stresses are tensile within both the coating layer and substrate layers. This is because, both the coating and substrate layers have coefficient of thermal expansion within the same range. For this reason, after cooling the deposited coating to room temperature, there is no reversal of stress state as shown in Figure 9-21. Also, the tensile residual stresses developed within the coating layer are not balanced by compressive residual stresses on the substrate side. This signifies low adhesion strength in metallic coatings. Consequently, metallic coatings are commonly deposited with faster spray process (such as HVOF) that induces high peening (compressive) stresses.

Therefore, the quenching stress contributes more to the severity of residual stress developed in metallic Ni-20%Al coating as previously observed by Sebastian et al. [178]. By comparing Figure 9-21 (a) and (b), it can be seen that the in-plane tensile quenching and residual stresses (with values fluctuating from 50 to 300 MPa) developed in x-direction along point A differs from that developed along point B as observed for the case of YSZ coating. Figure 9-21 also shows that the in-plane quenching and residual stresses (acting in x and y directions) are equi-biaxial. The equi-biaxial stresses (shown in Figure 9-21) are fairly comparable to the results of the hole drilling experiment (previously shown in Figure 7-18). The slight deviation of stress values from one location/direction to another is attributed to the presence of discontinuities or imperfections within the simulated microstructure and other reasons such as randomization of process parameters.

Figure 9-22 shows the variation of other stress components along the thickness of the coating and substrate layers. The contour plots of other stress components are shown in Appendix, Figure A9. It can be seen that, unlike in the YSZ coating, the normal (out-of-plane) residual stress acting in the z-direction is low and compressive. This is because of the stress triaxiality attributed to the nature of the in-plane biaxial stresses. Also, Figure 9-22 (b) shows that the in-plane shear quenching and residual stresses (in xy plane) are also low as observed from the hole drilling experiment. Figure 9-22 (c) shows that the von Mises residual stress developed along the coating thickness is high and within range of the magnitudes of the coating yield strength.

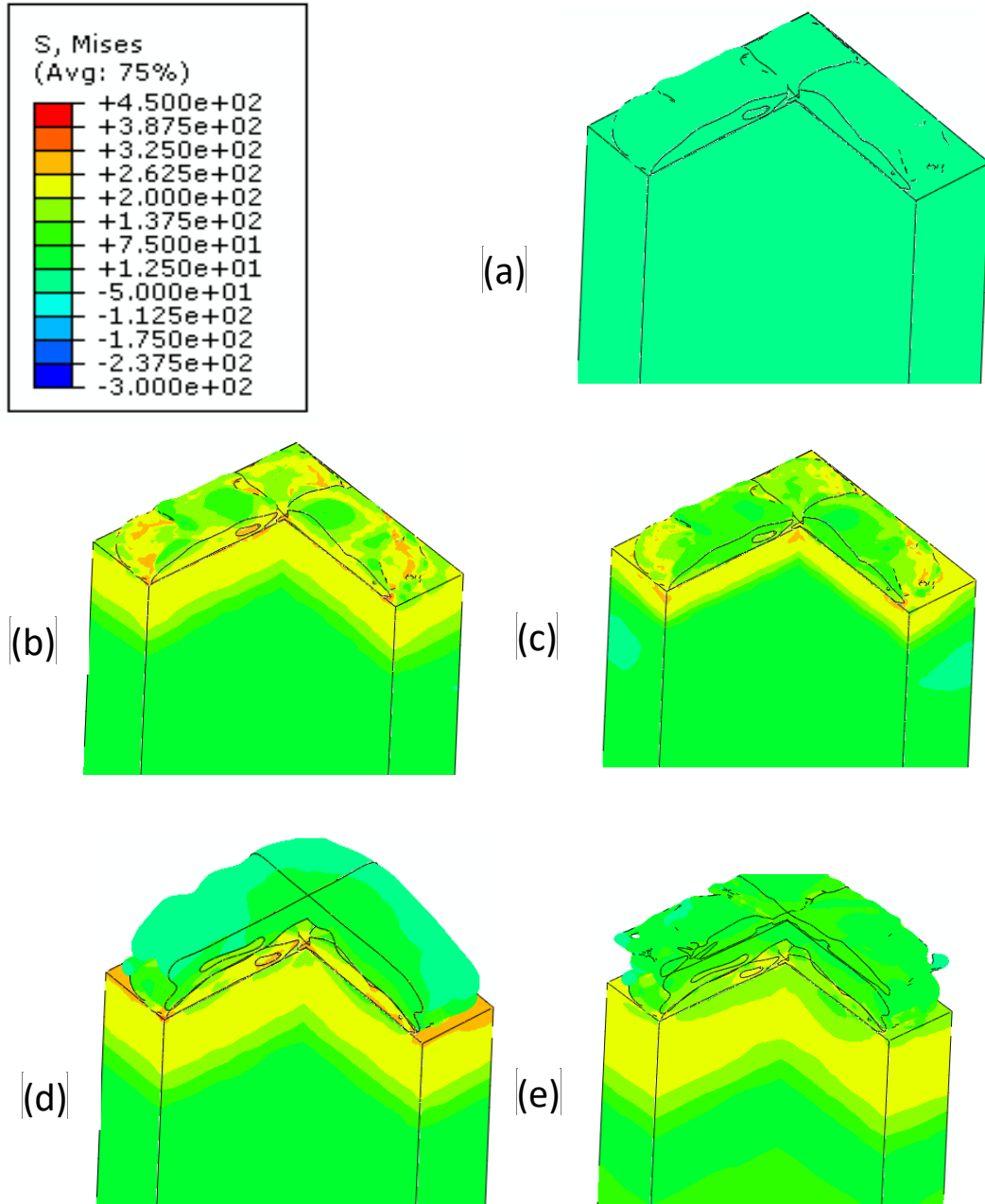


Figure 9-19: Temperature distribution ($^{\circ}\text{C}$) developed during solidification of Ni-20%Al coating: (a) first pass at 0 μs , (b) at first pass at 100 μs , (c) first pass at 500 μs , (d) second pass at 1300 μs , and (e) third pass at 2100 μs

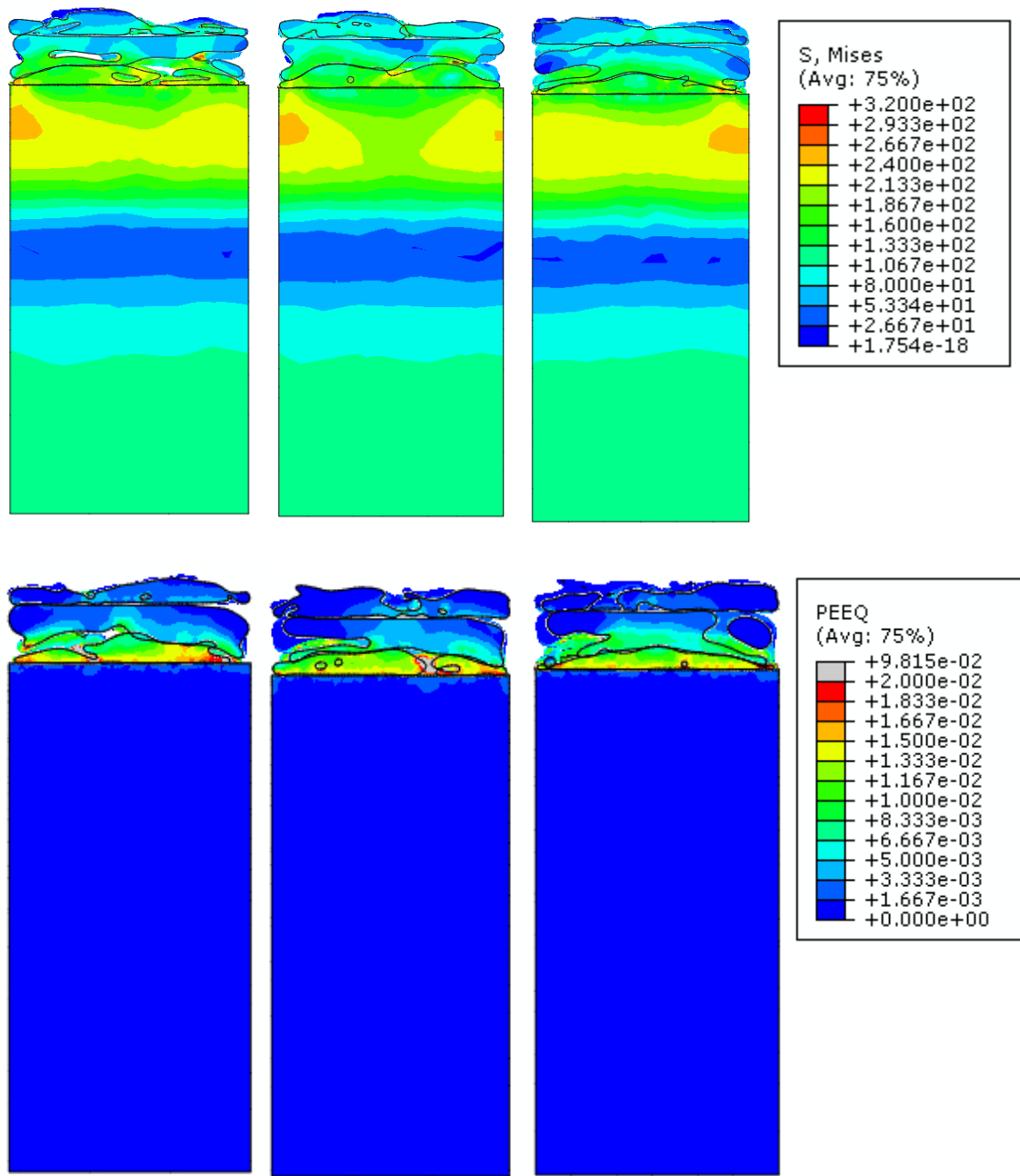


Figure 9-20: (a) to (f)- Temperature distribution (°C) at several cross sections after complete solidification of fourth pass of YSZ coating

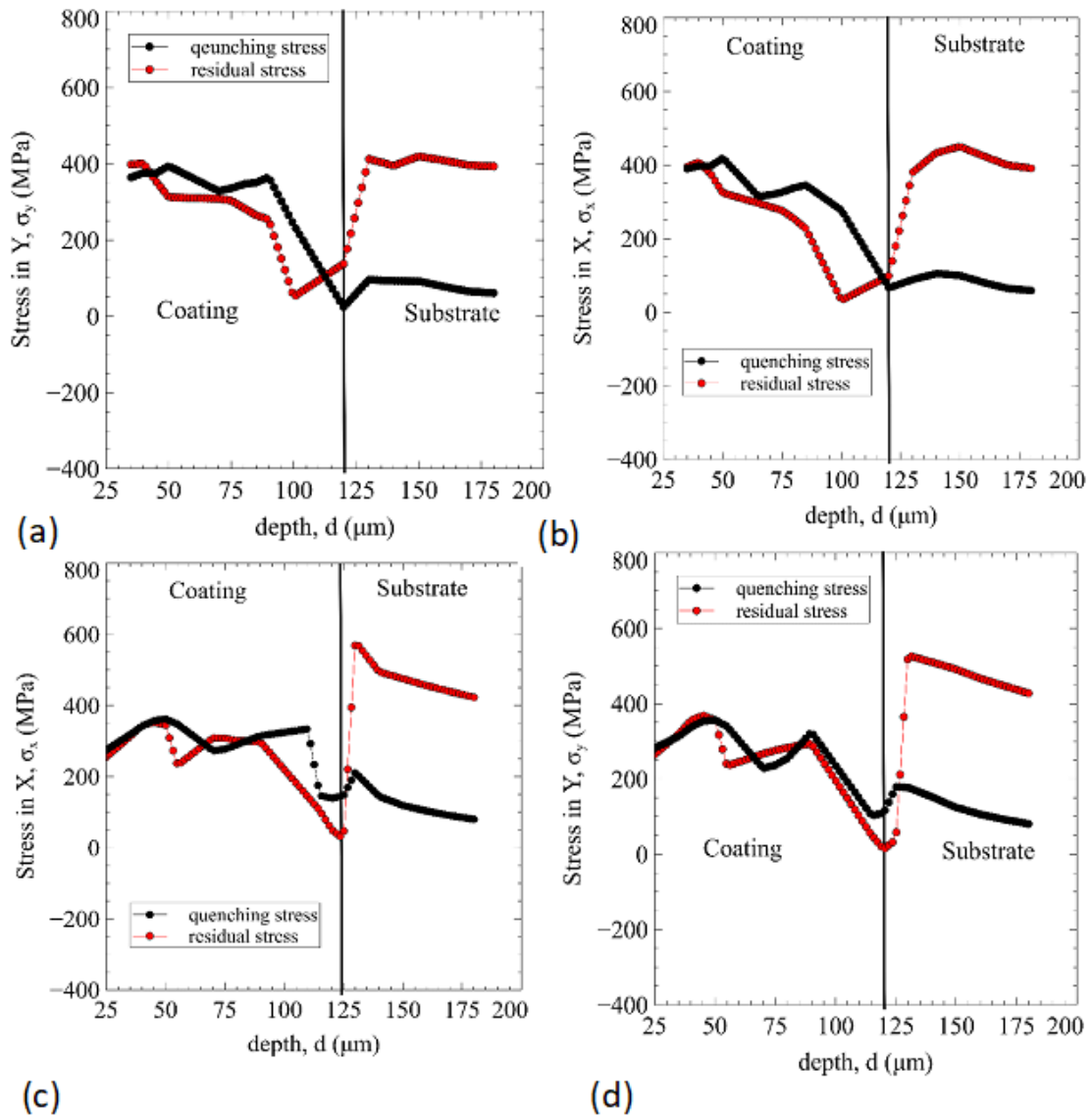


Figure 9-21: Quenching and residual stress profile along depth of coating: (a) Stress in X-direction at A, (b) Stress in X-direction at B, (c) Stress in Y-direction at A, and (d) Stress in Y-direction at B

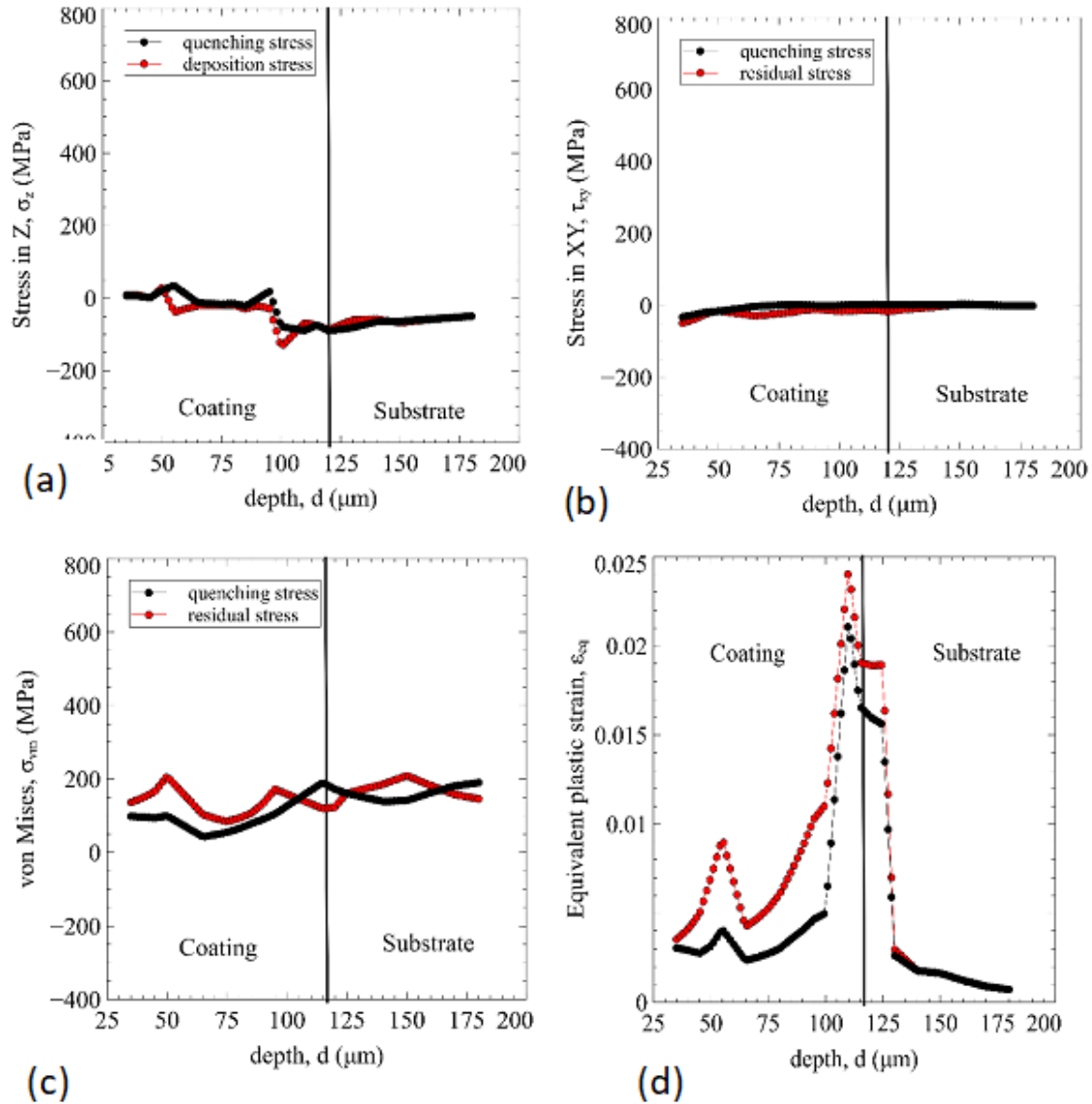


Figure 9-22: Quenching and residual stress profile along depth of coating: (a) Stress in Z-direction at A, (b) Stress in XY-direction at A, (c) von Mises stress at A, and (d) Equivalent tensile strain at A

9.4 Concluding remarks

In the present section, the computational efficiency and accuracy of the hybrid computational approach has been improved using a new scheme that considers modeling of spray process in batch of coating layers (or passes). With the new scheme, the interfaces of splats deposited in each pass are merged. The new scheme has been used to predict residual stress evolution in thicker ceramic (YSZ) and metallic (Ni-20%Al)

coatings that are deposited on SS310. The thermo-mechanical analysis is conducted with the same constitutive models used in chapter 7 and 8. Quenching stresses and associated ceramic microcracking that occurs during solidification of ceramic YSZ deposits are first predicted. Then, residual stress is obtained by cooling the deposited coating layer to room temperatures. It is found that residual stress developed in YSZ coating layer is mainly compressive. Also, microcracking of the YSZ layer predominantly occurs within the first pass. On the other hand, tensile residual stresses are developed in the Ni-20%Al coating layer. It is found that, the numerically-predicted residual stresses are comparable to that of hole drilling experiment presented in chapter 6. The results show that the multi-pass model can capture the nonlinearity, process and position dependence of residual stress field as previously predicted with the multilayered model. It is found that, the new scheme of merging multiple splat interfaces is effective in predicting the non-uniform temperature distribution, evolution of residual stress and internal defects in TSCs at moderate computational cost; thus, paving the way for more realistic estimation of residual stress in TSCs.

CHAPTER 10

CONCLUSIONS AND RECOMMENDATIONS

Residual stress is considered to have a significant influence on constitutive behavior, lifetime and integrity of thermal spray coatings (TSCs). Due to the complex interaction between process parameters and presence of numerous defects, numerical modeling of residual stresses in TSCs has been challenging. Moreover, all available experimental set-ups for residual stress measurements have one or more limitations that make it difficult to thoroughly assess the residual stress profile developed in coatings. Therefore, in the current dissertation work, an innovative numerical modeling approach for thermal spray coating deposition process is proposed, implemented and evaluated. The proposed approach is hybrid in nature and able to predict evolution of residual stress very effectively. Being hybrid, the approach combines the use of point cloud and finite elements to model droplets impact/deformation and thermo-mechanical analyses of deposited coating respectively. The approach is used to predict residual stresses and associated defects developed in plasma-sprayed ceramic (YSZ) and metallic (Ni-20%Al) coatings deposited on stainless steel substrate. The numerical predictions are validated against experimental results obtained from microscopic studies, mechanical tests and hole drilling experiments.

Based on the results obtained from the various studies conducted, several conclusions can be made from the dissertation work as discussed in next section.

10.1 Major findings from experimental work

The following conclusions can be derived from the various experimental studies conducted:

1. The metallic Ni-20%Al coating is less porous and contains fewer micro-cracks as compared to the YSZ coating layer. Consequently, the effective elastic modulus and hardness of the Ni-20%Al coating has been found to be higher than that of the YSZ top coat.
2. The residual stress profile developed along depth of coating layers is highly non-linear, position-dependent as well as equi-biaxial. However, a repeatable trend of stress values is observed. The metallic Ni-20%Al coating develop tensile residual stresses because of severe plastic deformation occurring during splats solidification (or quenching) as well as the low structural mismatch occurring between the coating and substrate layers. The YSZ top coat of TBC develops compressive residual stress profile due to tensile stress relaxation and high structural mismatch occurring between the coating and substrate layers. In both cases, the stress profile was found to be highly non-linear due to highly inhomogeneous nature of the coating layers. Furthermore, very low shear stresses were measured for the Ni-20%Al and YSZ coating layers. This is because, thermal spray deposition is conducted layer-by-layer such that multiple impacting droplets deform to form layer of flattened disks (i.e. splats) that solidify along length and undergoes substantial lateral deformation.
3. The residual stress profile developed along depth of coating layers strongly affects their cohesive strength (or integrity). However, it is found that other

properties related to interfacial diffusion and chemical compatibility between the coating and substrate layers affects the failure mechanism of the coatings considered.

10.2 Major findings from numerical work

The new hybrid approach has proven to be an efficient computational tool for the numerical prediction of residual stresses in TSCs. The theoretical framework developed in the present work is the first contribution where vigorous process modeling (taking process parameters as inputs) is used to numerically predict the evolution of residual stress in TSCs. Even though the approach was implemented with help of standard packages (i.e. ABAQUS and MeshLab), it is implementable in any platform and regardless of the numerical methods used for discretization or types of coating-substrate materials used. The approach is expected to be the dawn of a new era on the computational modeling of the relationship between thermal spray process parameters (such as initial sprayed particle parameters, spray path, spray angle, gun speed, stand-off distance, spray rate, substrate temperature, substrate geometry, surface roughness, coating-substrate material types, environmental effects, etc.) and the evolution of microstructure, residual stress and damage in coatings. Thus, it will serve as a viable tool for thermal spray process optimization or design of coatings.

Specifically, the following conclusions were derived from the numerical work conducted:

1. It has been shown that, the use of realistic process parameters has yielded more reliable estimation of residual stress as compared to previous models. As observed experimentally, the computational model predicted a residual stress profile that is

position-dependent and highly non-linear along the length and thickness of the Ni-20%Al and YSZ coating layer. This is attributed to factors such as the randomly varying process parameters used as well as the presence of numerous internal defects within the coating layers, which are adequately captured by the proposed methodology. Also, the residual stress profiles developed in the Ni-20%Al and YSZ coating layers are equi-biaxial and having very low shear stress as measured experimentally. Furthermore, it is found that the Ni-20%Al coating developed a tensile residual stress profile along depth. While, the YSZ top coat developed compressive stress profile along depth. Both stress profiles compare well to the results obtained experimentally. As discussed previously, the metallic Ni-20%Al coating develop tensile residual stresses because of severe plastic deformation occurring during splats solidification (or quenching) as well as the low structural mismatch occurring between the coating and substrate layers. While, the YSZ top coat of TBC develops compressive residual stress profile because of relaxation of tensile stresses by microcracking as well as the high structural mismatch occurring between the coating and substrate layers.

2. Splat solidification has strong influence on the evolution of temperature and residual stress during the spray process. The complex thermal interaction attributed from the presence of multiple discontinuities in the coating layers (such as pores, cracks, interfaces, etc.) results in a highly complex temperature distribution as well as nonlinear quenching stress field. In the Ni-20%Al coating, the tensile quenching stress field results in large plastic deformation during splats solidification. While, in the ceramic YSZ coating, the tensile quenching stress

field leads to development of multiple cracks along the depth of coating layer. It is found that, the region of the YSZ coating layer that is nearest to the substrate exhibits the highest crack density. It is also found that the quenching stress developed in the Ni-20%Al coating layer is considerably lower as compared to that of the YSZ coating. This is because of the ductile nature of the Ni-20%Al coating layer as well as the lower temperature gradient developed during its deposition.

10.3 Recommendation for future directions

In order to improve the computational efficiency and accuracy of the hybrid approach, several aspects of proposed methodology need to be addressed as discussed on next section.

10.3.1 Point cloud deposition model

The point cloud deposition model should be improved further to address the necessary assumptions adopted in the present study.

1. Enhanced solidification and surface tension models should be adopted such that the influence of temperature and contact angle on splat geometry can be adequately captured. During numerical implementation of the hybrid approach, this was difficult to achieve with the meshless SPH. Incorporating these models will improve the credibility of the developed code. Even though, considering the length scale of analysis considered here, the overall influence of temperature and contact angle is not very significant.

2. New SPH formulations for numerical modeling two-phase or porous droplet impact should be developed. The reality is that, TSC powders are usually designed to serve specific purposes upon being deposited as coating layer. In most cases, each powder particle contains more than one phase and sometimes deliberately made hollow.
3. The overall computational efficiency and accuracy of the SPH code should be improved by utilizing enhanced solvers with capability for parallel processing. Also, the SPH code should be improved further such that any unwanted penetration at interacting boundaries are eliminated. Furthermore, peening stresses should be fully accounted for during numerical modeling of droplet impact; especially when the code is applied to high speed spray processes such as HVOF and D-Gun.

10.3.2 Point cloud processing algorithms

The various algorithms used to convert the point cloud into meshed bodies should be greatly enhanced. In future works, this is expected to be the key area where the quality of numerical results predicted here can be improved. Specific problems to be addressed include:

1. Reducing the number of hours (for the 12 million point sets) consumed by the poison disk-sampling algorithm.
2. Eliminating any possibility for the formation of unwanted holes on the STL mesh generated by poison surface reconstruction algorithm.

3. Enhancing the geometrical accuracy of the conversion process by improving both 3D alpha shape and poisson surface reconstruction algorithm. The possibility for the creation of any form of gap or overlap at splat interfaces should be eliminated.
4. Development of faster and more efficient algorithm for the conversion of STL mesh into a coherent 3D FE mesh. Even though complex shapes are best represented with tetrahedral elements, algorithms should be developed for conversion of STL mesh into combination of tetrahedral and hexahedral elements. This is because the latter are more suitable for non-linear finite element analysis.
5. Development of better algorithm for the merging of splat interfaces.

10.3.3 Thermo-mechanical finite element modeling

The finite element model can also be improved further by addressing the following issues:

1. To improve numerical convergence of analysis, the quality of contact between deposited layers should be improved using user-defined contact algorithms.
2. Several smaller portions of the microstructure modeled, in the form of representative volume element (RVE), should be integrated into a multiscale modeling framework (based on using computational homogenization (Ref 46,47)) for the investigation of the impact of local residual stress fluctuation on effective properties and lifetime of coatings.
3. Intensive process optimization (with the aim of reducing the severity of residual stresses) is also another possibility which will give new insights on thermal spray process design.

4. The modeling approach should be applied to other widely used spray processes (such as: HVOF and cold spray)

10.3.4 Experimental measurements

As the hole drilling residual stress measurement method has several limitations, there is need for in-depth experimental residual stress analysis using advanced techniques such as FIB-hole drilling in combination with digital image correlation, high energy synchronous XRD, neutron diffraction, curvature measurement with ICP sensor, etc.

References

- [1] F. Hermanek, "Thermal spray terminology and company origins," 2001.
- [2] P. L. Fauchais, J. V. R. Heberlein, and M. Boulos, *Thermal Spray Fundamentals: From Powder to Part*. Springer Science & Business Media, 2014.
- [3] R. B. Heimann, *Plasma-Spray Coating: Principles and Applications*. John Wiley & Sons, 2008.
- [4] Begriffe and Einteilung, "DIN EN 657; Thermal Spray – Terminology and Classification," Berlin, Heidelberg, 1994.
- [5] L. Pawlowski, "The Science and Engineering of Thermal Spray Coatings," p. 656, 2008.
- [6] A. McDonald, "Analysis of Thermal Spraying in the Industries of Western Canada," in *International Thermal Spray Conference and Exposition (ITSC)*, 2015.
- [7] M. Gaona, R. S. Lima, and B. R. Marple, "Influence of particle temperature and velocity on the microstructure and mechanical behaviour of high velocity oxy-fuel (HVOF)-sprayed nanostructured titania coatings," *J. Mater. Process. Technol.*, vol. 198, no. 1–3, pp. 426–435, Mar. 2008.
- [8] T. S. Sidhu, S. Prakash, and R. D. Agrawal, "Studies on the properties of high-velocity oxy-fuel thermal spray coatings for higher temperature applications," *Mater. Sci.*, vol. 41, no. 6, pp. 805–823, Nov. 2005.
- [9] D. Cheng, G. Trapaga, J. W. McKelliget, and E. J. Lavernia, "Mathematical Modeling of High Velocity Oxygen Fuel Thermal Spraying: An Overview," *Key Eng. Mater.*, vol. 197, pp. 1–26, 2001.
- [10] H. Herman, *Plasma-sprayed coatings*, vol. 259:3. 1988.
- [11] M. Oksa, E. Turunen, T. Suhonen, T. Varis, and S.-P. Hannula, "Optimization and characterization of high velocity oxy-fuel sprayed coatings: techniques, materials, and applications," *Coatings*, vol. 1, no. 1, pp. 17–52, 2011.
- [12] S. Sampath, U. Schulz, M. O. Jarligo, and S. Kuroda, "Processing science of advanced thermal-barrier systems," *MRS Bull.*, vol. 37, no. 10, pp. 903–910, 2012.
- [13] T. W. Clyne and S. C. Gill, "Residual Stresses in Thermal Spray Coatings and Their Effect on Interfacial Adhesion: A Review of Recent Work," *J. Therm. Spray Technol.*, vol. 5, no. 4, pp. 401–418, Dec. 1996.
- [14] P. Araujo, D. Chicot, M. Staia, and J. Lesage, "Residual stresses and adhesion of thermal spray coatings," *Surf. Eng.*, vol. 21, no. 1, pp. 35–40, Jul. 2005.

- [15] Z. Xue, A. G. Evans, and J. W. Hutchinson, "Delamination Susceptibility of Coatings Under High Thermal Flux," *J. Appl. Mech.*, vol. 76, no. 4, p. 041008, Jul. 2009.
- [16] V. Teixeira, M. Andritschky, W. Fischer, H. P. Buchkremer, and D. Stöver, "Effects of deposition temperature and thermal cycling on residual stress state in zirconia-based thermal barrier coatings," *Surf. Coatings Technol.*, vol. 120–121, no. 1999, pp. 103–111, Nov. 1999.
- [17] K. . Khor and Y. . Gu, "Effects of residual stress on the performance of plasma sprayed functionally graded ZrO₂/NiCoCrAlY coatings," *Mater. Sci. Eng. A*, vol. 277, no. 1–2, pp. 64–76, Jan. 2000.
- [18] N. P. Padture, M. Gell, and E. H. Jordan, "Thermal barrier coatings for gas-turbine engine applications.," *Science*, vol. 296, no. 5566, pp. 280–4, Apr. 2002.
- [19] A. N. Khan, J. Lu, H. Liao, A. Nusair Khan, J. Lu, and H. Liao, "Effect of residual stresses on air plasma sprayed thermal barrier coatings," *Surf. Coatings Technol.*, vol. 168, no. 2–3, pp. 291–299, May 2003.
- [20] J. Zhu, H. Xie, Z. Hu, P. Chen, and Q. Zhang, "Residual stress in thermal spray coatings measured by curvature based on 3D digital image correlation technique," *Surf. Coatings Technol.*, vol. 206, no. 6, pp. 1396–1402, Dec. 2011.
- [21] S. Kuroda, T. Dendo, and S. Kitahara, "Quenching stress in plasma sprayed coatings and its correlation with the deposit microstructure," *J. Therm. Spray Technol.*, vol. 4, no. 1, pp. 75–84, Mar. 1995.
- [22] R. Gadow, M. J. Riegert-Escribano, and M. Buchmann, "Residual Stress Analysis in Thermally Sprayed Layer Composites, Using the Hole Milling and Drilling Method," *J. Therm. Spray Technol.*, vol. 14, no. March, pp. 100–108, 2005.
- [23] M. H. Staia, E. Ramos, A. Carrasquero, A. Roman, J. Lesage, D. Chicot, and G. Mesmacque, "Effect of substrate roughness induced by grit blasting upon adhesion of WC-17% Co thermal sprayed coatings," *Thin Solid Films*, vol. 377, pp. 657–664, 2000.
- [24] J. Matejicek, S. Sampath, D. Gilmore, and R. Neiser, "In situ measurement of residual stresses and elastic moduli in thermal sprayed coatings part 1: Apparatus and analysis," *Acta Mater.*, vol. 51, no. 3, pp. 863–872, Feb. 2003.
- [25] Y. Song, Z. Lv, Y. Liu, X. Zhuan, and T. J. Wang, "Effects of coating spray speed and convective heat transfer on transient thermal stress in thermal barrier coating system during the cooling process of fabrication," *Appl. Surf. Sci.*, vol. 324, no. 2015, pp. 627–633, Jan. 2015.
- [26] J. Zhu, W. Chen, and H. Xie, "Simulation of residual stresses and their effects on thermal barrier coating systems using finite element method," *Sci. China Physics, Mech. Astron.*, vol. 58, no. 3, pp. 1–10, 2014.

- [27] S. C. Gill and T. W. Clyne, "Stress distributions and material response in thermal spraying of metallic and ceramic deposits," *Metall. Trans. B*, vol. 21, no. 2, pp. 377–385, Apr. 1990.
- [28] A. M. Limarga, R. Vaßen, and D. R. Clarke, "Stress Distributions in Plasma-Sprayed Thermal Barrier Coatings Under Thermal Cycling in a Temperature Gradient," *J. Appl. Mech.*, vol. 78, no. 1, p. 011003, 2011.
- [29] A. A. Abubakar, A. F. M. Arif, K. S. Al-Athel, S. S. Akhtar, and J. Mostaghimi, "Modeling Residual Stress Development in Thermal Spray Coatings: Current Status and Way Forward," *J. Therm. Spray Technol.*, pp. 1–31, 2017.
- [30] O. P. P. Oladijo, A. M. M. Venter, L. A. A. Cornish, and N. Sacks, "X-ray diffraction measurement of residual stress in WC-Co thermally sprayed coatings onto metal substrates," *Surf. Coatings Technol.*, vol. 206, no. 23, pp. 4725–4729, Jul. 2012.
- [31] B. S. Yilbas and A. F. M. Arif, "Residual stress analysis for hvof diamalloy 1005 coating on Ti–6Al–4V alloy," *Surf. Coatings Technol.*, vol. 202, no. 3, pp. 559–568, Dec. 2007.
- [32] C. Lyphout, P. Nylén, A. Manescu, and T. Pirling, "Residual Stresses Distribution through Thick HVOF Sprayed Inconel 718 Coatings," *J. Therm. Spray Technol.*, vol. 17, no. 5–6, pp. 915–923, 2008.
- [33] Y. Santana, J. G. La Barbera-Sosa, M. H. Staia, J. Lesage, E. S. Puchi-Cabrera, D. Chicot, and E. Bemporad, "Measurement of residual stress in thermal spray coatings by the incremental hole drilling method," *Surf. Coatings Technol.*, vol. 201, no. 5, pp. 2092–2098, Oct. 2006.
- [34] T. Valente, C. Bartuli, M. Sebastiani, and A. Loreto, "Implementation and Development of the Incremental Hole Drilling Method for the Measurement of Residual Stress in Thermal Spray Coatings," *J. Therm. Spray Technol.*, vol. 14, no. 4, pp. 462–470, Dec. 2005.
- [35] J. Mostaghimi, S. Chandra, A. Dolatabadi, R. Ghafouri-Azar, and A. Dolatabadi, "Modeling thermal spray coating processes: A powerful tool in design and optimization," *Surf. Coatings Technol.*, vol. 163–164, no. 2003, pp. 1–11, 2003.
- [36] R. Ghafouri-Azar, J. Mostaghimi, and S. Chandra, "Modeling development of residual stresses in thermal spray coatings," *Comput. Mater. Sci.*, vol. 35, no. 1, pp. 13–26, 2006.
- [37] J. Prehm, L. Xin, K. Möhwald, and F. W. Bach, "Coupled Coating Formation Simulation in Thermal Spray Processes using CFD and FEM," *CFD Lett.*, vol. 3, no. 2, pp. 89–99, 2011.
- [38] R. T. R. McGrann, D. J. Greving, J. R. Shadley, E. F. Rybicki, T. L. Kruecke, and B. E. Bodger, "The effect of coating residual stress on the fatigue life of thermal

- spray-coated steel and aluminum,” *Surf. Coatings Technol.*, vol. 108–109, pp. 59–64, Oct. 1998.
- [39] S. Takeuchi, M. Ito, and K. Takeda, “Modelling of residual stress in plasma-sprayed coatings: Effect of substrate temperature,” *Surf. Coatings Technol.*, vol. 43–44, no. 1990, pp. 426–435, Dec. 1990.
- [40] S. Kuroda, Y. Tashiro, H. Yumoto, S. Taira, H. Fukanuma, and S. Tobe, “Peening Action and Residual Stresses in High-Velocity Oxygen Fuel Thermal Spraying of 316L Stainless Steel,” *J. Therm. Spray Technol.*, vol. 10, no. 2, pp. 367–374, Jun. 2001.
- [41] S. Sampath, X. . Y. Jiang, J. Matejcek, L. Prchlik, A. Kulkarni, and A. Vaidya, “Role of thermal spray processing method on the microstructure, residual stress and properties of coatings: An integrated study of Ni-5 wt. % Al bond coats,” *Mater. Sci. Eng. A*, vol. 364, no. 1–2, pp. 216–231, Jan. 2004.
- [42] T.-G. Wang, S.-S. Zhao, W.-G. Hua, J.-B. Li, J. Gong, and C. Sun, “Estimation of residual stress and its effects on the mechanical properties of detonation gun sprayed WC–Co coatings,” *Mater. Sci. Eng. A*, vol. 527, no. 3, pp. 454–461, Jan. 2010.
- [43] K. Al-Athel, K. Loeffel, H. Liu, and L. Anand, “Modeling decohesion of a top-coat from a thermally-growing oxide in a thermal barrier coating,” *Surf. Coatings Technol.*, vol. 222, no. 2013, pp. 68–78, May 2013.
- [44] A. A. A. A. Abubakar, S. S. S. S. Akhtar, and A. F. M. A. F. M. Arif, “Phase field modeling of V₂O₅ hot corrosion kinetics in thermal barrier coatings,” *Comput. Mater. Sci.*, vol. 99, no. 2015, pp. 105–116, Mar. 2015.
- [45] K. A. Khor, Z. L. Dong, and Y. W. Gu, “Plasma sprayed functionally graded thermal barrier coatings,” *Mater. Lett.*, vol. 38, no. 6, pp. 437–444, Mar. 1999.
- [46] A. A. A. A. Abubakar, S. S. S. S. Akhtar, A. F. M. A. F. M. Arif, and J. Mostaghimi, “The effect of porosity on the hot corrosion failure of thermal barrier coatings,” *Model. Simul. Mater. Sci. Eng.*, vol. 23, no. 7, p. 075001, Oct. 2015.
- [47] V. Luzin, K. Spencer, and M.-X. M.-X. Zhang, “Residual stress and thermo-mechanical properties of cold spray metal coatings,” *Acta Mater.*, vol. 59, no. 3, pp. 1259–1270, Feb. 2011.
- [48] B. Klusemann, R. Denzer, and B. Svendsen, “Microstructure-based modeling of residual stresses in WC-12Co-sprayed coatings,” *J. Therm. Spray Technol.*, vol. 21, no. 1, pp. 96–107, 2012.
- [49] R. Ahmed, M. E. Fitzpatrick, and N. H. Faisal, “A comparison of neutron diffraction and hole-drilling residual strain measurements in thermally sprayed coatings,” *Surf. Coatings Technol.*, vol. 206, no. 19–20, pp. 4180–4185, 2012.

- [50] N. H. Faisal, R. Ahmed, A. K. Prathuru, S. P. Katikaneni, M. F. A. Goosen, and S. Y. Zhang, “Neutron diffraction residual strain measurements of molybdenum carbide-based solid oxide fuel cell anode layers with metal oxides on hastelloy X,” *Exp. Mech.*, vol. 58, no. 4, pp. 585–603, 2018.
- [51] Q. Chen, W. G. Mao, Y. C. Zhou, and C. Lu, “Effect of Young’s modulus evolution on residual stress measurement of thermal barrier coatings by X-ray diffraction,” *Appl. Surf. Sci.*, vol. 256, no. 23, pp. 7311–7315, 2010.
- [52] R. Schönggrundner, R. Treml, T. Antretter, D. Kozic, W. Ecker, D. Kiener, and R. Brunner, “Critical assessment of the determination of residual stress profiles in thin films by means of the ion beam layer removal method,” *Thin Solid Films*, vol. 564, pp. 321–330, 2014.
- [53] C. Li, X. Zhang, Y. Chen, J. Carr, S. Jacques, J. Behnsen, M. di Michiel, P. Xiao, and R. Cernik, “Understanding the residual stress distribution through the thickness of atmosphere plasma sprayed (APS) thermal barrier coatings (TBCs) by high energy synchrotron XRD; digital image correlation (DIC) and image based modelling,” *Acta Mater.*, vol. 132, pp. 1–12, 2017.
- [54] R. Kingswell, K. T. Scott, and B. Sorensen, “Measurement of residual stress in plasma sprayed ceramic coatings,” in *Proc. 2nd Plasma-Technik Symp*, 1991, pp. 377–388.
- [55] T. M. Tien, N. V. Phoi, L. A. Tuyen, and L. L. Nguyen, “Study of Strain and Residual Stress Distribution in the Thickness Direction by Layer Removal Method and X-Ray Diffraction,” in *Green Technology and Sustainable Development (GTSD), International Conference on*, 2016, pp. 155–160.
- [56] G. G. Stoney, “The tension of metallic films deposited by electrolysis,” *Proc. R. Soc. London. Ser. A, Contain. Pap. a Math. Phys. Character*, vol. 82, no. 553, pp. 172–175, 1909.
- [57] A. Brenner and S. Senderoff, “Calculation of stress in electrodeposits from the curvature of a plated strip,” *J. Res. Natl. Bur. Stand. (1934)*, vol. 42, no. 2, p. 105, 1949.
- [58] M. Mutter, G. Mauer, R. Mücke, R. Vaßen, H. C. Back, and J. Gibmeier, “Investigations on the initial stress evolution during atmospheric plasma spraying of YSZ by in situ curvature measurement,” *J. Therm. Spray Technol.*, vol. 25, no. 4, pp. 672–683, 2016.
- [59] T. C. Totemeier and J. K. Wright, “Residual stress determination in thermally sprayed coatings—a comparison of curvature models and X-ray techniques,” *Surf. Coatings Technol.*, vol. 200, no. 12, pp. 3955–3962, 2006.
- [60] S. Sampath, V. Srinivasan, A. Valarezo, A. Vaidya, and T. Streibl, “Sensing, Control, and In Situ Measurement of Coating Properties: An Integrated Approach Toward Establishing Process-Property Correlations,” *J. Therm. Spray Technol.*,

vol. 18, no. 2, pp. 243–255, 2009.

- [61] X. Zhang, M. Watanabe, and S. Kuroda, “Effects of processing conditions on the mechanical properties and deformation behaviors of plasma-sprayed thermal barrier coatings: Evaluation of residual stresses and mechanical properties of thermal barrier coatings on the basis of in situ curvature mea,” *Acta Mater.*, vol. 61, no. 4, pp. 1037–1047, 2013.
- [62] F. A. Kandil, J. D. Lord, A. T. Fry, and P. V Grant, “A review of residual stress measurement methods,” *A Guid. to Tech. Sel. NPL, Rep. MATC*, vol. 4, 2001.
- [63] G. Montay, A. Cherouat, A. Nussair, and J. Lu, “Residual stresses in coating technology,” *J. Mater. Sci. Technol*, vol. 20, pp. 81–84, 2004.
- [64] M. Escribano and R. Gadow, “Residual stress measurement and modeling for ceramic layer composites,” *27th Int. Cocoa Beach Conf. Adv. Ceram. Compos. A*, pp. 615–622, 2003.
- [65] M. Buchmann, R. Gadow, and J. Tabellion, “Experimental and numerical residual stress analysis of layer coated composites,” *Mater. Sci. Eng. A*, vol. 288, no. 2, pp. 154–159, 2000.
- [66] K. Berreth, M. Buchmann, R. Gadow, and J. Tabellion, “Evaluation of residual stresses in thermal sprayed coatings,” in *Proc. of International Thermal Spray Conference, Düsseldorf*, 1999.
- [67] E. Held and J. Gibmeier, “Application of the Incremental Hole-Drilling Method on Thick Film Systems—An Approximate Evaluation Approach,” *Exp. Mech.*, vol. 55, no. 3, pp. 499–507, 2015.
- [68] P. Grant, J. Lord, P. Whitehead, and a. T. Fry, “The application of fine increment hole drilling for measuring machining-induced residual stresses,” in *Applied Mechanics and Materials*, 2005, vol. 3, no. 2005, pp. 105–110.
- [69] M. Sebastiani, C. Eberl, E. Bemporad, and G. M. Pharr, “Depth-resolved residual stress analysis of thin coatings by a new FIB–DIC method,” *Mater. Sci. Eng. A*, vol. 528, no. 27, pp. 7901–7908, 2011.
- [70] A. M. Korsunsky, M. Sebastiani, and E. Bemporad, “Focused ion beam ring drilling for residual stress evaluation,” *Mater. Lett.*, vol. 63, no. 22, pp. 1961–1963, 2009.
- [71] B. Winiarski and P. J. Withers, “Micron-scale residual stress measurement using micro-hole drilling and digital image correlation,” *Exp. Mech.*, vol. 52, no. 4, pp. 417–428, 2012.
- [72] S. Kuroda and T. W. Clyne, “The quenching stress in thermally sprayed coatings,” *Thin Solid Films*, vol. 200, no. 1, pp. 49–66, May 1991.
- [73] S. Widjaja, A. M. Limarga, and T. H. Yip, “Modeling of residual stresses in a

- plasma-sprayed zirconia/alumina functionally graded-thermal barrier coating,” *Thin Solid Films*, vol. 434, no. 1–2, pp. 216–227, Jun. 2003.
- [74] S. Kuroda, T. Fukushima, and S. Kitahara, “Significance of quenching stress in the cohesion and adhesion of thermally sprayed coatings,” *J. Therm. Spray Technol.*, vol. 1, no. 4, pp. 325–332, Dec. 1992.
- [75] H.-J. J. Kim and Y.-G. G. Kweon, “Elastic modulus of plasma-sprayed coatings determined by indentation and bend tests,” *Thin Solid Films*, vol. 342, no. 1, pp. 201–206, Mar. 1999.
- [76] Y. Tan, A. Shyam, W. B. Choi, E. Lara-Curzio, and S. Sampath, “Anisotropic elastic properties of thermal spray coatings determined via resonant ultrasound spectroscopy,” *Acta Mater.*, vol. 58, no. 16, pp. 5305–5315, Sep. 2010.
- [77] T. Valente, C. Bartuli, M. Sebastiani, and F. Casadei, “Finite element analysis of residual stress in plasma-sprayed ceramic coatings,” *Proc. Inst. Mech. Eng. Part L J. Mater. Des. Appl.*, vol. 218, no. 4, pp. 321–330, Oct. 2004.
- [78] J. Stokes and L. Looney, “Predicting Quenching and Cooling Stresses within HVOF Deposits,” *J. Therm. Spray Technol.*, vol. 17, no. 5–6, pp. 908–914, Nov. 2008.
- [79] J. Matejcek and S. Sampath, “In situ measurement of residual stresses and elastic moduli in thermal sprayed coatings: Part 1: apparatus and analysis,” *Acta Mater.*, vol. 51, no. 3, pp. 863–872, Feb. 2003.
- [80] H. Liao, P. Vaslin, Y. Yang, and C. Coddet, “Determination of residual stress distribution from in situ curvature measurements for thermally sprayed WC/Co coatings,” *J. Therm. spray Technol.*, vol. 6, no. 2, pp. 235–241, 1997.
- [81] K. G. Soderberg and A. K. Graham, “Stress in Electrodeposits Its Significance,” *Proc. Am. Electroplat. Soc.*, vol. 34, pp. 74–79, 1947.
- [82] S. TIMOSHENKO, “ANALYSIS OF BI-METAL THERMOSTATS,” *J. Opt. Soc. Am.*, vol. 11, no. 3, p. 233, Sep. 1925.
- [83] C. H. HSUEH and A. G. EVANS, “Residual Stresses in Meta/Ceramic Bonded Strips,” *J. Am. Ceram. Soc.*, vol. 68, no. 5, pp. 241–248, May 1985.
- [84] H. C. Liu and S. P. Murarka, “Elastic and viscoelastic analysis of stress in thin films,” *J. Appl. Phys.*, vol. 72, no. 8, p. 3458, Oct. 1992.
- [85] L. F. Francis, A. V. McCormick, D. M. Vaessen, and J. A. Payne, “Development and measurement of stress in polymer coatings,” *J. Mater. Sci.*, vol. 37, no. 22, pp. 4717–4731, 2002.
- [86] Z. Q. Jiang, Y. Huang, and A. Chandra, “Thermal Stresses in Layered Electronic Assemblies,” *J. Electron. Packag.*, vol. 119, no. 2, p. 127, Jun. 1997.

- [87] K. D. Cowley and P. W. R. Beaumont, "The measurement and prediction of residual stresses in carbon-fibre/polymer composites," *Compos. Sci. Technol.*, vol. 57, no. 11, pp. 1445–1455, Jan. 1997.
- [88] G. P. Cherepanov, "On the theory of thermal stresses in a thin bonding layer," *J. Appl. Phys.*, vol. 78, no. 11, p. 6826, Dec. 1995.
- [89] Y. Wen and C. Basaran, "An analytical model for thermal stress analysis of multi-layered microelectronic packaging," *Mech. Mater.*, vol. 36, no. 4, pp. 369–385, Apr. 2004.
- [90] C.-H. H. Hsueh, "Modeling of elastic deformation of multilayers due to residual stresses and external bending," *J. Appl. Phys.*, vol. 91, no. 12, pp. 9652–9656, May 2002.
- [91] X. C. Zhang, B. S. Xu, H. D. Wang, and Y. X. Wu, "An analytical model for predicting thermal residual stresses in multilayer coating systems," *Thin Solid Films*, vol. 488, no. 1–2, pp. 274–282, Sep. 2005.
- [92] P. H. Townsend, D. M. Barnett, and T. A. Brunner, "Elastic relationships in layered composite media with approximation for the case of thin films on a thick substrate," *J. Appl. Phys.*, vol. 62, no. 11, p. 4438, Dec. 1987.
- [93] C. H. Hsueh and S. Lee, "Modeling of elastic thermal stresses in two materials joined by a graded layer," *Compos. Part B Eng.*, vol. 34, no. 8, pp. 747–752, Dec. 2003.
- [94] X. C. C. Zhang, B. S. S. Xu, H. D. D. Wang, Y. Jiang, and Y. X. X. Wu, "Modeling of thermal residual stresses in multilayer coatings with graded properties and compositions," *Thin Solid Films*, vol. 497, no. 1–2, pp. 223–231, Feb. 2006.
- [95] X.-Y. Gong and D. R. Clarke, "On the Measurement of Strain in Coatings Formed on a Wrinkled Elastic Substrate," *Oxid. Met.*, vol. 50, no. 5–6, pp. 355–376, 1998.
- [96] C. H. Hsueh and E. R. Fuller, "Analytical modeling of oxide thickness effects on residual stresses in thermal barrier coatings," *Scr. Mater.*, vol. 42, no. 8, pp. 781–787, 2000.
- [97] X. C. Zhang, B. S. Xu, H. D. Wang, and Y. X. Wu, "Effects of oxide thickness, Al₂O₃ interlayer and interface asperity on residual stresses in thermal barrier coatings," *Mater. Des.*, vol. 27, no. 10, pp. 989–996, Jan. 2006.
- [98] M. SONG, Y. MA, and S. GONG, "Analysis of residual stress distribution along interface asperity of thermal barrier coating system on macro curved surface," *Prog. Nat. Sci. Mater. Int.*, vol. 21, no. 3, pp. 262–267, Jun. 2011.
- [99] Y. C. Tsui and T. W. Clyne, "An analytical model for predicting residual stresses in progressively deposited coatings Part 1: Planar geometry," *Thin Solid Films*,

- vol. 306, no. 1, pp. 23–33, Aug. 1997.
- [100] G. Bolelli, V. Cannillo, L. Lusvarghi, R. Rosa, A. Valarezo, W. B. Choi, R. Dey, C. Weyant, and S. Sampath, “Functionally graded WC–Co/NiAl HVOF coatings for damage tolerance, wear and corrosion protection,” *Surf. Coatings Technol.*, vol. 206, no. 8–9, pp. 2585–2601, Jan. 2012.
- [101] L. Wu, J. Zhu, and H. Xie, “Numerical and experimental investigation of residual stress in thermal barrier coatings during APS process,” *J. Therm. Spray Technol.*, vol. 23, no. 4, pp. 653–665, 2014.
- [102] J. Liu, R. Bolot, and S. Costil, “Residual stresses and final deformation of an alumina coating: Modeling and measurement,” *Surf. Coatings Technol.*, vol. 268, no. 2015, pp. 241–246, 2014.
- [103] Z. Gan, H. W. Ng, and A. Devasenapathi, “Deposition-induced residual stresses in plasma-sprayed coatings,” *Surf. Coatings Technol.*, vol. 187, no. 2–3, pp. 307–319, 2004.
- [104] G. Qian, T. Nakamura, and C. C. Berndt, “Effects of thermal gradient and residual stresses on thermal barrier coating fracture,” *Mech. Mater.*, vol. 27, no. 2, pp. 91–110, Feb. 1998.
- [105] F. Kroupa, “Nonlinear Behavior in Compression and Tension of Thermally Sprayed Ceramic Coatings,” *J. Therm. Spray Technol.*, vol. 16, no. 1, pp. 84–95, 2007.
- [106] R. Musalek, J. Matejicek, M. Vilemova, and O. Kovarik, “Non-Linear Mechanical Behavior of Plasma Sprayed Alumina Under Mechanical and Thermal Loading,” *J. Therm. Spray Technol.*, vol. 19, no. 1, pp. 422–428, 2010.
- [107] Y. Liu, T. Nakamura, V. Srinivasan, A. Vaidya, A. Gouldstone, and S. Sampath, “Non-linear elastic properties of plasma-sprayed zirconia coatings and associated relationships with processing conditions,” *Acta Mater.*, vol. 55, no. 14, pp. 4667–4678, Aug. 2007.
- [108] S. C. Gill and T. W. Clyne, “Thermomechanical Modeling of the Development of Residual Stress during Thermal Spraying,” in *2nd Plasma Technik Symposium*, 1991, pp. 227–238.
- [109] S. C. Gill and T. W. Clyne, “Property Data Evaluation for the Modeling of Residual Stress Development during Vacuum Plasma Spray Deposition,” in *1st European Conf. on Adv. Mats. and Procs. (Euromat '89)*, 1990, pp. 1221–1230.
- [110] G. A. Keramidas and E. C. Ting, “A finite element formulation for thermal stress analysis. Part I: Variational formulation,” *Nucl. Eng. Des.*, vol. 39, no. 2–3, pp. 267–275, Nov. 1976.
- [111] T. R. Chandrupatla, A. D. Belegundu, T. Ramesh, and C. Ray, “Introduction to

finite elements in engineering,” Upper Saddle River: Prentice Hall, 1997, pp. 279–300.

- [112] Y. Jiang, B. S. S. Xu, H. D. D. Wang, and Y. H. H. Lu, “Finite element modeling of residual stress around holes in the thermal barrier coatings,” *Comput. Mater. Sci.*, vol. 49, no. 3, pp. 603–608, 2010.
- [113] J. Stokes and L. Looney, “Residual stress in HVOF thermally sprayed thick deposits,” *Surf. Coatings Technol.*, vol. 177–178, pp. 18–23, Jan. 2004.
- [114] X. C. Zhang, B. S. Xu, H. D. Wang, and Y. X. Wu, “Modeling of the residual stresses in plasma-spraying functionally graded ZrO₂/NiCoCrAlY coatings using finite element method,” *Mater. Des.*, vol. 27, no. 4, pp. 308–315, Jan. 2006.
- [115] M. Buchmann and R. Gadow, “Estimation of residual stresses from the simulation of the deposition process of ceramic coatings on light metal cylinder liners,” in *25th Annual Conference on Composites, Advanced Ceramics, Materials, and Structures: B*, 2001, pp. 67–74.
- [116] M. Wenzelburger, M. Escribano, R. Gadow, M. Xue, S. Chandra, J. Mostaghimi, S. Chandra, M. Charmchi, M. Jadidi, M. Mousavi, S. Moghtadernejad, A. Dolatabadi, T. Wiederkehr, H. Mu, T. Wiederkehr, H. Mu, T. Universita, A. Ceramics, M. Escribano, R. Gadow, P. Bansal, P. H. Shipway, S. B. Leen, A. Kout, T. Wiederkehr, H. Müller, Y. Jia-sheng, Y. U. Jian-hua, Z. Xing-hua, Z. Hua-yu, S. E. E. Publication, T. Valente, C. A. Bartuli, M. Sebastiani, F. Casadei, E. Lugscheider, K. Bobzin, R. Nickel, T. Wiederkehr, H. Mu, L. Ri, H. H. P. Ri, R. Iru, R. Ehwzhq, U. U. Dqg, D. Ri, F. Pifurvwuxfwxuh, D. Q. G. Frdwlqj, S. Edvhg, S. Dqg, Z. Suhflvh, N. Ri, P. Ghsrvlwrq, S. Lv, S. Surfhhv, K. H. F. Yhorflw, Q. Iru, S. Sduwlfohv, W. R. Dgkhu, D. Q. G. Iorz, R. Q. Lpsdfw, L. V Fruuhodwhg, W. R. Whpshudwxuh, U. U. Dqg, W. R. Iorz, R. Q. Vxevwudwh, D. U. H. Lpsruwdqw, X. Iru, F. Ghsrvlwrq, Q. Vlpodwlrvq, G. Khdylo, R. Q. H. Sdudphwhul, D. Vfkphv, D. Q. G. Vlpsohu, F. Ghsrvlwrq, R. D. Door, D. Q. G. Pxlw, F. Pl, R. I. Gliihuhqw, S. Kdyh, I. Lqfuhdvhg, W. K. H. Frpsoh, D. V. Sk, V. Edvhg, P. Ghsrvlwrq, K. H. Ghsrvlwrq, S. Ghshqgv, R. Q. Pdwhuldo, U. Dw, K. Vkhdu, U. Dfurvv, Z. Udqjh, R. I. Whpshudwxuhv, R. Iruflv, L. Q. Wkh, D. Vfdoh, D. Q. G. Pdwhuldo, G. Suhglfwlrq, R. I. Vkhdu, L. Duh, L. Idfruv, I. R. U. Fuhdwlqj, P. Prgho, R. I. Ghsrvlwrq, P. Prgho, I. R. U. Pdvlyho, S. Frpsxwlqj, H. Zloo, E. H. Suhvhqwhg, Z. Sduwlfoh, W. Duh, I. Lqyhvwljdwgh, W. R. Vwxg, P. Lpsdfw, I. Dqg, D. Vl, H. Rq, D. Dqg, G. Rq, S. Xvlqj, D. Prohfxodu, V. Zloo, E. H. Ghprqvwudwhg, K. Iru, W. K. H. Pxlwvfdoh, V. Vxfk, D. V Lpsohphqwdwlrv, R. I. Lqwhuphwdoolf, U. Rq, G. Xvlqj, V. D. Q. G. Ioxlg, Q. Phwkrgv, I. R. U. Fkdudfwhul, D. Ri, W. Hiihfwv, Z. Eh, H. H. P. Ri, L. Dqg, H. H. P. Ri, I. N. Kellner, M. F. Zaeh, W. Li, K. Yang, D. Zhang, X. Zhou, M. Franz, S. Guessasma, G. Montavon, C. Coddet, S. E. E. Publication, D. A. Stepanenko, M. Li, P. D. Christofides, J. Mostaghimi, S. Chandra, A. Dolatabadi, X. Yuan, B. Zha, G. Hou, P. Hou, L. Jiang, H. Wang, M. Buchmann, R. Gadow, D. Lopez, M. Wenzelburger, M. Buchmann, M. Lee, B. Lee, J. Lim, M. Kim, D. Liu, S. T. Kyaw, P. E. J. Flewitt, M. Seraffon, N. J. Simms, M. Pavier, I. A. Jones,

- J. Zimmerman, Z. Lindemann, D. Golański, T. Chmielewski, and W. Włosiński, "Modeling of thermally sprayed coatings on light metal substrates : layer growth and residual stress formation," *Surf. Coat. Technol.*, vol. 181, no. 2004, pp. 429–435, 2004.
- [117] M. Wenzelburger, M. J. Riegert-Escribano, and R. Gadow, "Methods of residual stress analysis in layer composites and their application," in *Mechanical Properties and Performance of Engineering Ceramics and Composites: A Collection of Papers Presented at the 29th International Conference on Advanced Ceramics and Composites*, 2009, vol. 286, p. 371.
- [118] H. Zhao, J. Zhang, Z. Wang, P. Lin, and Z. Wang, "Adhesion and residual stress of plasma sprayed Alumina–titania coatings," *J. Adhes. Sci. Technol.*, vol. 29, no. 10, pp. 991–1001, 2015.
- [119] P. Fogarassy, F. Turquier, and A. Lodini, "Residual stress in plasma sprayed zirconia on cylindrical components," *Mech. Mater.*, vol. 35, no. 7, pp. 633–640, Jul. 2003.
- [120] E. Lugscheider and R. Nickel, "Finite element simulation of a coating formation on a turbine blade during plasma spraying," *Surf. Coatings Technol.*, vol. 174–175, no. 2003, pp. 475–481, Sep. 2003.
- [121] M. Lee, B. Lee, J. Lim, and M. Kim, "Residual stress analysis of the thermal barrier coating system by considering the plasma spraying process †," vol. 28, no. 6, pp. 2161–2168, 2014.
- [122] L. Wang, Y. Wang, X. G. G. Sun, J. Q. Q. He, Z. Y. Y. Pan, and C. H. H. Wang, "Finite element simulation of residual stress of double-ceramic-layer La₂Zr₂O₇/8YSZ thermal barrier coatings using birth and death element technique," *Comput. Mater. Sci.*, vol. 53, no. 2012, pp. 117–127, 2012.
- [123] P. Bengtsson and C. Persson, "Modelled and measured residual stresses in plasma sprayed thermal barrier coatings," *Surf. Coatings Technol.*, vol. 92, no. 1–2, pp. 78–86, Jun. 1997.
- [124] L. R. Alejano and A. Bobet, "Drucker-Prager criterion," *Rock Mech. Rock Eng.*, vol. 45, no. 6, pp. 995–999, 2012.
- [125] H. W. Ng and Z. Gan, "A finite element analysis technique for predicting as-sprayed residual stresses generated by the plasma spray coating process," *Finite Elem. Anal. Des.*, vol. 41, no. 13, pp. 1235–1254, 2005.
- [126] J. Zimmerman, "Finite Element Modelling of the Residual Stresses Induced in Thermally Deposited Coatings," *Arch. Metall. Mater.*, vol. 59, no. 2, pp. 593–599, 2014.
- [127] J. Zimmerman, Z. Lindemann, D. Golański, T. Chmielewski, and W. Włosiński, "Modeling residual stresses generated in Ti coatings thermally sprayed on Al₂O₃

- 3 substrates,” *Bull. Polish Acad. Sci. Tech. Sci.*, vol. 61, no. 2, pp. 515–525, 2013.
- [128] P. Bansal, P. H. Shipway, and S. B. Leen, “Residual stresses in high-velocity oxy-fuel thermally sprayed coatings – Modelling the effect of particle velocity and temperature during the spraying process,” *Acta Mater.*, vol. 55, no. 2007, pp. 5089–5101, 2007.
- [129] P. Bansal, P. H. Shipway, and S. B. Leen, “Effect of Particle Impact on Residual Stress Development in HVOF Sprayed Coatings,” *J. Therm. Spray Technol.*, vol. 15, no. 4, pp. 570–575, 2006.
- [130] M. Elhoriny, M. Wenzelburger, A. Killinger, and R. Gadow, “Experimental Investigation and Finite Element Simulation of Residual Stress Development in Thermally Sprayed Coatings,” in *International Thermal Spray Conference and Exposition*, 2015.
- [131] S. J. Hollister and B. A. Riemer, “<title>Digital-image-based finite element analysis for bone microstructure using conjugate gradient and Gaussian filter techniques</title>,” in *SPIE’s 1993 International Symposium on Optics, Imaging, and Instrumentation*, 1993, pp. 95–106.
- [132] K. Terada, T. Miura, and N. Kikuchi, “Digital image-based modeling applied to the homogenization analysis of composite materials,” *Comput. Mech.*, vol. 20, no. 4, pp. 331–346, Sep. 1997.
- [133] S. A. Langer, E. R. Fuller, and W. C. Carter, “OOF: an image-based finite-element analysis of material microstructures,” *Comput. Sci. Eng.*, vol. 3, no. 3, pp. 15–23, 2001.
- [134] C.-H. H. Hsueh, J. A. Haynes, M. J. Lance, P. F. Becher, M. K. Ferber, E. R. Fuller, S. A. Langer, W. C. Carter, and W. R. Cannon, “Effects of Interface Roughness on Residual Stresses in Thermal Barrier Coatings,” *J. Am. Ceram. Soc.*, vol. 82, no. 4, pp. 1073–1075, Apr. 1999.
- [135] R. Berthelsen, D. Tomath, R. Denzer, and A. Menzel, “Finite element simulation of coating-induced heat transfer: application to thermal spraying processes,” *Meccanica*, vol. 51, no. 2, pp. 291–307, 2016.
- [136] A. Farrokhpahan, M. Bussmann, and J. Mostaghimi, “A New Smoothed Particle Hydrodynamics (SPH) Formulation for Modelling Heat Conduction with Solidification and Melting,” *arXiv Prepr. arXiv1608.04400*, vol. 71, no. 4, pp. 299–312, 2017.
- [137] R. Das and P. W. W. Cleary, “Three-dimensional modelling of coupled flow dynamics, heat transfer and residual stress generation in arc welding processes using the mesh-free SPH method,” *J. Comput. Sci.*, vol. 16, pp. 200–216, 2016.
- [138] P. Profizi, A. Combescure, and K. Ogawa, “SPH modeling of adhesion in fast dynamics: Application to the Cold Spray process,” *Comptes Rendus - Mec.*, vol.

- 344, no. 4–5, pp. 211–224, 2016.
- [139] J. Lu, J. Qian, and W. Han, “Discrete gradient method in solid mechanics,” *Int. J. Numer. Methods Eng.*, vol. 74, no. 4, pp. 619–641, 2008.
- [140] J. Lu and J. Qian, “Discrete gradient method over polygon mesh,” *Int. J. Numer. Methods Eng.*, vol. 78, no. 5, pp. 505–527, 2009.
- [141] E. B. Chin, J.-B. Lasserre, and N. Sukumar, “Modeling crack discontinuities without element-partitioning in the extended finite element method,” *Int. J. Numer. Methods Eng.*, 2016.
- [142] B. L. Talamini and R. Radovitzky, “A parallel discontinuous Galerkin/cohesive-zone computational framework for the simulation of fracture in shear-flexible shells,” *Comput. Methods Appl. Mech. Eng.*, vol. 317, pp. 480–506, 2016.
- [143] S. Rezaei, S. Wulfinghoff, and S. Reese, “Prediction of fracture in grain boundaries of nano-coatings using cohesive zone elements,” *PAMM*, vol. 16, no. 1, pp. 163–164, 2016.
- [144] V. Kouznetsova, M. G. D. Geers, and W. A. M. Brekelmans, “Multi-scale constitutive modelling of heterogeneous materials with a gradient-enhanced computational homogenization scheme,” *Int. J. Numer. Methods Eng.*, vol. 54, no. 8, pp. 1235–1260, 2002.
- [145] M. G. D. Geers, V. G. Kouznetsova, and W. A. M. Brekelmans, “Multi-scale computational homogenization: Trends and challenges,” *J. Comput. Appl. Math.*, vol. 234, no. 7, pp. 2175–2182, 2010.
- [146] A. M. Kamara and K. Davey, “A numerical and experimental investigation into residual stress in thermally sprayed coatings,” *Int. J. Solids Struct.*, vol. 44, no. 25, pp. 8532–8555, 2007.
- [147] S. Chandra and P. Fauchais, “Formation of solid splats during thermal spray deposition,” *J. Therm. Spray Technol.*, vol. 18, no. 2, pp. 148–180, 2009.
- [148] M. Corsini, P. Cignoni, and R. Scopigno, “Efficient and flexible sampling with blue noise properties of triangular meshes,” *IEEE Trans. Vis. Comput. Graph.*, vol. 18, no. 6, pp. 914–924, 2012.
- [149] X. Ying, Z. Li, and Y. He, “A parallel algorithm for improving the maximal property of Poisson disk sampling,” *Comput. Des.*, vol. 46, no. 1, pp. 37–44, 2014.
- [150] H. Edelsbrunner and E. P. Mücke, “Three-dimensional alpha shapes,” *ACM Trans. Graph.*, vol. 13, no. 1, pp. 43–72, 1994.
- [151] G. Kamberov, G. Kamberova, and A. Jain, “3D Shape from Unorganized 3D Point Clouds BT - Advances in Visual Computing: First International Symposium, ISVC 2005, Lake Tahoe, NV, USA, December 5-7, 2005. Proceedings,” G. Bebis, R. Boyle, D. Koracin, and B. Parvin, Eds. Berlin, Heidelberg: Springer Berlin

Heidelberg, 2005, pp. 621–629.

- [152] H. Hoppe, “Poisson surface reconstruction and its applications,” in *Proceedings of the 2008 ACM symposium on Solid and physical modeling*, 2008, p. 10.
- [153] M. Kazhdan and H. Hoppe, “Screened poisson surface reconstruction,” *ACM Trans. Graph.*, vol. 32, no. 3, p. 29, 2013.
- [154] M. M. . b Garland and Y. b Zhou, “Quadric-based simplification in any dimension,” *ACM Trans. Graph.*, vol. 24, no. 2, pp. 209–239, 2005.
- [155] S. Boyé, G. Guennebaud, and C. Schlick, “Least squares subdivision surfaces,” in *Computer Graphics Forum*, 2010, vol. 29, no. 7, pp. 2021–2028.
- [156] S. D. Aziz and S. Chandra, “Impact, recoil and splashing of molten metal droplets,” *Int. J. Heat Mass Transf.*, vol. 43, no. 16, pp. 2841–2857, 2000.
- [157] Y. Shao, B. Liu, X. Wang, L. Li, J. Wei, and F. Song, “Crack propagation speed in ceramic during quenching,” *J. Eur. Ceram. Soc.*, vol. 38, no. 7, pp. 2879–2885, 2018.
- [158] M. Elhoriny, M. Wenzelburger, A. Killinger, and R. Gadow, “Finite Element Simulation of Residual Stress Development in Thermally Sprayed Coatings,” *J. Therm. Spray Technol.*, vol. 26, no. 4, pp. 735–744, 2017.
- [159] Oerlikon Metco, “Nickel Chromium – Aluminum Thermal Spray Powders,” 2017. [Online]. Available: https://www.oerlikon.com/ecomaXL/files/metco/oerlikon_DSMTS-0091.5_NiCrAl.pdf&download=1.
- [160] J.J.~Monaghan and J.J.Monaghan, “Smoothed Particle Hydrodynamics,” *Annu.~Rev.~Astron.~Astrophys.*, vol. 30, pp. 543–574, 1992.
- [161] L. Chen and L. Yueming, “Interface stress evolution considering the combined creep–plastic behavior in thermal barrier coatings,” *Mater. Des.*, vol. 89, pp. 245–254, 2016.
- [162] S. Matthews, Y. Zhang, M. Hyland, S. Matthews, and M. Hyland, “Role of solidification in the formation of plasma sprayed nickel splats through simulation and experimental observation,” *Int. J. Heat Mass Transf.*, vol. 115, pp. 488–501, 2017.
- [163] M. Y. Zhang, H. Zhang, and L. L. Zheng, “Simulation of droplet spreading, splashing and solidification using smoothed particle hydrodynamics method,” *Int. J. Heat Mass Transf.*, vol. 51, no. 13, pp. 3410–3419, 2008.
- [164] Z. Zhu, S. Kamnis, and S. Gu, “Numerical study of molten and semi-molten ceramic impingement by using coupled Eulerian and Lagrangian method,” *Acta Mater.*, vol. 90, pp. 77–87, 2015.

- [165] J. W. Adams, R. Ruh, and K. S. Mazdidasni, “Young’s modulus, flexural strength, and fracture of yttria-stabilized zirconia versus temperature,” *J. Am. Ceram. Soc.*, vol. 80, no. 4, pp. 903–908, 1997.
- [166] H. Hayashi, T. Saitou, N. Maruyama, H. Inaba, K. Kawamura, and M. Mori, “Thermal expansion coefficient of yttria stabilized zirconia for various yttria contents,” *Solid state ionics*, vol. 176, no. 5, pp. 613–619, 2005.
- [167] F. Cverna, *Worldwide guide to equivalent irons and steels*. ASM international, 2006.
- [168] Oerlikon Metco, “80 % Nickel / 20 % Aluminum Chemically Clad Powders,” 2017.
- [169] Oerlikon Metco, “8 % Yttria Stabilized Zirconia Agglomerated and HOSP Thermal Spray Powders,” pp. 1–6, 2017.
- [170] W. C. Oliver and G. M. Pharr, “An improved technique for determining hardness and elastic modulus using load and displacement sensing indentation experiments,” *J. Mater. Res.*, vol. 7, no. 6, pp. 1564–1583, 1992.
- [171] I. N. Sneddon, “The relation between load and penetration in the axisymmetric boussinesq problem for a punch of arbitrary profile,” *Int. J. Eng. Sci.*, vol. 3, no. 1, pp. 47–57, May 1965.
- [172] V. P. Group, “Measurement of Residual Stresses by the Hole-Drilling* Strain Gage Method,” *Tech Note TN-503*, vol. 11053, pp. 19–33, 2010.
- [173] Vishay-Micromeritics, “Instruction Bulletin B-129-8: Surface Preparation for Strain Gage Bonding,” 2014.
- [174] Vishay-Micromeritics, “Instruction Bulletin B-127-14: Strain Gage Installations with M-Bond 200 Adhesive,” 2014.
- [175] P. Weidmann, U. Weber, S. Schmauder, and V. M. García, “Investigation of influence factors on residual stress determination within coated surfaces in consideration of the differential and integral method,” *Adv. Mater. Res.*, vol. 996, 2014.
- [176] E. Obelode and J. Gibmeier, “Residual stress analysis on thick film systems by the incremental hole-drilling method—simulation and experimental results,” *Exp. Mech.*, vol. 53, no. 6, pp. 965–976, 2013.
- [177] Michael Baucio, Ed., *ASM Engineered Materials Reference Book*, Second. Materials Park, OH: ASM International, 1994.
- [178] M. Sebastiani, G. Bolelli, L. Lusvardi, P. P. Bandyopadhyay, and E. Bemporad, “High resolution residual stress measurement on amorphous and crystalline plasma-sprayed single-splats,” *Surf. Coatings Technol.*, vol. 206, no. 23, pp. 4872–4880, 2012.

- [179] Z. Chen, H. Zheng, G. Li, H. Li, and P. Peng, “Mechanism of crack nucleation and growth in YSZ thermal barrier coatings corroded by CMAS at high temperatures: First-principles calculation,” *Corros. Sci.*, vol. 142, pp. 258–265, 2018.
- [180] C. R. C. Lima, J. Nin, and J. M. Guilemany, “Evaluation of residual stresses of thermal barrier coatings with HVOF thermally sprayed bond coats using the Modified Layer Removal Method (MLRM),” *Surf. Coatings Technol.*, vol. 200, no. 20–21, pp. 5963–5972, 2006.
- [181] R. Ghafouri-Azar, J. Mostaghimi, S. Chandra, and M. Charmchi, “A Stochastic Model to Simulate the Formation of a Thermal Spray Coating,” *J. Therm. Spray Technol.*, vol. 12, no. 1, pp. 53–69, 2003.
- [182] R. Soltani, T. W. Coyle, J. Mostaghimi, R. S. Lima, and C. Moreau, “Thermophysical properties of plasma sprayed Yttria Stabilized Zirconia Coatings,” *Surf. Coatings Technol.*, vol. 202, no. 16, pp. 3954–3959, 2008.
- [183] M. Mutter, G. Mauer, R. Mücke, O. Guillon, and R. Vaßen, “Correlation of splat morphologies with porosity and residual stress in plasma-sprayed YSZ coatings,” *Surf. Coatings Technol.*, vol. 318, pp. 157–169, 2017.
- [184] S. Schuster and J. Gibmeier, “Incremental hole drilling for residual stress analysis of strongly textured material states—a new calibration approach,” *Exp. Mech.*, vol. 56, no. 3, pp. 369–380, 2016.
- [185] A. A. Abubakar and A. F. M. Arif, “A hybrid computational approach for modeling thermal spray deposition,” *Surf. Coatings Technol.*, vol. 362, pp. 311–327, 2019.
- [186] A. A. Abubakar, A. F. M. Arif, S. S. Akhtar, and J. Mostaghimi, “Splats Formation, Interaction and Residual Stress Evolution in Thermal Spray Coating Using a Hybrid Computational Model,” *J. Therm. Spray Technol.*, vol. 28, no. 3, pp. 359–377, 2019.
- [187] C. Guinard, G. Montay, V. Guipont, M. Jeandin, J. Girardot, M. Schneider, B. Coats, C. Guinard, G. Montay, V. Guipont, M. Jeandin, J. Girardot, and M. Schneider, “Residual stress analysis of laser-drilled thermal barrier coatings involving various bond coats,” *J. Therm. Spray Technol.*, vol. 24, no. January, pp. 252–262, 2015.
- [188] M. Vardelle, A. Vardelle, A. C. Leger, P. Fauchais, and D. Gobin, “Influence of particle parameters at impact on splat formation and solidification in plasma spraying processes,” *J. Therm. Spray Technol.*, vol. 4, no. 1, pp. 50–58, 1995.
- [189] M. Pasandideh-Fard, V. Pershin, S. Chandra, and J. Mostaghimi, “Splat shapes in a thermal spray coating process: simulations and experiments,” *J. Therm. Spray Technol.*, vol. 11, no. 2, pp. 206–217, 2002.
- [190] S. Alavi and M. Passandideh-Fard, “Numerical Simulation of Droplet Impact and

Solidification Including Thermal Shrinkage in a Thermal Spray Process,” in *2010 14th International Heat Transfer Conference*, 2010, no. 2, pp. 731–739.

- [191] K. Shinoda, J. Colmenares-Angulo, A. Valarezo, and S. Sampath, “Effect of deposition rate on the stress evolution of plasma-sprayed yttria-stabilized zirconia,” *J. Therm. Spray Technol.*, vol. 21, no. 6, pp. 1224–1233, 2012.
- [192] H. Liu, F. Azarmi, M. Bussmann, J. Mostaghimi, and T. W. Coyle, “Experiments and simulation of rapid solidification of air plasma sprayed alloy 625 on stainless steel,” *Surf. Coatings Technol.*, vol. 204, no. 9–10, pp. 1521–1527, 2010.

Appendix

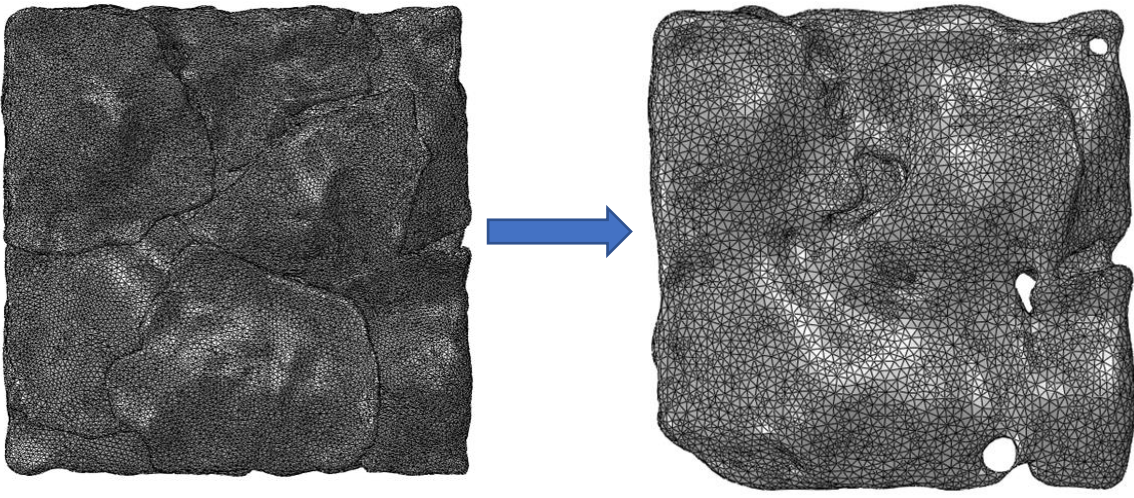
Table-A1: Comparison of numerical results obtained with birth-death technique with experiments

Coating material, material model and model geometry	Maximum residual stress and location	Validation	Deviation from experimental result	Source
Titania ¹ , 3D cylindrical substrate	$\sigma_{1,2} = -50MPa$ at S $\sigma_{1,2} = -5MPa$ at I	[a]	>100%	[115]
Alumina ¹ , 3D cylindrical substrate	$\sigma_{1,2} = -10MPa$ at S and I		0 → >300%	[65]
AT13 ² , 3D	$\sigma_r = 244MPa$, $\sigma_a = 240MPa$ at an edge near coating surface	[b]	-51.5% → 49.5%	[118]
Alumina ² , 3D	$\sigma_{1,2} = -55MPa$ at S $\sigma_{1,2} = -65MPa$ at I	[a]	-66.7% → -20%	[77]
Alumina ² , 3D	$\sigma_x = -422MPa$ at S $\sigma_x = -92MPa$ at S	[d]	15.6%	[102]
nickel–cobalt ² , axisymmetric	$\sigma_r = 2.6GPa$ at I	[d]	unpredictable	[103]
TBC ² , axisymmetric	$\sigma_r = -80MPa$ at S $\sigma_r = -60MPa$ at I	[e]	-300%	[123]
TBC ¹ , 2D curved geometry	$\sigma_a = 190MPa$ at I $\sigma_a = 10MPa$ at S	[c]	-77.25% → 127.5%	[119]
TBC ¹ , 3D turbine blade geometry	$\sigma_{vm} = 3.37GPa$ at blade profile edge	-	-	[120]
TBC ¹ , axisymmetric	$\sigma_{vm} = 145MPa$ at I	-	-	[121]
TBC ¹ , axisymmetric-on SCL and DCL	DCL showed lower residual stresses in all cases	-	-	[122]
TBC ² , axisymmetric	$\sigma_r = -130MPa$ at S $\sigma_r = -150MPa$ at I	[d]	Good agreement on displacements	[101]
Titanium ³ ,	$\sigma_r = 60MPa$ at S	[d]	Fair	[126],

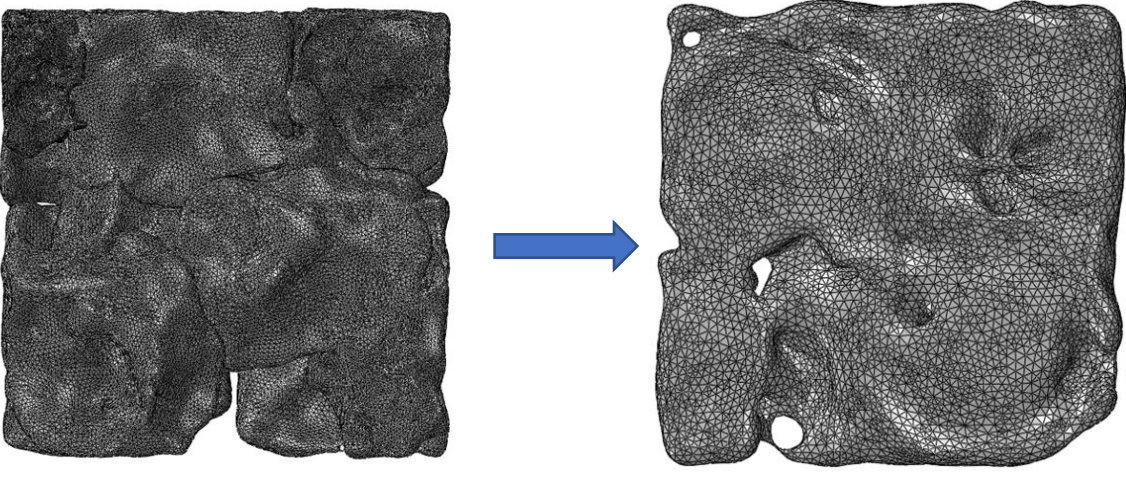
axisymmetric	$\sigma_r = -60MPa$ at I for $1.45 \mu m$ thickness		agreement on displacements	[127]
IN718 ³ , single- particle model	$\sigma_a = 400MPa$ $\sigma_r = 1000MPa$ at contact region	-	-	[32]
SS 316 ³ , axisymmetric	$\sigma_r = -250MPa$ at S $\sigma_r = 500MPa$ at I for coatings deposited at $610 m/s$ and 1593 K	[b]	-2.08% → 2.08%	[128], [129]

1-elastic, 2-elasto-plastic, 3-elasto-plastic with contact formulation, a-incremental hole drilling method, b-XRD, c-neutron diffraction, d-curvature measurement, e-modified layer removal method, $\sigma_{1,2}$ -in-plane stress, σ_x -longitudinal stress, σ_r -radial stress, σ_a -axial stress, σ_{vm} -von Mises stress, S-coating surface, I-coating-substrate interface.

|



(a)



(b)

Figure A1: Conversion to merged mesh for Pass-3: (a) top view and (b) bottom view (LEFT-layer-by-layer mesh, RIGHT-merged mesh)

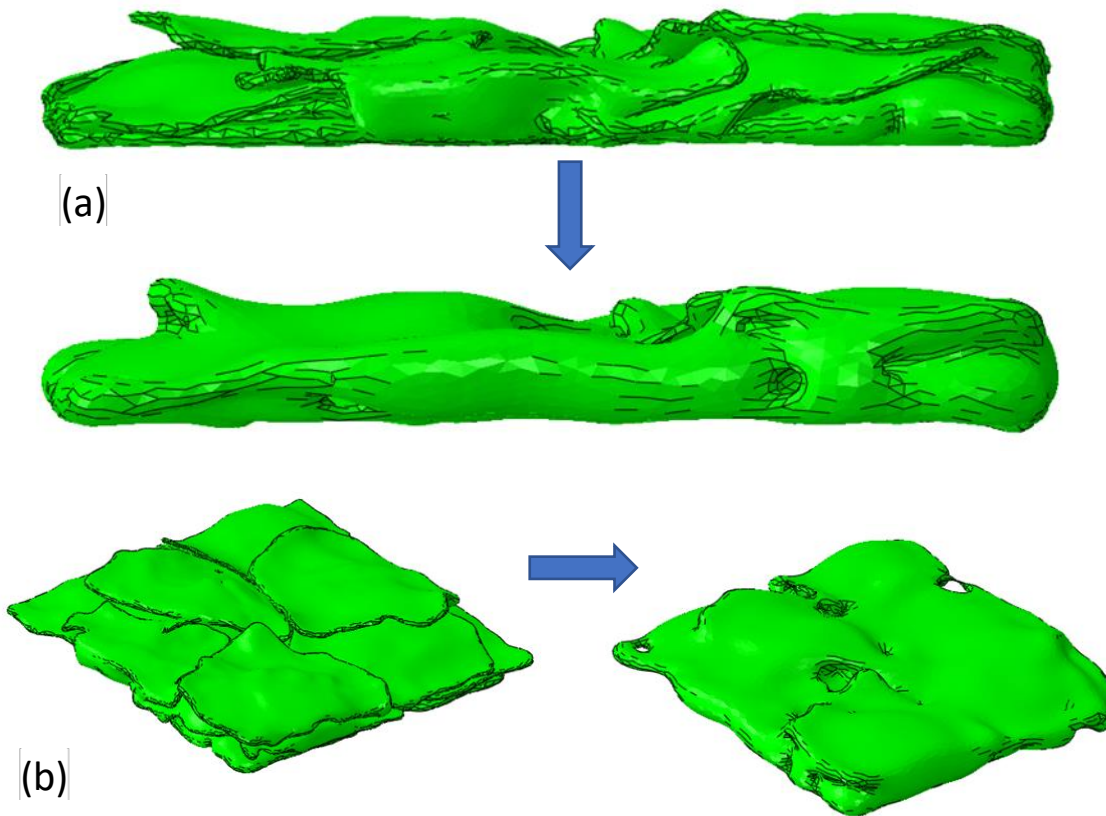
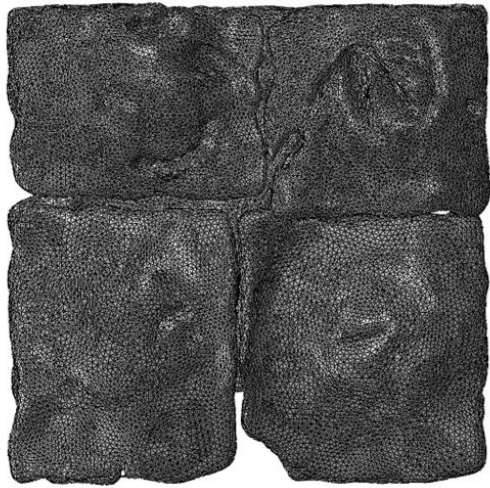
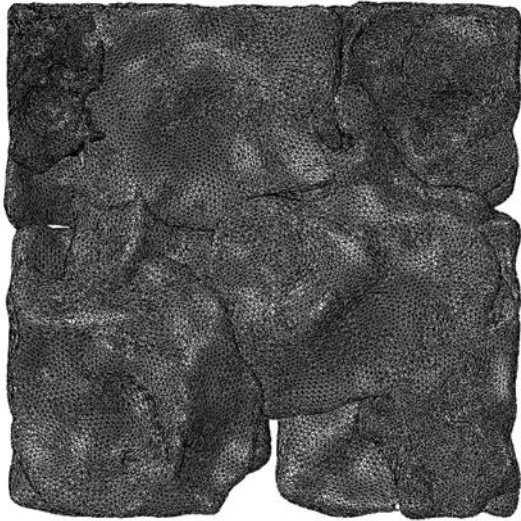
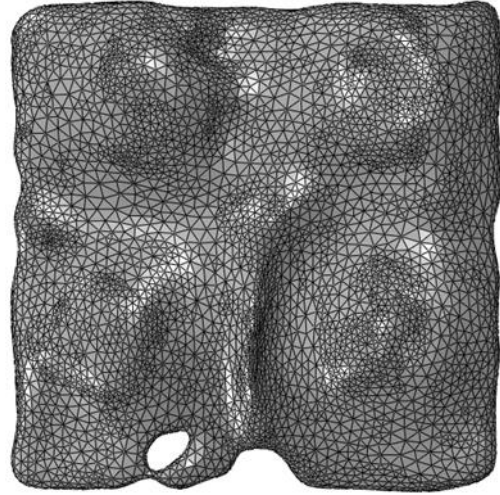


Figure A2: Conversion to merged mesh for Pass-3: (a) side view and (b) isometric view (LEFT-layer-by-layer mesh, RIGHT-merged mesh)



(a)



(b)

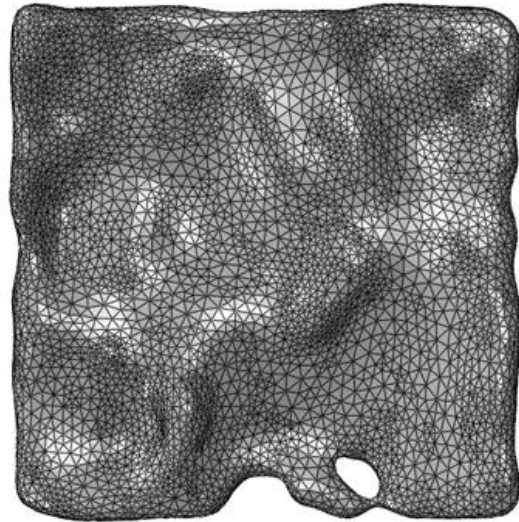


Figure A3: Conversion to merged mesh for Pass-4: (a) top view and (b) bottom view (LEFT-layer-by-layer mesh, RIGHT-merged mesh)

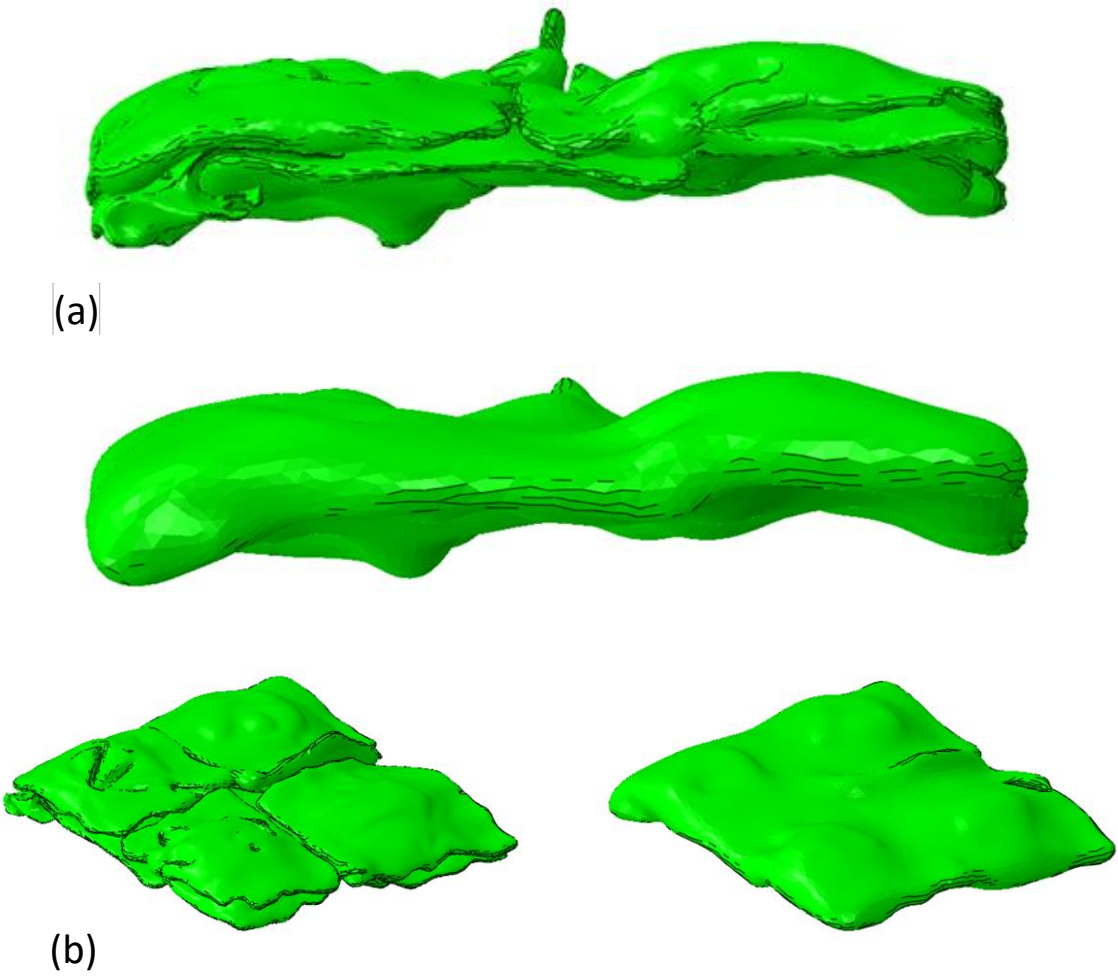


Figure A4: Conversion to merged mesh for Pass-3: (a) side view and (b) isometric view (LEFT-layer-by-layer mesh, RIGHT-merged mesh)

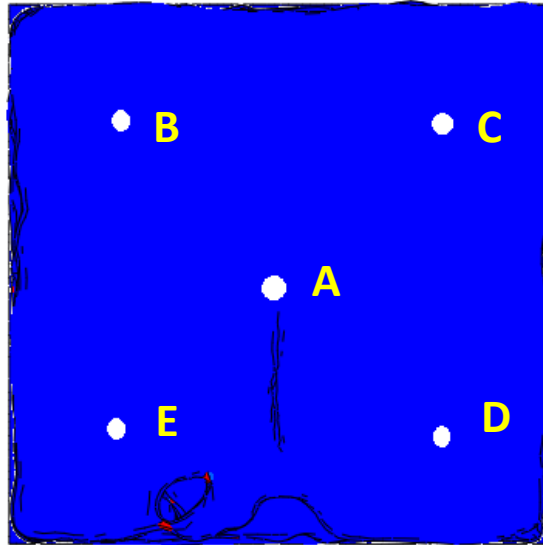


Figure A5: Five points selected for analysis: A (0,0), B(-125, 125), C(125,125), D(125,-125), and E (-125,-125). All dimensions in mm.

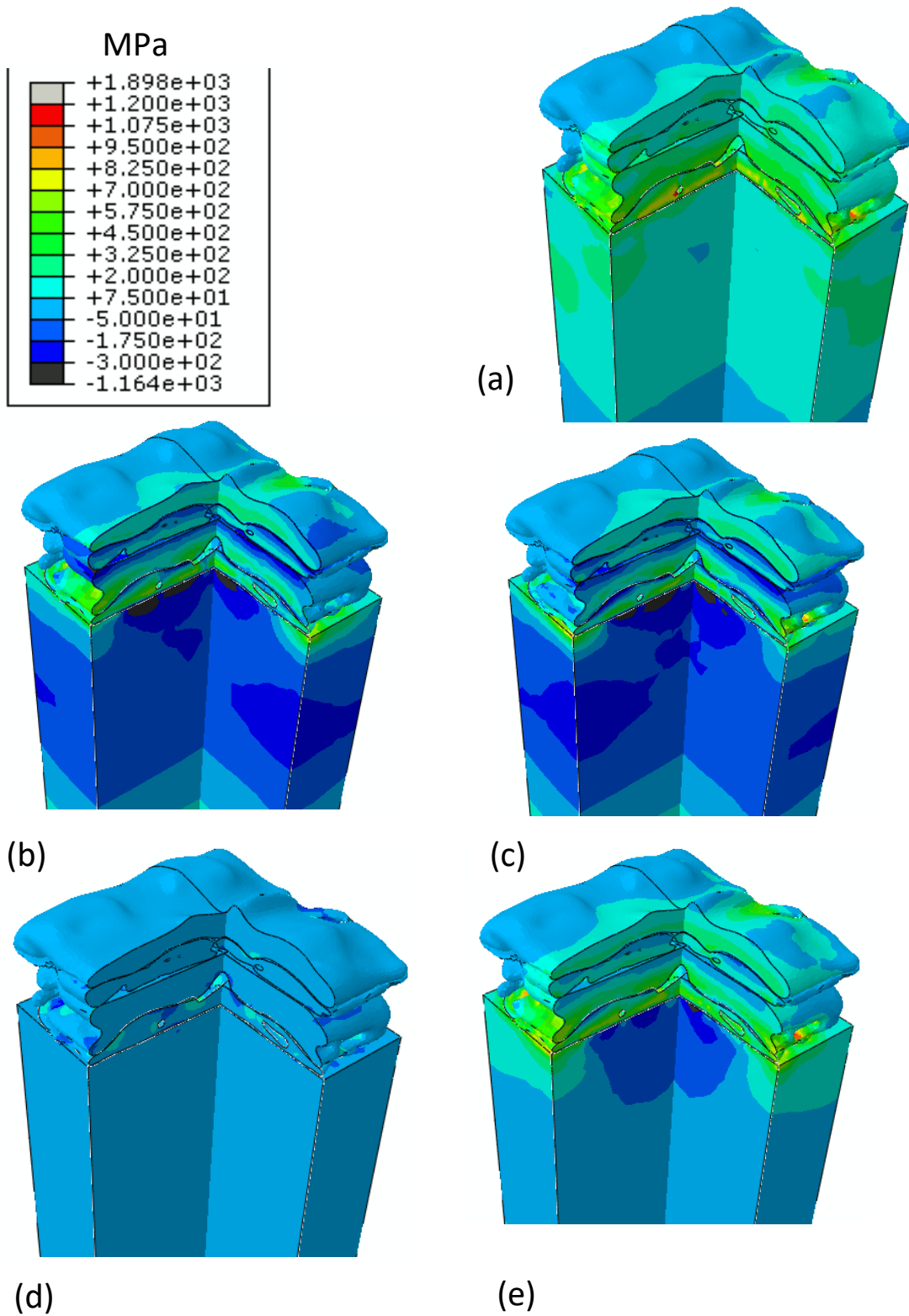


Figure A6: Quenching stress developed after solidification of fourth pass of YSZ coating: (a) von Mises stress, (b) normal stress in x-direction, (c) normal stress in y-direction, (d) shear stress in xy-plane, and (e) maximum principal stress

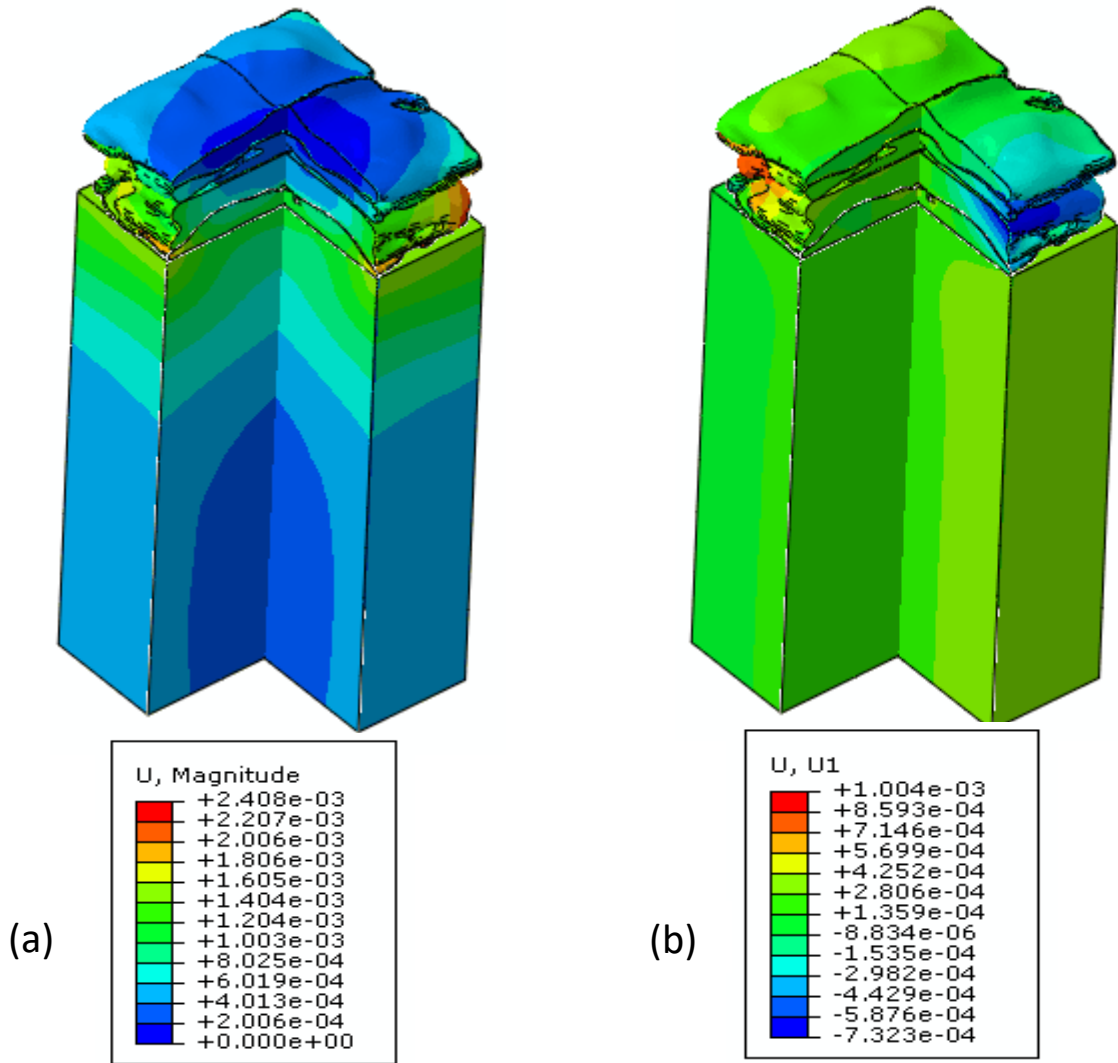


Figure A7: Displacement field (mm) developed after solidification of fourth pass of YSZ coating: (a) displacement magnitude and (b) displacement in x-direction

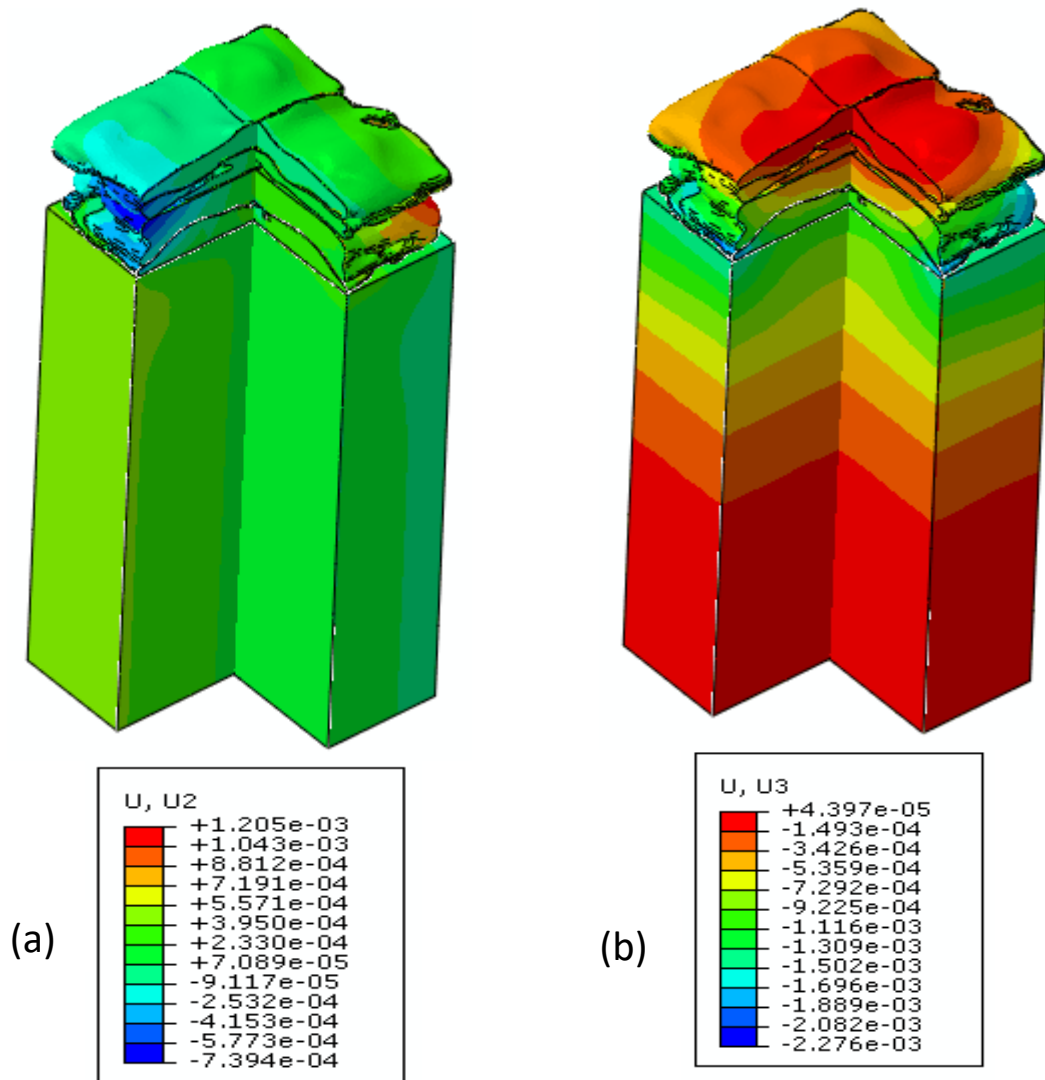


Figure A8: Displacement field (mm) developed after solidification of fourth pass of YSZ coating: (a) displacement magnitude and (b) displacement in x-direction

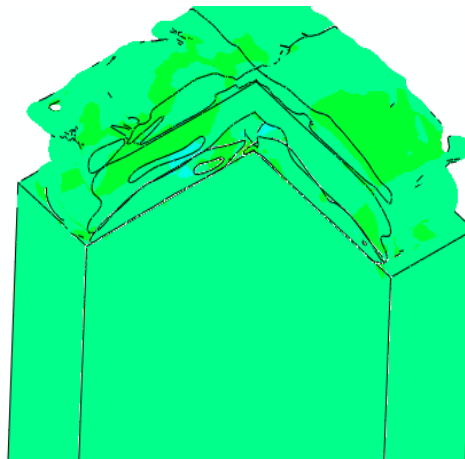
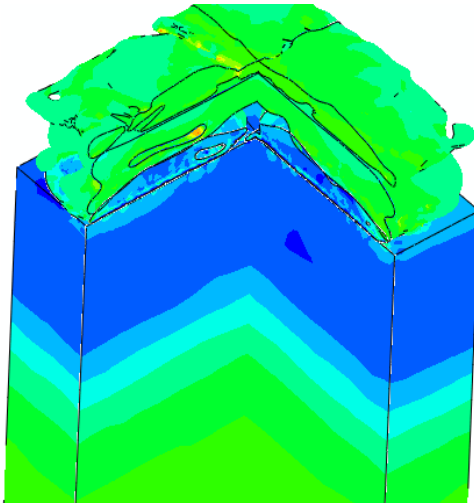
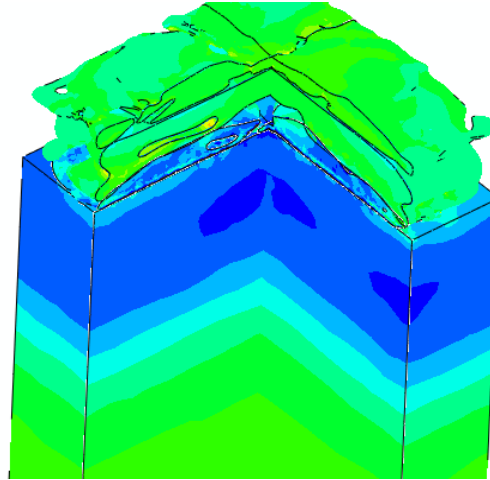
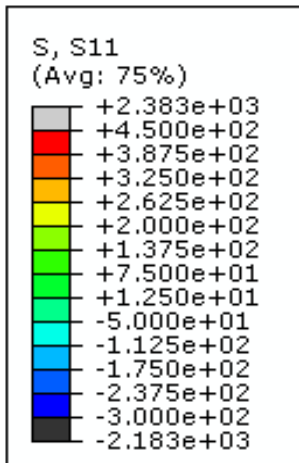


Figure A9: Quenching stress developed after solidification of fourth pass of Ni-20%Al coating: (a) normal stress in x-direction, (b) normal stress in y-direction, and (c) shear stress in xy-plane.

Vitae

Name :[Abba Abdulhamid Abubakar]
Nationality :[Nigerian]
Date of Birth :[9/2/1988]
Email :[abbamec@yahoo.com]
Permanent Home Address :[Garba Abdulhamid Ahmed Furnitures, No. 7, Zakat and Endowment Plaza II,
Unguwar Dallatu, 860211, Gusau, Zamfara State, Nigeria]

Academic Background:

MSc Mechanical Engineering (2014)

King Fahd University of Petroleum & Minerals,

Dhahran, Saudi Arabia

B.Eng Mechanical Engineering (2011)

Bayero University Kano,

Kano, Nigeria

Publications from Dissertation Work

Journal papers

1. **Abubakar, Abba A.**, Abul Fazal M. Arif, Khaled S. Al-Athel, S. Sohail Akhtar, and Javad Mostaghimi. "Modeling residual stress development in thermal spray coatings: current status and way forward." *Journal of Thermal Spray Technology* 26, no. 6 (2017): 1115-1145.
2. **Abubakar, Abba A.**, Abul Fazal M. Arif, Syed Sohail Akhtar, and Javad Mostaghimi. "Splats Formation, Interaction and Residual Stress Evolution in Thermal Spray Coating Using a Hybrid Computational Model." *Journal of Thermal Spray Technology* 28, no. 3 (2019): 359-377.

3. **Abubakar, Abba A.**, and Abul Fazal M. Arif. "A hybrid computational approach for modeling thermal spray deposition." *Surface and Coatings Technology* 362 (2019): 311-327.
4. **Abubakar, Abba A.**, Akeem Y. Adesina, Abul Fazal M. Arif., Jafar Albinmoussa, Syed Sohail Akhtar "Characterization and understanding of residual stress in thermal spray coatings." *Material Sci. & Engr. A* (under review).
5. **Abubakar, Abba A.**, and Abul Fazal M. Arif. "Crack formation and residual stress evolution in TBC." *Journal of European Ceramic Society* (under review).

Conference proceedings

6. **Abubakar, Abba A.**, Abul Fazal M. Arif, Khaled S. Al-Athel, and S. Sohail Akhtar. "Prediction of Residual Stress and Damage in Thermal Spray Coatings Using Hybrid Computational Approach." In ASME 2018 International Mechanical Engineering Congress and Exposition, pp. V002T02A041-V002T02A041. American Society of Mechanical Engineers, 2018.